



# Durham E-Theses

---

## *Control of Dynamic Supramolecular Systems*

HUSSEIN, BURHAN,AHMED

### How to cite:

---

HUSSEIN, BURHAN,AHMED (2023) *Control of Dynamic Supramolecular Systems*, Durham theses, Durham University. Available at Durham E-Theses Online: <http://etheses.dur.ac.uk/15046/>

### Use policy

---

The full-text may be used and/or reproduced, and given to third parties in any format or medium, without prior permission or charge, for personal research or study, educational, or not-for-profit purposes provided that:

- a full bibliographic reference is made to the original source
- a [link](#) is made to the metadata record in Durham E-Theses
- the full-text is not changed in any way

The full-text must not be sold in any format or medium without the formal permission of the copyright holders.

Please consult the [full Durham E-Theses policy](#) for further details.



Durham  
University

Department of Chemistry

# **Control of Dynamic Supramolecular Systems**

Burhan Ahmed Hussein

A Thesis Submitted for the Degree  
of Doctor of Philosophy

April 2023

*Dedicated to my role models, and my most  
supportive champions – my parents.*

*Ahmed Duale*

*Aisha Mohammed*

## Table of Content

Abstract .....	vii
Declaration .....	viii
Conferences Attended and Presentations Given .....	ix
Awards, Grants and Scholarships .....	ix
Publications.....	ix
Acknowledgments.....	x
List of Abbreviations .....	xii
Thesis Layout .....	xiv

## Chapter 1 | Ion Transport Across Lipid Membranes

<b>1.0 Synopsis.....</b>	<b>2</b>
<b>1.1 Photosynthesis in Plants .....</b>	<b>2</b>
1.1.1 Cell Membrane.....	2
1.1.2 Light-Dependent Reactions.....	3
1.1.3 Light-Independent Reactions .....	4
<b>1.2. Ion Transport in Biological Systems .....</b>	<b>6</b>
1.2.1 Transport Proteins for Passive Ion Transport .....	7
1.2.2 Transport Proteins for Active Ion Transport.....	7
1.2.3 Ionophores in Biological Systems.....	9
<b>1.3 Supramolecular Ionophore Systems.....</b>	<b>10</b>
1.3.1 Monitoring Ion Transport.....	11
1.3.1.1 NMR Studies.....	11
1.3.1.2 Ion Selective Electrodes .....	12
1.3.1.3 Fluorescence Assays .....	13
<b>1.4 Synthetic Anion Transporters.....</b>	<b>13</b>
1.4.1 NH and OH Hydrogen bond donors .....	14
1.4.2 CH donor.....	17
1.4.3 Chalcogen and Halogen bonds.....	19
1.4.4 Self-Assembled Ion Pores .....	20
1.4.5 Monomeric Ion Channels.....	20
<b>1.5 Switchable Ion Transport.....</b>	<b>24</b>
1.5.1 Light-Switchable Ionophores .....	24
1.5.2 Redox-Switchable Ionophores .....	26
<b>1.6 Fuel-Driven Anion Transport .....</b>	<b>28</b>
1.6.1 pH Gradient Fueled Anion Transport .....	28

1.6.2 Redox-Active Switchable Ionophores.....	29
<b>1.7 Overview .....</b>	<b>30</b>
<b>1.8 References .....</b>	<b>32</b>

## **Chapter 2 | Ion Redox-Active Molecular Ion Carriers for Active Ion Transports**

<b>2.0 Synopsis .....</b>	<b>36</b>
<b>Acknowledgment .....</b>	<b>36</b>
<b>2.1 Introduction .....</b>	<b>37</b>
2.1.1 Aims & Objectives .....	39
<b>2.2 Synthesis of redox-active transporter.....</b>	<b>39</b>
2.2.1 Urea-based RAMCs .....	39
<b>2.3 Anion Binding Studies .....</b>	<b>40</b>
2.3.1 NMR Binding Studies .....	40
<b>2.4. X-Ray Crystal Structure of UHQ<sub>6</sub>.....</b>	<b>47</b>
<b>2.5 Electrochemical Analysis of RAMCs.....</b>	<b>48</b>
2.5.1 Cyclovoltammetry of UQ <sub>6</sub> .....	48
2.5.2 Chemical Oxidation and Reduction of RAMCs.....	49
<b>2.6 Vesicle transport studies.....</b>	<b>50</b>
2.6.1 Dynamic Light Scattering of LUVs .....	51
2.6.2 Passive Ion Transport Liposomal Assay .....	52
2.6.3 Hill Plot Analysis .....	55
2.6.4 Active Transport Liposomal Assays .....	58
<b>2.7 Biological Testing of Urea Transporters.....</b>	<b>62</b>
<b>2.8 Conclusion and Future Work.....</b>	<b>66</b>
<b>2.9 Experimental.....</b>	<b>67</b>
2.9.1 Synthesis.....	67
2.9.2 Ion Transport Studies .....	72
<b>2.10 References .....</b>	<b>75</b>

## **Chapter 3 | Shapeshifting Fluxional Carbon Cages**

<b>3.0 Synopsis .....</b>	<b>77</b>
<b>3.1 Fluxional Molecules.....</b>	<b>77</b>

<b>3.2 Shapeshifting Fluxional Molecules .....</b>	<b>77</b>
<b>3.3 Dynamic Pericyclic Rearrangements .....</b>	<b>80</b>
<b>3.4 Syntheses of Bullvalene.....</b>	<b>80</b>
3.4.1 Recent Advances in Bullvalene Synthesis and Analysis .....	83
<b>3.5 Bullvalene's Dynamic Behaviour.....</b>	<b>85</b>
<b>3.6 Barbaralane .....</b>	<b>89</b>
3.6.1 Recent Advances in Barbaralane Synthesis .....	91
<b>3.7 Adaptation of simple nondegenerate mixtures.....</b>	<b>92</b>
<b>3.8 References .....</b>	<b>95</b>

## **Chapter 4 | Covalent Control of Fluxional Carbon Cages**

<b>4.0 Synopsis.....</b>	<b>99</b>
<b>4.1 Introduction.....</b>	<b>100</b>
4.1.1 Aims & Objectives .....	101
<b>4.2 Dynamic sp<sup>3</sup>-Carbon Centre Chirality of Fluxional Carbon Cages .....</b>	<b>102</b>
<b>4.3 Synthesis of Fluxional Carbon Cages.....</b>	<b>103</b>
<b>4.4 Reversible Freezing of Fluxional Cages .....</b>	<b>104</b>
<b>4.5 Diastereomeric Adaptation .....</b>	<b>105</b>
4.5.1 Characterisation of the Fluxional Nature of Chiral Barbaralanes .....	107
4.5.2 Variable-Temperature (VT) NMR Spectroscopy of ( <i>R,S</i> )/( <i>S,S</i> )-4.10 .....	108
4.5.3 Modelling Fluxional Behaviour of Chiral Barbaralanes .....	111
<b>4.6 Metal Coordination of Chiral Fluxional Carbon Cages.....</b>	<b>111</b>
4.6.1 Pd (II) Chiral at Metal Barbaralane Complexes.....	112
4.6.2 Interfacing Ligand Exchange on Chiral at Metal Barbaralane Complexes..	115
<b>4.7 Controlling Bullvalene Isomerisation using Phosphorus-Olefin Ligands ...</b>	<b>121</b>
<b>4.8 Synthesis Towards Phosphite BV Ligands .....</b>	<b>122</b>
<b>4.9 Fluxional Cages Influencing Carbamate Rotamers.....</b>	<b>126</b>
<b>4.10 Modelling the Interplay between Rotational and Constitutional Isomerism of Bullvalene Carbamates.....</b>	<b>129</b>
<b>4.11 Solution State NMR Analysis of Fluxional Cage Carbamates.....</b>	<b>133</b>
<b>4.12 Solid State Computational Analysis .....</b>	<b>141</b>
<b>4.13 Conclusions and Outlook .....</b>	<b>144</b>
<b>4.14 Experimental .....</b>	<b>146</b>
4.14.1 General Considerations .....	146
4.14.2 In Silico Modelling .....	169

4.14.3 Bullvalene Carbamate Structure Elucidation .....	172
4.14.4 X-Ray Crystallographic Analysis .....	172
<b>4.15 Experimental.....</b>	<b>183</b>

## **Chapter 5 | Non-Covalent Control of Fluxional Carbon Cages**

<b>5.0 Synopsis.....</b>	<b>187</b>
<b>5.1 Non-Covalent Control of Dynamic Regioisomersim of Fluxional Cage.....</b>	<b>188</b>
5.1.1 Aims & Objectives .....	189
<b>5.2 Synthesis and Characterisation of Metal-Organic Molecular Cage, Pd M<sub>6</sub>L<sub>4</sub> .....</b>	<b>190</b>
5.2.1 Structure Determination of Metal-Organic Molecular Cage, Pd M <sub>6</sub> L <sub>4</sub> .....	191
<b>5.3 Encapsulation of Barbaralanes using a Metal-Organic Molecular Cage, Pd M<sub>6</sub>L<sub>4</sub>.....</b>	<b>193</b>
5.3.1 Solution-State Analysis of the Encapsulation of Control Barbaralanes using Metallocage 5.1 .....	194
<b>5.4 Encapsulation of 1, 9 Disubstituted Barbaralanes using Metallocage 5.1 ...</b>	<b>197</b>
<b>5.5 Solid State Analysis of Encapsulation of Barbaralanes using Metallocage .</b>	<b>199</b>
<b>5.6 Non-Covalent Control of Dynamic Point Chirality of Fluxional Cage .....</b>	<b>203</b>
<b>5.7 Encapsulation of 9-Barbaralols using β-CD as a Host.....</b>	<b>205</b>
5.7.1 Solution State Analysis of Encapsulation .....	205
<b>5.8 Solid-State Analysis of Encapsulation of 9-Barbaralol using β-CD .....</b>	<b>211</b>
<b>5.9 Conclusion and Outlook .....</b>	<b>215</b>
<b>5.10 Experimental.....</b>	<b>218</b>
5.10.1 Synthesis.....	218
5.10.2 Enantioselective Oxidation Encapsulation of Barbaralols using β-CD .....	219
5.10.3 ITC Experiments .....	220
<b>5.11 References .....</b>	<b>221</b>



## Abstract

This thesis explores the control and application of complex dynamic system chemistry in the nanoscale by (1) manipulating interactions across lipid membranes and on the molecular level (2) through the manipulation of shapeshifting molecules. (1) This project involves the design and development of a library of artificial molecular carriers to be tested for successful bicarbonate targeting. These molecules are designed to instigate the active transport of ions across lipid membranes, 'pumping' ions from areas of low concentration to areas of higher concentration. These carriers can do this by consuming a fuel–redox energy supplied by the charge separation already present in photosynthetic apparatus. The preliminary data of our molecular artificial devices in the presence of plant cells suggest that these transporters have an influence on cell morphology due to possible cell membrane incorporation. Furthermore, emission studies revealed that molecular devices have an impact on the photosynthetic apparatus of the cell which is desired. These results are encouraging for the incorporation of molecular devices in plants. (2) In dynamic covalent chemistry, dynamic covalent rearrangements of fluxional carbon cages, such as bullvalenes and barbaralanes, impart shapeshifting molecular properties which have sparingly been studied. This research project focuses on developing methodologies to concretely control these dynamic fluxional carbon cages to simplify and analyse their structural complexity. Non-covalent control was achieved through the encapsulation of these fluxional molecules. This host-guest chemistry can control the dynamic regioisomerism & stereochemistry through molecular metal-organic cages and chiral macrocycles. For covalent control, the configuration of the cage is controlled by covalently tethered functional moieties. These methodologies involve incorporating phosphine-based ligands to control shapeshifting molecules through metal coordination. The development of such techniques will allow routine access to shapeshifting systems to explore their properties and application beyond synthetic, physical organic chemistry, and at the interfaces with materials chemistry and biology.

**Declaration**

The scientific work described in this Thesis was carried out in the Chemistry Department at Durham University between April 2019 and October 2022. Unless otherwise stated, it is the work of the author and has not been submitted in whole or in support of an application for another degree or qualification at this or any other University or institute of learning.

Signed:

Date: 3<sup>rd</sup> April 2023

## Conferences Attended and Presentations Given

1. **SOFI CDT Soft Matter Conference**, University of Leeds, UK, July 2019, Poster presentation: *Manipulating Interactions across Lipid Membranes*.
2. **RSC Macrocyclic and Supramolecular Chemistry Meeting**, University of Durham, UK, December 2019. Poster presentation: *Waving and Ruffling in 3-D Hypervalent Siloxane Porphyrins*.
3. **SCI 3rd Annual Scholars Showcase**, (Online) London, UK, July 2021. Poster presentation: *Manipulating Interactions across Lipid Membranes*.
4. **1st International Supramolecular Chemistry Summer School**, Cagliari, Italy, May 2022. Poster presentation: *Control of Shapeshifting Compounds*.
5. **Canadian Chemistry Conference and Exhibition**, Calgary, Canada, June 2022. Oral Presentation: *Control of Shapeshifting Compounds*.
6. **16th International Symposium of Macrocyclic and Supramolecular Chemistry**, Eugene, US, June 2022. Poster Presentation: *Control of Shapeshifting Compounds*.
7. **SOFI CDT Soft Matter Conference**, University of Leeds, UK, July 2022, Poster presentation: *Control of Shapeshifting Compounds*.

## Awards, Grants and Scholarships

1. **Durham Energy Institute PhD Fellowship**, Durham Energy Institute, Durham, UK, 2019.
2. **SCI Scholarship**, Society of Chemical Industry, July 2020.
3. **Postgraduate Scholarship – Doctoral (PGSD)**, NSERC Research Council, Canada, May 2020.

## Publications

1. A. N. Bismillah, B. M. Chapin, B. A. Hussein, and P. R. McGonigal. Shapeshifting molecules: The story so far and the shape of things to come. *Chem. Sci.* **2020**, *11*, 324-332.
2. B. A. Hussein, Z. Shakeel, A. T. Turley, A. N. Bismillah, K. Wolfstadt, J. Pia, M. Pilkington, P. R. McGonigal, and M. J. Adler. Control of Porphyrin Planarity and Aggregation by Covalent Capping: Bissilyloxy Porphyrin Silanes. *Inorg. Chem.* **2020**, *59*, 13533–13541.
3. A. N. Bismillah, T. G. Johnson, B. A. Hussein, A. T. Turley, H. Wong, A. J. Aguilar, S. D. Yufit, and P. R. McGonigal. (2023) Control of Dynamic sp<sup>3</sup>-C Stereochemistry. *Nat. Chem.* **2023**, <https://doi.org/10.1038/s41557-023-01156-7>.

## Acknowledgements

*Geelka ween meesah u maro ayuu midka yarna maraa*

– Somali proverb

**My Parents.** I am truly grateful I was blessed to have you raise, guide, and support me throughout the years. Your hardships, new beginnings in a country that is not your home and your inspiring journeys through life have been the bed stone that allowed me to become the scientist that I am today. This collection of my experiments that is a part of my scientific journey is only possible because you believed in my dream and pushed me to take this uphill journey. Thank you Hooyo & Aabe, Aisha Mohamed & Ahmed Duale, I hope honoured your efforts and sacrifice.

**Family.** Thanks to all my family that have made me who I am today and cheered me on while I was away from home. I would especially like to thank Ayeeo Hawa Jibril, Ayeeo Fadumo Jimcaarle, Habaryar Suado Mohamed, Abti Abdirahim Mohamed, Abti Abdirahman Mohamed, my brother Duale Hussein, and my sister Iman Hussein.

**Paul McGonigal.** Thank you for emailing Bryan all those years ago looking for a Canadian PhD student. This email catalysed the adventure of a lifetime. Your generosity and support allowed me to achieve things I did not think possible. Your approach to solving chemistry problems and truly thinking outside the box of possibilities had greatly influenced how I think about chemistry. You have raised my standards of how to conduct, think and analysis of chemistry with your interdisciplinarity approach and gifted me with inspiration on how to solve issues at the frontier of chemistry in future. Thank you for being a great PhD supervisor and I am glad took the chance of coming to the UK to work with you.

**CG235.** I would like to thank all the members of the McGonigal, Avestro and Walton groups that resided in CG235 over the years for your friendship and support. You accepted me into the team and made me feel very welcome, it was a pleasure to be part of that space where the success of fellow graduate students & postdocs could be celebrated, the deep conversations, the joking around and long scientific discussions happened. Thank you for being a part of my UK family. Thank you, Dr. Andrew Turley, Dr. Aisha Bismillah, Promeet Saha, Dr. Phil Hope, Kasid Khan, Dr. Abhijit Mallick, Dr. Pavan Yerramsetti, Dr. Jack Williamson, Dr. Luke Williams, Dr. Atreyee Mishra, Dr. Akkharadet Piyasaengthong, Will Maturi, Ho Chi Wong, Dr. Senthil Kumar, Yuzhen Wen, Mary Kate Rynolds, Reece Macdonald, Juliet Barclay, Ash Carter, Dr. Yulong Sun, and Beth Beck.

**SOFI & Cohort 5.** I would like to thank all the members of Cohort 5 in the soft matter and functional interfaces CDT. All of you were the first people I meet when I moved to this country. Those first 6 months of learning soft matter science, the get-togethers in the dorms and moving around the north UK are cherished memories. Thank you for the friendship through the years and collective support as we all moved forward in this PhD journey. Thank you, Lloyd Shaw, Lucas Le Nagard, Sam Meacham, Marie Rapin, Kalila Cook, Kate Lefroy, Jenny Maunder, James Cochran, Sam Brown, Veronica McKinny, Jack

Hocking, Charlotte Pugsley, Adele Parry, Beth Beck Merin Joseph, Seth Price, Ruth McTierman, and Jordan Hobbs. I would also like to thank Prof Lian Hutchings, Prof Richard Thompson, and Linda Grieve for all the support throughout my PhD at SOFI CDT and Durham.

**Durham Chemistry Community.** It was a pleasure to be a part of this chemistry community at Durham University. Meeting people from all over the world in a small department in the countryside was a unique experience. The coffee breaks, the chats in the hallways, catch-ups in the NMR room, and after-work hangs at the pub are all part of the experience that keep me going during the up & downs of my PhD. I want to especially thank Dr. Matthew Kitching, Dr. Clare Mahon, and Dr. Russell Taylor for being great chemistry buddies and mentors during my time at Durham.

**Friends.** Thanks to all my friends throughout my time pursuing science as a career, you all supported me in different ways that brought me to this point in my life. Special thank you to Vitor Santos de Carvalho, Kelly Groundwater, Shari Fearon, Tyrell Black, Fadumo Arwo, Laura Acevedo, Agnes Klimowski, and Chris Helmeste for all the support throughout the years.

## List of Abbreviations

Ac	Acetyl
ADP	Adenosine diphosphate
ASAP	Atmospheric solids analysis probe
ATP	Adenosine triphosphate
BB	Barbaralane
BB+	Barbaralyl Cation
BBO	Barbaralone
BDT	Bicyclo[4.2.2]deca-2,4,7,9-tetraene
BINOL	1,1'-Bi-2-naphthol
br	Broad
BV	Bullvalene
BVO	Bullvalone
Bu	Butyl
$\beta$ -CD	beta-Cyclodextrin
CAN	Ceric ammonium nitrate
CF	Cystic fibrosis
CFTR	Cystic fibrosis transmembrane conductance regulator
COSY	Correlation spectroscopy
COTT	Cyclooctatetraene
d	Doublet
DCE	1,2-Dichloroethane
DFT	Density functional theory
DIPEA	<i>N,N</i> -Diisopropylethylamine
DMAP	4-(Dimethylamino)pyridine
DMF	Dimethylformamide
DMSO	Dimethyl sulphoxide
equiv.	Equivalents
EXSY	Exchange spectroscopy
ESI	Electrospray ionisation
Et	Ethyl
HMBC	Heteronuclear multiple-bond correlation spectroscopy
HPLC	High-performance liquid chromatography
HR	High resolution
HSQC	Heteronuclear single-quantum correlation spectroscopy
IPr	1,3-Bis(2,6-diisopropylphenyl)imidazole-2-ylidene
JohnPhos	(2-Biphenyl)di- <i>tert</i> -butylphosphine.
LDA	Lithium Diisopropylamide
m	Multiplet
Me	Methyl
Mosher's Acid	$\alpha$ -Methoxy- $\alpha$ -trifluoromethylphenyl acetic acid
M.P.	Melting point
MS	Mass spectrometry
NMR	Nuclear magnetic resonance
NOESY	Nuclear overhauser effect spectroscopy
Ph	Phenyl
q	Quartet

ROESY	Rotating frame nuclear overhauser effect spectroscopy
rt	Room temperature
s	Singlet
SBV	Semi-Bullvalene
ssNMR	Solid-state nuclear magnetic resonance
t	Triplet
TFA	Trifluoroacetic acid
THF	Tetrahydrofuran
TLC	Thin-layer chromatography
TOCSY	Total Correlation Spectroscopy
UV	Ultraviolet
VT	Variable-temperature
VT	NMR Variable-temperature nuclear magnetic resonance
XRD	X-ray diffraction

Note: conventional abbreviations for units, physical quantities and stereochemical terms are not included here.

## Thesis Layout

Chapter 1 introduces photosynthesis in plants and how ion transport in such biological systems. This introduction leads to the discussion of synthetic mimics of ion transport in supramolecular chemistry. Chapter 2 focuses on the design and development of a library of artificial molecular carriers to be tested for successful bicarbonate targeting. Chapter 3 introduces fluxional carbon cages, discussing their properties, initial synthetic efforts, and the modern-day approaches by which they can be accessed. The applications of fluxional carbon cages are also discussed where analyte binding can occur through covalent bonding and noncovalent bonding interactions. Chapter 4 discusses the covalent control of dynamic chiral  $sp^3$  carbon centre in fluxional carbon cages which is present in adapted form from a published paper in a peer-reviewed journal. The methodologies from this work were applied to the more complex bullvalene and this chemistry is discussed in this chapter. Chapter 5 discusses non-covalent control over the regioisomerism of fluxional carbon cages and a fluxional  $sp^3$ -carbon stereocentre in solution and in the solid state.



# Chapter 1 | Ion Transport Across Lipid Membrane

## 1.0 Synopsis

This chapter is an introduction to anion transport across cell membranes in relation to important function in plant photosynthesis and how chemists have tried to synthetically make anion transporters, understanding the supramolecular interactions between anions and transporter. The different application of these transporters in lipid membranes is discussed and how researchers have approached mimicking active ion transport done in biological systems is also explored.

## 1.1 Photosynthesis in Plants

Plants that are photoautotrophs rely on photosynthesis to produce the food they need to grow. Utilizing photosynthesis, a process using a source of carbon (ex.  $\text{CO}_2$ ) and water to convert energy from light (photons) to a chemical fuel which can be used produce carbohydrates and oxygen. This conversion happens through a network of proteins, electron transfer chains driven by light, and corresponding proton gradients.<sup>1</sup> During photosynthesis, light-dependent reactions (photosystem I & photosystem II) and light-independent reactions (Calvin cycle, carbon concentrating mechanisms). In plants and algae, photosynthesis happens in organelles called chloroplasts. Chloroplasts are located on the periphery of plant cells, enclosed by the cell membrane.

### 1.1.1 Cell Membrane

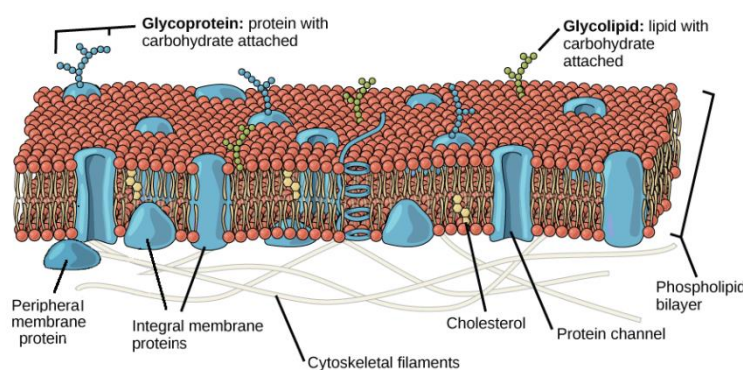


**Figure 1.1.** An illustration of the cell membrane showing the phospholipid bilayer with embedded proteins and glycolipids, cholesterol.<sup>2</sup>

By mass, approximately half of a cell membrane's weight is comprised of membrane-embedded proteins and the other half by lipids, which give the cell its structure.<sup>3</sup> These lipids come in three varieties: phospholipids, glycolipids, and neutral lipids, such as cholesterol (Figure 1.1 & 1.2). Though the exact composition of the membrane varies

depending on the cell type, phospholipids are the most prevalent. The membrane is held together by noncovalent interactions between the hydrophobic tails of the phospholipid, forming a phospholipid bilayer. The bilayer can be strengthened through the presence of cholesterol, which positions itself in the gaps between the unsymmetrical hydrophobic tails, thereby protecting the cell membrane from structural deterioration over longer periods of time.<sup>4</sup>

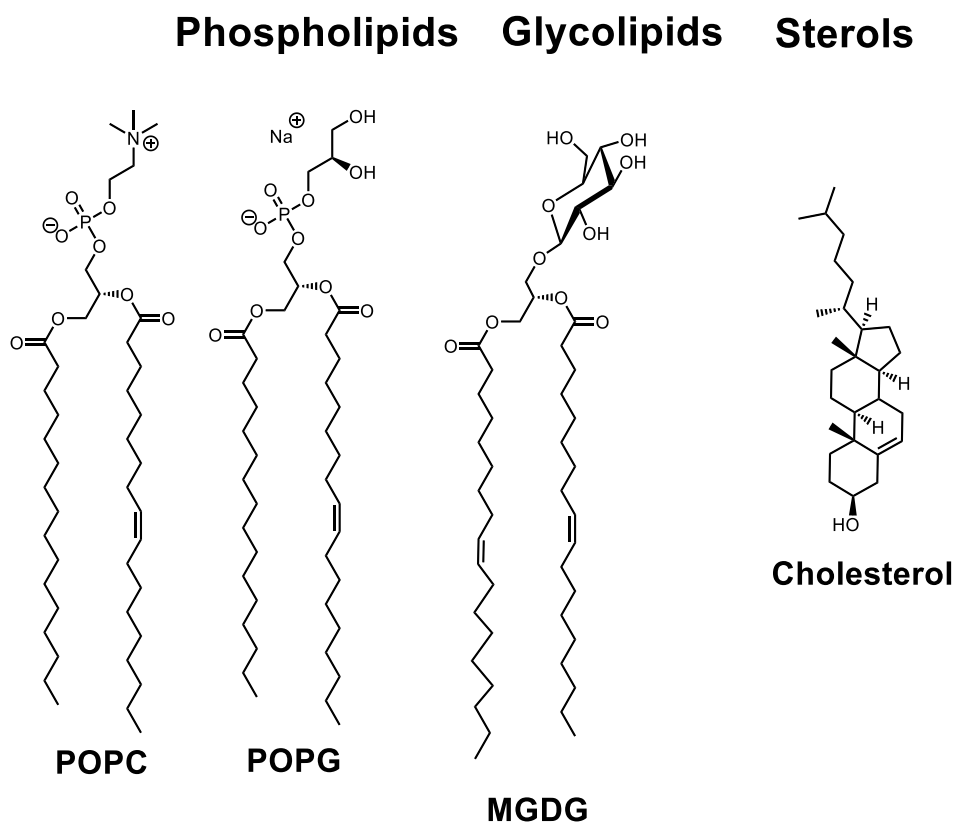


**Figure 1.2.** Examples of major membrane lipids: Phospholipids, Glycolipids, and Sterols.

### 1.1.2 Light-Dependent Reactions

In photosynthesis, within the stroma, embedded in the thylakoid membrane, light-dependent reactions are responsible for converting energy from photons to the chemical fuels, ATP and NADPH (Figure 1.3).<sup>5</sup> First, a photon is absorbed by one of the many pigments in photosystem II, the energy is passed inward from pigment to pigment until it reaches the reaction center of the complex. There, energy is transferred to chlorophyll dimer(P680) and this energy is used to excite an electron. The excited electron carried by mobile quinone-based carrier, plastoquinone, and continues through electron flow to cytochrome b6f to plastocyanin which transfers the electrons to photosystem I (PSI). At PSI, photons are absorbed by the complex to excite the electron to a higher energy

level, which in turn is utilized to reduce  $\text{NADP}^+$  to  $\text{NADPH}$ . Figure 1.3 illustrate this process. At the same time, a proton gradient is generated in lumen that drives the ATP synthesis by ATP synthase. Both the  $\text{NADPH}$  and ATP are required for light-independent reactions during photosynthesis to generate carbohydrates.

Another light-dependent reaction is water photolysis<sup>5</sup> (Figure 1.3) which occurs at the functionalized interface of the cell membrane. The transport of electrons needed to reduce  $\text{NADP}^+$  to  $\text{NADPH}$  leaves reaction centers of photosystem I & II oxidized. In both photosystem I & II, the oxidized chlorophyll needs external electrons to regenerate the reaction center. The source of electrons for regeneration of the photosystems is water, which is oxidized by the catalytic redox-active structure of P680. Protons and oxygen are produced by this reaction and are released in thylakoid lumen contributing to the proton gradient need for ATP synthesis.

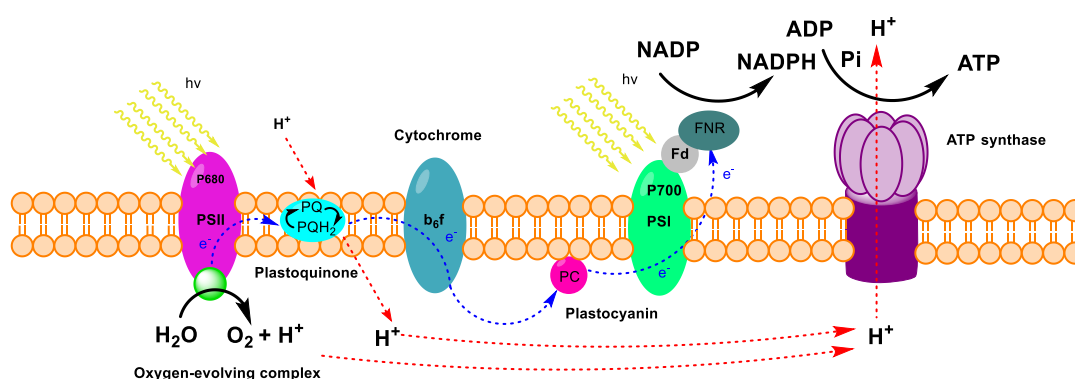


**Figure 1.3.** Light-dependent reactions of photosynthesis at the thylakoid membrane.

### 1.1.3 Light-Independent Reactions

Most plants use  $\text{C}_3$  metabolic pathway which uses  $\text{CO}_2$  as carbon source.<sup>6</sup> This pathway's Calvin Cycle has three stages illustrated in Figure 1.4.<sup>7,8</sup> Carbon fixation of  $\text{CO}_2$  occurs utilizing ribulose 1,5-bisphosphate and the enzyme, ribulose-1,5-bisphosphate carboxylase/oxygenase (RuBisCO) to produce 3-phosphoglycerate. Once carbon fixation occurs, the second phase of the cycle involves the use the ATP produced in the light-dependent reactions to phosphorylate 3-phosphoglycerate. The resulting compound is then reduced with  $\text{NADPH}$  from light-dependent reactions to produce glyceraldehyde, which is used to make carbohydrates. After, a series of reactions leads to the regeneration of ribulose, completing the cycle. This pathway, unfortunately, is inefficient, which causes to RuBisCO to use oxygen in order to

produce the carbohydrates. This use of oxygen, produced in photosynthesis, therefore makes this a wasteful metabolic process.<sup>9</sup>

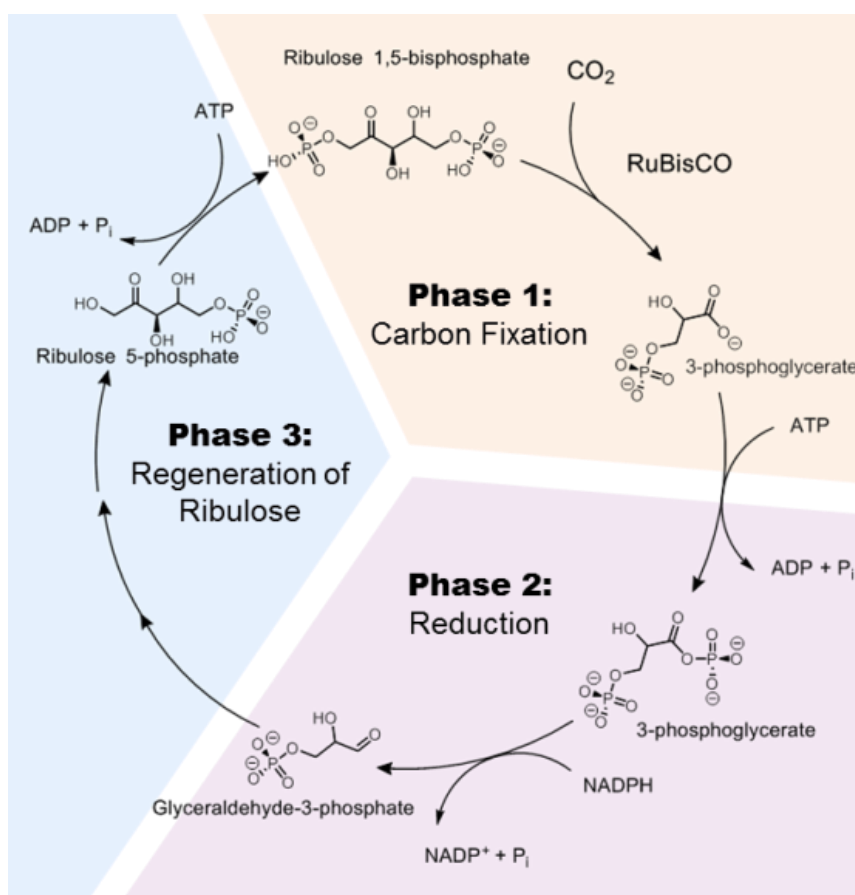


**Figure 1.4.** Carbon fixation of photosynthesis for C<sub>3</sub> pathway toward carbon sources.

C<sub>4</sub> plants are believed to be the evolutionary adaption of C<sub>3</sub> plants. Their light-independent carbon fixation process is enhanced by the inclusion of a carbon-concentrating mechanism.<sup>10</sup> Figure 1.5 shows that mechanism of the carbon-concentrating mechanism of C<sub>4</sub> plants<sup>11</sup>, which allows for higher concentrations of CO<sub>2</sub> to be shuttled to RuBisCO. C<sub>4</sub> plants have two carbon fixation pathways, where CO<sub>2</sub> and bicarbonate (HCO<sub>3</sub><sup>-</sup>) can be used as a carbon source. Additionally, the C<sub>4</sub> pathway uses a great amount of energy (ATP), therefore these plants require more exposure to external light energy in order to generate ATP from photosynthesis. This reason is why C<sub>4</sub> plants are found in hot, sunny climates.<sup>12</sup> This new photosynthetic pathway leads to a significant enhanced rate of carbon dioxide fixation in light conditions compared to dark conditions.<sup>10</sup> Interestingly, C<sub>4</sub> plants only account for about 3% of all known land plant species.<sup>12</sup>

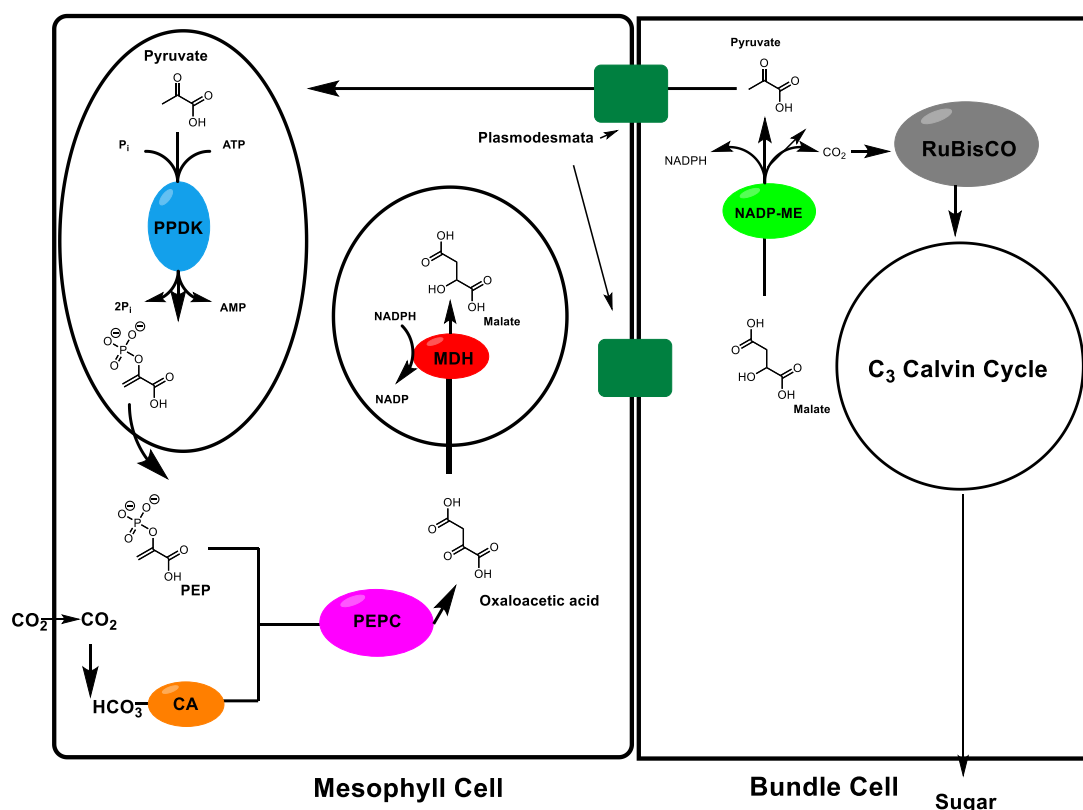


**Figure 1.5.** The C<sub>4</sub> plants' light-independent pathway involves the carbon shuttling between a mesophyll cell (left) and a bundle sheath cell (right). CO<sub>2</sub> from the atmosphere diffuses into the mesophyll cell and is reduced by carbonic anhydrase (CA). Phosphoenolpyruvate carboxylase (PEPC) then binds the HCO<sub>3</sub><sup>-</sup> and phosphoenolpyruvate (PEP) to produce the four carbon, oxaloacetate (OAA). OAA is reduced to malate (MAL) by malate dehydrogenase (MDH) and MAL is transported to the bundle sheath via plasmodesmata. CO<sub>2</sub> is removed from MAL by NADP-ME and is picked up by RuBisCO, which reduces it and initiates the C<sub>3</sub> cycle to produce sugars. The pyruvate released by the decarboxylation of malate is returned to the mesophyll cell where it is phosphorylated by pyruvate phosphate dikinase (PPDK) to regenerate PEP.

## 1.2. Ion Transport in Biological Systems

Photosynthesis requires the movement of ions across cell membranes of plant cell, particularly CO<sub>2</sub> in the form of HCO<sub>3</sub><sup>-</sup> and CO<sub>3</sub><sup>2-</sup> anions. In general for biological systems, be it plants or animals, the movement of ions across cell membranes is vital for biological function in living organisms.<sup>13</sup> However, ions are charge species in solution that cannot readily diffuse through cell membranes (hydrophobic) on account of their hydrophilic nature. Biological systems use selective transport proteins and ionophore molecules that mediate the selective passage of ions across the membrane, allowing the cell to control the ionic composition of its cytoplasm.<sup>14</sup>

### 1.2.1 Transport Proteins for Passive Ion Transport

In living cells, the transport of ions across cell membranes is controlled by transport proteins. There are two classes of transport pathways: passive ion transport and active ion transport. Passive transport involves the diffuse of usually small molecules through a semi-permeable cell membrane that is driven by concentration gradients.<sup>15</sup> This process does not consume energy and is driven by entropy. However, for the transport of ions, embedded transport proteins are used to facilitate the translocation of charged species.<sup>16</sup> This facilitated diffusion utilizes ion channel proteins that have selective channels that act as open pores in the cell membrane. Ion channels are highly selective because the narrow pores in the channel restrict passage to ions of the appropriate size and charge. Ion channels utilize “gates” to regulate the influx/efflux of ions in the cell of ions. In response to stimuli, the transport protein can undergo a conformational change which allows ion flow (open gate) or inhibit ion flow (closed gate). The movement of ions through channel proteins is driven by ion concentration gradients across the cell membrane. The opening and closing of ion channels can happen through such external stimuli as binding of neurotransmitters. In these instances, the channels are known as ligand-gated channels.<sup>14</sup> Another mode of conformation change-response is the modulation of electric potential across the cell membrane. These channels are known as voltage-gated channels.<sup>13</sup>

### 1.2.2 Transport Proteins for Active Ion Transport

The movement of ions through ion channels is energetically a downhill process determined by a concentration gradient across the cell membrane. However, in biological systems, cells need to be able to transport ions across membrane against a concentration gradient. This “active” transport occurs in cell membranes by the use of energy provide from a chemical fuel such as ATP hydrolysis which is used to drive uphill ion transport.<sup>17</sup> Ion pumps are used for active transport in such biological systems.<sup>18</sup> There are two classes of active transport: primary and secondary transport.<sup>18</sup> For primary active transport, the example above is such a process, the movement of an ion across a membrane through energy fuel consuming uphill process using chemical fuel ATP hydrolysis (Figure 1.6). This type of transport is called uniport.<sup>14,16</sup>

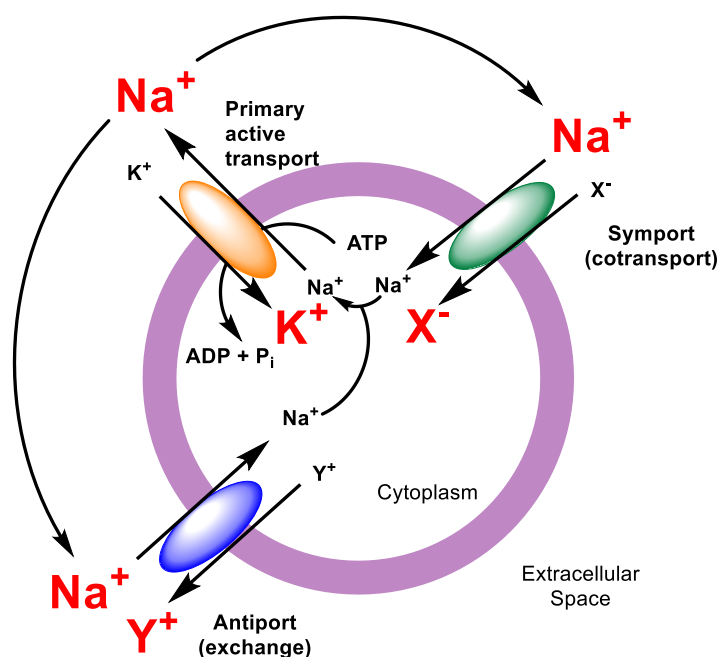


**Figure 1.6.** Schematic representation of secondary active transport illustrating the movement of a driving ion ( $\text{Na}^+$ ) down an electrochemical gradient is used to drive the uphill transport of another ion/molecule against a concentration or electrochemical gradient. Two types of secondary active transport processes exist: cotransport (also known as symport) and exchange (also known as antiport). In cotransport, the direction of transport is the same for both the driving ion and driven molecule/ion, whereas in exchange, the driving ion and driven ion/molecule are transported in opposite directions. X and Y represent transporter substrates.

Secondary active transport occurs when a carrier protein couples the movement of a specific ion to a downhill energy process, using a favourable concentration/electrochemical gradient of one ion to drive uphill movement of another ion against its own concentration/electrochemical gradient (Figure 1.6). This ion-coupled transport needs both the driving and driven species bound to the transporter for movement across the membrane to occur. The free energy used for this process comes from the stored energy of concentration/electrochemical gradient of the driving ion undergoes the downhill movement. In most cases, in order for secondary active transport to occur in biological systems, primary active transport proteins (i.e., ion pumps) are needed to maintain concentration/electrochemical gradients that drive secondary active transport.  $\text{Na}^+$  ions are commonly used as driving ion for secondary active transport ions in a myriad of mammalian cells due to the steep  $\text{Na}^+$  ion concentration gradient across cell membranes which is maintained from  $\text{Na}^+/\text{K}^+/\text{ATPase}$  primary active transporter protein.<sup>14,16,19</sup> This allows access to large

free energy storage in the  $\text{Na}^+$  electrochemical gradient, which can drive secondary transport.

For secondary active transport, there are two types of transport: symport and antiport.<sup>20</sup> Since secondary active transport involves the translocation of two ions simultaneously, there is an aspect of directionality of ion flow across membranes. The movement of two ions across in the same direction in or out of a cell (cotransport) is symport and the transporter protein is known as a cotransporter. Movement of two ions in opposite directions in or out of a cell (exchange) is antiport and the transporter is known as exchangers. Electrochemical control of ion transport is also very important in active or passive transport. A result of movement of ions across a membrane can lead to a net translocation of charge. For transporters that leads to the net translocation of charge across the membrane are known as electrogenic.<sup>21</sup> While transporters that move ions across membrane that lead to no change in net charge are electroneutral.<sup>21</sup>

### 1.2.3 Ionophores in Biological Systems

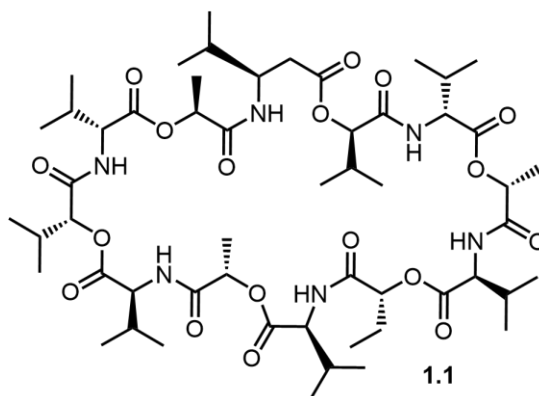


**Figure 1.7.** Molecular structure of Valinomycin **1.1**.

There are other means of ion transport across cell membranes aside membrane embedded proteins. Ionophores are molecular carriers that have the capability of transporting ions across cell membranes.<sup>22</sup> These ionophores are not part of the structure of the membrane. Ionophores operate in similar manner as carrier proteins in the sense that they bind ions, enveloping the charged species and facilitating diffusion of the ions across the lipophilic membrane. Ionophores are involved in uniport, symport, antiport as well as electrogenic or electroneutral transport, just like their protein counterparts.

Valinomycin **1.1** is a naturally occurring ionophore (Figure 1.7). It is a cation transporter that is capable of carrying  $\text{Na}^+$  or  $\text{K}^+$  by a passive transport pathway.<sup>23</sup> **1.1** is a macrocyclic molecule containing twelve carbonyl groups from alternating amino acids and esters that can bind to metal ions in similar manner as crown ethers through the cavity where carbonyl can bind selectively to  $\text{K}^+$  ions.  $\text{Na}^+$  ion can also weakly bind to the **1.1** cavity compared to  $\text{K}^+$ . This naturally occurring ionophore undergoes electrogenic uniport across cell membranes for  $\text{K}^+$  and  $\text{Na}^+$  ions.<sup>23</sup>

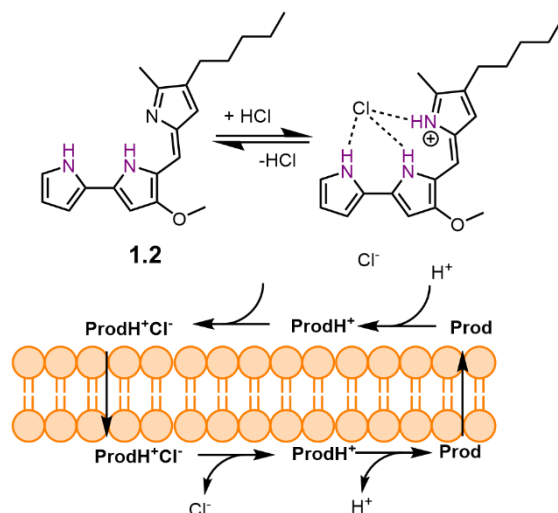


**Figure 1.8.** The electroneutral  $\text{H}^+/\text{Cl}^-$  symport across a bilipid membrane with Prodigiosin.

Prodigiosin **1.2** is also another naturally occurring ionophore isolated from bacteria of the *Serratia* and *Streptomyces* genera, along with its synthetic analogues are known for their ability to symport  $\text{H}^+$  and  $\text{Cl}^-$  across lipid membranes.<sup>24</sup> This electroneutral ionophore has promise to treat several types of cancer. Many types of cancerous cells are known to have a more acidic intracellular pH compared to healthy cells. Prodigiosin allows for  $\text{H}^+$  efflux, leading to deacidification of the cell's cytoplasm, causing apoptosis (cell death).<sup>25</sup>

### 1.3 Supramolecular Ionophore Systems

Genetic diseases can cause hindrance of ion transport due to mutations leading to the modification of the structure of ion channels. These diseases, such as cystic fibrosis (CF) caused by the dysfunction of the cystic fibrosis transmembrane conductance regulator (CFTR), are collectively known as channelopathies.<sup>26</sup> To some degree, channelopathies have driven the development of synthetic transporters and transmembrane channels of these supramolecular constructs to treat such diseases.

Several groups use large unilamellar vesicles (LUVs) lipid or lipid/cholesterol mixtures as model systems for biological cell membranes to measure the efficiencies of their synthetic ion transporters.<sup>26</sup> Developing supramolecular systems to have therapeutic benefit to function in biological systems has led to interesting anion transporters and methods to monitor ion transport which will be discussed below.

### 1.3.1 Monitoring Ion Transport

As mentioned above, large unilamellar vesicles (LUVs) that are typically 100–200 nm in size, are used to mimic cell membranes when testing the ion transport properties of synthetic transporters.<sup>27</sup> The composition of such LUVs to mimic relevant biological membranes have been studied by Spooner and Gale<sup>27</sup> using a variety of phospholipids such as POPC, POPG, and POPE. In practice, most groups now use POPC for transport studies or POPC/cholesterol mixture, using cholesterol to stabilize the membrane.<sup>28,29</sup>

#### 1.3.1.1 NMR Studies

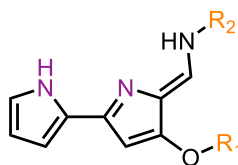


**Figure 1.9.** The tambjamine-based molecules studied by Quesada et al.

NMR spectroscopy has been utilized to study ion transport in LUVs by several groups. Quesada *et al.* have used  $^{13}\text{C}$  NMR to monitor  $\text{HCO}_3^- / \text{Cl}^-$  exchange across a POPC bilayer, mediated by tambjamine-based ionophores **1.3** (Figure 1.9).<sup>30</sup> Figure 1.10 illustrates the use such technique to monitor such transport.  $^{13}\text{C}$  enriched bicarbonate  $\text{HCO}_3^-$  is encapsulated in the vesicles and upon the addition of anionophore and HCl, the bicarbonate is transported outside the vesicles.  $\text{MnCl}_2$  is added to the suspension, forming a paramagnetic species that cannot be detected by NMR. The drawback of this method is the lack of ability to measure quantitative data to obtain rates of ion influx/efflux of the vesicle.

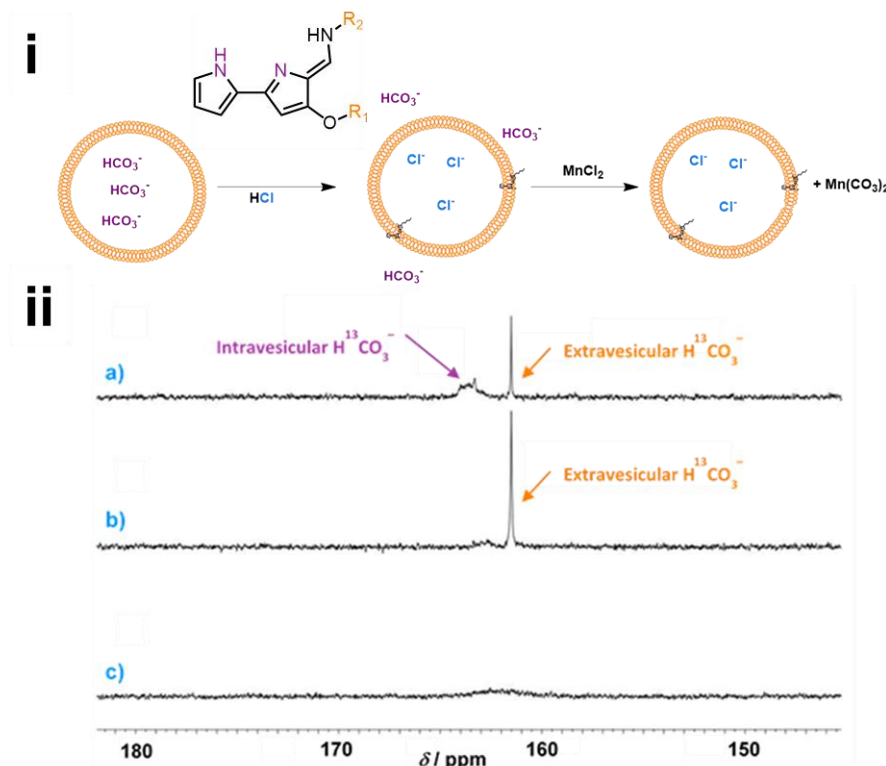


**Figure 1.10.**  $^{13}\text{C}$  NMR spectra showing evidence for transmembrane bicarbonate transport.<sup>31</sup> i) Schematic representation of vesicle experiment. ii) a) POPC vesicles were loaded with 500 mM  $\text{NaH}^{13}\text{CO}_3$  dispersed in 162 mM  $\text{Na}_2\text{SO}_4$ , buffered at pH 7.2. b) 50 mM tamajamine carrier (0.16% mol carrier to lipid conc.) was added. A weakening of the “ $\text{H}^{13}\text{CO}_3^-$  in” peak is observed, signaling bicarbonate efflux. c) Addition of 0.5 mM  $\text{MnCl}_2$ , a paramagnetic signal broadening reagent that only affects extravesicular  $\text{H}^{13}\text{CO}_3^-$  ions. The “ $\text{H}^{13}\text{CO}_3^-$  out” peak can no longer be observed.<sup>30</sup>

### 1.3.1.2 Ion Selective Electrodes

Ion-selective electrodes have been widely adopted as method to obtain quantitative rates of ion transport across membranes.<sup>26</sup> LUVs encapsulating a particular ionic species are suspend in a buffer solution. Addition of ion transporter leads to ion efflux from the vesicle. The ion electrode measures the ion efflux over a certain period, and then the vesicles are lysed with the addition of a surfactant leading to the leaching of the remaining ions. The initial value is set to 0% efflux, the final value is calibrated to 100%, and the efficacy of the ionophore is evaluated by its initial rate of chloride release ( $k_{\text{ini}} / \% \text{ s}^{-1}$ ). Gale et al. used this method to evaluate a series of phenylthiourea compounds for  $\text{Cl}^-$  transport across membranes.<sup>31</sup> It has since become one of the standard methods for monitoring  $\text{Cl}^-$  transport. A drawback to this method is the potential lack of solubility of the ion transporter in aqueous media, as the transporter must be added to the LUV suspension as an aqueous solution. Poor solubility of the ion

receptor can lead to precipitation instead of diffusion into the lipid. This method is not compatible with pre-incorporating the ion receptor into the lipid bilayer during LUV preparation.

### 1.3.1.3 Fluorescence Assays

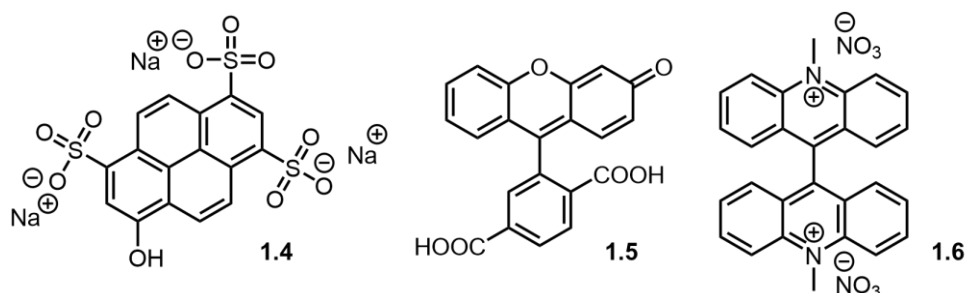


**Figure 1.11.** The fluorophores HPTS **1.4**, carboxyfluorescein **1.5**, and lucigenin **1.6**.

The development of fluorescence assays that are sensitive to the transport of ions across membranes has led to the ability obtain quantitative rates of ion influx/efflux. Figure 1.11 shows the most commonly used fluorescent dyes used for these studies. **1.4** is a pH-sensitive fluorophore ( $pK_a \sim 7.3$ ) and is used as internal probe that is encapsulated in the LUVs.<sup>32</sup> The pH sensitivity of the two excitation maxima from the protonated/deprotonated forms allow for the ratiometric detection of pH changes in double-channel fluorescence measurements. The HPTS assay relies on the influx of  $H^+$  or  $OH^-$ , so cotransport is needed in this assay, however, this makes HPTS assay useful since you can study a wide array of ions transport coupled with the influx of  $H^+$  or  $OH^-$ . Carboxyfluorescein **1.5** is used as a non-specific internal probe based on self-quenching at higher concentrations inside in LUVs. This means it only measures ion efflux. If there are large pores, the dye can leach, leading to a reduction of the self-quenching.<sup>33</sup> A more recent assay developed is the lucigenin assay. Lucigenin **1.6** is a chloride specific internal probe where the lucigenin's fluorescence is quenched in the presence of chloride. LUVs encapsulate lucigenin assay in a chloride-free environment and the anion transporters allows for  $Cl^-$  influx, quenching the emission.<sup>34</sup>

## 1.4 Synthetic Anion Transporters

This group of anion transporters utilize hydrogen bond donors to coordinate an anion. For this review, ion transport facilitated by NH, OH, and CH hydrogen bond donors, chalcogens, and halogen bonds will be discussed.

## 1.4.1 NH and OH Hydrogen bond donors

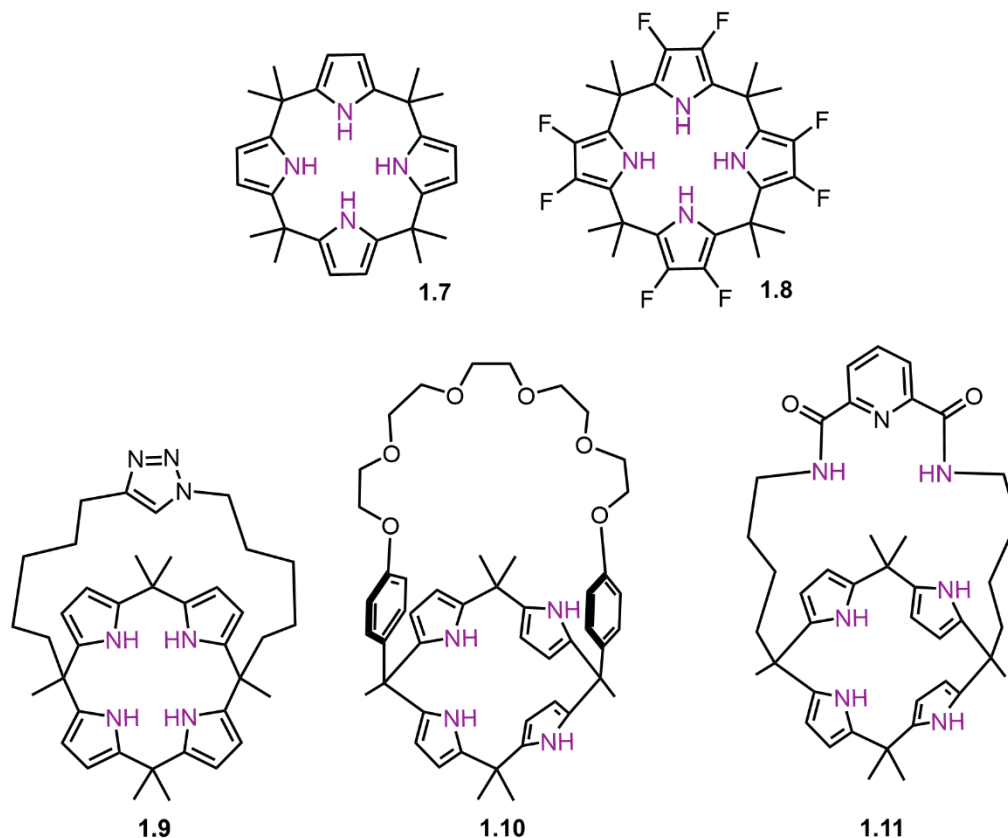


**Figure 1.12.** A select series of calix[4]pyrrole derivatives.

The calix[4]pyrrole transporters are one platform for the development of versatile anion transporters.<sup>35–37</sup> A series reported calix[4]pyrrole are presented in Figure 1.12. These macrocycles are capable of binding to anions through the pyrrolic N–H groups. They can simultaneously bind to large polarizable cations through their macrocyclic  $\pi$ -donor aromatic cup. Gale et al. reported that **1.7** promotes the electroneutral symport of CsCl across POPC membranes. Sessler et al. further showed that the fluorinated calix[4]pyrrole **1.8** showed enhanced the acidity of the N–H bond allowing for stronger N–H $\cdots$ Cl $^-$  hydrogen bond formation. This modification significantly changed the transport capacity of calix[4]pyrrole to a potent electroneutral antiport exchange for a series of MCl (M = Li, Na, K, Rb, Cs) and the uniport of Cl $^-$ . The addition of bridged triazole in **1.9** increased chloride efflux in Cl $^-$ /NO $_3^-$  exchange assay compared to the parent **1.7**. Lee et al. reported **1.10**, which bears a crown ether-like cap that can form complexes with LiCl and NaCl. However, **1.10** still favours the cotransport of CsCl and Cl $^-$ /NO $_3^-$  exchange. The biological activity of compound **1.11** was studied in a

myriad of cell lines by Gale, Sessler and Shin.<sup>35</sup> These compounds were shown to mediate both chloride and sodium influx as well as to induce cell apoptosis.<sup>35</sup>

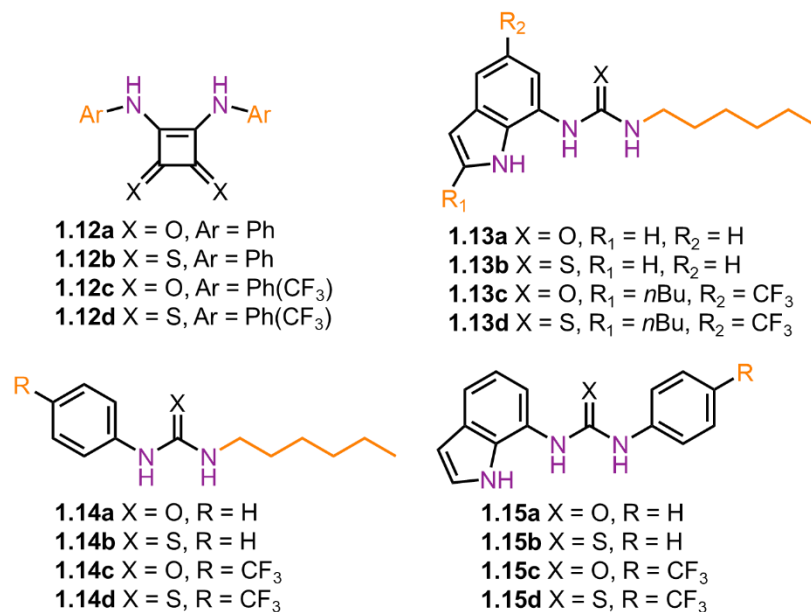


**Figure 1.13.** Select series of urea based anionophores synthesized by Gale et al.

Simple urea N–H donor analogues have been developed over the years to obtain efficient anion transporters. The molecular design strategy of incorporating acidic –NH urea groups has led to ureas, squaramides, indole ureas, and the thiocarbonyl analogues ureas, squaramides, indole ureas, and the thiocarbonyl analogues shown in Figure 1.13.<sup>29,30,38</sup> Hill plot analyses of these molecules revealed that these analogues tend to favour a mobile carrier mechanism, although a few ionophores (**1.12c-d** and **1.14c**) displayed possible channel formation mechanism. All transporters shown below were effective at Cl<sup>–</sup>/NO<sub>3</sub><sup>–</sup> and Cl<sup>–</sup>/HCO<sub>3</sub><sup>–</sup> antiport, with the most active ionophore **1.13d** showing transport at concentrations as low as 1:20000 carrier to lipid ratios. Compounds **1.13-1.15** were capable of antiport Cl<sup>–</sup>/citrate. Generally, the thiocarbonyl analogues have outperformed the parent compounds due to sulfur increasing the lipophilicity of the transporter, allowing faster diffusion across the lipid bilayers. This urea motif was further developed by the incorporation of scaffolds to allow for high activity and higher selectivity. Davis et al. have developed a series of potent anionophores based on cyclohexane, trans-decalin, and steroidal backbones (**1.16–1.19**) that promote Cl<sup>–</sup>/NO<sub>3</sub><sup>–</sup> exchange, but failed to efficiently transport HCO<sub>3</sub><sup>–</sup> and SO<sub>4</sub><sup>2–</sup> ions (Figure 1.14).<sup>28,39</sup> The most effective transporter, **1.16e**, was active at

concentrations as low as 1:500000 transporter:lipid. Further, the fluorinated analogues demonstrated higher activity than the non-fluorinated parent compounds, as the CF<sub>3</sub> groups increased the carrier's lipophilicity, metabolic stability, and the acidity of the binding site. Davis et al. transporters' efficiency can be attributed to two factors: Firstly, they have multiple preorganized anion binding sites, which leads to more entropically favorable binding. Secondly, the transporters possess an even distribution of the lipophilic/hydrophilic groups.<sup>39</sup>

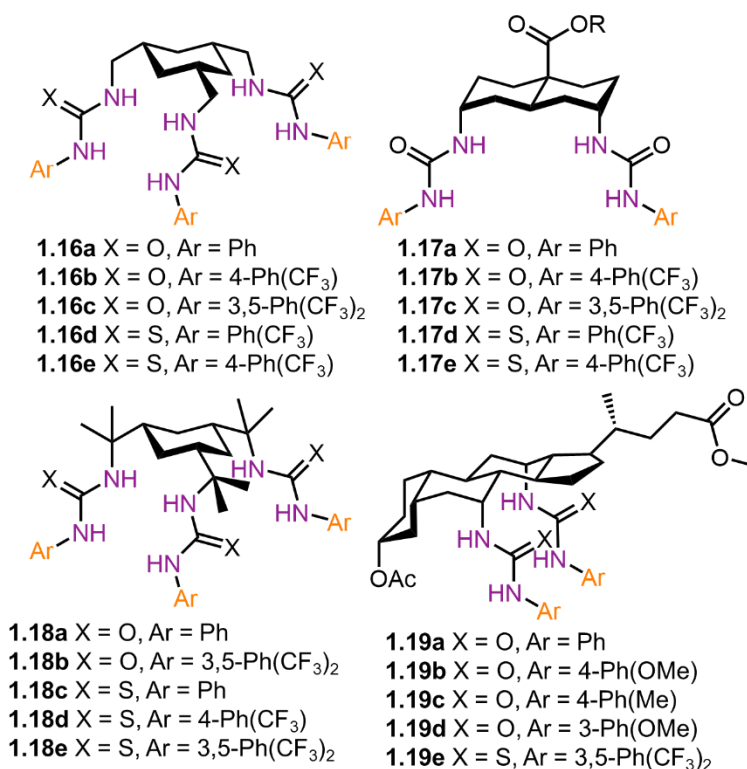


**Figure 1.14.** Select series of urea-based anionophores synthesized by Davis et al.<sup>29,30,38</sup>

## 1.4.2 CH donor

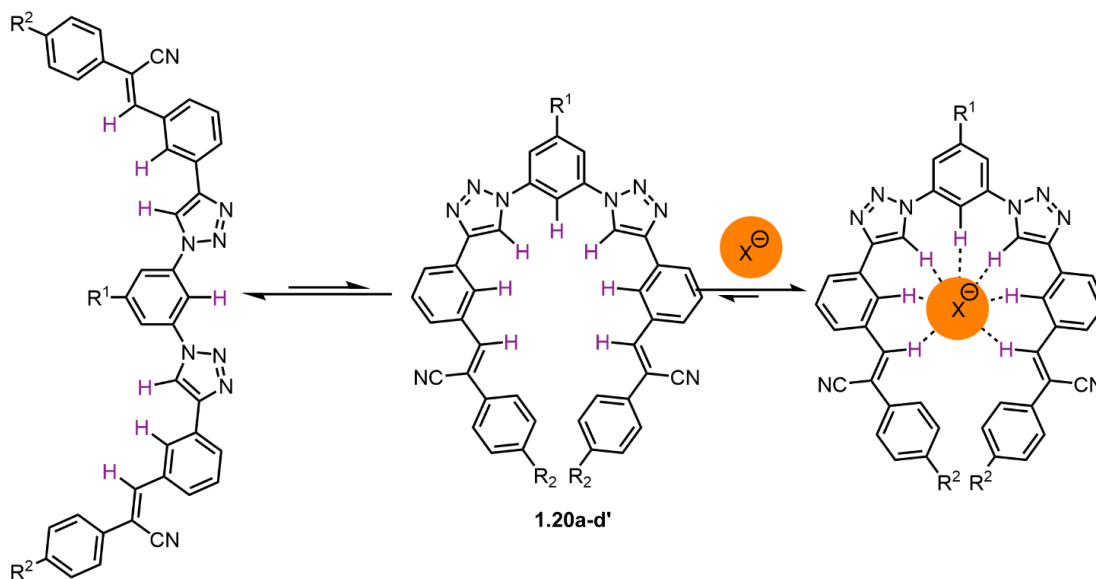


**Figure 1.15.** Folding triazole-cyanostilbene, **1.20a-b**, that binds to a series of anions, **1.20b** shows that the CH donors of this molecule keeps the molecule folded.

Hydrogen donor using NH bonds for anion transport is popular concept in terms of molecular design, however, there are cases where CH bond donors can also be used. Mondal et al. reported a series of triazole–cyanostilbene receptors **1.20a-b** were designed and synthesized as transmembrane anion transporters (Figure 1.15).<sup>40</sup> The receptor binds with the anions through various  $CH \cdots$  anion hydrogen bonding interactions, where strong binding was observed for  $SO_4^{2-}$  anions followed by  $Cl^-$ ,  $Br^-$ ,  $NO_3^-$ , and  $I^-$ , calculated from the  $^1H$  NMR titration experiment. The NOESY NMR experiment of the receptor confirmed the formation of anion-induced folded conformation. The  $CH \cdots$  anion hydrogen bonding interaction-mediated anion recognition and foldamer formation were further confirmed from geometry optimization studies of the anion-bound complex. The receptor transports  $Cl^-$  anions efficiently compared to  $SO_4^{2-}$  anions across the lipid bilayer membrane via a mobile carrier mechanism. This observation was determine using a liposomal assay using  $Cl^-$  ion selective electrode.

These synthetic transporters have great promise in medicinal chemistry however, there have been very few reports of artificial transmembrane chloride transporters which are not toxic to cells.<sup>41</sup> In an effort to address this concern, Talukdar et al. replaced one of the amide linkages with its bioisostere 1,2,3-triazole that is shown in Figure 1.16, as

the moiety is known to be less toxic but still possesses anion-binding ability (**1.21**).<sup>42</sup> The second amide moiety was retained in the structure to ensure the strong amide-anion binding and water solubility. A series of compounds **1.21a-d** was created to tune the binding affinity, lipophilicity, and membrane permeability of the anion transporter. The dose-responsive ion transport studies using HPTS assay provided the half-maximal activity ( $EC_{50}$ ) values of 1.68  $\mu$ M, *i.e.*, 2.5 mol%, relative to lipid concentration for the most active compound **1.21d** and the Hill coefficient “*n*” equal to 1, implying that a single molecule is sufficient to form the active transport complex.<sup>42</sup>

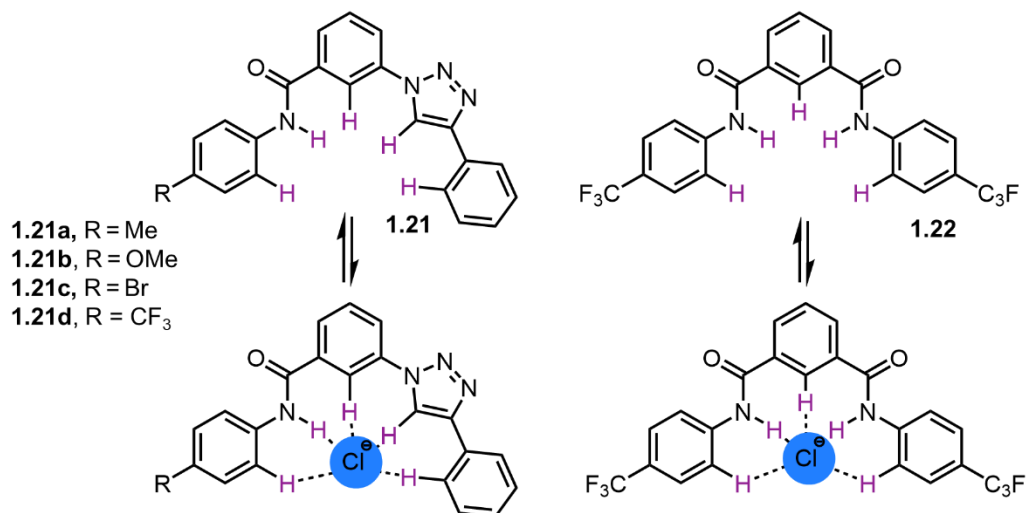


**Figure 1.16.** Structures of bioisostere 1,2,3-triazole (**1.21a-d**) transporter molecules of toxic anion transport **1.22**.<sup>43</sup>

Transporter **1.21d** was found to be most selective toward chloride ions, and such selectivity was further confirmed by monitoring its efflux using a chloride ion selective electrode (ISE). Mechanistic studies further confirmed an antiport mechanism of transport. MQAE is a 6-methoxyquinolinium derivative and is a fluorescent indicator for intracellular Cl<sup>-</sup>.<sup>42</sup> This dye detects the ion via diffusion-limited collisional quenching. MQAE has greater sensitivity to Cl<sup>-</sup>. The MQAE assay proved that it effectively transports Cl<sup>-</sup> ions into the cells (**1.21d**), and more importantly, MTT-based viability assays confirmed that the compound is nontoxic.

## 1.4.3 Chalcogen and Halogen bonds

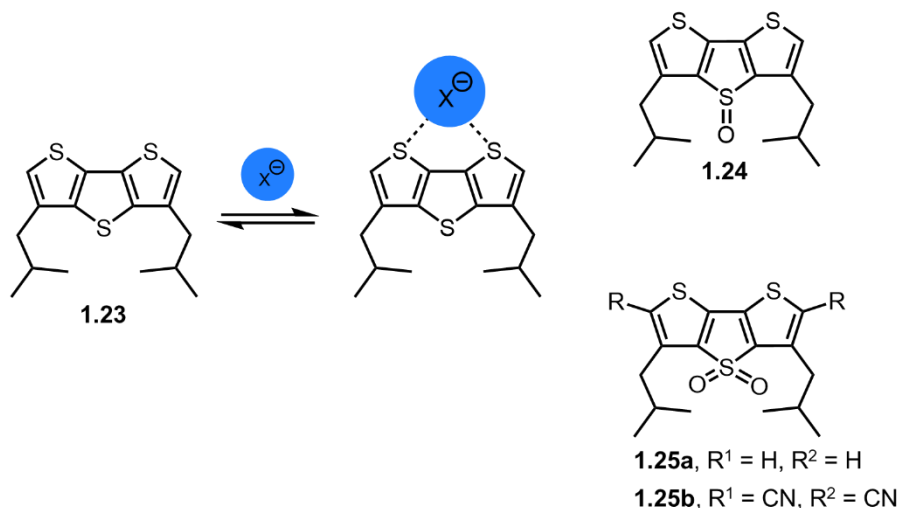


**Figure 1.17.** Electron-deficient dithieno[3,2-*b*;2',3'-*d*]thiophenes **1.23-1.25** using chalcogen bonds for anion binding for ion transport across lipid membranes.

Another class of anion binding other than using H donors are binding with sigma holes in certain atoms. Sigma holes are electron-deficient regions which arise from anisotropic distribution of electron density on a main-group atom bonded to an electron withdrawing group and leads to the formation of halogen (group 17), and chalcogen (group 16) bonds.<sup>43</sup> Chalcogen bonds comes from  $\sigma$  holes on electron-deficient sulfur, selenium, or tellurium for example.<sup>43</sup> Matile et al. introduce synthetic anion transporter that operate with chalcogen bonds. Electron-deficient dithieno[3,2-*b*;2',3'-*d*]thiophenes (DTTs, **1.23-1.25ab**) are identified as ideal to bind anions in the focal point of the  $\sigma$  holes on the cofacial endocyclic sulfur atoms.<sup>43</sup> Anion binding in solution and anion transport across lipid bilayers are found to increase with the depth of the  $\sigma$  holes of the DTT anionophores. A series of anions could bind to the DTTs such as  $ClO_4^-$ ,  $F^-$ ,  $Ac^-$ ,  $Br^-$ ,  $Cl^-$ ,  $I^-$ , and  $NO_3^-$  determined by NMR titration studies. For lipid transport studies,  $OH^-$  was used as the anion of choice using HPTS assay for this study. Hill coefficients were near  $n = 1$  for all transporters supported by curve fits and Job plots for anion binding in solution, suggesting that DTTs transport anions as monomers.

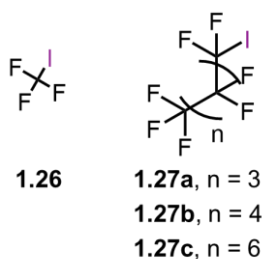


**Figure 1.18.** Select series perfluorinated iodoalkanes capable using forming halogen bond with anions.

Anions transport across lipid membranes can be achieved using halogen bonds, Matile et al. report that anion transport across lipid bilayers can be achieved with small perfluorinated molecules that are equipped with halogens capable of anion binding.<sup>44</sup> Anion transport for  $\text{OH}^-$  through halogen binding was determined by using HPTS assay to determine that iodobutane **1.27b** performed the best ( $\text{EC}_{50} = 21.6 \mu\text{M}$ ). The Hill coefficient  $n = 4.7$  for **1.27b** is consistent with computational results for halogen-bonded capsules as active structures for hydroxides in cooperative binding/channel formation. In contrast, the inability of iodobutane **4** to transport the much larger 5(6)-carboxyfluorescein (CF) demonstrated that leakage-free activity is recorded in the HPTS assay.

#### 1.4.4 Self-Assembled Ion Pores

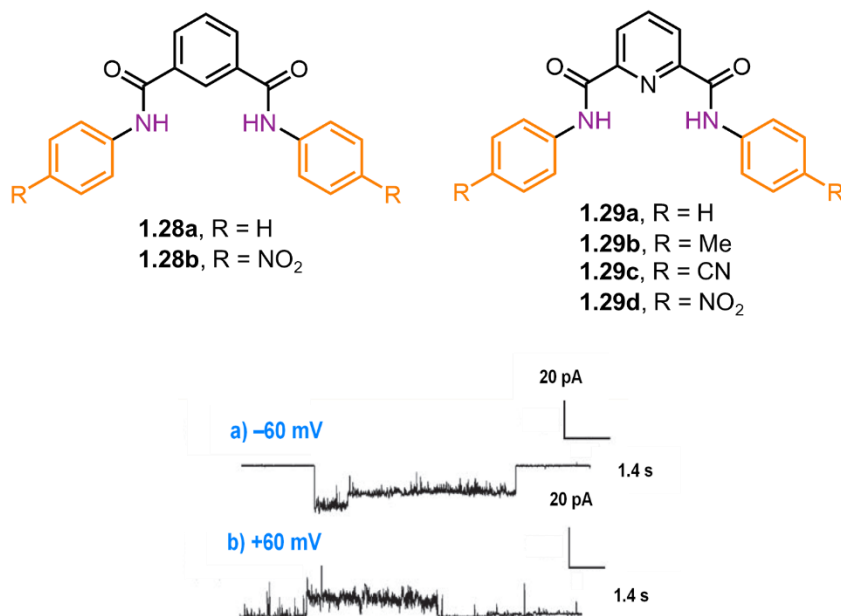


**Figure 1.19.** Isophthalamides based transporters and the pyridine derivatives (top left) studied by Gokel et al., and the planar bilayer conductance measurements of isophthalamide **1.29d** showing step-like changes in the current measured, upon application of a voltage of a)  $+60 \text{ mV}$  b)  $-60 \text{ mV}$ .<sup>45</sup>

Gokel et al. have reported a series of isophthalamide-based compounds and their pyridine derivatives that can facilitate chloride ion transport in DOPC vesicles (Figure 1.19).<sup>45</sup> Compound **1.29d** showed ion channel properties at physiologically relevant voltages, shown by planar bilayer conductance experiments. The application of a voltage across a planar lipid bilayer containing **1.29d**, step-like changes were observed, characteristic of voltage-gated ion channels in biological systems. Further, a Hill plot analysis yielded a Hill coefficient of  $n \sim 2$  at high transporter concentrations indicating channel formation. Additionally, evidence of aggregation was given by the X-ray crystal structure of **1.29d** due to strong aromatic interactions in the solid state. Gokel et al. found that in the presence of DOPC vesicles in DMSO, **1.29d** exhibited an excimer peak corresponding to face-to-face interactions between the aromatic rings. The authors hypothesize that the aggregation of 8–10 monomer units would be required to form a membrane-spanning channel (approximately 34 Å in length).

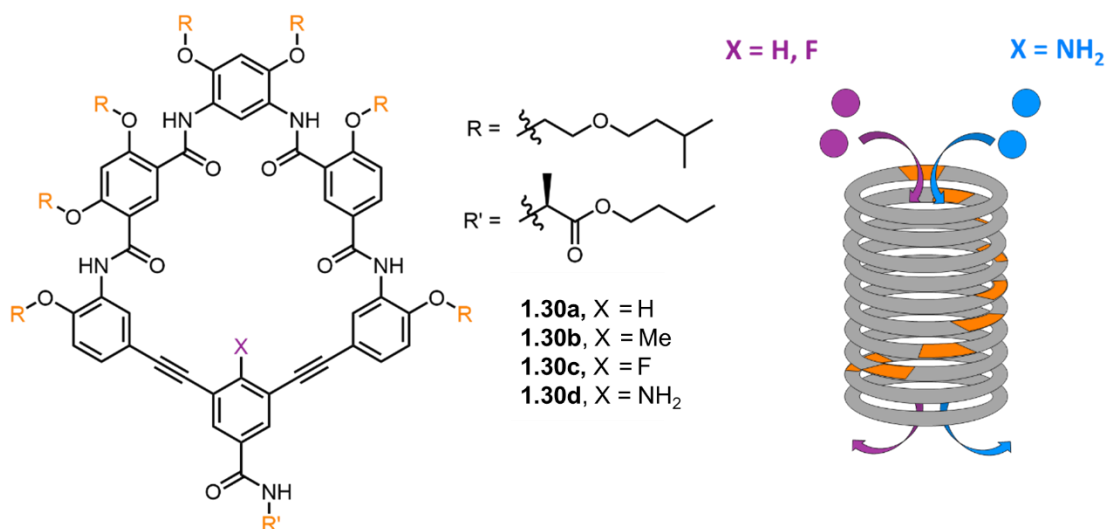


**Figure 1.20.** The macrocycles **1.30a-d** synthesized by Gong et al. and their helical stacking in a lipid bilayer.<sup>46</sup>

Gong et al. have developed an ion channel like transporter comprising rigid aromatic oligoamide macrocycles, which forms by the self-assembly of macrocycle units (Figure 1.20).<sup>46</sup> The transporter's ion channel properties were investigated by planar bilayer conductance experiments displaying step-like conduction changes. The self-assembly of the macrocycles was demonstrated by their fluorescence spectra in non-polar solvents. Both the amine (**1.30d**, X = NH<sub>2</sub>) and non-amine (**1.30c**, X = H, F) derivatives revealed an excimer-like emission band, due to the face-to-face, helical stacking of the macrocycles. The inward-facing functional group of the macrocycle allows for

selectivity in ion binding revealing the amine analogue selectively transports proton, whereas the non-amine analogue allows for  $\text{Cl}^-$  transport.

Talukdar et al. reported small molecules composed of 1,3-diethynylbenzene core and vicinal diols (**1.31**) that self-assemble in the lipid bilayer.<sup>47</sup> This self-assembly due to intermolecular hydrogen bonding forming a barrel-rosette type ion channel (Figure 1.21) capable of  $\text{Cl}^-/\text{OH}^-$  exchange which induces apoptosis in human cells through the disruption of  $\text{Cl}^-$  homeostasis. Evidence for ion channel formation was given by planar bilayer conductance experiments.

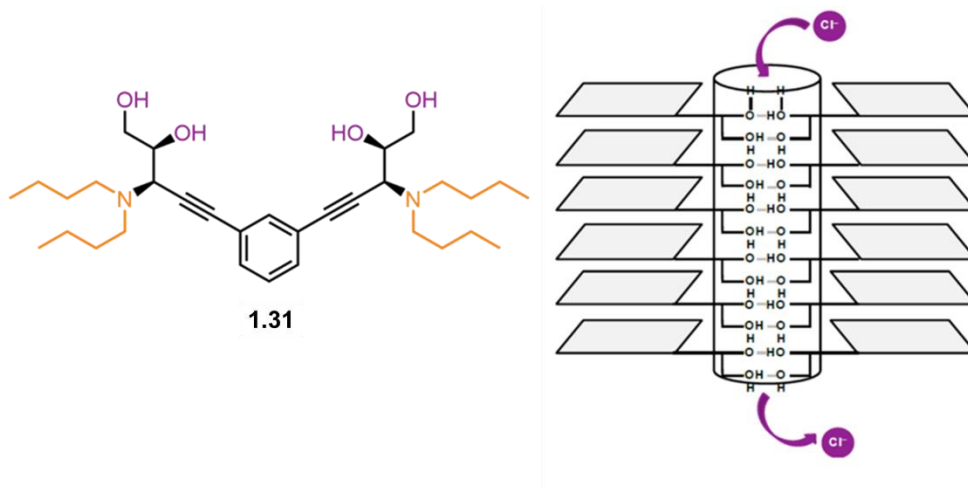


**Figure 1.21.** Bis-diols based transporter **1.31** studied by Talukdar et al., and their intermolecular hydrogen bonding-aided self-assembly in the lipid bilayer.<sup>47</sup>

More recently Gale et al. reported the synthesis of a fluorinated tetraurea macrocycle (Figure 1.22).<sup>48</sup> The macrocycle **1.32b** has a strong tendency to self-associate into columnar aggregates through intermolecular hydrogen bonds and aromatic interaction. Interestingly, in aqueous solutions **1.32b** generates solvent-shielding and size-selective binding pockets showing favourable hydrogen bonding with chloride. This aggregation property of **1.32b** allows it to strongly bind chloride ions within a hydrophobic microenvironment in 60% water/acetonitrile with a  $K_a = 1.4 \times 10^5 \text{ M}^{-1}$ . Further studies revealed that **1.32b** had the highest  $\text{H}^+/\text{Cl}^-$  symport activity among synthetic anion transporters reported.<sup>49</sup>

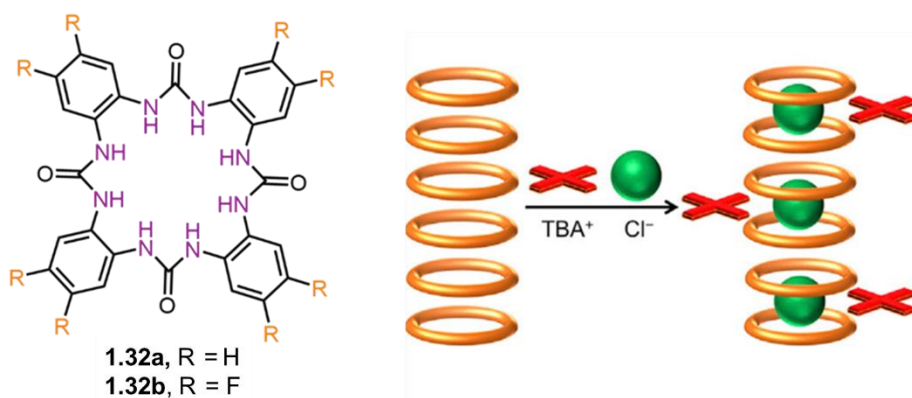


**Figure 1.22.** Tertaurea macrocyclic channel transporters **1.32a-b**, and schematic representation of chloride binding to columnar aggregates of **1.32a-b**.<sup>48,49</sup>

#### 1.4.5 Monomeric Ion Channels

Gokel et al. have reported structurally simple amphiphilic compounds called aplosspans, **1.33-1.34** spanning the length of the lipid bilayer (Figure 1.23).<sup>50</sup> These aplosspans are capable of transmembrane  $\text{Na}^+$ ,  $\text{K}^+$ ,  $\text{Cl}^-$ , and  $\text{Br}^-$  transport. These compounds incorporate *m*-phenylenediamine, diethanolamine, and crown ethers as ion-binding moieties, which operate ion transport through a relay mechanism.

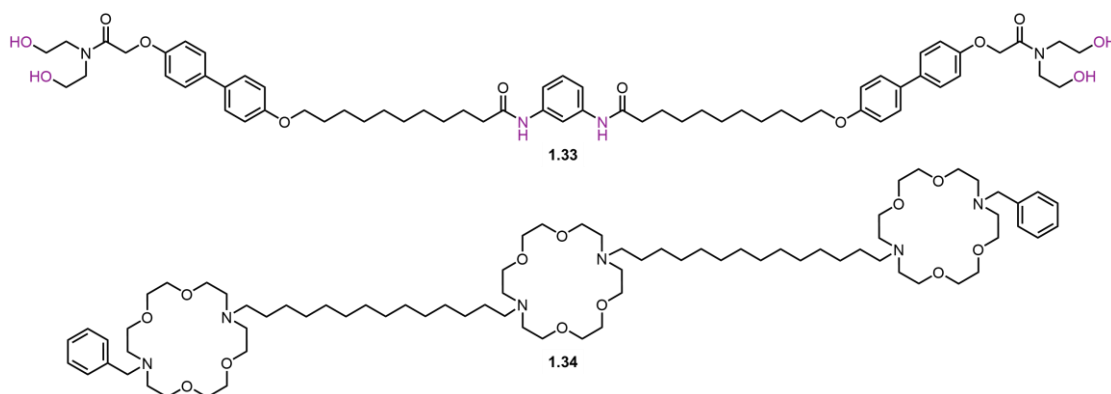


**Figure 1.23.** The membrane-spanning anion and cation transporters **1.33** and **1.34** reported by Gokel et al.<sup>50</sup>

Tian et al. has developed a monomeric ion channel by introducing a molecular machine comprising of a rotaxane with a tethered crown ether acting as a  $\text{K}^+$  carrier (**1.35**, Figure 1.24). This machine functions via a “molecular shuttle” type mechanism.<sup>51</sup> The rotaxane axle contains two benzylalkylammonium stations and a central *N*-methyltriazolium motif, while the macrocycle consists of a 24-crown-8 ether, and the ion receptor is an 18-crown-6 ether. At a neutral pH, all three moieties are protonated, and the macrocycle can shuttle across the axle in a random manner, enabling passive transport of  $\text{K}^+$  across the membrane. However, a pH increase can deprotonate the

benzylalkylammonium groups, immobilizing the macrocycle at the central station, preventing ion transport.

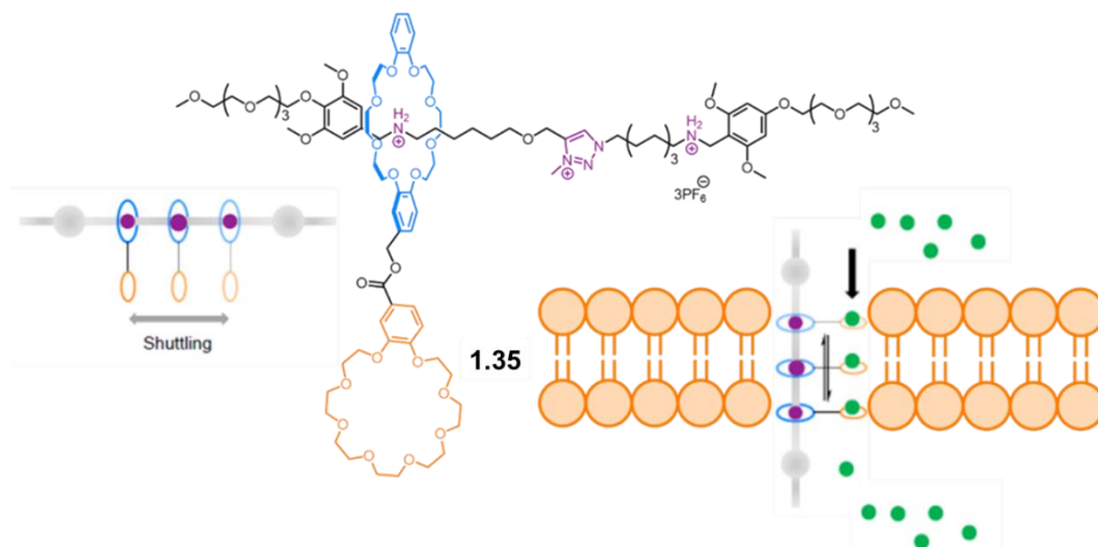


**Figure 1.24.** Structure of the rotaxane **1.35** synthesized by Tian et al. A schematic representation of the diffusion of the rotaxane's macrocycle along the axle, allowing for shuttling of the macrocycle, which allows for the passive transmembrane transport of  $K^+$  ions.<sup>51</sup>

## 1.5 Switchable Ion Transport

The ion transporters discussed thus far are only capable of passive ion transport controlled by an equilibrium established between the intracellular and extracellular ion concentrations. To get controlled ion transport, the transporter must be able to respond to stimuli, such as light, pH, or chemical fuel.

### 1.5.1 Light-Switchable Ionophores

Jeong et al. developed a series of light-switchable azobenzene transporters for  $Cl^-$  ion transport (Figure 1.25).<sup>52</sup> The *trans*-isomers showed poor transport activity, while the *cis*-isomers were highly active. The large enhancement in transport activity is attributed to the *cis*-isomers' four preorganized  $-NH$  groups available to chelate to an anion, whereas the *trans*-isomer only has two. For example, **1.36e** had a binding affinity ( $Cl^-$ ) for the *trans*-isomer of a  $K_a = 610\text{ M}^{-1}$  compared to  $K_a = 5900\text{ M}^{-1}$  for the *cis*. Additionally, the authors demonstrated the light-controlled switching of the most active transporter by irradiating the *trans*-isomer in situ (i.e., in POPC vesicles), which allowed anion transport to be switched “on” or “off” as desired.<sup>52</sup>

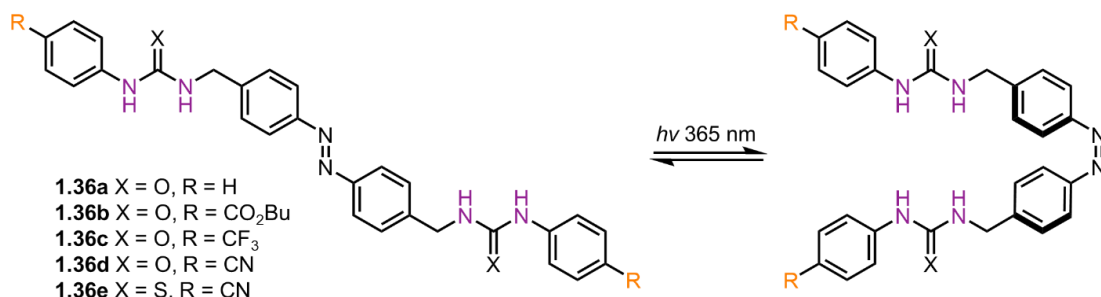


**Figure 1.25:** Select series of azobenzene transporters (**1.36a-e**) and the photoisomerization from the *trans*- to the *cis*-isomers.<sup>52</sup>

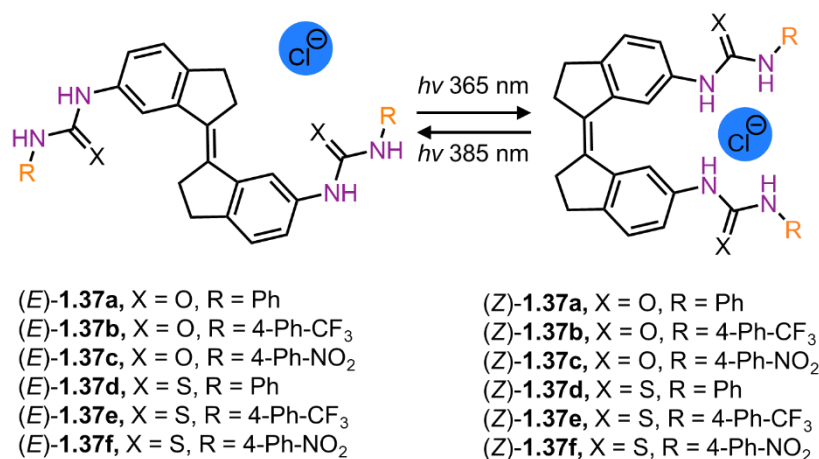


**Figure 1.26.** *E-Z* Photoisomerization of stiff-stilbene based bis(thio)ureas.<sup>53</sup>

A more recent example by Wezenberg and Gale et al. demonstrated photocontrol of transmembrane transport and electric potential using bis(thio)ureas derived from stiff-stilbene shown in Figure 1.26.<sup>53</sup> UV-vis and <sup>1</sup>H NMR spectroscopy were used to monitor *E-Z* photoisomerization of these bis(thio)ureas revealing stronger binding of chloride ions to the (*Z*)-form than to the (*E*)-form. For example (*E*)-**1.37a** has  $K_a = 17 \text{ M}^{-1}$  compared (*Z*)-**1.37a** has  $K_a = 66 \text{ M}^{-1}$  showing the (*Z*)-form binding chloride is stronger to the (*E*)-form. Importantly, the (*Z*)-isomers are much more active in transmembrane transport than the respective (*E*)-isomers as shown through various assays demonstrating a controllable ion carrier system driven by light.

## 1.5.2 Redox-Switchable Ionophores

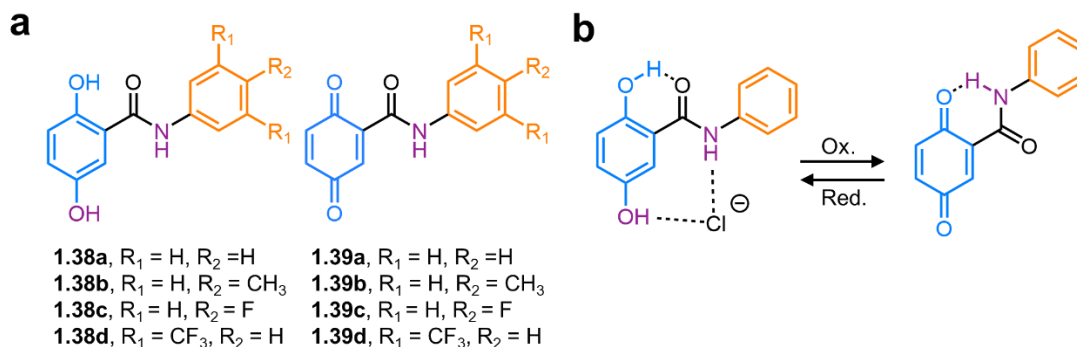


**Figure 1.27.** Gale et al hydroquinone-based receptors. a) Family of hydroquinone and quinone receptors synthesized in study. b) Mechanism of chloride binding for hydroquinone and quinone.<sup>54</sup>

In 2019, Gale et al. have reported a series of redox active hydroquinone-based anion receptors for chloride binding (Figure 1.27).<sup>54</sup> This scaffold was designed with using redox mediated conformational switch on chloride recognition. Hydroquinone compounds **1.38a–b** binding affinities were studied by <sup>1</sup>H-NMR spectroscopy titration with TBACl salt to reveal that in two complexation modes. First, a 2:1 complex form is made in small concentrations of Cl<sup>−</sup> ions, while in higher concentration 1:1 complex forms. Table 1.1 shows the binding constants for hydroquinone (2:1, 1:1) as well as quinone form binding constants. The hydroquinone compounds showed a positive cooperation Cl<sup>−</sup> anion binding with increased chloride concentration. Hydroquinone compounds did not follow the expected pattern that adding strong electron withdrawing will increase the binding affinity by creating a more acidic N-H bond which should increase the strength of hydrogen bonding. For the quinone **1.39a–d** have a stronger chloride affinity with increasingly electron-withdrawing appendages. The quinone had weaker affinity to chloride according to Table 1.1. No vesicles studies were done for these compounds to show any passive or active transport capabilities.

**Table 1.1.** Overview of the 2:1 association constant for the complexation of hydroquinone receptors **138a-c** with  $\text{Cl}^-$  (as TBA salt) in  $\text{CD}_3\text{CN}/1\%$   $\text{DMSO-d}_6$ , their interaction parameters, and the 1:1 association constants for the complexation of quinone Compounds **139a-d** with  $\text{Cl}^-$  in pure  $\text{CD}_3\text{CN}$ .

Hydroquinone Receptor	$K_{2:1}$	$K_{1:1}$	$a$	Quinone Receptor	$K_a^a$
<b>1.38a</b>	679.5	112.96	24.06	<b>1.39a</b>	11.2
<b>1.38b</b>	665.6	191.36	13.91	<b>1.39b</b>	11.39
<b>1.38c</b>	517.76	30.76	67.33	<b>1.39c</b>	19.64
<b>1.38d</b>	336.49	54.44	24.72	<b>1.39d</b>	67.72

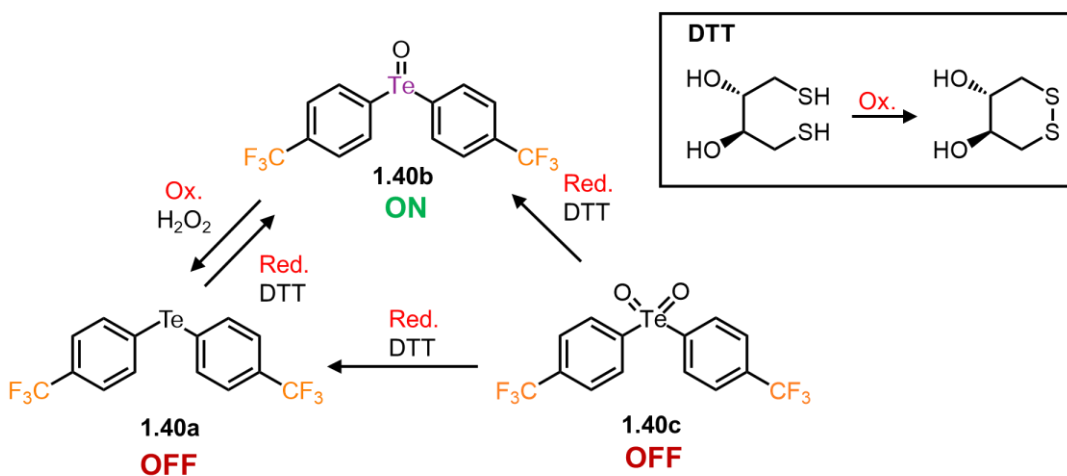


**Figure 1.28.** Summarized Redox Transformations between **1.40a**, **1.40b**, and **1.40c**, mediated by DTT or peroxide that affects anion transport across lipid membranes.

As mentioned earlier has chalcogen-donors for anion binding as become popular in application of anion receptor chemistry. Recently Langton et al. reported the first example of multistate redox-switchable transmembrane anion transport (**1.40a-c**)<sup>55</sup> Using Tellurium as the chalcogen centre, the compounds studied are highlighted in Figure 1.28. By employing reduction or oxidation conditions to obtain Te(VI), Te(IV), and Te(II) states, Langton et al. demonstrated reversibly switch between ON and OFF transport states *in situ* in the membrane. The reduction of the telluroxides and tellurones to the corresponding tellurides was achieved using a soluble glutathione mimics called dithiothreitol. The only active form for anion transport was the tellurones Te(IV) compared to the tellurides and telluroxides in transmembrane ion transport assays.<sup>55</sup>

## 1.6 Fuel Driven Anion Transport

### 1.6.1 pH Gradient Fueled Anion Transport

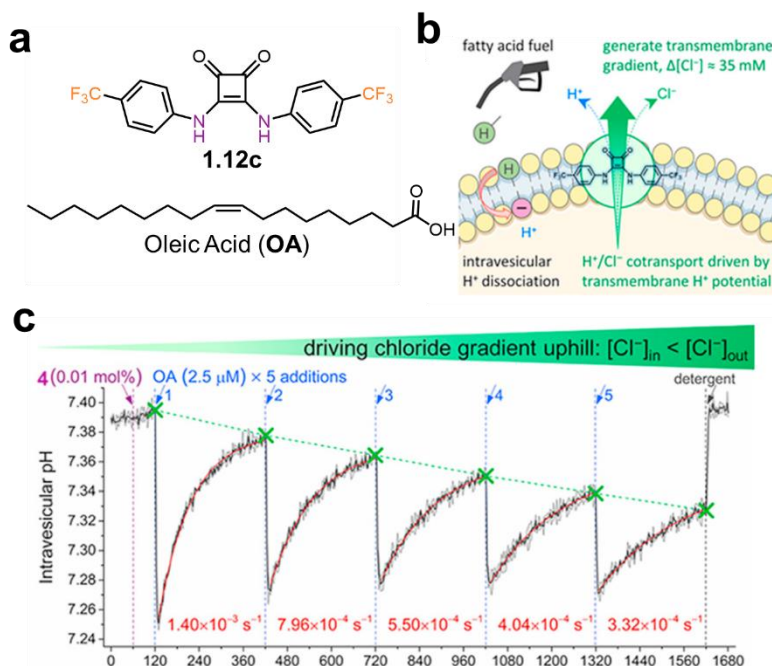


**Figure 1.29.** a) Chemical structures of squaramide **1.12c** and oleic acid (OA). b) Schematic illustration of OA fueled transmembrane chloride transport mediated by **4**. (c) Plot of intravesicular pH monitored by HPTS assay, with **4** added at  $t = 60 \text{ s}$  and OA (2.5 mM) at  $t = 120 \text{ s}$  and at ensuing 5 min time intervals to a total of five additions.<sup>56</sup>

In 2019, Gale and co-workers reported that by harnessing the transmembrane pH gradient established by OA, appropriately chosen synthetic chloride anion transporters could promote H<sup>+</sup>/Cl<sup>-</sup> cotransport, thereby generating a transmembrane Cl<sup>-</sup> gradient in LUVs.<sup>56</sup> As shown in Figure 1.29, squaramide **1.12c** is a powerful chloride anionophore and can mediate H<sup>+</sup>/Cl<sup>-</sup> cotransport. Upon addition of OA to LUVs, the intracellular pH decreased, thus generating a pH gradient as illustrated in Figure 1.27b. However, the addition of squaramide **1.12c** dissipates the pH gradient leading to the efflux of Cl<sup>-</sup> to maintain charge balance across the lipid bilayer. In the presence of chloride transporter **1.12c**, multiple pulsed additions of OA (at 5 min time intervals) resulted in the alternating generation and dissipation of pH gradients (Figure 1.27c). This result allows for the creation of new ion pumping systems where an external fuel is used to drive transmembrane ion transport.

## 1.6.2 Redox-active switchable Ionophores

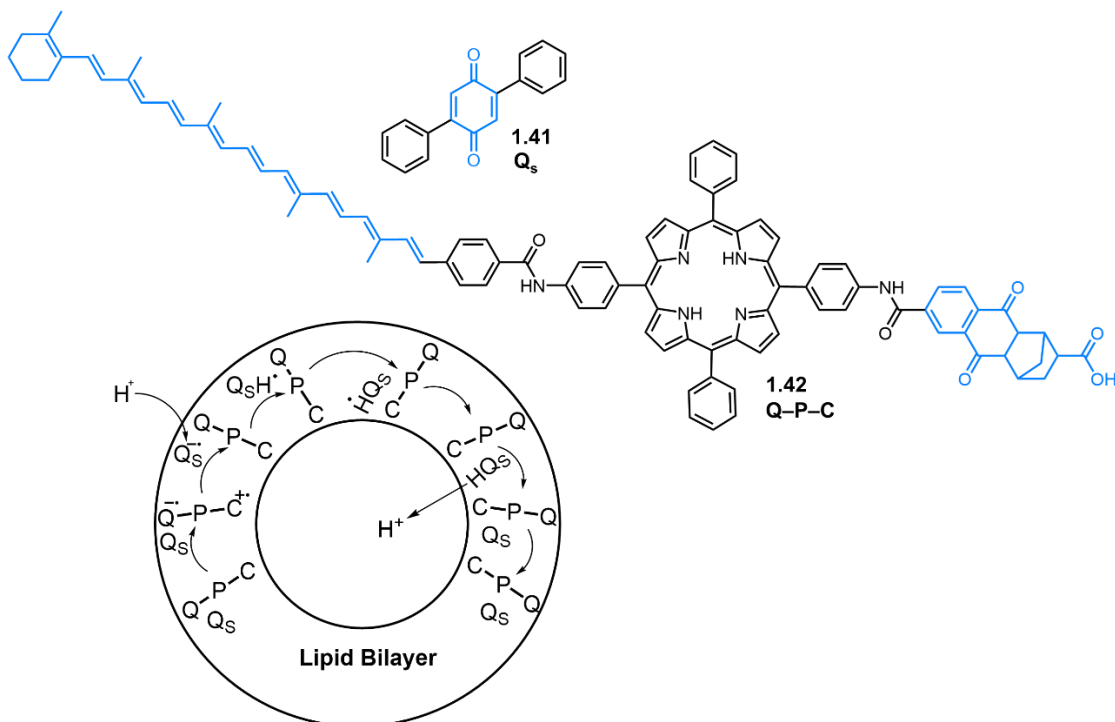


**Figure 1.30.** The redox-active quinone (**1.41**) and the photosensitive ion pump (**1.42**) that facilitate active transport. A schematic representation of the transport mechanism is shown as well.<sup>57</sup>

Gust and Moore et al. have developed a photosensitive ion pump that enables active transport of  $H^+$  ions across lipid bilayers (Figure 1.30).<sup>57</sup> As mentioned earlier, ion pumps facilitate active transport upon the input of energy to drive the thermodynamically unfavorable process of transporting a species against a concentration gradient. The pump consists of two components: a molecular triad **1.42** and a freely diffusing 2,5-diphenylbenzoquinone molecule (**1.41** or  $Q_s$ ). The molecular triad comprises a photosensitive tetraarylporphyrin unit (P) linked to a carotenoid polyene (C) and a naphthoquinone motif fused to a norbornene bearing a carboxylic acid group (Q). Irradiation (430 nm) generates the excited singlet state of the porphyrin unit, which is conjugated throughout the molecule to yield a charge separated species ( $C^+-P-Q^-$ ). The anionic  $Q^-$  can reduce the quinone ( $Q_s$ ), allowing it to bind to protons and shuttle them across the bilayer. At the cationic end ( $C^+$ ), the semiquinone ( $HQ_s^\bullet$ ) is oxidized, allowing it to release the proton in the internal medium. Further work on this system showed it promoted the active transport of  $Ca^{2+}$  (Figure 1.31).<sup>58</sup> The  $Ca^{2+}$  pump uses the molecular triad **1.42** and a redox-active hydroquinone **1.43a**, which binds to  $Ca^{2+}$  and transports it across the lipid bilayer. Based on  $^1H$  NMR titrations

experiments, two hydroquinone molecules bind to one  $\text{Ca}^{2+}$  ion ( $K_a = 820 \text{ M}^{-1}$ ), while the quinone molecules do not participate in binding. Upon the addition of  $\text{CaCl}_2$ , hydroquinones chelate to  $\text{Ca}^{2+}$  from the external aqueous medium and diffuse across the bilayer. Irradiation (430 nm) generates a redox potential as described above, leading to the formation of a cationic carotenoid moiety, which oxidizes the hydroquinone releasing  $\text{Ca}^{2+}$  into the internal medium. The quinone can then diffuse back across the bilayer to the anionic carboxylate end, where it is reduced back. Overall, this leads to the electrogenic active transport of  $\text{Ca}^{2+}$  into vesicles.

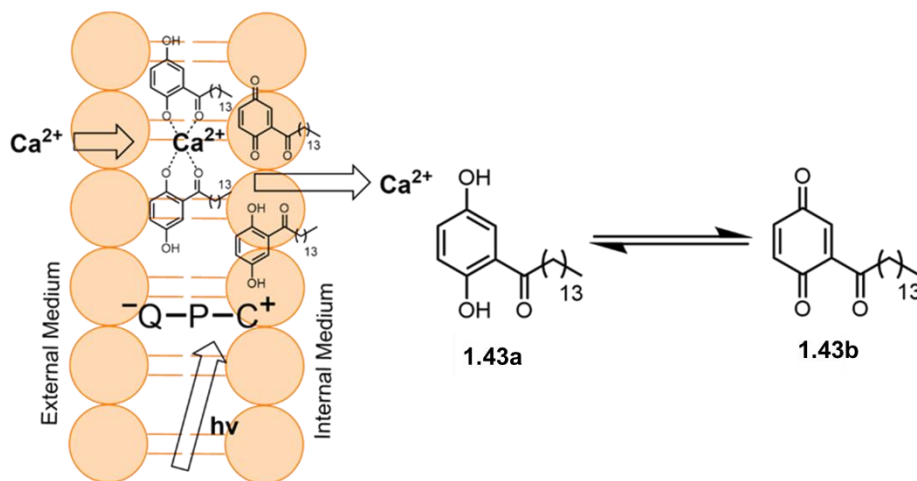


**Figure 1.31.** A schematic representation of the active transport of  $\text{Ca}^{2+}$  ions by the photosensitive molecular triad (**1.42**) and the lipophilic redox switchable hydroquinone/quinone (**1.43a-b**).<sup>58</sup>

## 1.7 Overview

Cellular membranes serve as barriers for the exchange of substrates into and out of a cell. The exchange of solutes between cells and their extracellular milieu is crucial for maintaining the normal operation of biological systems. Charge species such as ions require the assistance proteins that function ion carriers or transmembrane ion channels. This chapter discussed the state of the are synthetic mimics of these ion carriers and channels by using supramolecular chemistry in lipid membranes. A variety of examples using different non-covalent binding motifs were explored such as NH, OH and CH donors as wells chalcogen and halogen bonds. Most of these ion transporters are studied using liposomal assays that use kinetic spectroscopy techniques (fluorescence), NMR studies, selective ion electrodes and black lipid membranes experiments. The parameters need to study the performance of these transporters such as Hill coefficient, binding affinities and  $\text{EC}_{50}$  were considered. More sophisticated ionophore systems

were reviewed, such as switchable ionophores by light, redox fuel and pH gradients which at the forefront of this field. There are however very limited examples of active transport against chemical equilibrium which we attempt to tackle designing redox active ion transporters that can be capable of this feat.

## 1.8 References

- 1 E. L. Smith, *J. Gen. Physiol.*, 1938, **22**, 21–35.
- 2 S. Fowler, R. Roush, J. Wise, *Concepts of Biology*, Rice University, Houston, TX, 2013.
- 3 M. S. Bretscher, *Science*, 1973, **181**, 622–629.
- 4 C. Kirby, J. Clarke and G. Gregoriadis, *Biochem. J.*, 1980, **186**, 591–598.
- 5 G. Renger, *Curr. Sci.*, 2010, **98**, 1305–13.  
J. Singh, P. Pandey, D. James, K. Chandrasekhar, V. M. M. Achary, T. Kaul, B. C. Tripathy and M. K. Reddy, *Plant Biotechnol. J.*, 2014, **12**, 1217–1230.
- 6 A. T. Wilson and M. Calvin, *J. Am. Chem. Soc.*, 1955, **77**, 5948–5957.
- 7 M. Calvin, *Angew. Chem. Int. Ed.*, 1962, **1**, 65–75.
- 8 F. Kreuzaler, C. Peterhänsel and H. J. Hirsch, in *Bioengineering in Cell and Tissue Research*, 2008.
- 9 U. Gowik and P. Westhoff, *Plant Physiol.*, 2011, **155**, 56–63.
- 10 E. A. Kellogg, *Curr. Biol.*, 2013, **23**, 594–599.
- 11 C. P. Osborne and R. P. Freckleton, *Proc. R. Soc. B.* 2009, **276**, 1753–1760.
- 12 W. J. Bond, F. I. Woodward and G. F. Midgley, *New Phytol.*, 2005, **165**, 525–538.
- 13 D. C. Gadsby, *Nat. Rev. Mol. Cell Biol.*, 2009, **10**, 344–352.
- 14 W. Hasselbach and H. Oetliker, *Annu. Rev. Physiol.*, 1983, **45**, 325–339.
- 15 R. Pethig, *Modern Bioelectrochemistry*, 1986.
- 16 F. Hucho, *J. Cell. Sci.* 1996, **109**, 2401–2406.
- 17 A. Takeuchi, N. Reyes, P. Artigas and D. C. Gadsby, *Nature*, 2008, **456**, 413–416.
- 18 A. Accardi and C. Miller, *Nature*, 2004, **427**, 803–807.
- 19 A. S. Ethayathulla, M. S. Yousef, A. Amin, G. Leblanc, H. R. Kaback and L. Guan, *Nat. Commun.*, 2014, **5**, 3009.
- 20 J. P. Castillo, H. Rui, D. Babilio, A. Das, B. Roux, R. Latorre, F. Bezanilla and M. Holmgren, *Nat. Commun.*, 2015, **6**, 7622.
- 21 B. C. Pressman, *Annu. Rev. Biochem.*, 1976, **45**, 501–530.
- 22 S. Varma, D. Sabo and S. B. Rempe, *J. Mol. Biol.*, 2008, **376**, 13–22.
- 23 S. Rastogi, E. Marchal, I. Uddin, B. Groves, J. Colpitts, S. A. McFarland, J. T. Davis and A. Thompson, *Org. Biomol. Chem.*, 2013, **11**, 3834–3845.
- 24 P. A. Gale, R. Pérez-Tomás and R. Quesada, *Acc. Chem. Res.*, 2013, **46**, 2801–2813.
- 25 P. A. Gale, J. T. Davis and R. Quesada, *Chem. Soc. Rev.*, 2017, **46**, 2497–2519.
- 26 H. Valkenier, N. López Mora, A. Kros and A. P. Davis, *Angew. Chem. Int. Ed.*, 2015, **54**, 2137–2141.
- 27 A. V. Koulov, T. N. Lambert, R. Shukla, M. Jain, J. M. Boon, B. D. Smith, H. Li, D. N. Sheppard, J. B. Joos, J. P. Clare and A. P. Davis, *Angew. Chem. Int. Ed.*, 2003, **42**, 4931–4933.
- 28 S. J. Moore, M. Wenzel, M. E. Light, R. Morley, S. J. Bradberry, P. Gómez-

- Iglesias, V. Soto-Cerrato, R. Pérez-Tomás and P. A. Gale, *Chem. Sci.*, 2012, **3**, 2501–2509.
- 29 V. Saggiomo, S. Otto, I. Marques, V. Félix, T. Torroba and R. Quesada, *Chem. Commun.*, 2012, **48**, 5274–5276.
- 30 C. J. E. Haynes, N. Busschaert, I. L. Kirby, J. Herniman, M. E. Light, N. J. Wells, I. Marques, V. Félix and P. A. Gale, *Org. Biomol. Chem.*, 2014, **12**, 62–72.
- 31 A. V. Jentzsch, D. Emery, J. Mareda, S. K. Nayak, P. Metrangolo, G. Resnati, N. Sakai and S. Matile, *Nat. Commun.*, 2012, **3**, 905.
- 32 J. N. Weinstein, R. Blumenthal and R. D. Klausner, *Methods Enzymol.*, 1986, **128**, 657–668.
- 33 B. A. McNally, A. V. Koulov, B. D. Smith, J. B. Joos and A. P. Davis, *Chem. Commun.*, 2005, **8**, 1087–1089.
- 34 S. K. Ko, S. K. Kim, A. Share, V. M. Lynch, J. Park, W. Namkung, W. Van Rossom, N. Busschaert, P. A. Gale, J. L. Sessler and I. Shin, *Nat. Chem.*, 2014, **6**, 885–892.
- 35 I. W. Park, J. Yoo, B. Kim, S. Adhikari, S. K. Kim, Y. Yeon, C. J. E. Haynes, J. L. Sutton, C. C. Tong, V. M. Lynch, J. L. Sessler, P. A. Gale and C. H. Lee, *Chem. Eur. J.*, 2012, **18**, 2514–2523.
- 36 M. Yano, C. C. Tong, M. E. Light, F. P. Schmidtchen and P. A. Gale, *Org. Biomol. Chem.*, 2010, **8**, 4356–4363.
- 37 N. Busschaert, I. L. Kirby, S. Young, S. J. Coles, P. N. Horton, M. E. Light and P. A. Gale, *Angew. Chem. Int. Ed.*, 2012, **51**, 4426–4430.
- 38 J. A. Cooper, S. T. G. Street and A. P. Davis, *Angew. Chem. Int. Ed.*, 2014, **53**, 5609–5613.
- 39 M. J. Spooner and P. A. Gale, *Chem. Commun.*, 2015, **51**, 4883–4886.
- 40 M. Debashis, A. Manzoor Ahmad, P. Prakash, U. Avisikta, and P. Talukdar *J. Org. Chem.* **2022** 87, 10–17.
- 41 A. Mondal, M. Ahmad, D. Mondal and P. Talukdar, *Chem. Commun.*, **2023**, 59, 1917–1938
- 42 J. A. Malla, A. Upadhyay, P. Ghosh, D. Mondal, A. Mondal, S. Sharma, and P. Talukdar, *Org. Lett.* **2022**, 24, 4124–4128.
- 43 S. Benz, M. Macchione, Q. Verolet, J. Mareda, N. Sakai, and S. Matile, *J. Am. Chem. Soc.* 2016, **138**, 9093–9096.
- 44 A. V. Jentzsch, D. Emery, J. Mareda, S. K. Nayak, P. Metrangolo, G. Resnati, N. Sakai and S. Matile, *Nat. Commun.* **2012**, 3, 905.
- 45 C. R. Yamnitz, S. Negin, I. A. Carasel, R. K. Winter and G. W. Gokel, *Chem. Commun.*, 2010, **46**, 2838–2840.
- 46 X. Wei, G. Zhang, Y. Shen, Y. Zhong, R. Liu, N. Yang, F. Y. Al-Mkhaizim, M. A. Kline, L. He, M. Li, Z. L. Lu, Z. Shao and B. Gong, *J. Am. Chem. Soc.*, 2016, **138**, 2749–2754.
- 47 T. Saha, A. Gautam, A. Mukherjee, M. Lahiri and P. Talukdar, *J. Am. Chem. Soc.*, 2016, **138**, 16443–16451.
- 48 X. Wu, P. Wang, P. Turner, W. Lewis, O. Catal, D. S. Thomas and P. A. Gale, *Chem*, 2019, **5**, 1210–1222.

- 49 X. Wu, J. R. Small, A. Cataldo, A. M. Withecombe, P. Turner and P. A. Gale, *Angew. Chem. Int. Ed.*, 2019, **58**, 15142–15147.
- 50 W. Wang, R. Li and G. W. Gokel, *Chem. Eur. J.*, 2009, **15**, 10543–10553.
- 51 S. Chen, Y. Wang, T. Nie, C. Bao, C. Wang, T. Xu, Q. Lin, D. H. Qu, X. Gong, Y. Yang, L. Zhu and H. Tian, *J. Am. Chem. Soc.*, 2018, **140**, 17992–17998.
- 52 Y. R. Choi, G. C. Kim, H. G. Jeon, J. Park, W. Namkung and K. S. Jeong, *Chem. Commun.*, 2014, **50**, 15305–15308.
- 53 S. J. Wezenberg, L. Chen, J. E. Bos, B. L. Feringa, E. N. W. Howe, X. Wu, M. A. Siegler, and P. A. Gale. *J. Am. Chem. Soc.* 2022, **144**, 331–338.
- 54 D. A. McNaughton, X. Fu, W. Lewis, D. M. D'Alessandro, and P. A. Gale, *Chemistry*, 2019, **1**, 80–88.
- 55 A. Docker, T. G. Johnson, H. Kuhn, Z. Zhang, and M. J. Langton\*, *J. Am. Chem. Soc.* 2023, **145**, 4, 2661–2668.
- 56 E. N. W. Howe, and P. A. Gale, *J. Am. Chem. Soc.* 2019, **141**, 10654–10660.
- 57 G. Steinberg-Yfrach, P. A. Liddell, S. C. Hung, A. L. Moore, D. Gust and T. A. Moore, *Nature*, 1997, **385**, 239–241.
- 58 I. M. Bennett, H. M. Vanegas Farfano, F. Bogani, A. Primak, P. A. Liddell, L. Otero, L. Sereno, J. J. Silber, A. L. Moore, T. A. Moore and D. Gust, *Nature*, 2002, **420**, 398–401.

# Chapter 2 | Redox-Active Molecular Ion Carriers for Active Ion Transports

## 2.0 Synopsis

This chapter discusses the aim to interface the world of artificial molecular devices with the plant's internal machinery, thus increasing their photosynthesis efficiency and adaptability against the effects of global climate changes. We designed and synthesised redox-active quinone based artificial molecular carriers (RAMCs) that can recognise ions such as bicarbonate and chloride ions. The molecules are designed to instigate the active transport of ions across lipid membranes, 'pumping' ions from areas of low concentration to areas of higher concentration. We hypothesise that these carriers can consume a redox fuel which can be supplied by the charge separation already present in photosynthetic cells – to switch between hydroquinone and quinone forms. This project exploits a supramolecular system that moves away from equilibrium, which remains a contemporary challenge at the frontier of chemistry. These RAMCs is a rare demonstration of work towards active transport by a synthetic small molecule which is powered by a chemical fuel and that is designed to interface with cells. For this project, we synthesised new urea RAMCs with varying alkyl chain lengths. Analysis of the RAMCs supramolecular interactions was carried out with a series of anions utilizing  $^1\text{H}$  NMR spectroscopic titrations and detailed solid-state analysis such, as single crystal X ray diffraction and solid-state NMR. Investigation of active anion transport was attempted in artificial cells, i.e., vesicles, and analysed using fluorescence assays. Finally, we tested the compounds in plant cells and live plants through plant science collaborators.

## Acknowledgment

The following people are gratefully acknowledged for their contribution to this chapter: Dr. Brett Chapin carried out the NMR titrations. Dr. Mohamed Algaradah and Promeet Saha for doing preliminary work on developing the liposomal assays for passive and active ion transport. Mary Gibbins for screening reductants and oxidants for the redox-active molecular carriers. Lastly, Dr. Paul McGonigal for obtaining the single crystal of UHQ<sub>6</sub>.

## 2.1 Introduction

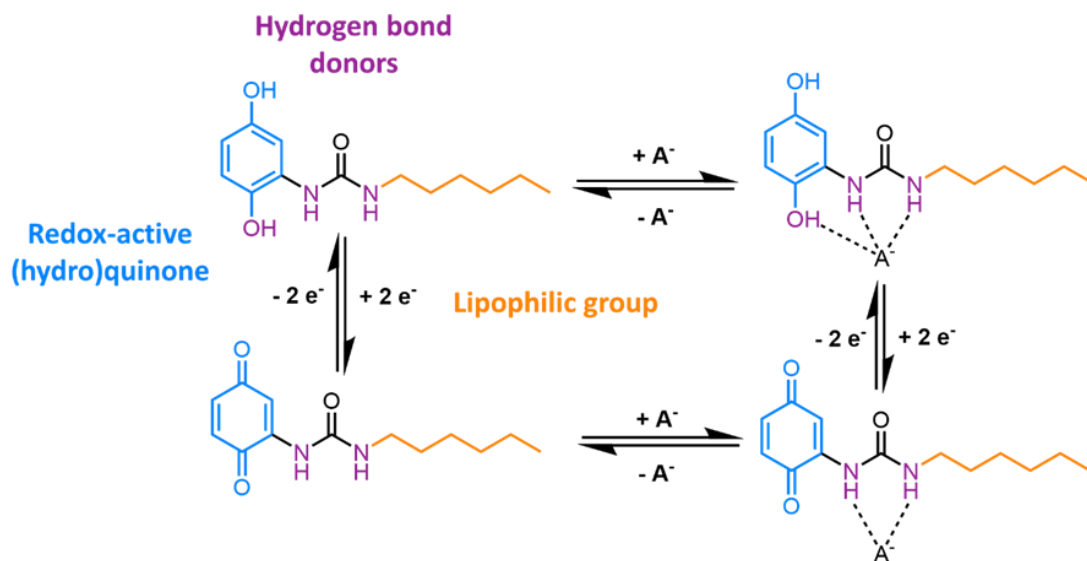


**Figure 2.1.** Example of redox-active artificial molecular carriers (RAMCs) based on lipophilic urea (hydro)quinone that can undergo a two electron redox processes. This reversible redox process changes the amount of and the acidity of NH donors which in turn modulates the carrier's affinity for ions.

As mentioned in chapter 1, Gust and Moore et al. have developed a photosensitive ion pump that enables active transport of  $H^+$  ions across lipid bilayers taking advantage of the hydroquinone/quinone systems.<sup>57</sup> Ion pumps facilitate active transport upon the input of energy to drive the thermodynamically unfavorable process of transporting a species against a concentration gradient. The pump consists of two components: a molecular triad **1.39** and a freely diffusing 2,5-diphenylbenzoquinone molecule. We take inspiration from this system by designing anion transporter using hydroquinone and quinone molecular scaffold in combination that can switch between the two forms using a redox fuel. These redox active molecular carriers (RAMCs) will have flanking urea groups capable of anion binding through NH and OH donor. Unlike Gust et al., these redox active molecular carriers or RAMCs are capable to transport anions across lipid membrane instead of  $H^+$ . A feature of our ionophore systems is the change of anion binding environment of the RAMCs by redox as the loss of proton from hydroquinone oxidation to quinone form (loss of OH donor) along with the electronic changes of the molecular scaffold (Figure 2.1). Additionally, we hypothesize that these RAMCs are capable to instigate the active transport (Figure 2.2) of ions across lipid

membranes, ‘pumping’ ions from areas of low concentration to areas of higher concentration.

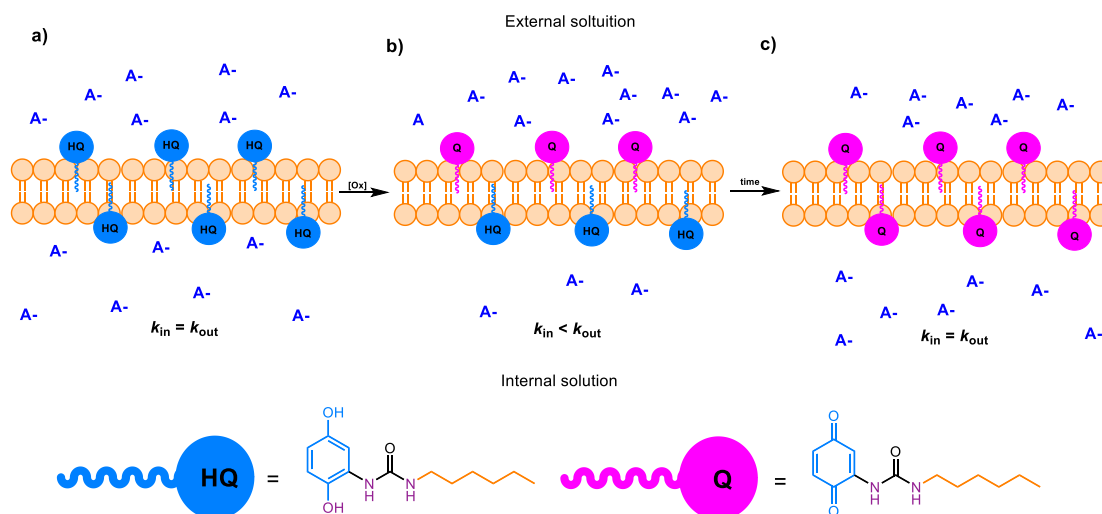


**Figure 2.2.** Schematic representation of the hypothetical mechanism of active transport facilitated by the redox-switchable quinone/hydroquinone transporter. A) hydroquinone transporters incorporated in the membrane without the presence of an oxidant. B) Addition of the oxidant leads to the formation of the quinone on the external side of the membrane interface, leading to change in equilibrium, transporting the anion. C) After certain time, all the RAMCs are oxidized, restoring the equilibrium.

### 2.1.1 Aims & Objectives

The long-term aim of this study is to interface the world of artificial molecular devices with the plant’s internal machinery, thus increasing their photosynthesis efficiency and adaptability against the effects of global climate changes (Figure 2.3). These RAMCs as shown in figure should be able recognise bicarbonate ions as a form of  $\text{Ci}$ , for the introduction of a  $\text{C}_4$ -like photosynthetic pathway in  $\text{C}_3$  plant. These RAMCs is a rare demonstration of work towards active transport by a synthetic small molecule which is powered by a chemical fuel and that is designed to interface with cells. For this study, we synthesized new urea based RAMCs with varying alkyl chain lengths. Analysis of the RAMCs supramolecular interactions was carried out with a series of anions utilizing  $^1\text{H}$  NMR spectroscopic titrations and detailed solid-state analysis such, as single crystal X ray diffraction and solid-state NMR. Investigation of active anion transport in artificial cells, i.e., vesicles, was analysed using fluorescence assays. Finally, we tested the compounds in plant cells and live plants through plant science collaborators.

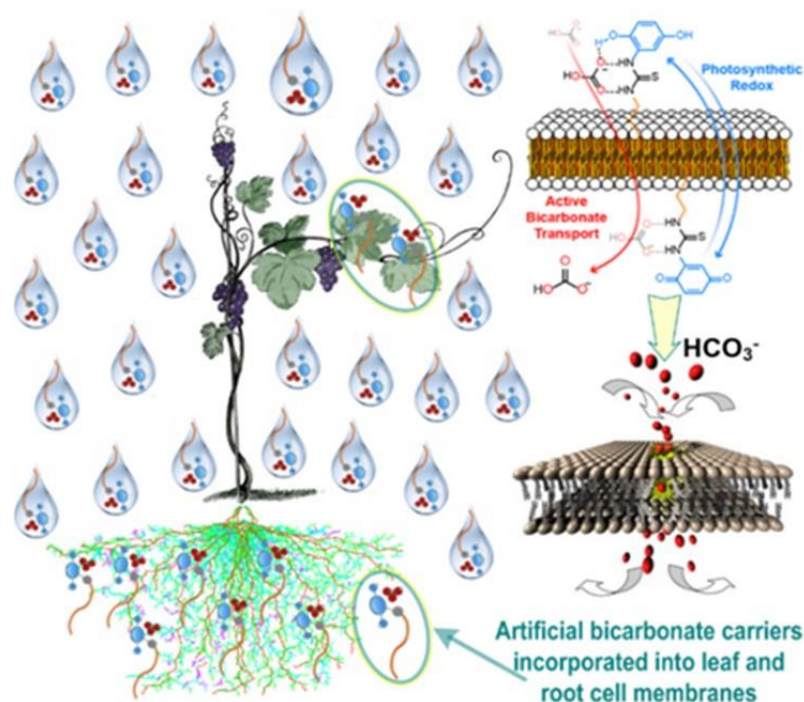
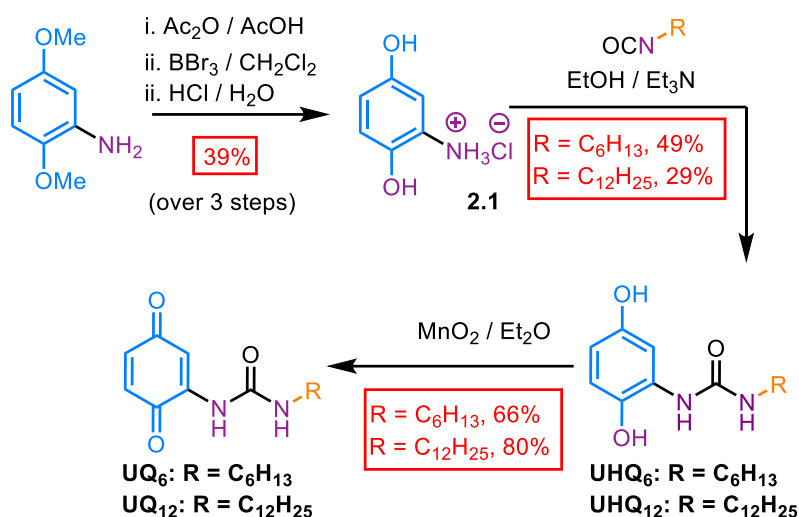


**Figure 2.3.** Artificial bicarbonate carriers bind and transport bicarbonate ( $\text{HCO}_3^-$ ) and carbonate ( $\text{CO}_3^{2-}$ ) across cell membranes in plants. The redox-active quinone that is part of the bicarbonate binding motif modulates the carrier's affinity for bicarbonate in response to redox processes occurring naturally during photosynthesis, creating an active transport pathway in chloroplasts. These artificial bicarbonate “engines” will be incorporated in the leaves and the root system to increase use of soil bicarbonates.

## 2.2 Synthesis of Redox-Active Transporter

### 2.2.1 Urea-based RAMCs

The synthesis of urea-based anionophores was previously developed by past members of the McGonigal group. The synthesis of the urea based RAMCs are illustrated in Scheme 2.1. Starting from the commercially available 2,5-dimethoxyaniline, the amine was acetylated using acetic anhydride to produce an acetamide. This protection allowed for the deprotection of methoxy groups to obtain the alcohol groups in the 2- and 5-positions using a Lewis acid  $\text{BBr}_3$  and water. Next, the acetamide hydrolysis was achieved under acidic conditions in  $\text{HCl}/\text{MeOH}$ , producing the ammonium salt, **2.1**, in an overall yield of 39% over 3 steps. The ammonium salt **2.1** was then deprotonated using trimethylamine and undergoes a nucleophilic addition to desired alkyl isocyanate to lead to hydroquinone compounds **UHQ<sub>6</sub>** and **UHQ<sub>12</sub>** in modest yields. In the presence of an oxidant,  $\text{MnO}_2$ , the hydroquinone compounds are oxidized to the quinone **UQ<sub>6</sub>**.



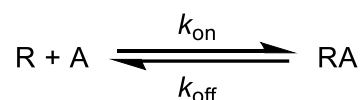
**Scheme 2.1.** Synthetic route to urea transporters **UHQ<sub>6</sub>**, **UHQ<sub>12</sub>**, **UQ<sub>12</sub>** and **UQ<sub>6</sub>**.

## 2.3 Anion Binding Studies

To understand the active transport properties of the urea RAMCs, the mechanism of ion transport for these compounds was investigated. A comprehensive mechanistic study would involve (1) anion binding studies to measure the binding affinities to  $\text{Cl}^-$ ,  $\text{NO}_3^-$ ,  $\text{HCO}_3^-$ ,  $\text{SO}_4^{2-}$ , etc. using  $^1\text{H}$  NMR spectroscopic titration and detailed solid-state studies, (2) the study of passive transport mode and capabilities at lipid membrane interface using lipid vesicles and lucigenin assays.

### 2.3.1 NMR Binding Studies

The binding constant or stability constant ( $K_a$ ) between a receptor (R) and an ion (A) can be determined for the following equilibrium:



The equilibrium constant for the above corresponds to  $K_a$ :

$$K_a = \frac{k_{\text{on}}}{k_{\text{off}}} = \frac{[\text{RA}]}{[\text{R}][\text{A}]}$$

A previous member of the McGonigal group (Dr. B.M. Chapin) used  $^1\text{H}$  NMR titrations  $\text{Et}_4\text{N} \cdot \text{HCO}_3$  and  $\text{Et}_4\text{N} \cdot \text{Cl}$  in  $(\text{CD}_3)_2\text{SO}$  to determine the binding affinities,  $K_a$ , for the redox active anionophores **UHQ<sub>6</sub>** and **UQ<sub>6</sub>**. A stock solution of **UHQ<sub>6</sub>** or **UQ<sub>6</sub>** receptor were prepared in  $(\text{CD}_3)_2\text{SO}$  (24.2 mM). **UHQ<sub>6</sub>** or **UQ<sub>6</sub>** stock solution (300  $\mu\text{L}$ ),  $(\text{CD}_3)_2\text{SO}$  (300  $\mu\text{L}$ ), and deionized water (3  $\mu\text{L}$ ) were combined in an NMR tube to

give the receptor solution (12.1 mM hydroquinone receptor, 0.5% deionized water in  $(\text{CD}_3)_2\text{SO}$ ). The tetraethylammonium salt of a given anion ( $\text{Et}_4\text{N}\cdot\text{X}$ , 0.15 mmol) was combined with hydroquinone stock solution (500  $\mu\text{L}$ ) and deionized water (5  $\mu\text{L}$ ) in a 1-mL volumetric flask. The volumetric flask was filled to 1 mL with  $(\text{CD}_3)_2\text{SO}$  to give the titrant solution (12.10 mM hydroquinone receptor, 150 mM anionic analyte, and 0.5% deionized water in  $(\text{CD}_3)_2\text{SO}$ ). Literature precedent established that binding interactions between anions and amphiphilic artificial anion transporters measured in  $(\text{CD}_3)_2\text{SO}$  stock solutions are relevant to anion transport processes at the interface between lipophilic membranes and water.<sup>1</sup> The titrant solution was added to the receptor solution in the NMR tube using a microsyringe. After each addition, the NMR tube was inverted several times, and a  $^1\text{H}$  NMR spectrum was acquired. Changes in the proton signals of the receptor shown in Figures 1.4, 1.5 & 1.6 were tractable through ppm shifting throughout the titration. The NH and OH proton signals of the receptor peaks that were tractable were chosen to develop a binding model to find the binding affinity of the anion binding, as a global fit would improve the quality of the model. The binding model was determined using the Bindfit program, an online binding fit calculator that uses non-linear regression analysis via a python program to develop a fit for classical supramolecular titration data.<sup>2</sup> After looking at all the different possible binding model, A 1:1 binding model fit the best for our data.

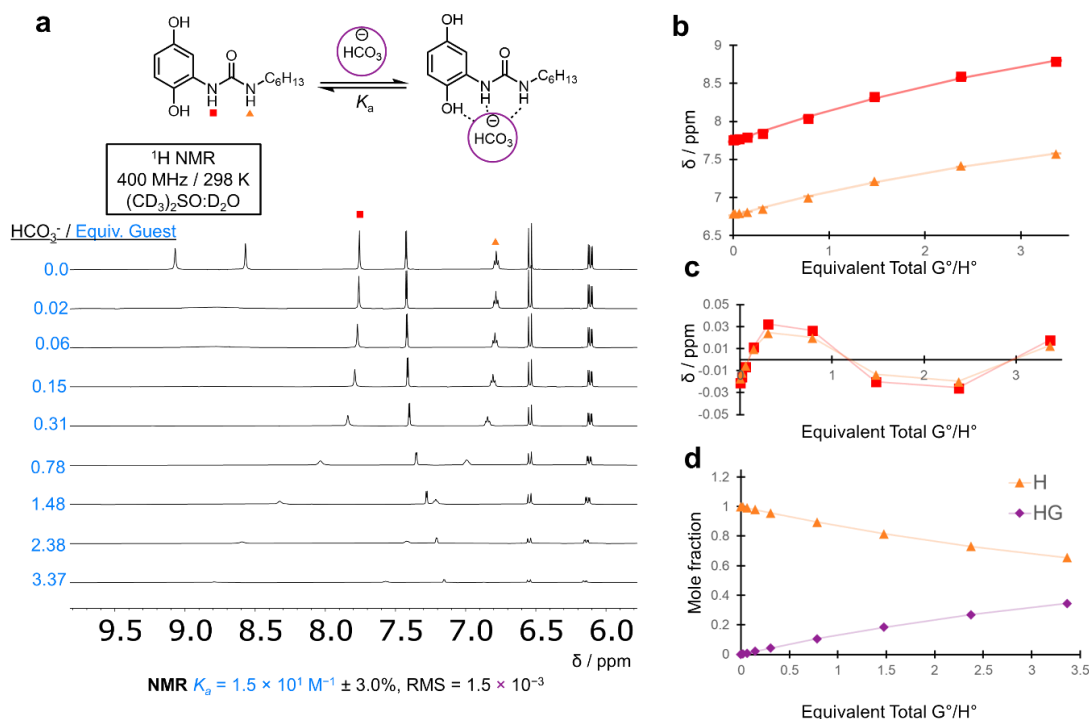


**Figure 2.4.**  $^1\text{H}$  NMR spectroscopic titrations of **UHQ<sub>6</sub>** using  $\text{Et}_4\text{N}^+\cdot\text{HCO}_3^-$  as a  $\text{HCO}_3^-$  sources. NMR quantification of its noncovalent interaction with  $\text{Et}_4\text{N}^+\cdot\text{HCO}_3^-$  is also shown with binding fit to elucidate  $K_a$ . a) Partial  $^1\text{H}$  NMR spectra of **UHQ<sub>6</sub>** (12.1 mM) in  $(\text{CD}_3)_2\text{SO}:\text{D}_2\text{O}$  95:5 solutions containing different concentrations of  $\text{Et}_4\text{N}^+\cdot\text{HCO}_3^-$ . b) Plot of the change of proton signals,  $\Delta\delta$ , of the H donors against the ratio guest ( $\text{HCO}_3^-$ )/host (**UHQ<sub>6</sub>**), the fit line was generated by Bindfit nonlinear regression analysis for 1:1 binding using L-BFGS-B method. c) Plot of residuals from line fit present in plot B showing the quality of fit. d) Plot of mole fractions of the host **UHQ<sub>6</sub>** and the 1:1 HG complex between **UHQ<sub>6</sub>** and  $\text{HCO}_3^-$  against the ratio of guest ( $\text{HCO}_3^-$ )/host (**UHQ<sub>6</sub>**).

For  $\text{HCO}_3^-$  binding, **UHQ<sub>6</sub>** has a  $K_a = 15.0 \text{ M}^{-1} \pm 3.0\%$  for  $\text{HCO}_3^-$  (Figure 2.4) which is relatively weak binding, however this may be sufficient for transport based on literature precedent.<sup>3</sup> Binding occurs at the urea moiety from the N-H donors. Conversely, binding of **UQ<sub>6</sub>** to  $\text{HCO}_3^-$  could not be observed (Figure 2.5) as it is reduced back into the hydroquinone **UHQ<sub>6</sub>** under these conditions. This could be due to the presence of  $\text{OH}^-$  which can attack the electrophilic ring of the quinone which is leading to hydroquinone like peaks. No reliable anion binding data could be seen in this experiment with  $\text{HCO}_3^-$ . This observation meant that using **UHQ<sub>6</sub>** and **UQ<sub>6</sub>** for bicarbonate transport in liposomal assay is most likely not possible as those conditions would mean that reliable oxidation of the hydroquinone **UHQ<sub>6</sub>** & **UHQ<sub>12</sub>** in active transport experiment could not be obtained; however, active transport with other anion such  $\text{Cl}^-$  is still a possibility for these compounds. Active transport of anion in liposomal

assay has still not been achieved using an ion carrier so we continued with the anion NMR studies to determine an anion candidate for this purpose.

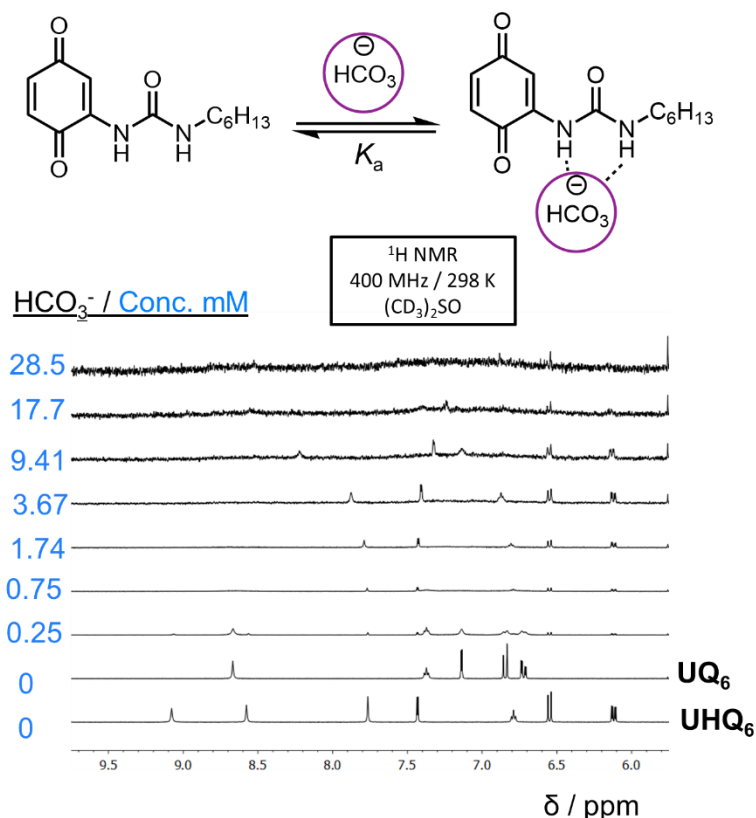


**Figure 2.5.**  $^1\text{H}$  NMR spectroscopic titrations of  $\text{UQ}_6$  using  $\text{Et}_4\text{N}\cdot\text{HCO}_3$  as a  $\text{HCO}_3^-$  sources. No binding occurs and the quinone is slightly reduced to  $\text{UHQ}_6$  in the presence of  $\text{HCO}_3^-$  in ( $\text{CD}_3$ ) $_2\text{SO}$ .

For  $\text{Cl}^-$  binding using  $\text{Et}_4\text{N}\cdot\text{Cl}$  in ( $\text{CD}_3$ ) $_2\text{SO}$ ,  $\text{UHQ}_6$  has a  $K_a = 1.2 \times 10^1 \text{ M}^{-1} \pm 1.3\%$  (Figure 2.6) and  $\text{UQ}_6$  has a  $K_a = 9.7 \text{ M}^{-1} \pm 1.2\%$  for  $\text{Cl}^-$  (Figure 2.7). Binding occurs at the urea moiety from the N-H donors, however, for  $\text{UHQ}_6$ , the OH group at the binding site also participated. The desired difference in binding affinities is promising for active transport. For active transport to occur using our system, there must be a binding affinity difference between both form of the RAMCs (hydroquinone vs quinone).

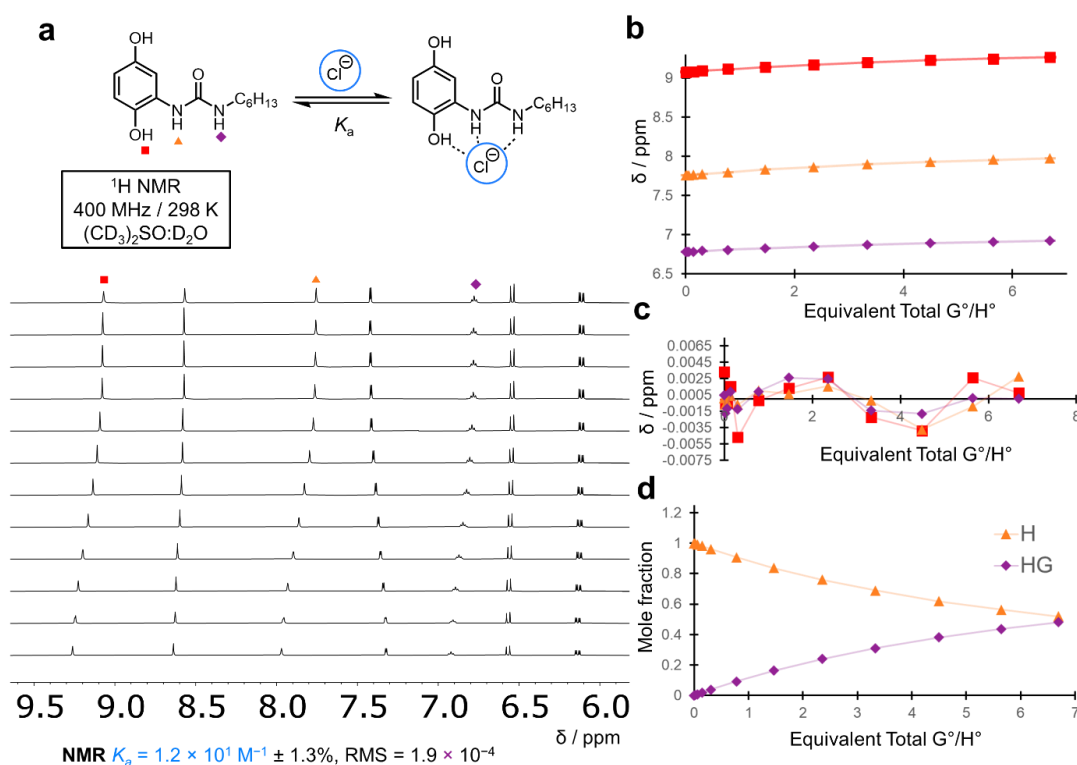


**Figure 2.6.**  $^1\text{H}$  NMR spectroscopic titrations of **UHQ<sub>6</sub>** using  $\text{Et}_4\text{N}\cdot\text{Cl}$  as a  $\text{Cl}^-$  sources. NMR quantification of its noncovalent interaction with  $\text{Et}_4\text{N}\cdot\text{Cl}$  is also shown with binding fit to elucidate  $K_a$ . a) Partial  $^1\text{H}$  NMR spectra of **UHQ<sub>6</sub>** (12.1 mM) in ( $\text{CD}_3$ )<sub>2</sub>SO: $\text{D}_2\text{O}$  95:5 solutions containing different concentrations of  $\text{Et}_4\text{N}\cdot\text{Cl}$ . b) Plot of the change of proton signals,  $\Delta\delta$ , of the H donors against the ratio guest ( $\text{Cl}^-$ )/host (**UHQ<sub>6</sub>**), the fit line was generated by Bindfit nonlinear regression analysis for 1:1 binding using L-BFGS-B method. c) Plot of residuals from line fit present in plot B showing the quality of fit. d) Plot of mole fractions of the host **UHQ<sub>6</sub>** and the 1:1 HG complex between **UHQ<sub>6</sub>** and  $\text{Cl}^-$  against the ratio of guest ( $\text{Cl}^-$ )/host (**UHQ<sub>6</sub>**).

We hypothesize that hydroquinone form should have larger binding affinity,  $K_a$ , than the quinone form of the ion carrier as there is an additional OH bond donor. As shown in Figure 2.2, for example, if a lipid membrane of vesicle with pre-incorporated hydroquinone ion carriers were exposed to external solution with an oxidant, then the hydroquinone ion carriers on the outer leaf of the membrane will start to be oxidized to the quinone form. For a certain period, due to the difference in binding affinity,  $K_a$ , the rate of anion flowing out of the cell will be favoured over anion influx as the inner leaf will still only have hydroquinone form ion carriers. Overtime, the ion carriers will percolate through the membrane where the distribution of oxidized ion carrier will be even across both faces of the membrane meaning the system will reach equilibrium in terms of anion transport ion carrier will be even across both faces of the membrane meaning the system will reach equilibrium in terms of anion transport. This action

would be active transport of ions across lipid membranes as the system is briefly biased out of equilibrium with chemical fuel (oxidant).

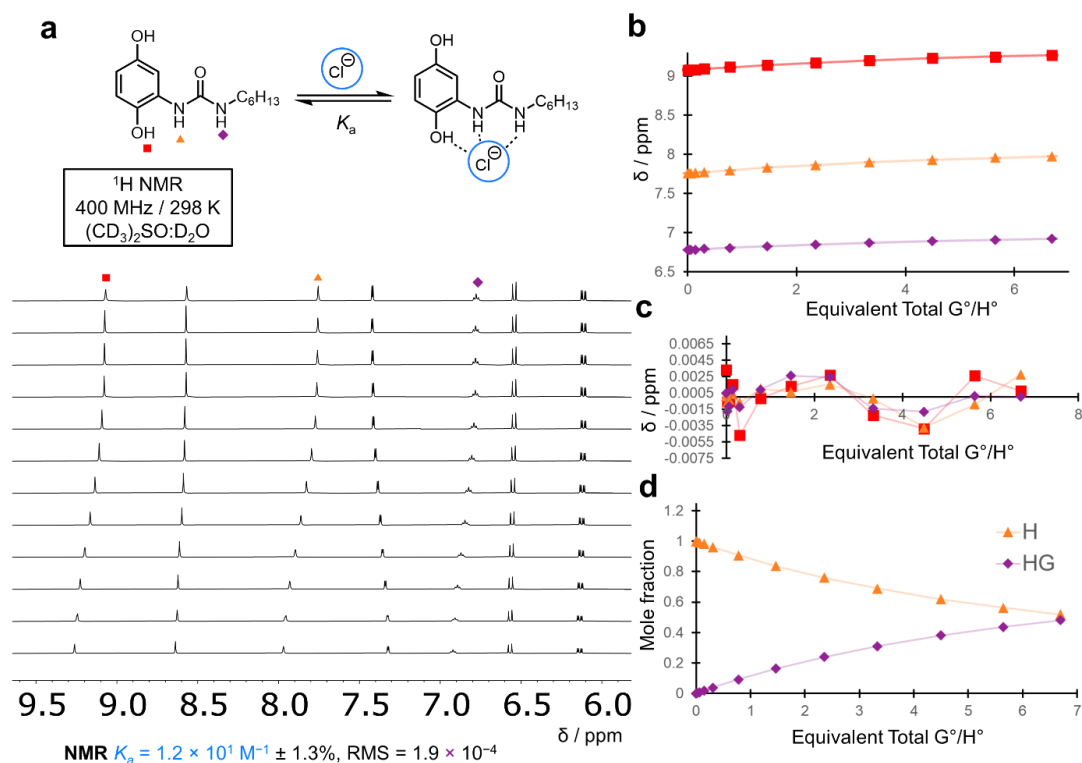


**Figure 2.6.**  $^1\text{H}$  NMR spectroscopic titrations of **UHQ<sub>6</sub>** using  $\text{Et}_4\text{N}^+\text{Cl}^-$  as a  $\text{Cl}^-$  sources. NMR quantification of its noncovalent interaction with  $\text{Et}_4\text{N}^+\text{Cl}^-$  is also shown with binding fit to elucidate  $K_a$ . a) Partial  $^1\text{H}$  NMR spectra of **UHQ<sub>6</sub>** (12.1 mM) in  $(\text{CD}_3)_2\text{SO}:\text{D}_2\text{O}$  95:5 solutions containing different concentrations of  $\text{Et}_4\text{N}^+\text{Cl}^-$ . b) Plot of the change of proton signals,  $\Delta\delta$ , of the H donors against the ratio guest ( $\text{Cl}^-$ )/host (**UHQ<sub>6</sub>**), the fit line was generated by Bindfit nonlinear regression analysis for 1:1 binding using L-BFGS-B method. c) Plot of residuals from line fit present in plot B showing the quality of fit. d) Plot of mole fractions of the host **UHQ<sub>6</sub>** and the 1:1 HG complex between **UHQ<sub>6</sub>** and  $\text{Cl}^-$  against the ratio of guest ( $\text{Cl}^-$ )/host (**UHQ<sub>6</sub>**).

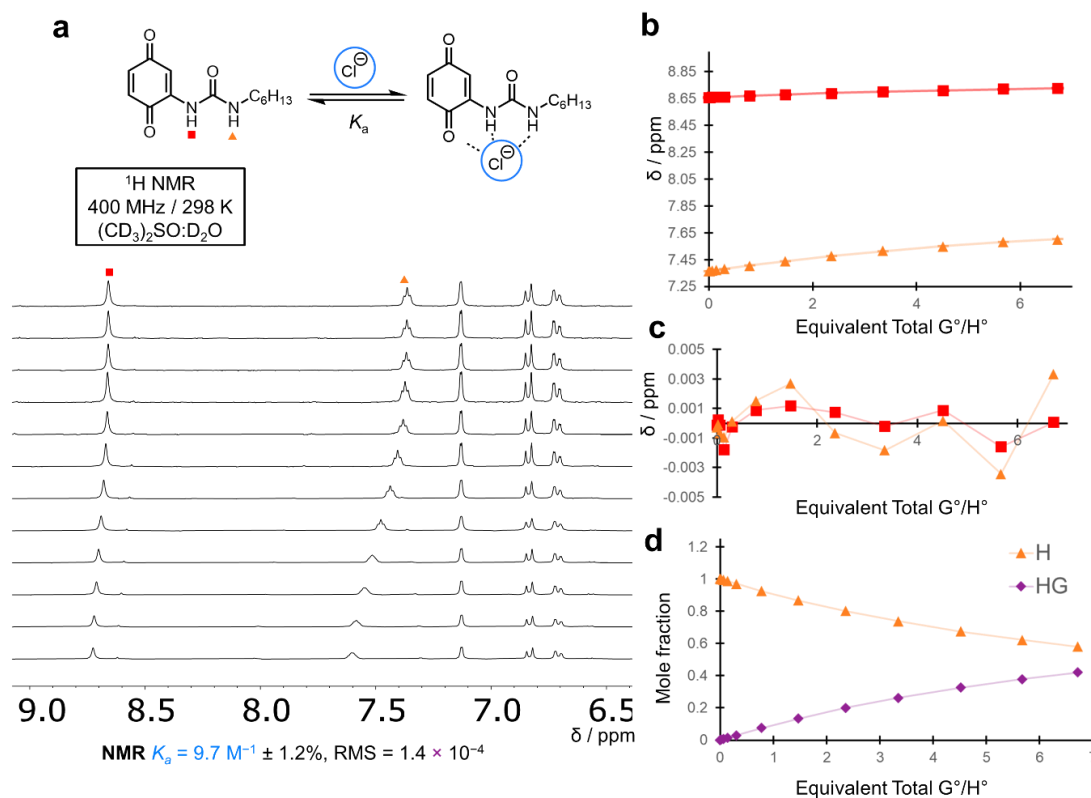


**Figure 2.7.**  $^1\text{H}$  NMR spectroscopic titrations of  $\text{UQ}_6$  using  $\text{Et}_4\text{N}^+\text{Cl}^-$  as a  $\text{Cl}^-$  source. NMR quantification of its noncovalent interaction with  $\text{Et}_4\text{N}^+\text{Cl}^-$  is also shown with binding fit to elucidate  $K_a$ . a) Partial  $^1\text{H}$  NMR spectra of  $\text{UQ}_6$  (12.1 mM) in  $(\text{CD}_3)_2\text{SO}:\text{D}_2\text{O}$  95:5 solutions containing different concentrations of  $\text{Et}_4\text{N}^+\text{Cl}^-$ . b) Plot of the change of proton signals,  $\Delta\delta$ , of the H donors against the ratio guest ( $\text{Cl}^-$ )/host ( $\text{UQ}_6$ ), the fit line was generated by Bindfit nonlinear regression analysis for 1:1 binding using L-BFGS-B method. c) Plot of residuals from line fit present in plot B showing the quality of fit. d) Plot of mole fractions of the host  $\text{UQ}_6$  and the 1:1 HG complex between  $\text{UQ}_6$  and  $\text{Cl}^-$  against the ratio of guest ( $\text{Cl}^-$ )/host ( $\text{UQ}_6$ ).

This system can work with a reductant using the quinone form and the direction of ions transport is dependent on the presence of the redox fuel in the external or internal solutions of the lipid vesicles. The NMR titrations in the membrane mimic solution ( $(\text{CD}_3)_2\text{SO}/\text{D}_2\text{O}$  95.5:0.5) revealed a small difference in  $K_a$  between  $\text{UHQ}_6$  and  $\text{UQ}_6$  which is encouraging for have the right molecular design to test our approach to active transport. As for  $\text{UHQ}_{12}$  and  $\text{UQ}_{12}$ , compared to the hexylurea receptors, the two sets of receptors only vary by the length of the alkyl chain used rather than the binding site itself. Therefore, we can assume the binding constants for the hexylurea receptors should be good approximation to the dodecylurea analogues. Compared to most mobile ion carriers reported in literature, the urea RAMCs have low binding constants for  $\text{Cl}^-$  transport.<sup>1</sup> However, transport across lipid membranes are still achievable with these binding constants and can be observed using lucigenin probe as mentioned in Chapter

1. To determine if lucigenin probe can be used for liposomal assay, Binding studies carried out using  $\text{Et}_4\text{N}\cdot\text{NO}_3$  as a source of  $\text{NO}_3^-$  ions (Figure 2.8) using **UHQ<sub>6</sub>**. The NMR titration were revealed that **UHQ<sub>6</sub>** have no measurable binding affinities towards nitrate ions when using the Bindfit software to generate binding fit model. This observation led us to use  $\text{NO}_3$  salts as passive ions in the vesicle experiments.

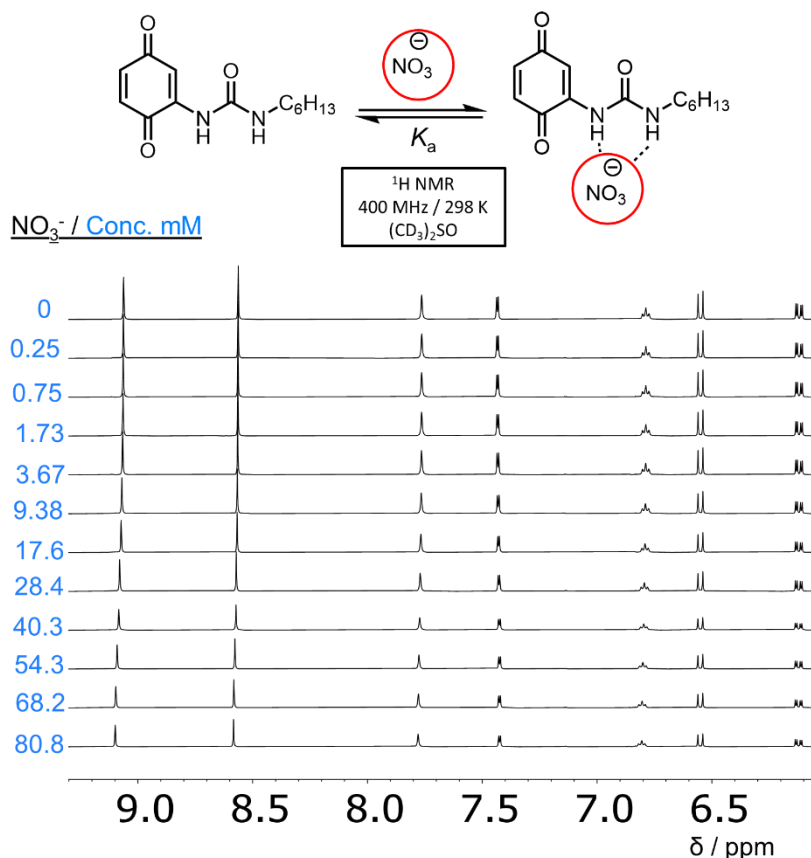


**Figure 2.8.**  $^1\text{H}$  NMR spectroscopic titrations of **UHQ<sub>6</sub>** using  $\text{Et}_4\text{N}\cdot\text{NO}_3$  as a  $\text{NO}_3$  sources. NMR quantification of its noncovalent interaction with  $\text{Et}_4\text{N}\cdot\text{NO}_3$  is also shown with binding fit to elucidate  $K_a$ . Partial  $^1\text{H}$  NMR spectra of **UHQ<sub>6</sub>** (12.1 mM) in  $(\text{CD}_3)_2\text{SO}:\text{D}_2\text{O}$  95:5 solutions containing different concentrations of  $\text{Et}_4\text{N}\cdot\text{NO}_3$

## 2.4. X-Ray Crystal Structure of **UHQ<sub>6</sub>**

A single crystal of **UHQ<sub>6</sub>** was obtained by slow evaporation of a saturated acetone solution. Analysis of a single crystal of **UHQ<sub>6</sub>** gave insights into its hydrogen bonding properties. The solid-state structure reveals (Figure 2.9a) hydrogen bonding interactions between the neighboring urea and hydroquinone units. The OH and NH groups of the hydroquinone and urea, respectively, are aligned with one another to create a series of three contiguous hydrogen bond donors oriented in the same direction, which form the basis of the interaction with anions such as bicarbonate or chloride in

our proposed mode of action. Observation of this hydrogen bonding motif in the solid state supports our hypothesis. Moreover, the extended superstructure of **UHQ<sub>6</sub>** shows (Figure 2.9b) segregation of the lipophilic hexamethylene chains and hydrophilic head groups, which supports that the RAMCs can operate at the interface of the cell membrane. This proposition is further supported by literature.<sup>3</sup>

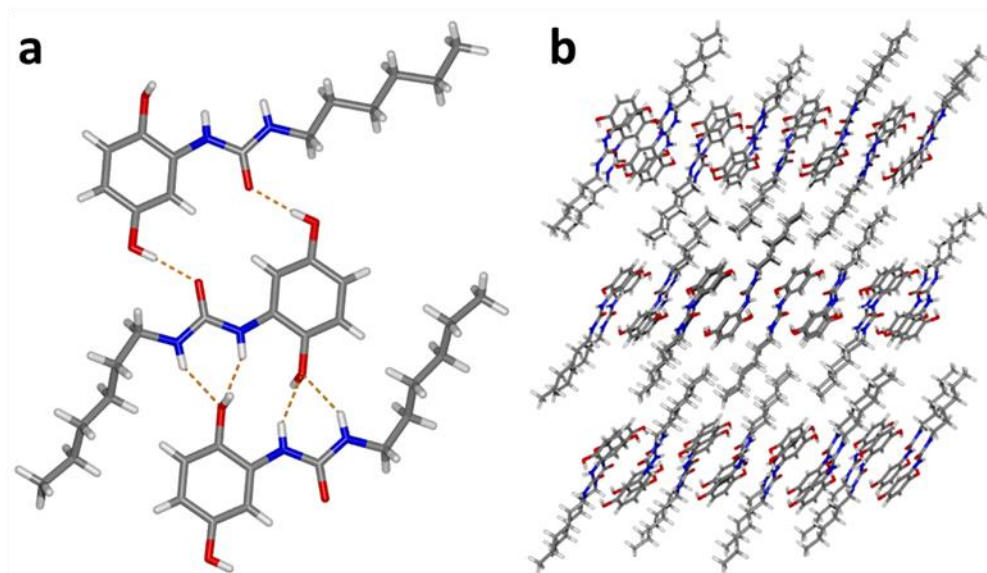


**Figure 2.9.** Solid-state superstructure of the hydroquinone transporter **UHQ<sub>6</sub>**

## 2.5 Electrochemical Analysis of RAMCs

To understand the redox potential of our urea based RAMCs, a series of electrochemical analysis was conducted using cyclic voltammetry and a screening of chemical oxidants and reductants.

### 2.5.1 Cyclovoltammetry of **UQ<sub>6</sub>**

To determine if our RAMCs are stable to oxidizing and reductive conditions which needed to use redox active fuel, we analyzed our system using cyclic voltammetry. We used **UQ<sub>6</sub>** as model compound as there was solubility issues for hydroquinones and the **UQ<sub>12</sub>** in acetonitrile. The cyclic voltagram shows that there is  $2e^-$  reversible reduction at  $E_{1/2} = -1.71 \times 10^{-1}$  V in acetonitrile compared to ferrocene internal standard. The reversible reduction behaviour of **UQ<sub>6</sub>** is good indication that our compounds will be stable in the membrane to oxidizing/reduction conditions.

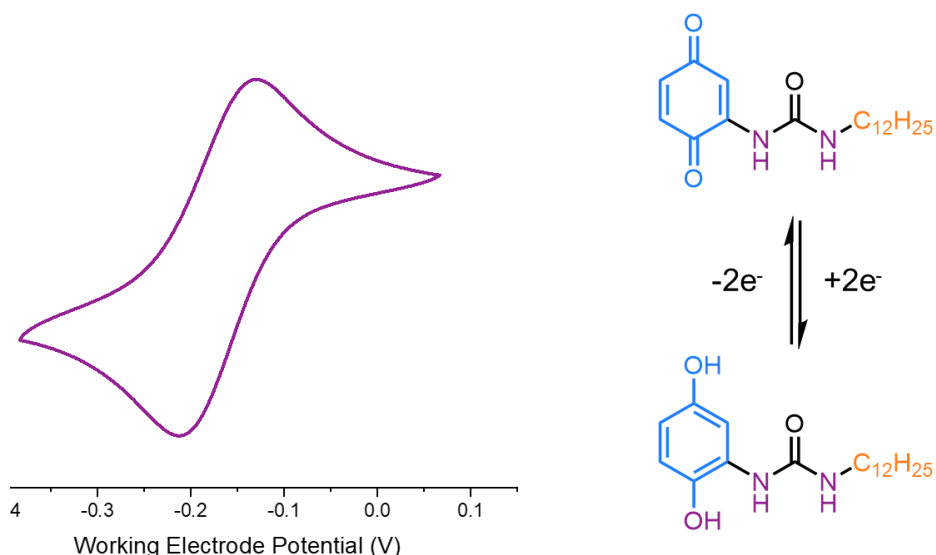


**Figure 2.10.** For electrochemical properties, using 0.1M  $\text{NBu}_4\text{PF}_6$  in MeCN at 100  $\text{mVs}^{-1}$   $\text{UQ}_{12}$  has  $E_{1/2} = -1.71 \times 10^{-1}$  V, ref. Ferrocene.

### 2.5.2 Chemical Oxidation and Reduction of RAMCs

A previous member of McGonigal group (Mary Gibbins) conducted a screening of different oxidants and reductants to react with the desired RAMCs are highlighted in Table 2.1 & Table 2.2. The best choice for liposomal assays in terms of conversion and isolated yield for an oxidant is ceric ammonium nitrate if the hydroquinone form of the RAMCs ( $\text{UHQ}_6$ ). For a reductant,  $\text{Na}_2\text{S}_2\text{O}_4$  performed the best for reduction of the quinone form of the RAMCs ( $\text{UQ}_6$ ) allow for  $\text{Na}_2\text{S}_2\text{O}_4$  to be used as chemical fuel for our active ion transport system.

**Table 2.1.** Oxidation screening for the hydroquinone molecular anion carrier ( $\text{UHQ}_6$ )

Oxidant	Conversion / %	Isolated Yield / %
$\text{FeCl}_3 / \text{HCl}$	>95	95
$\text{NaIO}_4$	>95	52
$\text{H}_2\text{O}_2 / \text{HCl}$	0	0
$(\text{NH}_4)_2\text{Ce}(\text{NO}_3)_6$	>95	85

**Table 2.2.** Reduction screening for the quinone molecular anion carrier (UQ<sub>6</sub>)

Reductant	Conversion / %	Isolated Yield / %
Na <sub>2</sub> S <sub>2</sub> O <sub>4</sub>	>99	36
NaN <sub>3</sub>	0	0
Activated zinc	45	34

## 2.6 Vesicle Transport Studies

The ion transport capabilities of the RAMCs were measured using the lucigenin Cl<sup>-</sup>/NO<sub>3</sub><sup>-</sup> assay. The large unilamellar vesicles (LUVs) used for this fluorescence assay have 7:3 1-palmitoyl-2-oleoyl-sn-glycero-3-phosphocholine (POPC)/cholesterol composition. These POPC/cholesterol vesicles were prepared by the standard procedure described in literature by Davis et al. which is used to as simple mimic for biological cell membrane. The formulation of these vesicles are illustrated in Figure 2.11.<sup>4</sup> Vesicles were prepared in a medium of lucigenin and NaNO<sub>3</sub> (aq) (0.8 mM and 225 mM, respectively) and extruded through a 200 nm polycarbonate filter to produce unilamellar vesicles. The external lucigenin (not entrapped inside vesicles) was removed using a desalting column to get the desired vesicle suspension for the ion transport experiments.

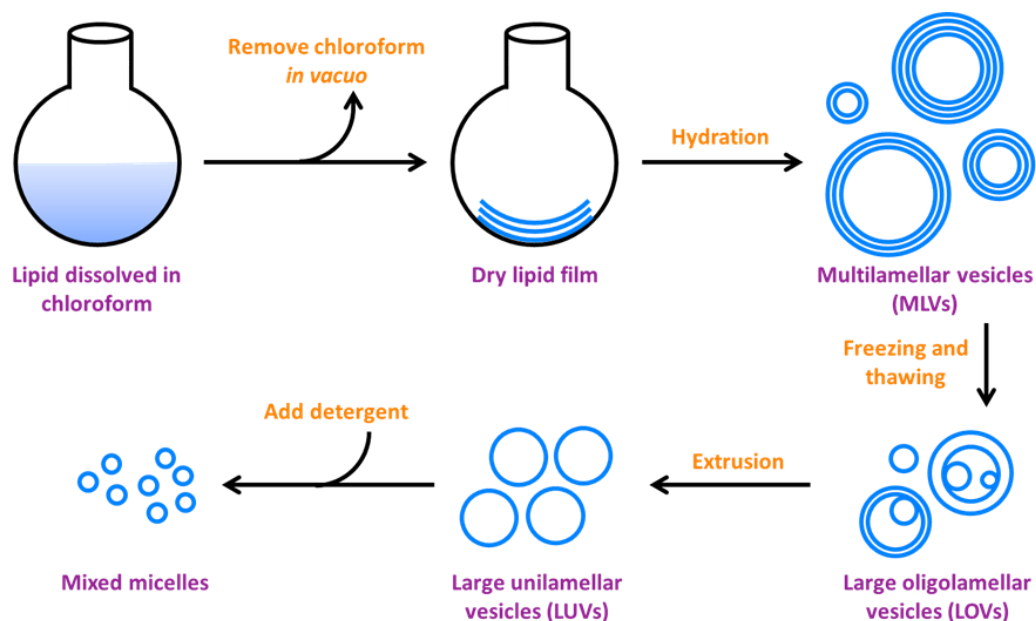


**Figure 2.11.** Formulation of 200 nm POPC/Cholesterol LUVs for anion transport experiments. Lipids and RAMCs are dissolved in chloroform and evaporated leaving a dry lipid film. The film hydrated with interior solution and quickly sonicated. This sonication makes multilamellar vesicles which undergo 10 freeze thaw cycles to obtain large oligolamellar vesicles (LOVs). Extrusion using a 200 nm polycarbonate filter leads to the desired LUVs for transport studies which are lysed at the end of the experiment using a detergent.

### 2.6.1 Dynamic Light Scattering of LUVs

To determine if the LUVs were the right size and were unilamellar, dynamic light scattering (DLS) experiments were conducted to get the size distribution of the LUVs. Figure 2.12 shows the control experiments with the POPC/cholesterol LUVs containing internal  $\text{NaNO}_3$  solution exclusively or an internal  $\text{NaNO}_3$  solution containing lucigenin. The DLS plots reveal that the vesicles produced have a uniform size distribution and the size average is within the desired size range.

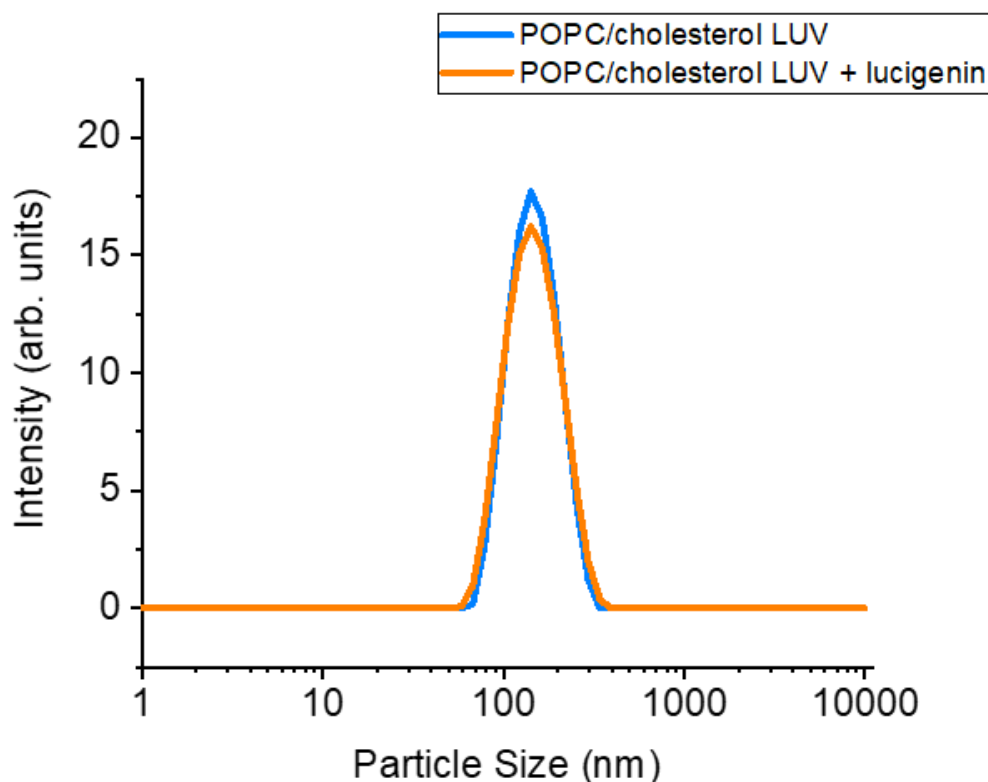


**Figure 2.12.** Plot of DLS measurements of POPC/Cholesterol LUVs. The control vesicles were loaded with  $\text{NaNO}_3$  (225 mM) or  $\text{NaNO}_3$  (225 mM) and lucigenin (0.8 M). These vesicles were suspended in an external solution of  $\text{NaNO}_3$  (225 mM).

### 2.6.2 Passive Ion Transport Liposomal Assay

Figure 2.13 illustrates the control experiment for passive ion transport studies. The  $\text{Cl}^-/\text{NO}_3^-$  exchange assay was chosen for initial investigations, as the carriers exhibit negligible  $K_a$  for nitrate, allowing us to monitor the desired species (chloride) as it is carried into the vesicles. For the passive transport study, 1 M NaCl and 225 mM  $\text{NaNO}_3$  solution was injected to the vesicle suspension, and the fluorescence decay of lucigenin was monitored over time. The vesicles were then lysed by addition of a surfactant (Triton X-100), causing the leaching of the internal lucigenin, and quenching by extravesicular chloride. In the lucigenin assay, nitrate behaves purely as a spectator ion; its transport does not produce any variation in lucigenin's fluorescence. Initially, the RAMCs were pre-incorporated into vesicles at a high concentration (5 mol% w.r.t. lipid concentration), to achieve the largest observable response.

For the kinetic emission spectrum presented in Figure 2.13, the y-axis is the  $F/F_0$  which is its fluorescence count over initial fluorescence at  $t = 0$  s. Over time, an initial sharp

decay in  $F/F_0$  is visible at  $t = 60$  s upon the addition of 1 M NaCl(aq), followed by a gradual decay. This significant decay is attributed to the presence of residual extravesicular (or “free”) lucigenin in the vesicle suspension not removed by the desalting column. The subsequent decay is caused by  $\text{Cl}^-$  transport until 900s, at which time the experiment is paused for the loading of the detergent. The second (and larger) decay at  $t = 960$  s is caused by the addition of the detergent, which lyses the vesicles, causing the extracellular  $\text{Cl}^-$  to quench the freed lucigenin’s fluorescence. This lysing process allows the system eventually reaches equilibrium. For analysis, the data is normalised so fluorescence of the suspension prior/at the addition of 1 M NaCl ( $t = 0$  or 60 s) corresponds to  $F/F_0 = 1$ , while its fluorescence after the addition of surfactant ( $t = 960 - 1200$  s) corresponds to  $F/F_0 = 0$ .

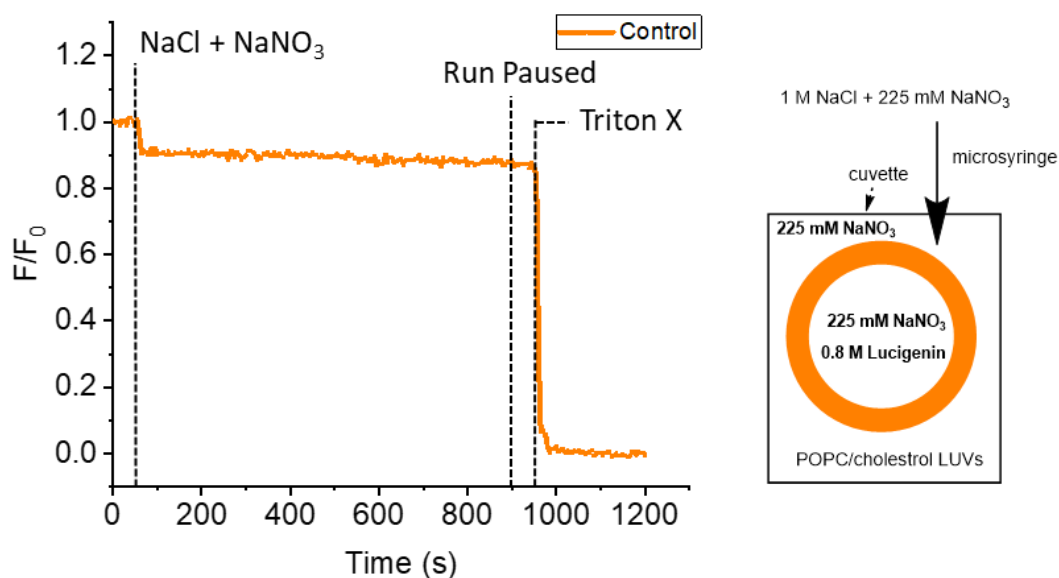


**Figure 2.13.** Control experiment for  $\text{Cl}^-$  influx without redox active transporters for vesicles transport studies. containing 225 mM  $\text{NaNO}_3$  and 0.8 mM lucigenin. The vesicles were loaded with  $\text{NaNO}_3$  (225 mM) and lucigenin (0.8 mM) and suspended in an external solution of  $\text{NaNO}_3$  (225 mM). NaCl (1 M) was added at 60 s, and detergent (Triton X) was added at 960 s.

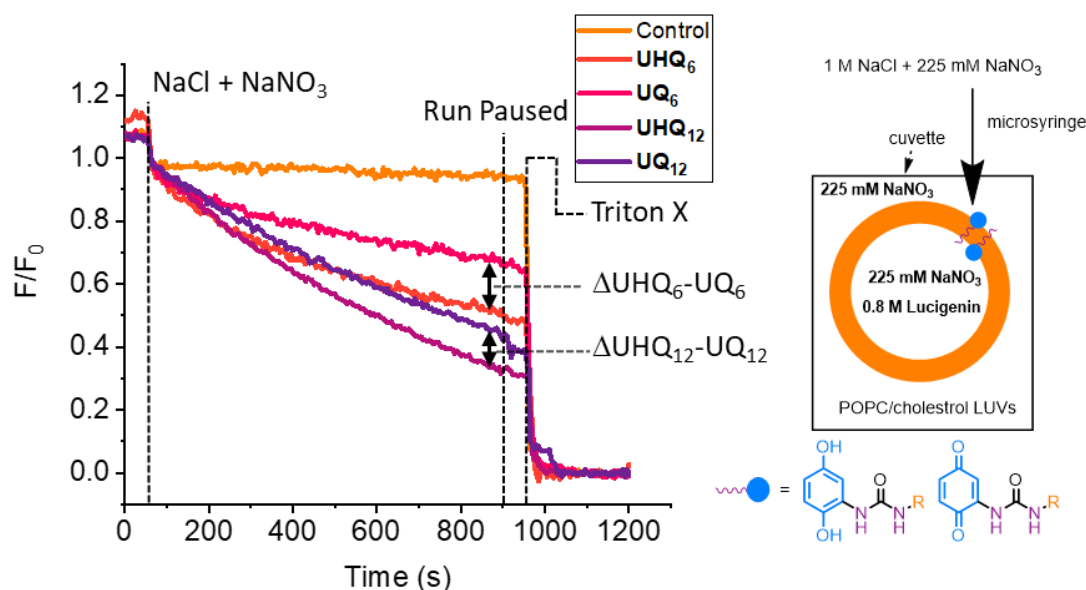


**Figure 2.14.** Fluorescence decay of lucigenin caused by the influx of  $\text{Cl}^-$  into 200 nm LUVs consisting of 7:3 POPC:cholesterol (0.4 mM lipid concentration in 225 mM  $\text{NaNO}_3$ ), with preincorporated hydroquinones RAMCs (**UHQ<sub>6</sub>** & **UHQ<sub>12</sub>**) and quinones RAMCs (**UQ<sub>6</sub>** & **UQ<sub>12</sub>**) at 2 mol% loading w.r.t. lipid concentration. These runs compared to the control (no carrier – blue), averaged over four runs. At  $t = 60$  s, a solution of 1 M NaCl + 225 mM  $\text{NaNO}_3$  (aq) (50  $\mu\text{L}$ , final  $\text{Cl}^-$  concentration 17 mM) and at  $t = 960$  s, a 5% solution of Triton X-100 (50  $\mu\text{L}$ ) were added.

Figure 2.14 illustrates the  $\text{Cl}^-$  transport of the urea based RAMCs, **UHQ<sub>6</sub>**, **UHQ<sub>12</sub>**, **UQ<sub>6</sub>** and **UQ<sub>12</sub>**. Comparing the hydroquinone form (**UHQ<sub>6</sub>** & **UHQ<sub>12</sub>**) of the RAMCs to their quinone forms (**UQ<sub>6</sub>** & **UQ<sub>12</sub>**), there is gap in the magnitude of  $\text{Cl}^-$  efflux where the hydroquinone forms (**UHQ<sub>6</sub>** & **UHQ<sub>12</sub>**) had faster  $\text{Cl}^-$  efflux compared to the oxidized form. This faster efflux observation revealed that the hydroquinone RAMCs (**UHQ<sub>6</sub>** & **UHQ<sub>12</sub>**) are better  $\text{Cl}^-$  carriers than the quinone RAMCs (**UQ<sub>6</sub>** & **UQ<sub>12</sub>**) agreeing with our hypothesis. For hexylurea RAMCs, there is a larger gap between  $\text{Cl}^-$  carrier capability between the two forms compared to the dodecylurea compounds. However, the hexylurea RAMCs are less effective  $\text{Cl}^-$  carriers than their dodecylurea counterpart as  $\text{Cl}^-$  efflux was lower compared to the longer alkyl chain anion transporter. This difference in transport rates between the hexyl and dodecylurea compounds are due to the higher lipophilicity present in the dodecylurea compounds. This increase in lipophilicity unfortunately reduces the gap in transport rate between the two forms for **UHQ<sub>12</sub>** and **UQ<sub>12</sub>**. Meaning, for active transport, **UHQ<sub>6</sub>** and **UHQ<sub>12</sub>** would be ideal candidates for the design a system capable of active transport. To determine if the LUVs with pre-incorporated RAMCs were the right size and was

unilamellar, DLS experiments were conducted to get the size distribution of the LUVs. Figure 2.15 shows the vesicle transport experiment with the POPC/cholesterol LUVs with pre-incorporated **UHQ<sub>6</sub>** containing internal solution of NaNO<sub>3</sub> and lucigenin suspended in aqueous NaNO<sub>3</sub> solution. The vesicle Cl<sup>-</sup> transport experiment was conducted using 1 M NaCl while doing DLS and size distribution was collected over time. The DLS plots show that the LUVs have a uniform size distribution within the desired size average through the transportation of Cl<sup>-</sup> and after lysing the vesicles. In addition, DLS plots shows a slight swelling of the vesicles because of Cl<sup>-</sup> influx, this observation is supported in literature.<sup>6</sup>

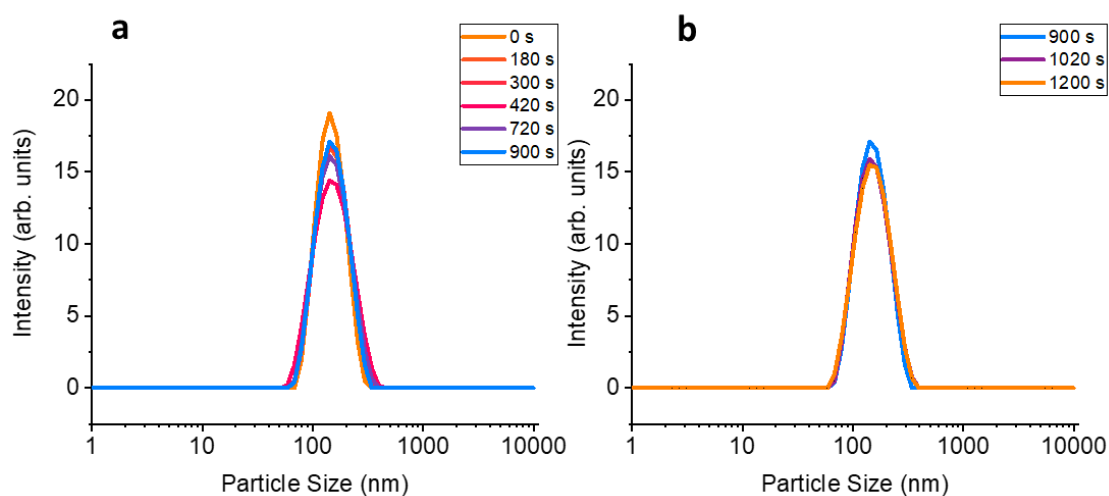


**Figure 2.15.** Plot of DLS measurements of Cl<sup>-</sup>/NO<sub>3</sub><sup>-</sup> symport facilitated by compound **UQ<sub>12</sub>** in POPC/Cholesterol LUVs with preincorporated **UQ<sub>6</sub>** (2 mol % compound: lipid ratio). The vesicles were loaded with NaNO<sub>3</sub> (225 mM) and lucigenin (0.8 mM) and suspended in an external solution of NaNO<sub>3</sub> (225 mM). NaCl (1 M) was added at 60 s, and detergent (Triton X) was added at 960 s. a) DLS plots for vesicle transport of Cl<sup>-</sup> between 0 – 960 s before lysing vesicles. b) DLS plots for vesicle transport of Cl<sup>-</sup> after lysing vesicles.

### 2.6.3 Hill Plot Analysis

To understand the binding cooperativity of RAMCs with Cl<sup>-</sup> species in the lipid membranes, Hill plot analysis was conducted. The Hill plot analysis involves plotting the Cl<sup>-</sup> influx promoted by the RAMCs after a certain period of time as a function of the transporter concentration used. Typically, a concentration range of 0.1 – 2 mol % w.r.t. lipid concentration is used, while the time period is restricted to 270 – 300 s to obtain 0 – 100% Cl<sup>-</sup> influx range.<sup>6,7,8,9,10</sup> However, due to our carriers' relatively low binding affinities for Cl<sup>-</sup>, the time period was extended to 900 s to allow for more accurate analysis. An alternate approach would involve using higher carrier

concentrations, to obtain 100 %  $\text{Cl}^-$  influx within the required time. However, loading concentrations higher than  $\sim 5$  mol % w.r.t. lipid concentration, the carrier precipitated out of solution instead of being incorporated into the lipid bilayer. Studies were performed using the dodecylurea compounds (**UHQ<sub>12</sub>** & **UQ<sub>12</sub>**) as higher concentration of hexylurea compounds ( $>2.0$  w.r.t lipid concentration) lead to the RAMCs to precipitate out of the lipid film during formulation of the vesicles. Hill coefficients ( $n$ ) and  $\text{EC}_{50}$  at 900 s values were calculated by fitting the curves to the following equation:

$$y = y_0 + (y_{\max} - y_0) \frac{x^n}{K + x^n}$$

Where  $y$  is  $F/F_0$  at 900 s value with the compound loaded at concentration  $x$ ,  $y_0$  is the  $F/F_0$  at 900s value obtained without the compound,  $y_{\max}$  is the maximum  $F/F_0$  value obtained,  $n$  is the Hill coefficient, and  $K$  is the  $\text{EC}_{50}$  at 900 s. The compound concentration is expressed as compound to lipid molar ratio. A Hill coefficient of  $n = 1$  indicates movement of anions through the membrane occurs by one molecular carrier binds to one anion (unimolecular binding) tumbling through lipid membrane. In this system, unimolecular transport would be between one redox-active molecular carrier and one chloride ion. Higher Hill coefficients ( $n > 1$ ) would indicate positive cooperativity, where multiple receptors are binding to a single  $\text{Cl}^-$  ion indicating possible channel formation in the membrane. Lower Hill coefficients ( $n < 1$ ), suggest negatively cooperative binding, where the binding of  $\text{Cl}^-$  to a carrier molecule reduces its affinity to bind to another carrier molecule indicating self-aggregation and inhibition of transport.

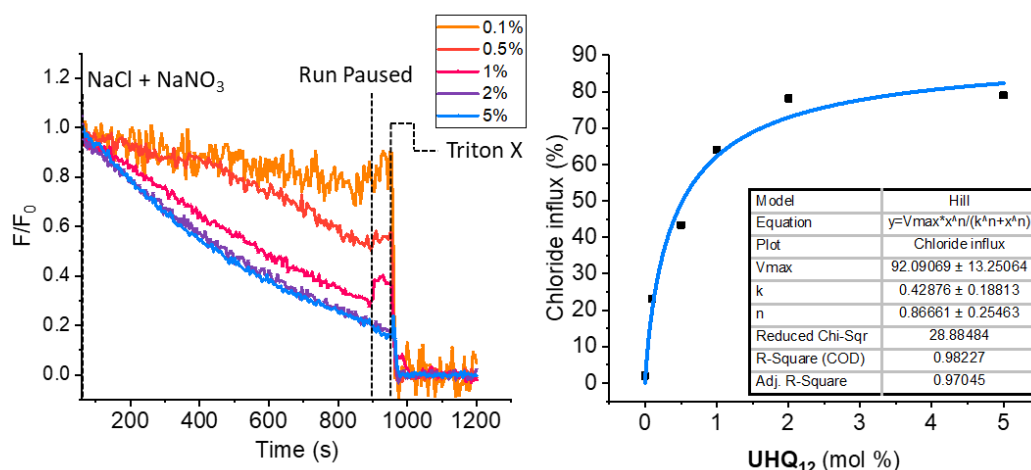


**Figure 2.16.** Hill plot analysis of  $\text{Cl}^-/\text{NO}_3^-$  antiport facilitated by compound **UHQ**<sub>12</sub>. The vesicles were loaded with  $\text{NaNO}_3$  (225 mM) and lucigenin (0.8 mM) and suspended in an external solution of  $\text{NaNO}_3$  (225 mM).  $\text{NaCl}$  (1 M) was added at 60 s, and detergent (Triton X) was added at 960 s. Compound concentrations are shown as compound to lipid molar ratios.

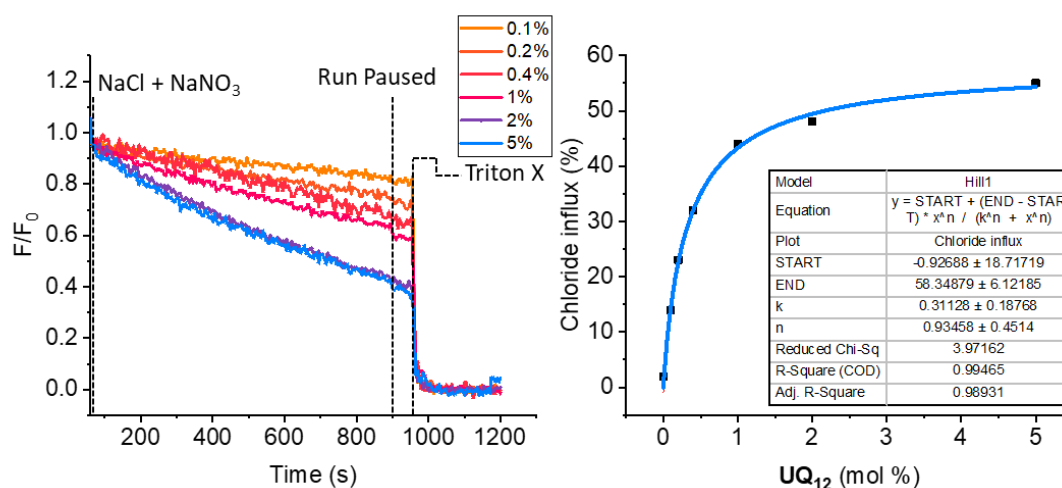


**Figure 2.17.** Hill plot analysis of  $\text{Cl}^-/\text{NO}_3^-$  symport facilitated by compound **UQ**<sub>12</sub>. The vesicles were loaded with  $\text{NaNO}_3$  (225 mM) and lucigenin (0.8 mM) and suspended in an external solution of  $\text{NaNO}_3$  (225 mM).  $\text{NaCl}$  (1 M) was added at 60 s, and detergent (Triton X) was added at 960 s. Compound concentrations are shown as compound to lipid molar ratios.

For **UHQ**<sub>12</sub> (Figure 2.16), the  $\text{EC}_{50}$  is  $0.42 \pm 0.18$  mol% w.r.t lipid concentration with a Hill coefficient  $n = 0.87 \pm 0.25$  according to the Hill plot fit. At the higher concentration, the  $\text{Cl}^-$  influx is approaching 100%, and according to the fit the  $y_{\text{max}}$  is  $92.3 \pm 13$  %, therefore a true  $\text{EC}_{50}$  value from the fit is obtained. The Hill coefficient is close to 1, meaning it is most like a unimolecular binding mode for  $\text{Cl}^-$  ion transport across a lipid membrane. For **UQ**<sub>12</sub> (Figure 2.17), according to the Hill plot fit, the  $y_{\text{max}}$  ( $\text{Cl}^-$  influx) is  $58.3 \pm 6.12$  %, which means we cannot get a true  $\text{EC}_{50}$ . However, we can get  $\text{EC}_{29} = 0.32 \pm 0.04$  mol % w.r.t lipid concentration (50% of  $y_{\text{max}}$ ). The Hill

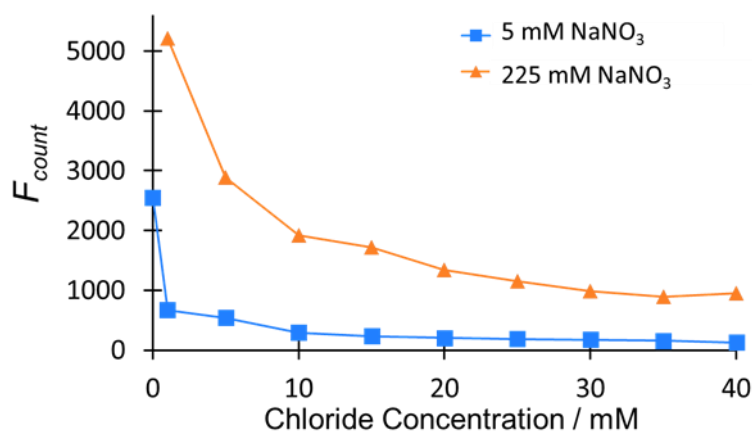
coefficient  $0.93 \pm 0.10$ , which is close to 1, meaning it is most like a unimolecular binding mode for  $\text{Cl}^-$  ion transport across a lipid membrane.

#### 2.6.4 Active Transport Liposomal Assays

The active transport properties of the redox-switchable quinone/hydroquinone carriers rely on the hydroquinone ion carrier (i.e. **UHQ<sub>6</sub>**) is a better  $\text{Cl}^-$  transporter than the oxidised quinone ion carrier (ie. **UQ<sub>6</sub>**). This desired property was demonstrated using a combination of NMR titration studies to determine binding affinities ( $K_a$ ) to chloride ions for both **UHQ<sub>6</sub>** & **UQ<sub>6</sub>** as well as liposomal assays for understanding passive ion transport capabilities of our RAMCs. For this system to undergo active ion transport across a lipid membrane, the redox potential of the carrier is our method of developing a chemical fuel to drive active transport. For example, if the quinone is pre-incorporated into the lipid bilayer, at any given time, as distribution of the molecules are expected to reside with the polar head in the extravesicular aqueous phase, while the other half have the polar head in the intravesicular phase. In the absence of a transmembrane  $\text{Cl}^-$  concentration gradient, the rates of  $\text{Cl}^-$  influx and efflux are equal (i.e.  $k_{\text{in}} = k_{\text{out}}$ ). The addition of a reducing agent converts the external quinones to hydroquinones, while the internal ones remain unreacted. As the hydroquinone is a faster  $\text{Cl}^-$  carrier,  $k_{\text{in}} > k_{\text{out}}$ , and there is overall  $\text{Cl}^-$  influx (active transport). Over time as the carriers diffuse across the bilayer, the internal quinone heads are also exposed to the reducing agent and are converted to hydroquinone, such that  $k_{\text{in}} = k_{\text{out}}$  once again. Previous work by the McGonigal group has identified sodium dithionite ( $\text{Na}_2\text{S}_2\text{O}_4$ ) as an effective reagent for this reduction as highlighted in Table 2.2.

The lucigenin assay has been a powerful tool to monitor passive transport was carried out in a medium of 225 mM  $\text{NaNO}_3$  and 1 M  $\text{NaCl(aq)}$  was added separately. However, the experimental design for active transport requires the preparation of a lucigenin solution containing  $\text{Cl}^-$ . It is commonly known that lucigenin's fluorescence is quenched by halides, such as  $\text{Cl}^-$ , so to understand the magnitude in change of fluorescence of lucigenin at different  $\text{Cl}^-$  ion concentrations, we conducted a concentration dependent ( $\text{Cl}^-$ ) fluorescence study of lucigenin. This study was done at two different concentrations of  $\text{NaNO}_3$  to understand the role of  $\text{NaNO}_3$  in fluorescence intensity of lucigenin. This fluorescence study is shown in Figure 2.18 revealing that at higher concentration of  $\text{NaNO}_3$ , the fluorophore's emission is higher (225 mM vs. 5

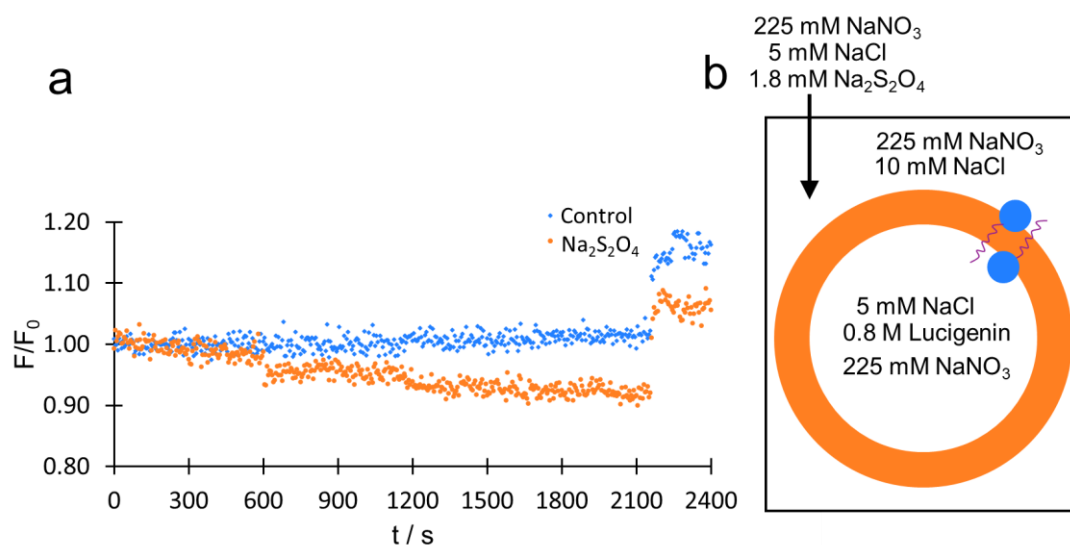
mM). When considering the fluorescence study at 225 mM  $\text{NaNO}_3$ , the fluorophore's emission drops significantly as the chloride concentration is increased; at 30 mM, lucigenin's fluorescence is only ~18% of its fluorescence at 1 mM. It is also noteworthy that at higher concentrations, lucigenin's fluorescence is less susceptible to concentration changes, elucidating that in this domain, the lucigenin method is more insensitive. While low concentrations offer more sensitivity, the relatively lower amount of  $\text{Cl}^-$  would allow for less  $\text{Cl}^-$  influx and hence would produce a smaller fluorescence drop. Overall, active transport was monitored at 5 mM and 10 mM chloride concentration.



**Figure 2.18.** The lucigenin calibration curve, following the fluorescence of 0.8 mM lucigenin ( $F$  / counts) in 5mM  $\text{NaNO}_3$  (aq) (blue) and 225 mM  $\text{NaNO}_3$  (aq) (orange) over a range of chloride concentrations ( $[\text{Cl}^-]$  / mM). This data was collected by Dr. M. Algaradah from the McGonigal group.

A control experiment was carried out to determine whether the reductant  $\text{Na}_2\text{S}_2\text{O}_4$  can quench lucigenin's fluorescence, causing a gradual drop in its emission (Figure 2.19). The control experiment was done with a chloride concentration of 5 mM, and as such, the vesicle suspension was prepared in a medium of 225 mM  $\text{NaNO}_3$  (aq) and 5 mM  $\text{NaCl}$ (aq) with pre-incorporated **UQ<sub>6</sub>**. Several aliquots of reductant were added ( $t = 300$  s, 600 s, 1200 s, and 1800 s) as the first aliquot did not produce any measurable response, however additional aliquots revealed a lowering in fluorescence. We decided to only add one aliquot of the  $\text{Na}_2\text{S}_2\text{O}_4$  solution moving forward in our active transport assay based on the control experiment. After the addition of the surfactant, there is an increase in fluorescence upon caused by surfactant solution which did not contain any

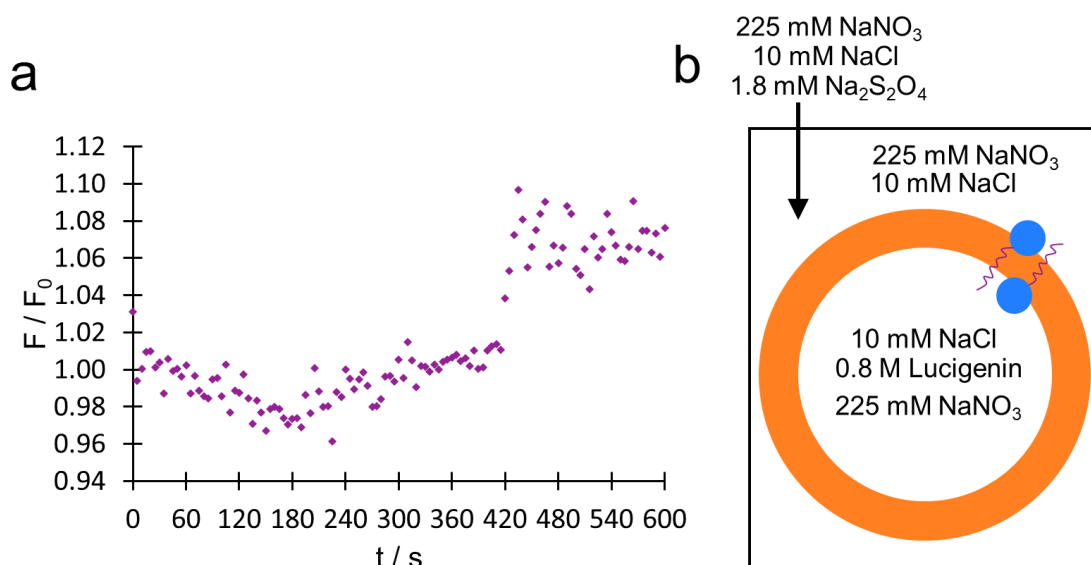
NaCl. Thus, its addition caused an overall dilution of the lipid suspension's  $\text{Cl}^-$  concentration, which led to an increase in  $F/F_0$ .



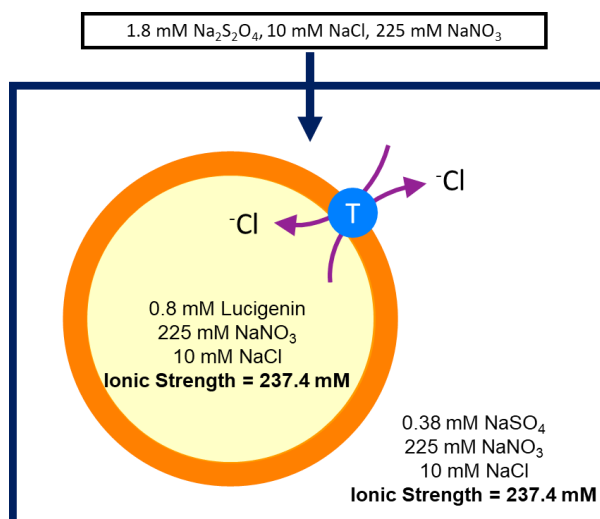
**Figure 2.19.** Testing active transport assay using lucigenin probe. a) the fluorescence decay of lucigenin (0.8 mM intravesicular concentration) entrapped in 200 nm LUVs consisting of 7:3 POPC: cholesterol (0.4 mM lipid concentration in 225 mM  $\text{NaNO}_3$  (aq), 5 mM  $\text{NaCl}$  (aq)), with pre-incorporated quinone carrier  $\text{UQ}_6$  (3.3 mol % w.r.t.) for control (blue) and reductant aliquots (orange). In the first run (blue), no reductant was added. In the second run (orange), an aliquot of  $\text{Na}_2\text{S}_2\text{O}_4$  (aq) (50  $\mu\text{L}$ , 12 mM in 225 mM  $\text{NaNO}_3$  (aq), 5 mM  $\text{NaCl}$  (aq)) was added at  $t = 300, 600, 1200$ , and  $1800$  s. In both runs, the vesicles were lysed with an aqueous solution of 5% Triton X-100 (50  $\mu\text{L}$ ).

Figure 2.20. illustrates an active transport assay conducted at 10 mM chloride concentration. After the addition of the aliquot of  $\text{Na}_2\text{S}_2\text{O}_4$  solution, there appears to be a decrease in  $F/F_0$  counts indicating active transport, however, this change is very minimal and the signal to noise ratio is too high to concretely determine if active transport is occurring. In quinone form, there should be a  $\text{Cl}^-$  influx ( $k_{\text{in}} > k_{\text{out}}$ ), so a decrease in emission should be observed, and after certain amount of time the fluorescence signal should return to baseline  $F/F_0$  before the aliquot was added. This behaviour can be seen in the kinetic fluorescence experiment shown in Figure 2.18, however, due to high signal to noise ratio this claim cannot be made without further exploration. Figure 2.21 illustrates the conditions to test active transport taking in consideration of pH, and ionic strength. Changes in pH over time can affect the hydroquinone form of the ion carriers as these OH donor can be deprotonated. The use of buffer (i.e., HEPES) can eliminate error produced by pH changes over the experiment. Ionic strength should also be taken into consideration as differences in

ionic strength of intravesicular vs extravesicular solutions can cause of movement of water across the lipid membrane *via* osmosis, which can have a significant effect on the fluorescence of lucigenin in this liposomal assay. Unfortunately, control experiments using these conditions without transporter revealed that leakage of the lucigenin dye was occurring due to poor membrane stability. This poor stability could come from the preparation of the lipid vesicles or quality of the lipids. Parameter mentioned were explored, however leakage issue was still occurring so further active transport assay studies using the redox-active molecular ion carriers could not be completed.



**Figure 2.20.** Fluorescence decay of lucigenin caused by the influx of  $\text{Cl}^-$  into 200 nm LUVs consisting of 7:3 POPC:cholesterol (0.4 mM lipid concentration in 225 mM  $\text{NaNO}_3$ ), with preincorporated quinone RABC  $\text{UQ}_6$  at 5 mol% loading w.r.t. lipid concentration. At  $t = 60$  s, a solution of 10 mM  $\text{NaCl}$  (aq), 225 mM  $\text{NaNO}_3$  (aq) + 12 mM  $\text{Na}_2\text{S}_2\text{O}_4$  followed by 10 additions of this solution every 100 s. At  $t = 420$  s, a 5% solution of Triton X-100 (50  $\mu\text{L}$ ) were added.



**Figure 2.21.** Active ion transport liposomal assay taking in consideration of pH (HEPES buffer) and ionic strength with addition of  $\text{NaSO}_4$  to the extravesicular solution.

## 2.7 Biological Testing of Urea Transporters

Transporter compounds **UHQ<sub>6</sub>**, **UQ<sub>6</sub>**, **UHQ<sub>12</sub>**, and **UHQ<sub>12</sub>** were sent to our plant scientist collaborators for preliminary studies to see if our compounds were viable with plant cells. *Arabidopsis thaliana* cells were cultivated in flask containing liquid medium in presence of different concentrations of transporters. *Arabidopsis thaliana* cells are present in multicellular tissue harbours stem cells that proliferate throughout the plant's life span.<sup>11</sup> After 5 days or 7 days of culture, the variation of cell dry weight, which indicates cell growing, was measured (Figure 2.22). The decrease of dry weight observed for 30  $\mu\text{M}$  and 100  $\mu\text{M}$  confirms the toxicity of these high concentrations. Thus, for the following experiments we only used the concentration of 3  $\mu\text{M}$  to test the urea redox active transporters.

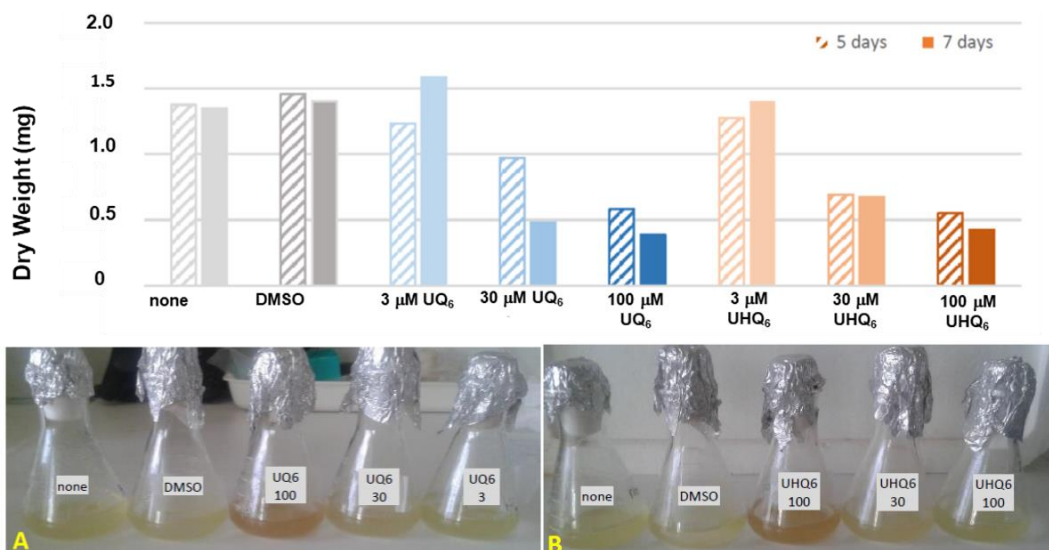


**Figure 2.22.** Dry weights from 3 cell samplings after 5 days (hatched bars) and 7 days (full bars) cultivated in medium containing transporters at different concentrations and controls (solvent DMSO or none). Arabidopsis cells for 1 day in medium containing transporters, a) UQ<sub>6</sub>, b) UHQ<sub>6</sub>, at different concentrations (100  $\mu\text{M}$ , 30  $\mu\text{M}$  or 3  $\mu\text{M}$ ). Flasks without transporter (none) or with DMSO (solvent of transporters) are the controls.

Cells of Arabidopsis and tobacco Xanthi cultivated in liquid suspension were treated with the four transporters (3  $\mu\text{M}$ ) or DMSO using 3 independent flasks. Different parameters were analyzed such as suspension pH and conductivity, or dry weight without obvious difference within sampling. A rapid microscopic analysis was performed for cells treated with 3  $\mu\text{M}$  of both transporters present and DMSO controls. For both Arabidopsis and Xanthi cell morphologies by microscopy, we observed differences when using UQ<sub>6</sub> and UHQ<sub>6</sub> transporters. The Arabidopsis cells treated with these transporters present, we observed an increase of the surface of some cells (arrows) of suspension treated with both UQ<sub>6</sub> and UHQ<sub>6</sub> (Figure 2.23). Those cells that respond to treatments are also more circular. These swelled cells are still alive, at least during the observation. Cell surface and circularity of UQ<sub>12</sub> and UHQ<sub>12</sub> are unchanged in comparison to the control (DMSO-treated cells). For Xanthi cells (Figure 2.24) a tendency of surface increase triggers by both UQ<sub>6</sub> and UHQ<sub>6</sub> was also observed. In contrary, as Xanthi cells are already rounder than Arabidopsis cells, cell circularity is not significantly changed. The increase of cell surface in some cells treated by UQ<sub>6</sub> and UHQ<sub>6</sub> may suggest an impact on osmotic pressure that can be influenced by varying water flux across cell membrane. This water flux can be due to the presences of the ion transporters which can cause a modification to the cell membrane properties.

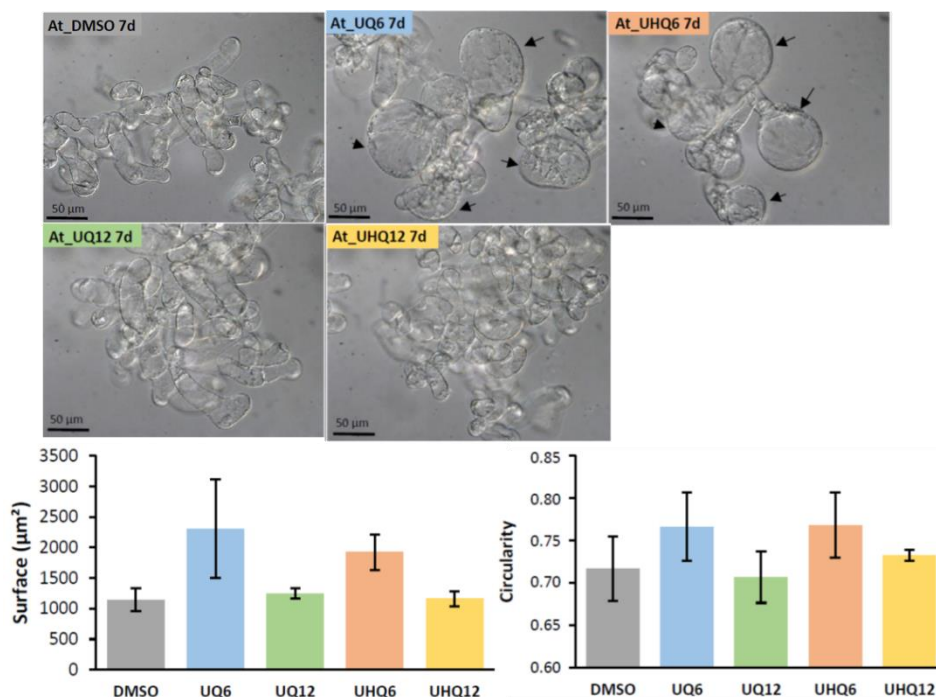


**Figure 2.23.** Arabidopsis thaliana cell (At) treated with 3  $\mu$  M of each transporter or DMSO (control) for 7 days. In these representative images, the arrows indicate cells with a swelling morphology. Histograms are quantification of cell surface and circularity (for a circle, circularity = 1) in each treatment.

From the same cell suspension used for cell morphology imaging, the impact of transporters on the spectral properties of cells were analysed. After 7 days of treatment, cell suspension was analyzed by emission studies (Figure 2.25). The cell suspension was excited at 435 nm to determine the emission properties of the chlorophyll present in the cells. Figure 2.25 shows the emission spectra of these suspensions showing two major peaks ( $\lambda_{em} = 552\text{nm}$ ,  $680\text{nm}$ ). The first large peak at 552 nm corresponds non identified fluorescent components, the second peak at 680 nm corresponds to chlorophyll.

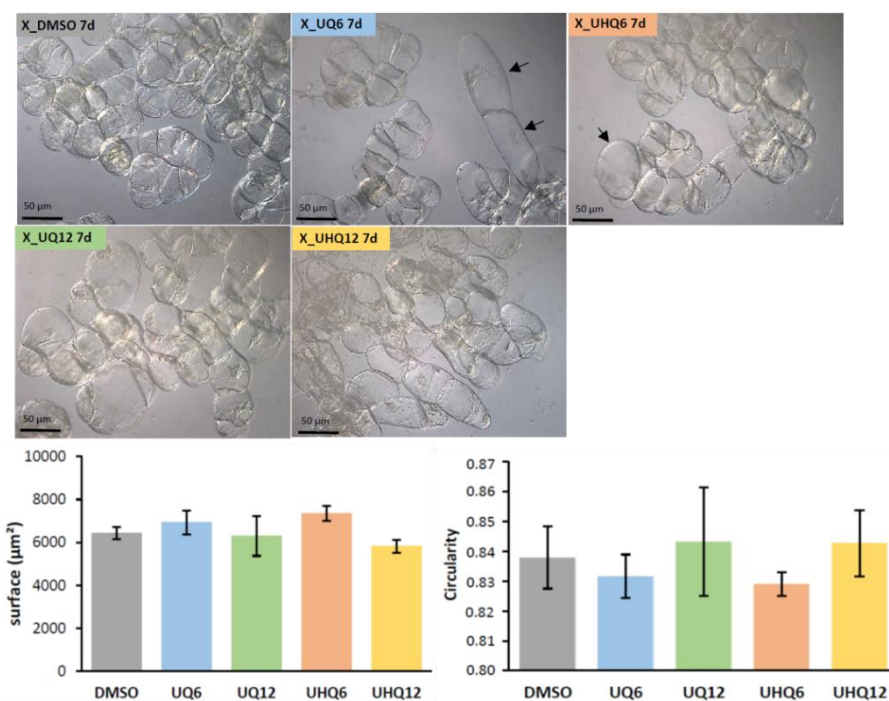


**Figure 2.24.** Xanthi cells (X) treated with 3  $\mu$ M of each transporter or DMSO (control) for 7 days. In these representative images, the arrows indicate cells with a swelling morphology. Histograms are quantification of cell surface and circularity (for a circle, circularity = 1) in each treatment.

The fluorescence emission of cells treated with DMSO (control) with the different transporters shows a decrease in intensity for the peak at 680 nm which corresponds to the chlorophyll. The decrease of chlorophyll peak in cells treated by RAMCs suggests a specific impact of these transporters on photosynthetic apparatus.

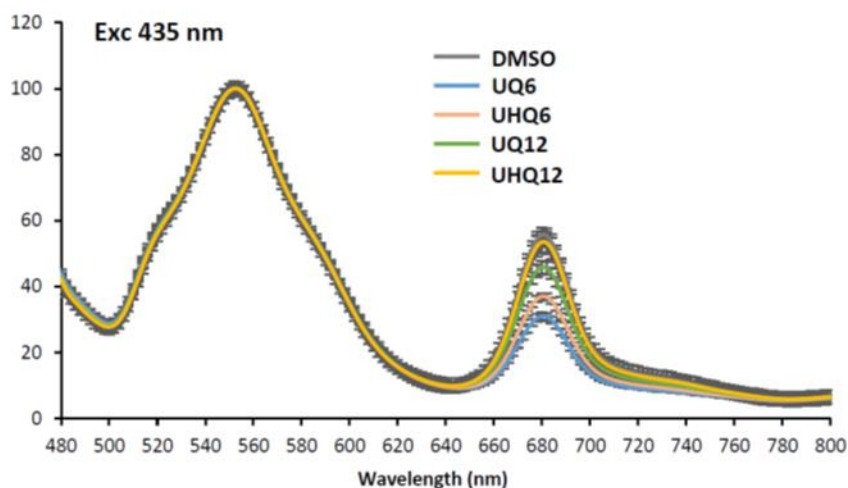


**Figure 2.25.** Emission spectra of 7 days Arabidopsis cells in presence of 3  $\mu$ M RAMCs or DMSO. Excitation wavelength was 435 nm (for chlorophyll excitation) and chlorophyll emission corresponds to the 680 nm peak.

## 2.8 Conclusion and Future Work

A series of urea based redox-active artificial molecular carriers (**UHQ<sub>6</sub>**, **UHQ<sub>12</sub>**, **UQ<sub>6</sub>**, **UQ<sub>12</sub>**) were successfully and fully characterized. Vesicle studies using the lucigenin method revealed the hydroquinone RAMCs achieved slightly higher rates of  $\text{Cl}^-$  transport than the quinone RAMCs. Increasing the alkyl length of the RAMCs amplifies the lipophilicity of these compounds, enhancing the rate of  $\text{Cl}^-$  influx across lipid membranes for the RAMCs. For the active transport studies, parameters need to be optimized to find conditions to properly study this phenomenon. The preliminary data of our RAMCs in presence of plant cells suggest that **UQ<sub>6</sub>** and **UHQ<sub>6</sub>** transporters have an influence on cell morphology due to possible cell membrane incorporation which is needed for this technology to work. Furthermore, the emission studies revealed that RAMCs have an impact on the photosynthetic apparatus of the cell which is desired. These results are encouraging for the incorporation of molecular devices in plants however further investigation is needed to understand how our RAMCs will affect photosynthesis in plants.

## 2.9 Experimental

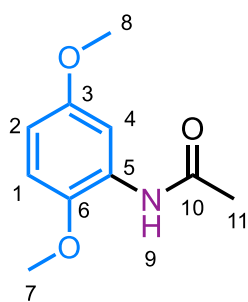
**Materials and Synthesis:** Unless otherwise stated, all reagents were purchased from Sigma Aldrich or Alfa Aesar and were used without further purification. Air sensitive reactions were carried out under an argon atmosphere using a Schlenk technique. Purification by flash column chromatography was carried out using Teledyne Isco CombiFlash Rf+ system, with pre-packed SiO<sub>2</sub> columns as the stationary phase. Analytical TLC was performed on neutral aluminium sheet silica gel plates (Fluka, 60778-25EA) and visualised under UV irradiation (254 nm). Microwave reactions were performed using an automated Biotage reactor, Robot-Sixty, model: Initiator EXP EU, 355301, 11327-36W. All analytical solutions were prepared using deionized water.

**Vesicle Preparation:** Vesicle extrusions were carried out using an Avanti Mini Extruder (Avanti Polar Lipids Inc.), 10 mm filter supports (Avanti Polar Lipids Inc.), and 200 nm polycarbonate Whatman Nucleopore Track-Etched Membranes. External lucigenin was removed using a disposable PD-10 desalting column with a Sephadex G-25 medium (GE Healthcare).

**Structural Characterisation:** <sup>1</sup>H, and <sup>13</sup>C NMR spectra were recorded in commercially available deuterated solvents on a Bruker (Avance III 400) spectrometer (400.13 MHz for <sup>1</sup>H, 100.62 for <sup>13</sup>C), a Varian VNMRs-600 spectrometer (<sup>1</sup>H at 599.60 MHz, <sup>13</sup>C at 150.78 MHz), or a Varian VNMRs-700 spectrometer (<sup>1</sup>H at 699.74 MHz, <sup>13</sup>C at 175.95 MHz) at a constant temperature of 298 K. Chemical shifts are reported in parts per million (ppm) relative to residual solvent as a reference. Coupling constants (*J*) are reported in hertz (Hz). Assignment of the <sup>1</sup>H/<sup>13</sup>C NMR signals was accomplished by two-dimensional NMR spectroscopy (COSY, HMBC, HSQC, DOSY). NMR spectra were processed using MestReNova. Data are reported as follows: chemical shift, integration, multiplicity, coupling constants and assignment. Multiplicities are reported as singlet (s), doublet (d), triplet (t), quartet (q), pentet (p), and multiplet (m). Atmospheric solids analysis probe mass spectrometry (ASAP-MS) was performed using an LCT Premier XE (Waters Ltd. UK) high resolution spectrometer. Electrospray mass spectra (MS-ES(+/-)) were recorded on a TQD mass spectrometer equipped with an Acquity UPLC system, a lock-mass electrospray ion source and an Acquity photodiode array detector (both systems Waters Ltd, UK). The

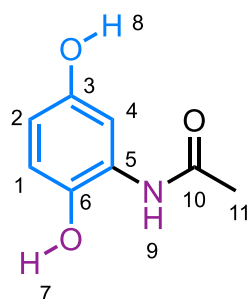
carrier solvents were acetonitrile or methanol. High resolution mass spectra (HRMS-ES(+/-)) were recorded in a LCT Premier XE mass spectrometer or a QToF Premier mass spectrometer, both of which were fitted with an Acquity UPLC system, a lock-mass electrospray ion source and an Acuity photodiode array detector (Waters Ltd, UK). Melting points were recorded using a Gallkanp (Sanyo) apparatus and are uncorrected. All fluorescence spectra were recorded in a 4 mL quartz cuvette (Hellma Analytics) on a Jobin Yvon Horiba Fluorolog 3. The data were visualized in FluorEssence for Windows and analyzed in Excel or OriginPro.

### 2.9.1 Synthesis



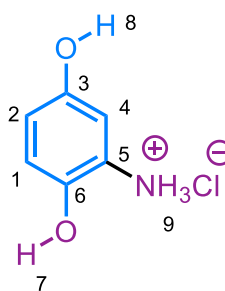
***N*-(2,5-dimethoxyphenyl)acetamide.** 2,5-Dimethoxyaniline (5.00 g, 32.6 mmol,) was dissolved in CH<sub>2</sub>Cl<sub>2</sub> (75 mL) and cooled to 0 °C. Et<sub>3</sub>N (5.50 mL, 39.2 mmol) was added, followed by Ac<sub>2</sub>O (3.70 mL, 39.2 mmol, 1.2 eq.), and DMAP (25.0 mg, 0.205 mmol). The cooling bath was removed, and the mixture was stirred at rt for 2 h. The reaction progress was monitored by TLC.

The organic layer was washed with water (3 × 75 mL), saturated NaHCO<sub>3</sub> (aq) (1 × 50 mL), brine (1 × 50 mL), and dried over MgSO<sub>4</sub>. The solvent was removed *in vacuo*, and the crude product was recrystallized from 1:5 MeCN/water to yield a brown solid (5.54 g, 87%). **M.P.** 89–90 °C. **<sup>1</sup>H NMR** (600 MHz, CDCl<sub>3</sub>) δ 8.09 (d, *J* = 3.0 Hz, 1H, H<sub>4</sub>), 7.75 (1H, s, H<sub>9</sub>), 6.76 (d, *J* = 8.9 Hz, 1H, H<sub>1</sub>), 6.54 (dd, *J* = 8.9, 3.1 Hz, 1H, H<sub>2</sub>), 3.82 (d, *J* = 1.3 Hz, 3H, H<sub>7</sub>), 3.76 (d, *J* = 1.2 Hz, 3H, H<sub>8</sub>), 2.18 (s, 3H, H<sub>11</sub>). **<sup>13</sup>C NMR** (151 MHz, CDCl<sub>3</sub>) δ 168.1 (C<sub>10</sub>), 153.9 (C<sub>6</sub>), 141.8 (C<sub>3</sub>), 128.4 (C<sub>5</sub>), 110.6 (C<sub>1</sub>), 108.3 (C<sub>2</sub>), 106.0 (C<sub>4</sub>), 56.1 (C<sub>7</sub>), 55.8 (C<sub>8</sub>), 25.0 (C<sub>11</sub>). **HRMS-ESI** *m/z* = 196.0974 [M+H]<sup>+</sup>, calculated for C<sub>10</sub>H<sub>15</sub>NO<sub>3</sub> 196.0974.



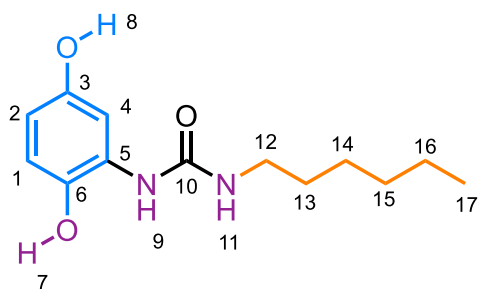
***N*-(2,5-dihydroxyphenyl)acetamide.** *N*-(2,5-dimethoxyphenyl)acetamide (4.50 g, 23.1 mmol) was placed in an oven-dried round-bottomed flask fitted with a septum under a nitrogen atmosphere and dissolved in anhydrous CH<sub>2</sub>Cl<sub>2</sub> (50 mL). The solution was cooled to −78 °C before addition of BBr<sub>3</sub> (50 mL, 50.0 mmol) by cannula over 20 min. The reaction mixture was stirred at −78 °C for 1 h and then allowed to reach rt overnight. After 16

h, water (80 mL) was added, and the mixture was stirred at r.t. for 2 h. The aqueous layer was extracted with EtOAc (5 × 100 mL). The combined organic extracts were washed with water (100 mL) and brine (100 mL), dried over MgSO<sub>4</sub>, and the solvent was removed *in vacuo*, to give a tan solid (2.57 g, 67%). **M.P.** 160–162 °C. **<sup>1</sup>H NMR** (600 MHz, (CD<sub>3</sub>)<sub>2</sub>CO): δ 9.05 (s, 1H, H<sub>9</sub>), 8.53 (s, 1H, H<sub>7</sub>), 7.81 (s, 1H, H<sub>8</sub>), 7.01 (d, *J* = 2.9 Hz, 1H, H<sub>4</sub>), 6.71 (d, *J* = 8.6 Hz, 1H, H<sub>1</sub>), 6.50 (dd, *J* = 8.6, 2.9 Hz, 1H, H<sub>2</sub>), 2.17 (s, 3H, H<sub>11</sub>). **<sup>13</sup>C NMR** (151 MHz, (CD<sub>3</sub>)<sub>2</sub>CO): δ 169.9 (C<sub>10</sub>), 150.4 (C<sub>3</sub>), 141.1 (C<sub>6</sub>), 127.1 (C<sub>5</sub>), 118.1 (C<sub>1</sub>), 112.1 (C<sub>2</sub>), 108.4 (C<sub>4</sub>). **HRMS-ESI-:** *m/z* = 168.0658 [M+H]<sup>+</sup>, calculated for C<sub>8</sub>H<sub>10</sub>NO<sub>3</sub>: 168.0661.



**2,5-dihydroxybenzenaminium chloride (2.1).** *N*-(2,5-Dihydroxyphenyl)acetamide (1.00 g, 5.98 mmol) was dissolved in 1:1 CH<sub>2</sub>Cl<sub>2</sub>/MeOH (50 mL) and degassed through three freeze-pump-thaw cycles. Conc. HCl (37%, 3.5 μL, 40.9 mmol) was added, and the mixture was left to reflux overnight under N<sub>2</sub>. After 16 h, the solvent was removed *in vacuo*, leaving a dark green solid.

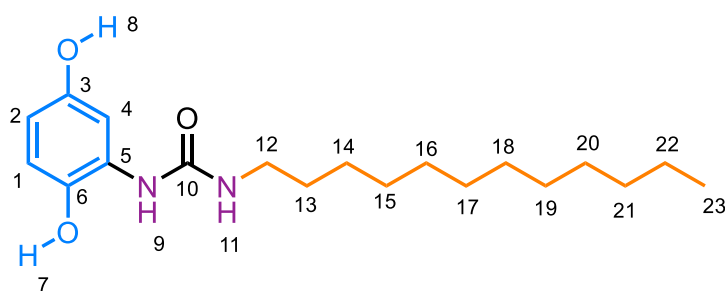
Toluene (30 mL) was added to the crude, then removed *in vacuo* (x 3) to remove all of the water. The crude was dissolved in minimal amount of MeOH (5 mL) and triturated with Et<sub>2</sub>O (40 mL). A gray precipitate was collected by filtration and left to dry overnight to yield a gray solid (860 mg, 89%). **M.P.** 212–214 °C. **<sup>1</sup>H NMR** (700 MHz, (CD<sub>3</sub>)<sub>2</sub>SO) δ 9.85 (s, 1H, H<sub>8</sub>), 9.75 (s, 3H, H<sub>9</sub>), 9.25 (s, 1H, H<sub>1</sub>), 6.83 (d, 1H, *J* = 8.7 Hz, H<sub>1</sub>), 6.81 (1H, d, *J* = 2.9 Hz, H<sub>4</sub>), 6.62 (1H, dd, *J* = 8.7, 2.9 Hz, H<sub>2</sub>). **<sup>13</sup>C NMR** (176 MHz, (CD<sub>3</sub>)<sub>2</sub>SO) δ 150.4 (C<sub>3</sub>/C<sub>6</sub>), 143.3 (C<sub>3</sub>/C<sub>6</sub>), 119.7 (C<sub>4</sub>), 117.3 (C<sub>6</sub>), 115.7 (C<sub>7</sub>), 111.1 (C<sub>3</sub>). **HR-ESI-MS** *m/z* = 161.8365 [M+H]<sup>+</sup>, calculated for C<sub>6</sub>H<sub>8</sub>NCl: 161.6823.



**1-(2,5-dihydroxyphenyl)-3-hexylurea (UHQ6).** Hexyl isocyanate (0.79 g, 6.19 mmol) and 2-aminohydroquinone hydrochloride (1.00 g, 6.19 mmol) were added to a microwave vial. EtOH (10.0 mL) and Et<sub>3</sub>N (0.193 mL) were added, and the

mixture was heated to 80 °C in a microwave reactor for 16 h. After cooling to rt, the mixture was concentrated under reduced pressure. The crude residue was purified by

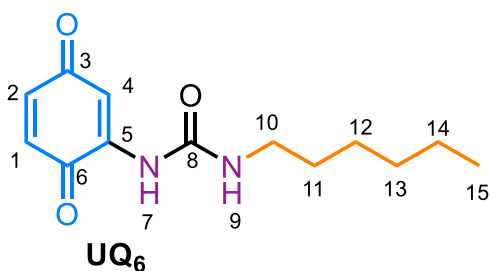
column chromatography (Teledyne Isco CombiFlash Rf+ system, 40 g SiO<sub>2</sub>, CH<sub>2</sub>Cl<sub>2</sub>–MeOH, gradient elution, 0–15 % MeOH) to yield a grey solid (0.77 g, 49 %). **<sup>1</sup>H NMR** (400 MHz, (CD<sub>3</sub>)<sub>2</sub>CO) δ 9.00 (s, 1H, H<sub>7</sub>), 7.74 (s, 1H, H<sub>8</sub>), 7.70 (s, 1H, H<sub>9</sub>), 6.99 (d, *J* = 2.9 Hz, 1H, H<sub>4</sub>), 6.65 (d, *J* = 8.6 Hz, 1H, H<sub>1</sub>), 6.36 (dd, *J* = 8.6, 2.9 Hz, 1H, H<sub>2</sub>), 6.28 (s, 1H, H<sub>11</sub>), 3.26–3.16 (m, 2H, H<sub>12</sub>), 1.51 (tt, *J* = 7.6, 6.9 Hz, 2H, H<sub>13</sub>), 1.41–1.24 (m, 6H, H<sub>14</sub>–H<sub>16</sub>), 0.95–0.81 (m, 3H, H<sub>17</sub>). **<sup>13</sup>C NMR** (176 MHz, (CD<sub>3</sub>)<sub>2</sub>CO) δ 157.6 (C<sub>10</sub>), 151.3 (C<sub>3</sub>), 141.0 (C<sub>5</sub>), 129.3 (C<sub>6</sub>), 118.1 (C<sub>1</sub>), 110.4 (C<sub>2</sub>), 108.2 (C<sub>4</sub>), 40.7 (C<sub>12</sub>), 32.2 (C<sub>15</sub>), 30.8 (C<sub>13</sub>), 27.2 (C<sub>14</sub>), 23.2 (C<sub>16</sub>), 14.3. (C<sub>17</sub>). **HRMS-ASAP** *m/z* = 253.1557 [M+H]<sup>+</sup> calculated for C<sub>13</sub>H<sub>21</sub>N<sub>2</sub>O<sub>3</sub>: 253.1552.



**1-(2,5-dihydroxyphenyl)-  
3-dodecylurea (UHQ<sub>12</sub>).**

Dodecyl isocyanate (0.65 g, 3.09 mmol) and 2,5-dihydroxyanilium chloride (0.50 g, 3.09 mmol) were

added to a microwave vial, followed by Et<sub>3</sub>N (0.313 g, 3.09 mmol), and EtOH (3.09 mL). The mixture was sonicated and heated to 80 °C in a microwave reactor for 16 h. After cooling to r.t., the solvent was removed *in vacuo*, and the crude residue was purified by column chromatography (Teledyne Isco CombiFlash Rf+ system, 40 g SiO<sub>2</sub>, CH<sub>2</sub>Cl<sub>2</sub>–MeOH, gradient elution, 0–15% MeOH) to give the title product as a beige solid (330 g, 29%). **M.P.** 107–109 °C. **<sup>1</sup>H NMR** (600 MHz, (CD<sub>3</sub>)<sub>2</sub>CO) δ 9.02 (s, 1H, H<sub>7</sub>), 7.82 (s, 1H, H<sub>8</sub>), 7.73 (s, 1H, H<sub>9</sub>), 7.02 (d, 1H, *J* = 2.9 Hz, H<sub>4</sub>), 6.64 (d, 1H, *J* = 8.6 Hz, H<sub>1</sub>), 6.35 (dd, 1H, *J* = 8.6, 2.9 Hz, H<sub>2</sub>), 6.33 (s, 1H, H<sub>11</sub>), 3.23–3.17 (m, 2H, H<sub>12</sub>), 1.50 (tt, 2H, *J* = 7.0 Hz, H<sub>13</sub>), 1.37–1.21 (m, 18H, H<sub>14</sub>–H<sub>22</sub>), 0.89 (m, 3H, H<sub>23</sub>). **<sup>13</sup>C NMR** (151 MHz, (CD<sub>3</sub>)<sub>2</sub>CO) δ 156.9 (C<sub>10</sub>), 150.5 (C<sub>3</sub>), 140.1 (C<sub>5</sub>), 128.4 (C<sub>6</sub>), 117.3 (C<sub>1</sub>), 109.6 (C<sub>2</sub>), 107.4 (C<sub>4</sub>), 39.9 (C<sub>12</sub>), 31.7 (C<sub>13</sub>), 30.0–26.7 (C<sub>14</sub>–H<sub>21</sub>), 22.4 (C<sub>22</sub>), 13.7 (C<sub>23</sub>). **HRMS-ASAP** *m/z* = 337.2478 [M+H]<sup>+</sup>, calculated for C<sub>19</sub>H<sub>33</sub>N<sub>2</sub>O<sub>3</sub> 337.2467.



**1-(3,6-dioxocyclohexa-1,4-dien-1-yl)-3-hexylurea (UQ<sub>6</sub>).**

*N*-(2,5-Dihydroxyphenyl)-3-hexylurea (0.10 g, 0.40 mmol) was dissolved in Et<sub>2</sub>O (30 mL). MnO<sub>2</sub> (0.35 g, 3.96 mmol) was added, and the reaction mixture was left to stir for 3.5 h. The mixture was filtered through

a syringe tip filter and purified by column chromatography (Teledyne Isco CombiFlash Rf+ system, 40 g SiO<sub>2</sub>, CH<sub>2</sub>Cl<sub>2</sub>–MeOH, gradient elution, 0–15% MeOH) to give the desired product as a red solid (67.4 mg, 269 μmol, 68%). **<sup>1</sup>H NMR** (400 MHz, (CD<sub>3</sub>)<sub>2</sub>CO) δ 8.09 (s, 1H, H<sub>7</sub>), 7.31 (d, *J* = 2.6 Hz, 1H, H<sub>4</sub>), 6.86 (s, 1H, H<sub>9</sub>), 6.79 (d, *J* = 10.1 Hz, 1H, H<sub>1</sub>), 6.68 (dd, *J* = 10.1, 2.6 Hz, 1H, H<sub>2</sub>), 3.24–3.18 (m, 2H, H<sub>10</sub>), 1.51 (dt, *J* = 14.7, 6.7 Hz, 2H, H<sub>11</sub>), 1.40–1.24 (m, 6H, H<sub>12–14</sub>), 0.90–0.84 (m, 3H, H<sub>15</sub>). **<sup>13</sup>C NMR** (176 MHz, (CD<sub>3</sub>)<sub>2</sub>CO) δ 188.3, 184.0, 154.4, 141.9, 138.7, 134.2, 111.2, 40.4, 32.3, 30.5, 27.2, 23.3, 14.3. **HRMS-ASAP** *m/z* = 251.1410 [M+H]<sup>+</sup> calculated for C<sub>13</sub>H<sub>19</sub>N<sub>2</sub>O<sub>3</sub>: 251.1396.



**1-(3,6-dioxocyclohexa-1,4-dien-1-yl)-3-dodecylurea (UQ<sub>12</sub>).**

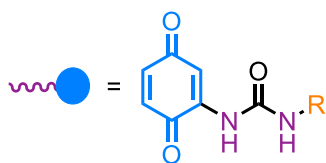
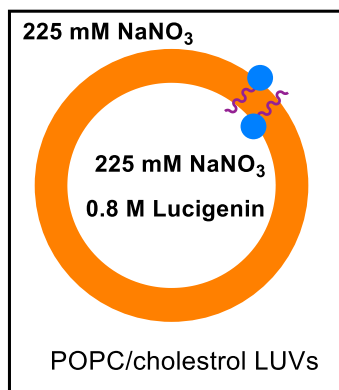
MnO<sub>2</sub> (0.65 g, 2.97 mmol) was added to a solution of *N*-(2,5-dihydroxyphenyl)-

3-dodecylurea (0.10 g, 0.3 mmol) in Et<sub>2</sub>O (30 mL), and the mixture was stirred at rt for 4 h. The mixture was filtered, and the solvent was removed *in vacuo*. The crude residue was purified by column chromatography (Teledyne Isco CombiFlash Rf+ system, 24 g SiO<sub>2</sub>, CH<sub>2</sub>Cl<sub>2</sub>–MeOH, gradient elution, 0–15% MeOH) to give the title compound as a red solid (90.0 mg, 87%). **M.P.** 130–132 °C. **<sup>1</sup>H NMR** (400 MHz, (CD<sub>3</sub>)<sub>2</sub>CO) δ 8.10 (s, 1H, H<sub>7</sub>), 7.34 (d, 2.6 Hz, 1H, H<sub>4</sub>), 6.86 (1H, s, H<sub>9</sub>), 6.81 (d, *J* = 10 Hz, 1H, H<sub>1</sub>), 6.70 (dd, *J* = 10, 2.6 Hz, 1H, H<sub>2</sub>), 3.26–3.21 (m, 2H, H<sub>10</sub>), 1.57–1.51 (m, 2H, H<sub>11</sub>), 1.40–1.25 (m, 18H, H<sub>12–20</sub>), 0.91–0.87 (m, 3H, H<sub>21</sub>). **HRMS-ASAP** *m/z* = 335.2330 [M+H]<sup>+</sup>, calculated for C<sub>19</sub>H<sub>33</sub>N<sub>2</sub>O<sub>3</sub>: 335.2335.

## 2.9.2 Ion Transport Studies

## Vesicle Studies with Embedded Receptors and Lucigenin

## Preparation of hydroquinone transporter (POPC/Cholesterol) vesicles containing lucigenin



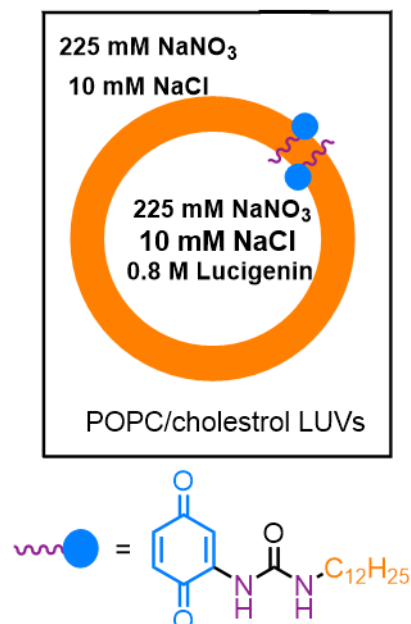
1-Palmitoyl-2-oleoyl-*sn*-glycero-3-phosphocholine (POPC) (3.6 mg, 4.74  $\mu\text{mol}$ ) of this compound was transferred to a 20 mL vial. Cholesterol chloroform solution (0.7 mL, 2.6 mM, 5.5  $\mu\text{mol}$ ) was added to the vial and POPC was dissolved and transferred to a 25 mL round-bottomed flask (RBF). The vial was washed four times with chloroform (0.5 mL  $\times$  4) and these washings were added to the RBF. **UQ<sub>12</sub>** methanol solution was added (50  $\mu\text{L}$ , 2 mM, 100 nmol). The solvent was removed under a flow of  $\text{N}_2$ , leaving behind a lipid film at the bottom of the RBF, which was further dried for 1

h under high vacuum. An aqueous solution of  $\text{NaNO}_3$ /lucigenin (0.5 mL, 225 mM  $\text{NaNO}_3$  (aq), 0.8 mM lucigenin) was then added to the lipid film. The mixture was sonicated until the film no longer adhered to the flask and stirred for 1 h at r.t. The mixture was left to stir vigorously at r.t for 1 h. The suspension mixture was then subjected to ten freeze/thaw cycles and allowed to age at r.t for 30 min. The mini-extruder was assembled and the yellow suspension was loaded into the syringe. 0.3 mL 225  $\text{NaNO}_3$  (aq) solution was used to wash the RBF and this washing was loaded into the syringe. The suspension was extruded 25 times through a 200-nm polycarbonate membrane filter installed in a mini-extruder to produce unilamellar vesicles.

The free lucigenin was separated from the vesicles using a PD-10 desalting column, with  $\text{NaNO}_3$  as the mobile phase.  $\text{NaNO}_3$  (aq) ( $5 \times 5$  mL, 225 mM) was used to equilibrate the column. Each aliquot was allowed to enter the column bed entirely prior to the addition of the next aliquot. The vesicle suspension (0.7 mL) was added to the column and allowed to enter it fully, followed by  $\text{NaNO}_3$  (aq) (1.8 mL, 225 mM). The liquid (2.5 mL) that left the column during loading were discarded.  $\text{NaNO}_3$  (aq) (2.0 mL, 225 mM) was added to the column and the liquid leaving the column was collected.

The suspension was diluted by addition of  $\text{NaNO}_3$  (aq) (10 mL, 225 mM) to a total volume of 12 mL (0.4 mM lipid), and its fluorescence measured immediately after preparation.

### Preparation of POPC Vesicles containing Lucigenin and Fluorescence Measurements for Active Transport Assays



1-palmitoyl-2-oleoyl-*sn*-glycero-3-phosphocholine (POPC) bottle was submerged in liquid  $\text{N}_2$  for 15 s and POPC (3.6 mg, 4.74  $\mu\text{mol}$ ) was added to a 20 mL vial and dissolved in dried chloroform. The solution was transferred to a 25 mL round bottomed flask (RBF), and the vial was washed with anhydrous chloroform ( $4 \times 0.5$  mL). These washings, along with a solution of cholesterol (0.7 mL, 1 mg / mL in chloroform, 1.8  $\mu\text{mol}$ ) and (3,6-dioxocyclohexa-1,4-dien-1-yl)dodecylurea (50  $\mu\text{L}$ , 2 mM in MeOH, 0.1  $\mu\text{mol}$ , 2 mol % w.r.t. lipid concentration) were added to the RBF. The mixture

was sonicated until the solids had dissolved. The solvent was removed under a high flow of  $\text{N}_2$ , leaving behind a lipid film at the bottom of the RBF, which was further dried for 1 h under high vacuum. A lucigenin solution (0.5 mL, 0.8 mM in 225 mM  $\text{NaNO}_3$  (aq) + 10 mM  $\text{NaCl}$  (aq)) was then added to the lipid film. The mixture was sonicated until the film no longer adhered to the flask and stirred for 1 h at r.t. The suspension was subjected to ten freeze/thaw cycles, allowed to age at r.t. for 30 min, and loaded onto a syringe. The RBF was washed with  $\text{NaNO}_3/\text{NaCl}$  (aq) (0.3 mL, 225 mM  $\text{NaNO}_3$  (aq) + 10 mM  $\text{NaCl}$  (aq)), and these washings were also loaded onto the syringe. The extruder was assembled, and the suspension was extruded 25 times through a 200 nm polycarbonate membrane filter to produce unilamellar vesicles.

Next, the free lucigenin was separated from the vesicles using a PD-10 desalting column, with  $\text{NaNO}_3$  (aq)/ $\text{NaCl}$  (aq) as the mobile phase.  $\text{NaNO}_3/\text{NaCl}$  (aq) ( $5 \times 5$  mL, 225 mM  $\text{NaNO}_3$  (aq) + 10 mM  $\text{NaCl}$  (aq)) was used to equilibrate the column. Each aliquot was allowed to enter the column bed entirely prior to the addition of the next aliquot. The vesicle suspension (0.7 mL) was added to the column and allowed to enter

it fully, followed by  $\text{NaNO}_3$  (aq)/ $\text{NaCl}$  (aq) (1.8 mL, 225 mM  $\text{NaNO}_3$ (aq) + 10 mM  $\text{NaCl}$  (aq)). The liquid (2.5 mL) that left the column during loading was discarded.  $\text{NaNO}_3$  (aq)/ $\text{NaCl}$  (aq) (2.0 mL, 225 mM  $\text{NaNO}_3$  (aq) + 10 mM  $\text{NaCl}$  (aq)) was added to the column and the liquid leaving the column was collected. The suspension was diluted by addition of  $\text{NaNO}_3$  (aq)/ $\text{NaCl}$  (aq) (4 mL, 25 mM  $\text{NaNO}_3$  (aq) + 10 mM  $\text{NaCl}$  (aq)) to a total volume of 6 mL (0.8 mM lipid), and its fluorescence measured immediately after preparation.

The vesicle suspension (3 mL, 0.8 mM lipid concentration) was transferred to a 4 mL plastic cuvette. On a Fluorolog 3 fluorimeter, a kinetic experiment was carried out over 1500 s with  $\lambda_{\text{ex}} = 450$  nm,  $\lambda_{\text{em}} = 535$  nm, slit widths 4 nm, and integration time 0.1 s. A bespoke injection system (lid and injection chamber) was used, allowing kinetic measurements to carry on without disruption. At the beginning of the experiment,  $\text{Na}_2\text{S}_2\text{O}_4$  (aq) (50  $\mu\text{L}$ , 12 mM in 225 mM  $\text{NaNO}_3$  (aq) + 10 mM  $\text{NaCl}$  (aq)) was loaded into the syringe, and the syringe was immersed in the cuvette under the surface of the solution. s.. At 1350 s the shutter was closed, and the run was paused, while the surfactant Triton X-100 (50  $\mu\text{L}$ , 5% aq. in 225 mM  $\text{NaNO}_3$  (aq) + 10 mM  $\text{NaCl}$  (aq)) was loaded into the syringe. The fluorescence was then resumed for 30 s prior to the addition of surfactant to lyse the vesicles and recorded until 1500 s was reached.

## 2.10 References

- 1) C. J. E. Haynes, S. N. Berry, J. Garric, J. Herniman, J. R. Hiscock, I. L. Kirby, M. E. Light, G. Perkes and P. A. Gale, *Chem. Commun.*, 2013, **49**, 246–248.
- 2) P. Thordarson, *Chem. Soc. Rev.*, 2011, **40**, 1305–1323.
- 3) H. Li, H. Valkenier, L. W. Judd, P. R. Brotherhood, S. Hussain, J. A. Cooper, O. Jurček, H. A. Sparkes, D. N. Sheppard and A. P. Davis, *Nat. Chem.*, 2016, **8**, 24–32.
- 4) H. Valkenier, C. J. E. Haynes, J. Herniman, P. A. Gale and A. P. Davis, *Chem. Sci.*, 2014, **5**, 1128–1134.
- 5) E. N. W. Howe and P. A. Gale, *J. Am. Chem. Soc.*, 2019, **141**, 10654–10660.
- 6) P. A. Gale, R. Pérez-Tomás and R. Quesada, *Acc. Chem. Res.*, 2013, **46**, 2801–2813.
- 7) M. Yano, C. C. Tong, M. E. Light, F. P. Schmidtchen and P. A. Gale, *Org. Biomol. Chem.*, 2010, **8**, 4356–4363.
- 8) 38 N. Busschaert, I. L. Kirby, S. Young, S. J. Coles, P. N. Horton, M. E. Light and P. A. Gale, *Angew. Chem. Int. Ed.*, 2012, **51**, 4426–4430.
- 9) C. R. Yamnitz, S. Negin, I. A. Carasel, R. K. Winter and G. W. Gokel, *Chem. Commun.*, 2010, **46**, 2838–2840.
- 10) M. S. Bretscher, *Science*, 1973, **181**, 622–629.

# Chapter 3 | Shapeshifting Fluxional Carbon Cages

### 3.0 Synopsis

This chapter introduces the concept of shapeshifting molecules in the field of dynamic covalent chemistry. These molecules are tricyclic carbon cages that undergo intramolecular cope rearrangement which impart shapeshifting molecular properties. The focus of the review is on bistable barbaralane which switch between two states and bullvalene which can access hundreds of thousands of isomers. In this chapter, the traditional and modern synthetic routes toward both bullvalene & barbaralanes is explored and the potential applications for these in novel chemical sensors is discussed. This chapter is an adaption of the Chemical Science mini review, “Shapeshifting molecules: the story so far and the shape of things to come” McGonigal et al. (2020).<sup>1</sup>

### 3.1 Fluxional Molecules

Fluxional molecules are dynamic compounds in which magnetically or chemically distinct groups can readily interchange positions.<sup>2</sup> In theory, all molecules are fluxional in some capacity, e.g. bond rotations in most organic compounds, however the term “fluxional” depends on the context and the method used to assess the molecular dynamics. Typically, a molecule is considered fluxional if the rate of this interchange of positions is faster than the time scale of spectroscopic measurement (i.e., NMR) at room temperature, indicated by line-broadening.<sup>3,4</sup> This spectroscopic line-broadening correlates to chemical exchange between different isomers that appear to be identical. Many fluxional processes do not involve bond breaking/making and examples of such processes are highlighted in Table 3.1.<sup>4</sup> The prototypical example of such a system is the axial-equatorial interconversion of the chair form of cyclohexane.<sup>3,4</sup> At room temperature the axial and equatorial protons are interchanged by a dynamic (fluxional) process in which the ring undergoes a "chair-chair" conformation change. Another example of a conformational fluxional molecule is internal rotation causing intramolecular stereomutations such as the berry pseudorotation of pentacoordinate compounds such as  $\text{PF}_6$ .<sup>3,4</sup> Another class of fluxional molecular processes involve a bond breaking/making event (Table 3.1).<sup>4</sup> An example of a class of dynamic processes that involves a bond breaking/making event are intramolecular isomerisation & rearrangements. These intramolecular processes involve just one reactive species (molecule, ion, ion pair). Types of these dynamic processes includes tautomerisation, sigmatropic processes, haptotropic processes, and cis/trans isomerisation.<sup>4</sup> This review

will be focusing on tricyclic fluxional carbon cages that undergo a dynamic sigmatropic processes.

**Table 3.1.** Examples of Fluxional processes

Intramolecular dynamics	Intermolecular dynamics
<b>Dynamics without bond breaking/making</b>	
Internal Rotation	Molecular Recognition
Interconnected rotors	H-bonding
Propellers	Charge transfer
Ring-flip in cyclic systems	Ion-pairs
	Host-guest
Stereomutation	Interlocked system dynamics
Chiral centre inversion	Shuttling
Cage inversion	Pirouetting
Helicity inversion	
<b>Dynamics with bond breaking/making</b>	
Migration	Interlocking
Tautomerisation	Substitution
Isomerisation	Ligand exchange
Rearrangement	Addition-elimination
Cyclisation	Redox processes

### 3.2 Shapeshifting Fluxional Carbon Cages

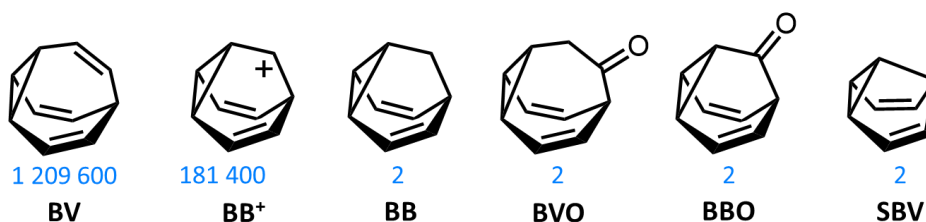


**Figure 3.1.** structural formulas of fluxional carbon cages **BV**, **BB<sup>+</sup>**, **BB<sup>-</sup>**, **BB**, **BVO**, **BBO**, and **SBV**. The number of degenerate isomers they each access is given below the structures.

The carbon–carbon bonds that hold together organic molecules are generally static, being localised at a fixed in position in a molecular structure. This carbon–carbon characteristic is often desirable as it imparts stability, allowing for routinely and predictably synthesise isolable new structures based on carbon skeletons. But a fixed covalent bonding constitution imposes some restrictions on the three-dimensional shapes accessible to a molecule, particularly for cyclic systems with their well-defined conformational degrees of freedom. The relatively fixed shape dictates physical properties and limits noncovalent bonding modes with the surrounding environment.

Shapeshifting compounds (Figure 3.1) are exceptions to these general rules. The fluxional tricyclic hydrocarbon cages bullvalene<sup>5</sup> **BV**, the barbaralyl cation<sup>6</sup> **BB<sup>+</sup>**,

barbaralane<sup>7</sup> **BB**, bullvalene<sup>8</sup> **BVO**, barbaralane<sup>8</sup> **BBO** and semibullvalene<sup>9</sup> **SBV** all undergo rapid and reversible pericyclic rearrangements, allowing their atomic skeletons to reconfigure dynamically without breaking apart. Some of these shapeshifting compounds are bistable, switching between two states such as barbaralane **BB**. Bullvalene **BV** can fluctuate between hundreds of thousands of conformational isomers (1, 209 600 isomers). Each of its methine vertices trades places (Fig 3.2a) with every other methine group through a series of Cope rearrangements, leading to  $10!/3$  discrete structural permutations. Functionalised derivatives of the fluxional cages take on rather unusual ‘shapeshifting’ properties, by substituting (Figure 3.2b) one or more of the hydrogen atoms of the parent structure with another group, the degeneracy of the system is reduced. The dynamic pericyclic rearrangements cause (Figure 3.2c) the relative positions and orientations of any appended functional groups to switch back and forth, producing distinct molecular shapes. These shapeshifting molecules, therefore, exist as fluxional mixtures that can be considered as self-contained dynamic structural libraries.

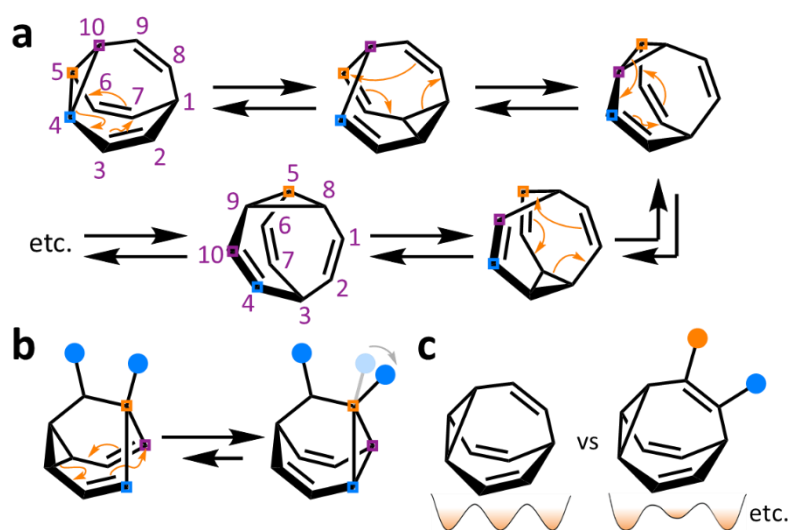


**Figure 3.2.** (a) **BV** and five of its valence isomers accessed through Cope rearrangements, where coloured squares and numbers show the movement of the cyclopropane carbon atoms from the initial structure. (b) A substituted barbaralane and its Cope rearrangement demonstrating dynamic constitutional isomerism, where coloured squares illustrate carbon atoms remaining in the same sequence in space. Blue and orange circles represent different functional groups. (c) Comparison of **BV** and a functionalised derivative, which can isomerise between nondegenerate regioisomers. A schematic representation illustrates changes in the degeneracy of the potential energy surfaces.

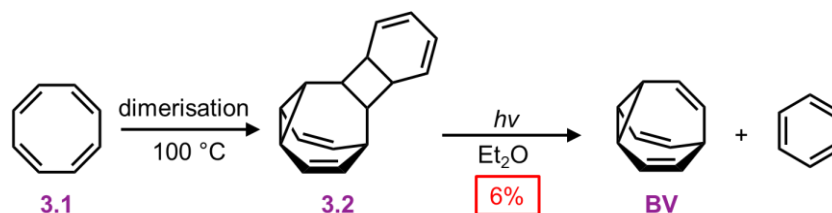
### 3.3 Dynamic Pericyclic Rearrangements

Reversible pericyclic processes underpin the constitutional dynamics of fluxional carbon cages. Neutral, closed-shell species such as **BV**, **BB**, **BVO**, **BBO**, **SBV** and their derivatives undergo strain-assisted Cope rearrangements – [3,3]-sigmatropic rearrangements whereby a  $\sigma$ -bond of the cyclopropyl group, flanked on two sides by vinyl  $\pi$ -electron systems, migrates (Figure 3.2a) along the  $\pi$ -system with a concerted redistribution of the two  $\pi$ -bonds. **BB**, **BVO**, **BBO** and **SBV** each possess just two olefin ‘arms’ connected to their cyclopropane ring. Consequently, there is only ever one pathway for a Cope rearrangement to follow, which reorganises the bonding electrons but does not change (Scheme 2.2b) the sequence of methine groups in three dimensional space. **BB**, **BVO**, **BBO**, **SBV** and their derivatives, therefore, fluctuate between just two isomers. The activation energies for the Cope rearrangements of **BV**, **BB**, **BVO**, **BBO**, and **SBV** are atypically low ( $\sim 30\text{--}50\text{ kJ mol}^{-1}$ ) when compared to Cope rearrangements of acyclic systems ( $\sim 150\text{ kJ mol}^{-1}$ ).<sup>10</sup> These low activation energy barriers arise because of (1) the ring strain of the cyclopropyl groups, which destabilises the ground states, and (2) the boat-like conformations enforced by the tricyclic systems, which resemble the transition-state geometries.<sup>5a</sup> Overall, the low energy barriers associated with these rearrangements causes isomers to interconvert extremely rapidly. The constitutional dynamics of the fluxional cages occur at rates more commonly associated with conformational dynamics, e.g., a cyclohexane chair flip proceeds with an energy barrier of  $45\text{ kJ mol}^{-1}$ .<sup>4</sup> Generally, when observed at room temperature by  $^1\text{H}$  NMR spectroscopy, the rapid interconversion of constitutional isomers results in exchanging nuclei appearing equivalent. For example, at room temperature the  $^1\text{H}$  NMR spectrum of **BV** exhibits just one broad proton resonance, which becomes a single sharp signal at higher temperatures.<sup>11</sup> The chemical shift of the resonance is a weighted average of the four distinct proton environments present in **BV**.

### 3.4 Syntheses of Bullvalene

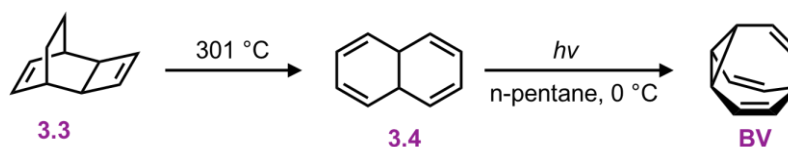
Due to **BV** having a large number of possible isomers, **BV** derivatives give access to complex dynamic mixtures. The structure and fluxional properties of **BV** were predicted in 1963 by von Doering.<sup>5a</sup> But, before the dynamics could be explored, new synthetic methods were required to prepare **BV**. Schröder reported the first synthesis

of **BV** (Scheme 3.1) occurred inadvertently during an investigation of the dimerisation of cyclooctatetraene.<sup>5c</sup> Dimerisation of **3.1** followed by photolysis of the dimer (**3.2**) yields a mixture of benzene and **BV** with a yield of 6%.



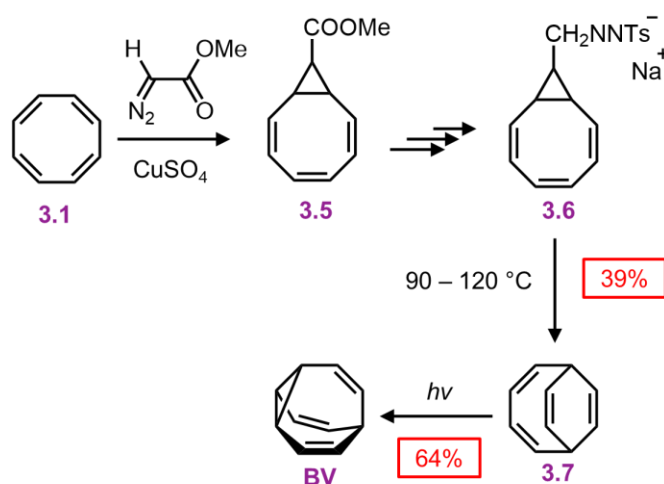
**Scheme 3.1.** first synthesis of **BV** as reported by Gerhard Schröder.

Doering et al. utilised photochemical transformations of an alicyclic precursor in developing methodology towards the synthesis of **BV** (Scheme 3.2).<sup>12</sup> Doering prepared **BV** via the partial thermal decomposition of Nenitzescu's hydrocarbon **3.3** followed by UV irradiation of **3.4** to obtain **BV**. However, this synthetic route is hindered by difficult-to-isolate **BV** due to the production of many side products including naphthalene during the photochemical conversion.



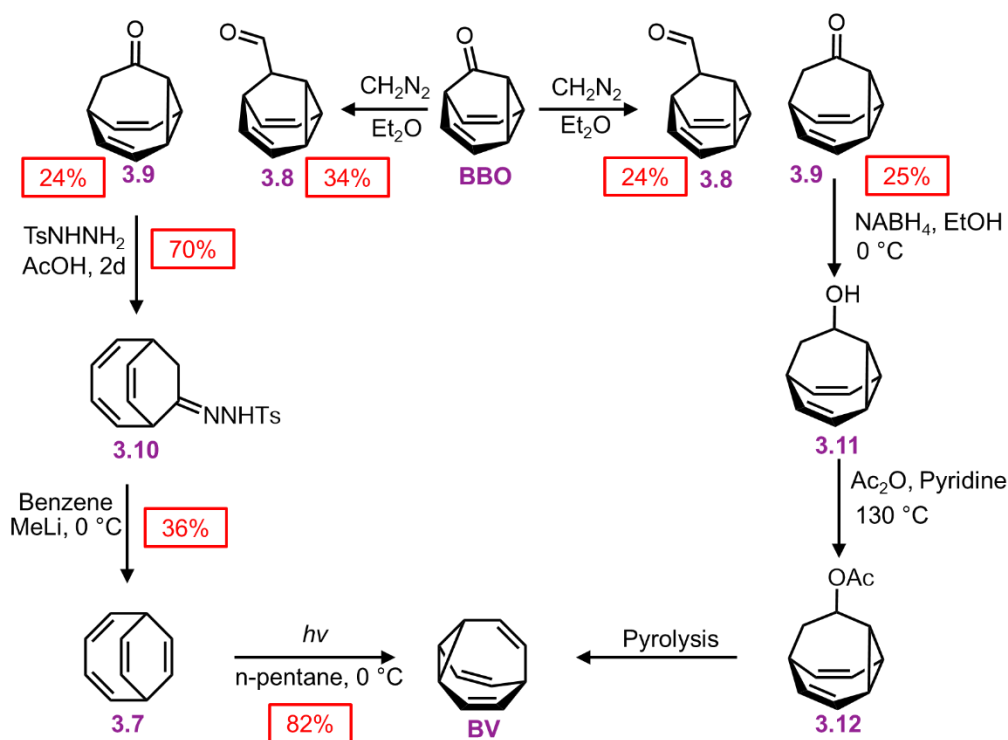
**Scheme 3.2.** photochemical transformations of an alicyclic precursor to form **BV** reported by von Doering.

Following Doering et al. photochemical synthesis of **BV**, Scott et al. further developed photochemical synthesis of **BV** via the irradiation of (2Z,4Z)-bicyclo[4.2.2]deca-2,4,7,9-tetraene (**3.7**, **BDT**).<sup>13</sup> Discovery of the photorearrangement of **2.7** to **BV** has been a dominant strategy to form **BV** which will be discussed further. Unfortunately, this method to produce **3.7** was challenging due long synthesis and the partial thermal decomposition of **3.6** to form **3.7** which generate a large amount of side products.



**Scheme 3.3.** Synthetic route to **BV** via the photoirradiation of BDT (**3.7**), reported by Jones and Scott.

Serrotosa et al.<sup>14</sup> and Doering et al.<sup>8</sup> subsequently reported synthetic routes to make **BV** from the sequential transformation of **BBO** (Scheme 3.4). Both routes proceed by initially treating **BBO** with diazomethane to induce a ring expansion of **BBO** to yield a mixture of **BVO** and the isomeric aldehyde **3.9**. Doering et al reduced the ketone functionality of **3.8** followed by acylation protection. **BV** was afforded by a final pyrolysis step conducted at high temperatures. Serrotosa's group et al. treated **3.9** with *p*-toluenesulfonyl hydrazide to yield tosylhydrazone **3.10**. Anionic fragmentation of **3.10** was induced using excess methyl lithium to give BDT **3.7**. The irradiation method reported by Scott et al. was then employed to yield **BV** **3.7**. Serrotosa's method involves nine steps in total and returns a yield of 2% in all.



**Scheme 3.4.** Synthetic route to **BV** including the photoirradiation of **BDT 2.7**, reported by Serratosa and Doering.<sup>8,14</sup>

### 3.4.1 Recent Advances in Bullvalene Synthesis and Analysis

Metal-catalysed cyclisation approaches have recently expanded the scope of easily accessible **BV** derivatives. Cycloadditions are one important class of reactions which can be TM-mediated. [6+2] cycloadditions of  $6\pi$  substrates such as cyclooctatetraene (COTT) allow access to a range of eight membered carbo and heterocyclic systems and are essential to recent **BV** syntheses.

Buono's group reported the first cobalt(I)-catalysed [6+2] cycloaddition of cycloheptatriene with various mono-substituted alkynes.<sup>15</sup> During screening of catalytic systems, the highest yields were observed using  $\text{CoI}_2(\text{dppe})$  as the catalyst, zinc metal as a reducing agent, zinc iodide as a Lewis acid and 1,2-dichloroethane as the solvent. This system proved to have high functional group tolerance for terminally substituted alkynes. Subsequent work by Buono's group employed the same conditions and alkynes. Subsequent work by Buono's group employed the same conditions and showed that a similar cycloaddition, of COTT with terminal alkynes, yields monosubstituted **BDTs** in fair to good yields (56-94%) (Figure 3.3).<sup>16</sup> Again, the reaction conditions showed good functional group tolerance. The [6 + 2] cycloaddition was also successful

as a reducing agent, zinc iodide as a Lewis acid and 1,2-dichloroethane as the solvent. when COTT was reacted with certain symmetrical di-substituted alkynes such as 2-butyne-1,4-diol.

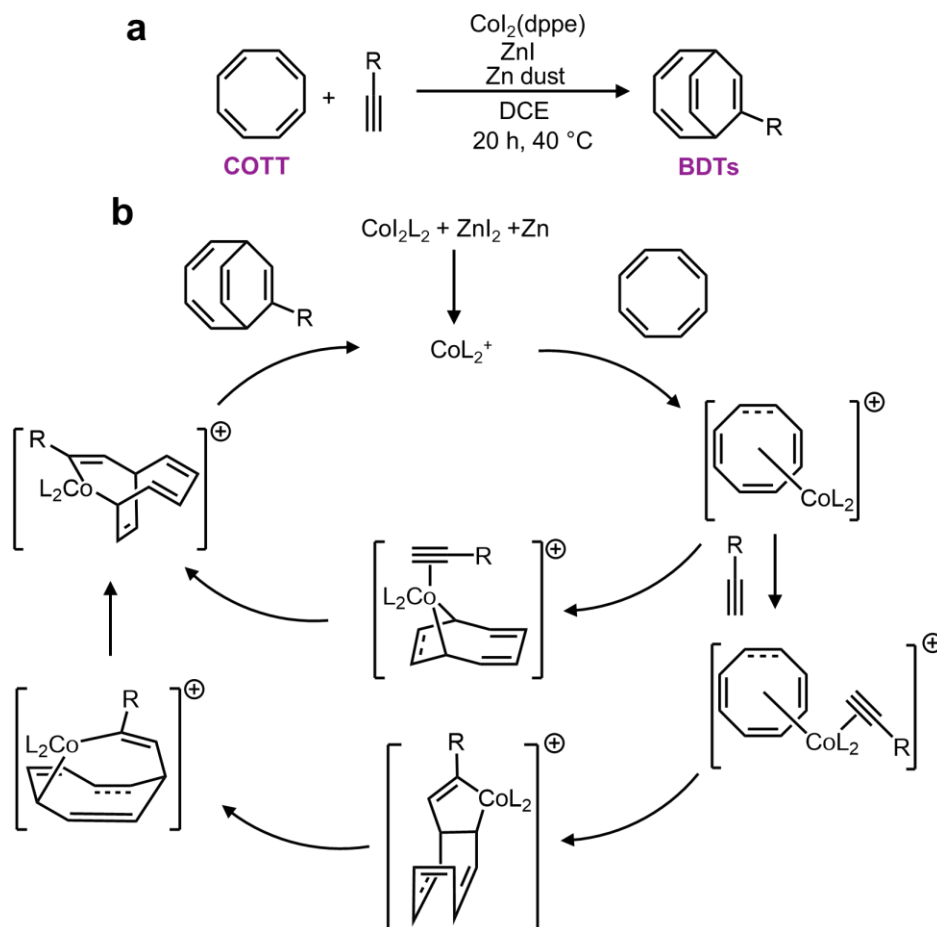
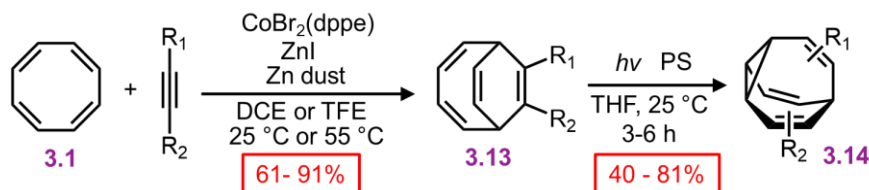


**Figure 3.3.** a) Synthetic route to monosubstituted **BDTs** by a cobalt-catalysed [6+2] cycloaddition as reported by Buono et al.<sup>15</sup> b) Two possible catalytic pathways proposed by the Buono group for the cycloaddition of COTT with terminally substituted alkynes.

Fallon's protocol converts (Scheme 3.5) cyclooctatetraene into **BV**, or a range of mono- and disubstituted analogues, through a two-step procedure in overall yields of 28–70%.<sup>17</sup> In the first step, bicyclo[4.2.2]deca-2,4,7,9-tetraene (**BDT**) intermediates **3.13** are prepared by [6 + 2] cycloaddition of cyclooctatetraene with alkynes in the presence of a  $\text{CoX}_2(\text{dppe})/\text{ZnI}_2/\text{Zn}$  catalyst system. In the second step, **3.13** undergoes a di- $\pi$ -methane photoisomerisation under UV irradiation to give the BV derivative **3.14**. This method was used by the group<sup>17,18</sup> to provide access to various monosubstituted **BVs**, including methyl **BV**, benzyl **BV** and hydroxymethylene **BV**, as well as the disubstituted **BVs**, bis(methylene-hydroxy)bullvalene and methyl(n-pentyl)bullvalene.

Fallon reported the successful application of this protocol to prepare trisubstituted BV derivatives. Trisubstituted analogues of BV are prepared in overall yields of 24–50% using trimethylsilylcyclooctatetraene in place of cyclooctatetraene.<sup>17,18</sup>



**Scheme 3.5.** Most practical and concise synthesis of bullvalene and a variety of mono- and di substituted analogues as reported by Fallon and co-workers.<sup>17,18</sup>

### 3.5 Bullvalene's Dynamic Behaviour

Bode developed an isomer coding system for the network analysis of **BV** derivatives and their substitution patterns.<sup>19</sup> A ten-digit code is assigned to each possible isomer, where each digit represents (Fig. 3.4) a position of the **BV** core and the number designates the type of substituent (e.g., using 0 for hydrogen, etc.). The barcode is read left to right and portioned in to three blocks of three digits followed by a final singular digit. The three blocks of three digits represent the carbon atoms of the vinyl bridges and the final singular digit the bridgehead carbon. Bode notes several advantages which this barcode system enables, including the two-way identification of **BVs** and ability to distinguish between enantiomers.

Fallon et al. built upon this isomer coding system for the network analysis of **BV** derivatives by developing an algorithm that integrates it with quantum-chemical energy calculations.<sup>17,20</sup> The algorithm generates all the possible BV structures in the dynamic network, identifying enantiomeric pairs and interconnections (i.e., transition states<sup>10</sup>) between isomers. The geometry of each isomer is then optimised, and their single-point energies are calculated through the ORCA 4.0 programme package,<sup>21</sup> forecasting the equilibrium distribution of isomers. Comparison (Fig. 3.4) of the experimental isomer ratios for mono-, di- and trisubstituted BV derivatives (determined by low-temperature NMR) with the modelled ratios illustrated the method's potential to function as a predictive tool.

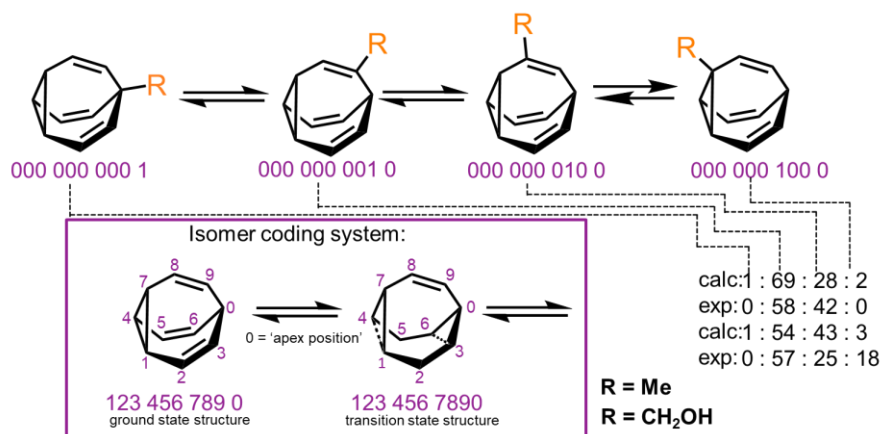


**Figure 3.4.** An isomer coding system for network analysis and the computationally predicted isomeric ratios for three monosubstituted BV derivatives.<sup>17,20</sup>

The Bode group have used tetrasubstituted BVs as adaptive sensors. In an initial design (**3.15**), shown in Figure 3.5, porphyrin substituents were included to enable  $\pi$ – $\pi$  interactions with C<sub>60</sub> and C<sub>70</sub> guest molecules.<sup>22</sup> The addition of analytes leads the isomer populations of **3.15** converge towards those with supramolecular structures which have the lowest free energy and give the strongest binding; this equilibrium shift is represented in Figure 3.15. In subsequent work, the group utilised a bis-boronic acid functionalised **BV** for the chemical sensing of polyols.<sup>23</sup> Incorporation of a <sup>13</sup>C label into the **BV** backbone allows the changes in equilibrium populations of the different isomers to be evaluated by a single <sup>13</sup>C NMR experiment.

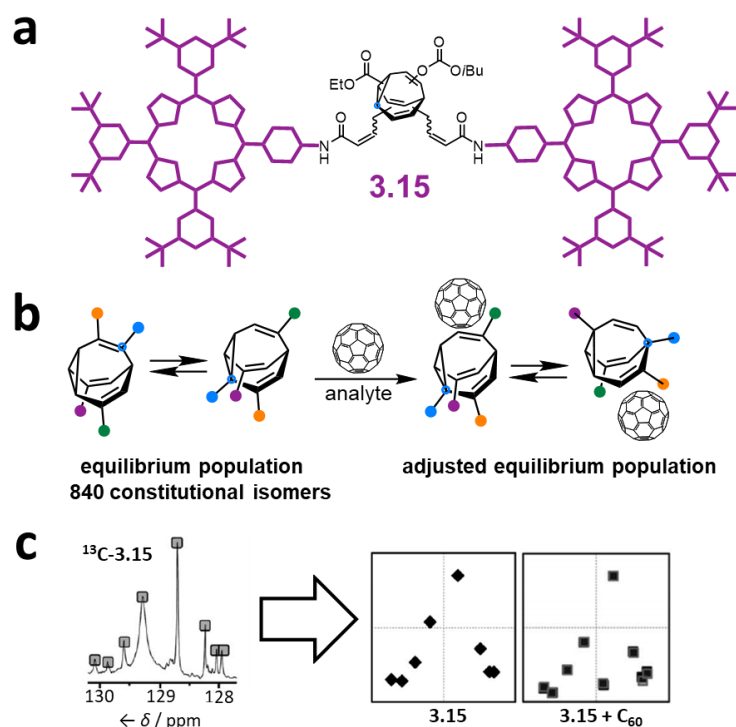


**Figure 3.5.** (a) Bode's bisporphyrin-bullvalene **3.15**, which was prepared with natural isotopic abundance, enriched in <sup>13</sup>C at one position of the dynamic C core, and functionalised with a photocleavable group. (b) The equilibrium distribution of isomers of shapeshifting molecules **3.15** are perturbed upon addition of a guest (illustrated with C<sub>60</sub>), favouring structures that form the most stable supramolecular complexes. Coloured dots represent pendant groups connected to the BV cores (c) The complex <sup>13</sup>C NMR spectra of the dynamic mixtures are converted to simplified representations, showing that the <sup>13</sup>C NMR spectrum of a mixture at equilibrium changes in the presence of fullerene guests.<sup>22,23</sup>

Recently, the Fallon group incorporated BV into the core of a bis-monodentate ligand (**3.16**) (Figure 3.6) which self assembles with Pt<sup>2+</sup> and Pd<sup>2+</sup>.<sup>24</sup> The system self assembles to a M<sub>2</sub>L<sub>4</sub> architecture in which the shape-shifting complexity of the bis-3-pyridyl BV ligands (**3.16**) is maintained. VT NMR experiments revealed that the free ligand exists in dynamic equilibrium of three principal constitutional isomers: **3.16a**, **3.16b** and **3.16c** (from a total of 15 possible isomers). The three principal constitutional isomers are capable of interconverting via a low energy circuit, shown in Figure 3.6, which includes only one other intermediate isomer, **3.16d**.

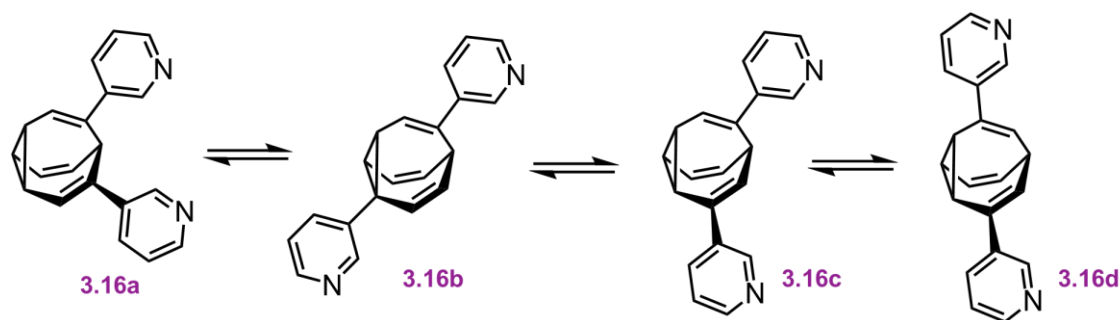


**Figure 3.4.** Low energy interconversion pathway of the three principal constitutional isomers (*a*, *c* and *d* of free ligand **3.16** which includes a fourth intermediate isomer (*b*).<sup>24</sup>

Inclusion of four BV ligands in a  $M_2L_4$  cage gives potential for extensive complexity; indeed,  $^{19}\text{F}$  NMR reveals that  $M_2L_4 \cdot \text{BF}_4^-$  is a complex mixture with  $\text{BF}_4^-$  encapsulated by various isomers of  $M_2L_4$ . However, upon exchange of the encapsulated  $\text{BF}_4^-$  anion with  $\text{Cl}^-$  or  $\text{I}^-$ , the  $^1\text{H}$  NMR solution state spectrum is significantly resolved to reveal one dominant cage species which only contains **3.16c**, the *cccc* cage (**3.17**). This convergence is shown in Figure 3.7. At room temperature, the  $^1\text{H}$  NMR spectra of **3.17** contain the broad peaks characteristic of BV thus indicating that a degree of dynamic activity is retained in the complex.

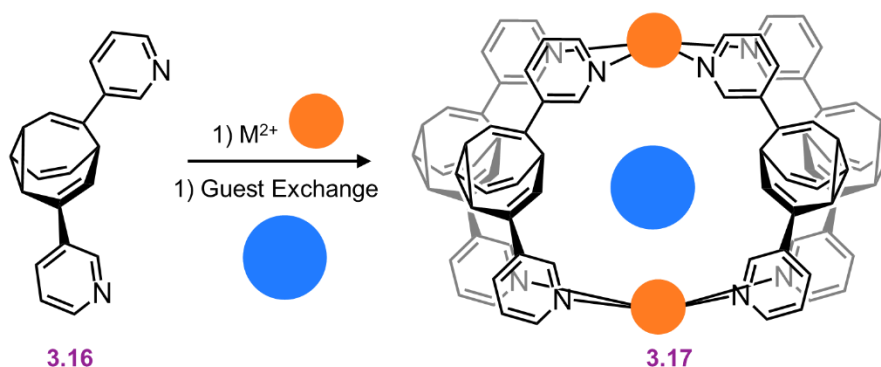


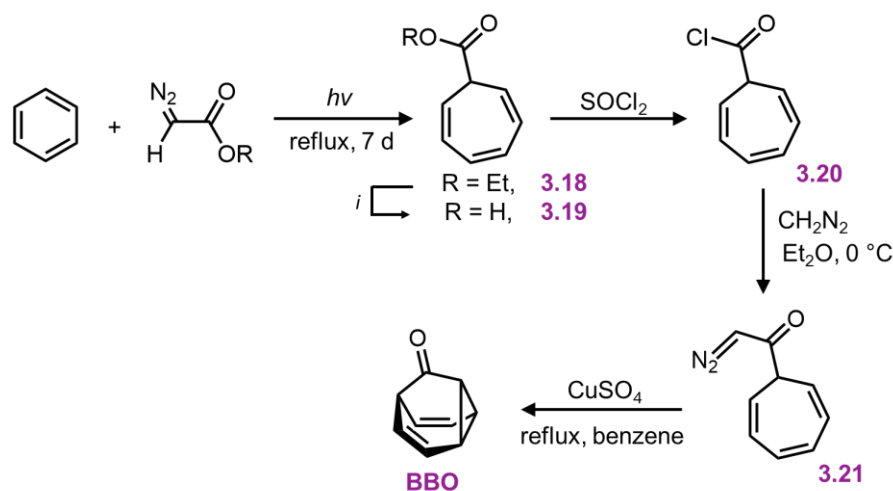
**Figure 3.7.** Metal mediated self-assembly of **3.16** to form a fluxional cage architecture ( $M^{2+} = \text{Pt}^{2+}$  or  $\text{Pd}^{2+}$ ). Guest exchange with  $\text{Cl}^-$  or  $\text{I}^-$  restricts fluxionality, causing convergence of the ligands to their **3.16c** form and formation of the *cccc* cage, **3.17**.<sup>24</sup>

*VOIDOO* calculations indicated that  $\text{Cl}^-$  and  $\text{I}^-$  give significantly decreased packing coefficients with **3.17** compared to  $\text{BF}_4^-$ . Thus, it is suggested that optimisation of host-guest interactions drives convergence of the cage ligands (**3.17c**) towards **3.16c**. DFT calculations were used to elucidate the energetically viable pathways of interconversion away from the *cccc* cage. Figure 3.6 shows that conversion from **3.16d** to **3.16a** involves transit through **3.16b**. In the cage structure, this involves a contraction of the Pd-Pd bond distance and an energy increase. Isomerisation to the *aaaa* cage involves a

Pd–Pd bond contraction to the extent that the anions studied ( $\text{Cl}^-$ ,  $\text{BF}_4^-$  and  $\text{I}^-$ ) could no longer be accommodated in the cavity. Thus, it was concluded that the cage ligands rapidly interconvert through a closed **3.16c** to **3.16d** to **3.16c** pathway. The nitrogen–nitrogen distances of the ligands are effectively fixed to allow inclusion of the guest anion within the cage, **3.17**. This acts as a geometric constraint on the ligands and inhibits access to certain BV isomers.

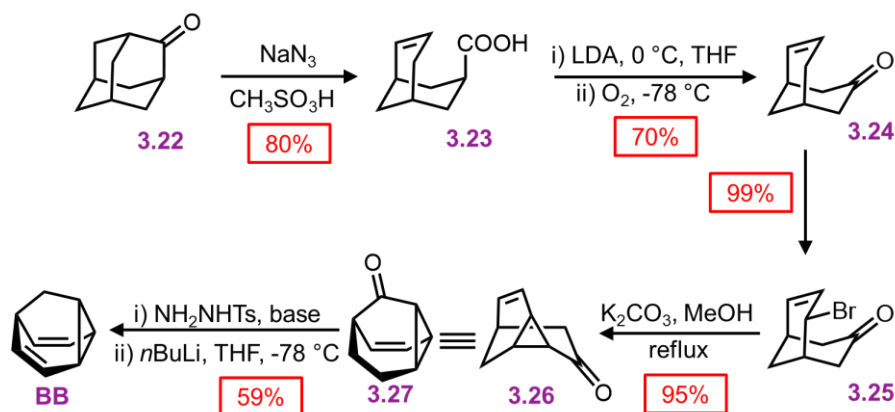
### 3.6 Barbaralane

The relative simplicity of bistable **BB** systems makes them attractive targets for developing a quantitative understanding of shapeshifting equilibria. **BBO** was first prepared as part of von Doering's investigations into thermal rearrangements that led to the **BV** structure being proposed.<sup>25</sup> The main strategy of this synthetic route to employ an intramolecular [2 + 1] cycloaddition of a carbene to a cycloheptatriene to form the tricyclic **BB** core (Scheme 3.1). Subsequently, methods have been developed that avoid the low-yielding cyclisation of a carbenoid intermediate.



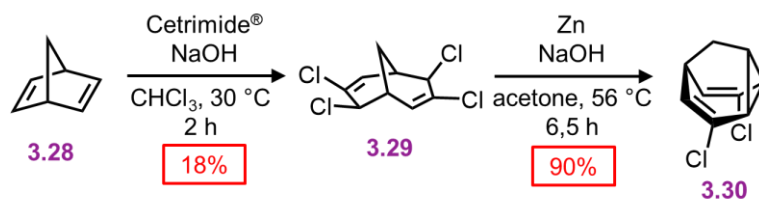
**Scheme 3.6.** Synthesis of barbaralane (**BBO**) by Doering and Roth. i) acidic conditions.

Henkel et al. reported a five-step synthesis of **BB** from 2-adamantanone (**3.22**) (Scheme 3.7) in an overall yield of 42%, proceeding by fragmentation of the adamantane system followed by a transannular ring closure.<sup>26</sup> Jefford et al. developed efficient syntheses of substituted **BB** derivatives have been developed that employ norbornadiene (**3.28**)<sup>27</sup> (Scheme 3.8) as starting materials using ring expansion followed by reductive cyclisation of a bicyclic precursor.

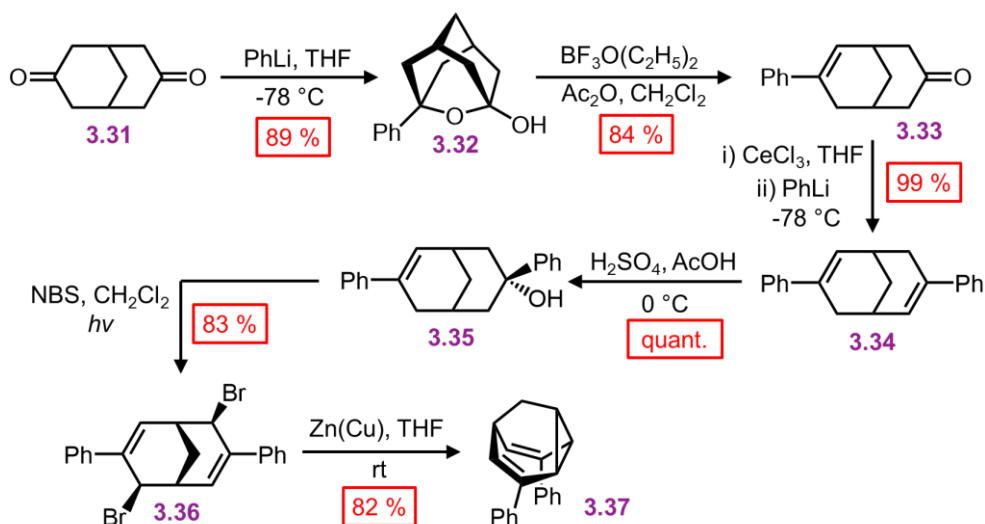


**Scheme 3.7.** Stepwise synthetic procedure of barbaralane from 2-adamantanone as demonstrated by Henkel and co-workers.

Quast and co-workers developed a synthetic procedure towards a series of 3,7-substituted barbaralanes with varying functionality starting from with 3,7-bicyclo[3.3.1]nonanedione (**3.31**) (Scheme 3.9) overall yield for this synthesis is 50% utilising by reductive cyclisation of a bicyclic precursor.<sup>28,29</sup> Quast et al.<sup>29a</sup> quantified the equilibria and rearrangements rates for disubstituted **BB** derivatives,<sup>29c</sup> demonstrating that judicious functionalisation of the vinyl groups with electron-donating or electron-withdrawing substituents tunes the barrier to Cope rearrangement over a wide range  $< 17.2\text{--}44.9\text{ kJ mol}^{-1}$ .



**Scheme 3.8.** Dihalogenated **BB** synthesis from norbornadiene.

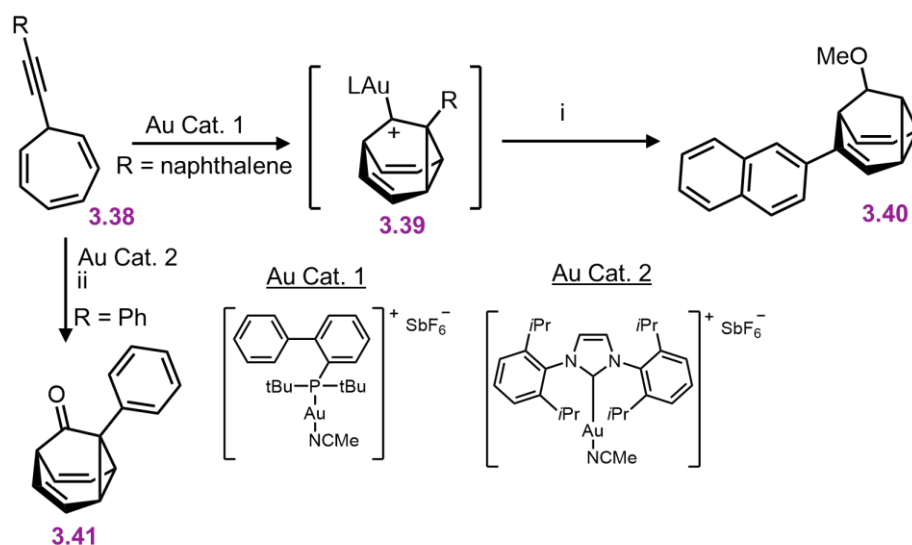


**Scheme 3.9.** Stepwise procedure to synthesise 3,7-phenylbarbaralane (**3.37**) as reported by Quast and co-workers.<sup>28,29</sup>

### 3.6.1 Recent Advances in Barbaralane Synthesis

The most recent and concise syntheses of **BB** derivatives have been reported by Echavarren et al.,<sup>30</sup> exploiting (Scheme 3.10) the ability of gold catalysts to activate enynes towards cycloisomerisation. Gold complexes promote a wide variety of enyne cyclisations under mild conditions while exerting exquisite control over competitive reaction pathways, oxygen stabilising intermediates with carbenoid character.<sup>31</sup> Alkynyl cycloheptatrienes **3.38** are first prepared by nucleophilic addition of an acetylide to the commercially available reagent<sup>32</sup> tropylium tetrafluoroborate. Activated ( $\eta^2$ -alkynyl)gold(I) complexes, formed from **3.38** in the presence of gold catalysts, cycloisomerise to gold stabilised fluxional barbaralyl cations **3.39**. In the absence of nucleophiles, these reactive intermediates transform irreversibly to indenenes. The **BB** framework can be trapped, however, if the barbaralyl cation **3.39** is intercepted by a nucleophile. By carrying out the cycloisomerisation using methanol as a cosolvent, Echavarren demonstrated that a barbaralane methyl ether **3.40** can be isolated (Scheme 3.10) as the major product, alongside a small amount of indenyl by-products. This short two-step pathway gives access to disubstituted **BB** derivatives in which one substituent has been introduced as part of the acetylide and the other is controlled through the choice of nucleophile. In 2016, Echavarren reported that **BBO** products functionalised at the 1-position, **3.41**, are formed selectively (Scheme 3.10) by including an oxidant in the reaction mixture. The optimised conditions employ diphenyl sulfoxide as oxidant in combination with a gold(I) catalyst bearing a N-heterocyclic carbene ancillary

ligand, [IPrAu(MeCN)][SbF<sub>6</sub>]. Two mechanisms have been proposed for the transformation. Either the oxidant reacts with the previously observed intermediate **3.39**, or the gold catalyst mediates oxidation of the alkyne to afford an  $\alpha$ -oxo gold(I) carbene intermediate, which then undergoes intramolecular cyclopropanation to produce **3.41**. The method was shown to be compatible with a series of alkynyl derivatives **3.38**, tolerating alkyl groups and electron-rich or electron-poor aromatic substituents bearing ortho-, meta- or para-groups. The isolated yields reported range from 45–97%. This synthesis of **BBO** derivatives is the shortest to date and provides straightforward access to substituted bistable fluxional carbon cages.



**Scheme 3.10.** Gold-catalysed transformation of alkynyl cycloheptatrienes **3.38** into a barbaralyl methyl ether **3.40** or barbaralones **3.41**. Reagents and conditions: (i) **3.38**, R = 2-naphthyl, Au Cat. 1 = [JohnPhosAu(MeCN)][SbF<sub>6</sub>] (5 mol%), CH<sub>2</sub>Cl<sub>2</sub>–MeOH (1:1), rt, 2 h, 40%; (ii) **3.38**, Au Cat. 2 = [IPrAu(MeCN)][SbF<sub>6</sub>] (5 mol%), Ph<sub>2</sub>SO, CH<sub>2</sub>Cl<sub>2</sub>, 1.5–12 h, rt, 35–97%. L = ancillary ligand, JohnPhos = (2-biphenyl)di-tert-butylphosphine, IPr = 1,3-bis(2,6-diisopropylphenyl)imidazol-2-ylidene.

### 3.7 Adaptation of simple nondegenerate mixtures

Investigations during the 1980s and 1990s showed that the dynamics of some shapeshifting molecules are suppressed<sup>33</sup> in the crystal state, while others remain<sup>34</sup> highly fluxional. Generally, the compounds that remain dynamic have globular structures, e.g., **BV**<sup>34d</sup> and some of its monohalogenated<sup>34e-g</sup> derivatives. In these cases, the Cope rearrangements are not associated with a significant change in the three-dimensional shape of the molecules, so the rearrangements can occur within the restricted environment of a crystal lattice. Less regularly shaped compounds, however, such as substituted **BB** derivatives, appear to be frozen in the solid state.<sup>33c</sup> Their

valence isomerism leads (Fig. 3.2c) to a significant shape change that is mismatched with the restricted environment of the crystal lattice.

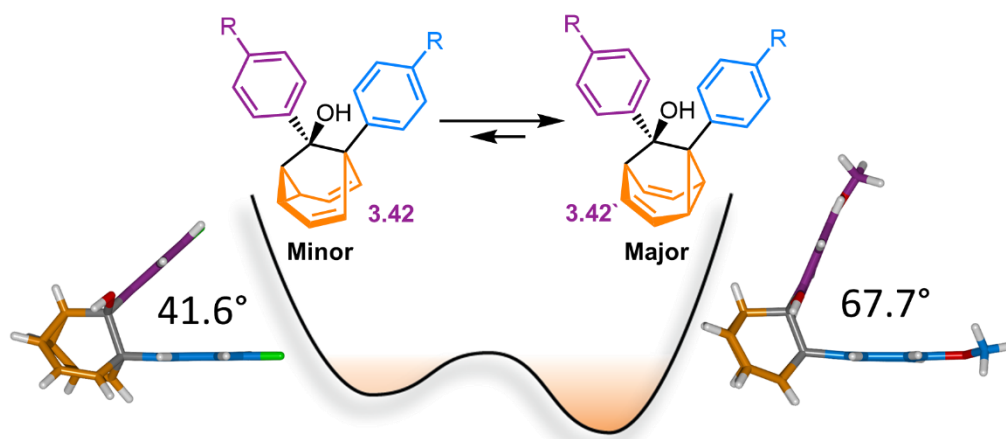


**Figure 3.8.** McGonigal reported a series of disubstituted BB derivatives, **3.42/3.42'**, that crystallise in a manner controlled by their shapes, preferring valence isomers that pack effectively in a crystal lattice.<sup>35</sup> In each case, the same isomer **3.42** is present as the major species in solution, but small changes in the aromatic substituent, R, favour different solid-state structures. In some cases, the minor solution-state valence isomer is the one observed in the solid state.

Recently, McGonigal has taken advantage of this phenomenon to quantitatively analyse the adaptation of simple nondegenerate **BB** mixtures upon changes (Fig. 3.8) in their environment.<sup>35</sup> The investigation started by preparing a series of **BB** derivatives that are bistable, fluctuating between structures **3.42** and **3.42'**. Precursors **3.42** were synthesised (Scheme 2.5) according to the gold catalysis method described above, before aryl Grignard reagents were added to afford **3.42/3.42'**. Each compound in the series possesses a tertiary alcohol and aromatic groups at the 1- and 9-positions. The aromatic groups were varied between *p*-anisyl, *p*-fluoro-phenyl and phenyl across the series. NMR analyses confirmed that these **BB** derivatives interconvert between two constitutional isomers, **3.42/3.42'**, in solution. Isomer **3.42** is the preferred solution-state isomer in every case and relatively small Gibbs free energy differences between isomers of  $\sim 3\text{--}5\text{ kJ mol}^{-1}$  were estimated based on low temperature NMR data and DFT calculations, suggesting that the positions of the **BB** equilibria would be sensitive to changes in the surrounding medium. Indeed, upon transitioning from solution to the solid state, the five compounds are no longer isostructural.

Three of the five **BB** derivatives were found (Fig. 3.8) to have the same constitution as their major solution-phase isomer **3.42** while two were found to take up the structure of the minor solution-phase isomer **3.42'**. In each case, only one of the two possible valence isomers was observed in the solid state. Variable-temperature X-ray analysis showed that the fluxional dynamics were suppressed. The simplicity of this bistable system and the relative lack of conformational freedom present in the substrates made it possible to analyse the reasons behind this behaviour in detail. Hirshfeld surfaces of each crystal structure were modelled and the interaction energies between neighbouring molecules in the crystals were calculated. The calculations revealed that, despite the presence of an alcohol group and mildly polarised aromatic rings, the crystal packing is not dictated by any significant and specific noncovalent bonding interactions. Instead, van der Waals interactions constitute the dominant contacts. Since the relatively small energy differences between valence isomers can be outweighed by differences in lattice enthalpies, it becomes possible for the preference for the shape of **3.42** or **3.42'** to bias crystallisation. Isomerisation is associated (Fig. 3.8) with changes in the dihedral angles between the aromatic groups, altering the crystal packing motif. Ultimately, these insights confirm the idea that finely balanced shapeshifting equilibria can adapt in response to changes in supramolecular self-assembly and the molecules' interactions with their surrounding medium. By gaining understanding of the dynamics, equilibria and energetics of bistable shapeshifting molecules, it will be possible to better rationalise and predict the adaptation of shapeshifting systems with more permutations operating in more complex environments.

Recent advance in synthetic methodology<sup>7,8</sup> towards these shapeshifting compounds in combination with computational calculations<sup>10</sup> have allowed for easier access to investigate the application of these dynamic fluxional systems as scaffolds for sensing molecules for structural complex analytes,<sup>30</sup> exploring complex biological systems and create novel functional materials. However, a major issue hindering the application of these shapeshifting molecules is their structural complexity. This complexity presents challenges for designing their syntheses and understanding their equilibria.

## 3.8 References

- 1 A. N. Bismillah, B. M. Chapin, B. A. Hussein, and P. R. McGonigal, *Chem. Sci.* 2020, **11**, 324–332.
- 2 A. F. Cotton, *Acc. Chem. Res.* 1968, **1**, 257–265.
- 3 M. L. McKee, M.L. *WIREs Comput. Mol. Sci.*, 2011, **1**, 943–951.
- 4 K. Nikitin, and R. O'Gara, *Chem. Eur. J.* 2019, **25**, 4551.
- 5 (a) W. v. E. Doering and W. R. Roth, *Tetrahedron*, 1963, **19**, 715; (b) G. Schroder, *Angew. Chem. Int. Ed.*, 1963, **2**, 481; (c) R. Merenyi, J. F. M. Oth and G. Schroder, *Chem. Ber.*, 1964, **97**, 3150; (d) A. Adult, *J. Chem. Educ.*, 2001, **78**, 924; (e) S. Ferrer and A. M. Echavarren, *Synthesis*, 2019, **51**, 1037.
- 6 (a) P. Ahlberg, D. L. Harris and S. Winstein, *J. Am. Chem. Soc.*, 1970, **92**, 4454; (b) D. Cremer, P. Svensson, E. Kraka and P. Ahlberg, *J. Am. Chem. Soc.*, 1993, **115**, 7445; (c) P. Ahlberg, J. B. Grutzner, D. L. Harris and S. Winstein, *J. Am. Chem. Soc.*, 1970, **92**, 3478; (d) J. B. Grutzner and S. Winstein, *J. Am. Chem. Soc.*, 1970, **92**, 3186.
- 7 (a) L. G. Greifenstein, J. B. Lambert, M. J. Broadhurst and L. A. Paquette, *J. Org. Chem.*, 1973, **38**, 1210; (b) G. G. Cristoph, S. Hardwick, U. Jacobsson, Y.-B. Koh, R. Moerck and L. A. Paquette, *Tetrahedron Lett.*, 1977, **14**, 1249; (c) C. Engdahl and P. Ahlberg, *J. Am. Chem. Soc.*, 1979, **101**, 3940.
- 8 W. v. E. Doering, B. M. Ferrier, E. T. Fossel, J. H. Hatenstein, M. Jones, G. Klumpp, R. M. Rubin and M. Saunders, *Tetrahedron*, 1967, **23**, 3943.
- 9 (a) H. E. Zimmerman and G. L. Grunewald, *J. Am. Chem. Soc.*, 1966, **88**, 183; (b) S. Zhang, W.-X. Zhang and Z. Xi, *Acc. Chem. Res.*, 2015, **48**, 1823.
- 10 R. Hoffmann and W.D. Stohrer, *J. Am. Chem. Soc.*, 1971, **93**, 6941.
- 11 J. F. M. Oth, K. Müllen, J. M. Gilles and G. Schröder, *Helv. Chim. Acta*, 1974, **57**, 1415.
- 12 W. v. E. Doering and J. W. Rosenthal, *J. Am. Chem. Soc.*, 1966, **88**, 2078.
- 13 M. Jones and L. T. Scott, *J. Am. Chem. Soc.*, 1967, **89**, 150–151.
- 14 J. Casas and F. Serratos, *An. Quim.*, 1977, **73**, 300.
- 15 M. Achard, A. Tenaglia and G. Buono, *Org. Lett.*, 2005, **7**, 2353.
- 16 M. Achard, M. Mosrin, A. Tenaglia and G. Buono, *J. Org. Chem.*, 2006, **71**, 2907–2910.
- 17 O. Yahiaoui, L. F. Pašteka, B. Judeel and T. Fallon, *Angew. Chem. Int. Ed.*, 2018, **57**, 2570–2574.
- 18 H. D. Patel, T.-H. Tran, C. J. Sumby, L. F. Pašteka and T. Fallon, *J. Am. Chem. Soc.*, 2020, **142**, 3680–3685.
- 19 M. He and J. W. Bode, *Org. Biomol. Chem.*, 2013, **11**, 1306–1317.
- 20 O. Yahiaoui, L. F. Pašteka, C. J. Blake, C. G. Newton and T. Fallon, *Org. Lett.*, 2019, **21**, 9574.
- 21 F. Neese, *Wiley Interdiscip. Rev.: Comput. Mol. Sci.*, 2012, **2**, 73.
- 22 A. R. Lippert, V. L. Keleshian and J. W. Bode, *Org. Biomol. Chem.*, 2009, **7**, 1529.
- 23 J. F. Teichert, D. Mazunin and J. W. Bode, *J. Am. Chem. Soc.*, 2013, **135**, 11314.

- 24 A. P. Birvé, H. D. Patel, J. R. Price, W. M. Bloch and Thomas Fallon, *Angew. Chem. Int. Ed.*, 2022, **61**, e202115468.
- 25 W. v. E. Doering and W. R. Roth, *Angew. Chem. Int. Ed.*, 1963, **2**, 115.
- 26 J. G. Henkel and J. T. Hane, *J. Org. Chem.*, 1983, **48**, 3858.
- 27 C. W. Jefford, J.-C. Rossier and J. A. Zuber, *Angew Chem. Int. Ed.*, 1982, **21**, 549.
- 28 (a) J. M. Mellor, B. S. Pons and J. H. A. Stibbard, *J. Chem. Soc., Chem. Commun.*, 1979, 759; (b) R. Trinks and K. Mullen, *Chem. Ber.*, 1987, **120**, 1481.
- 29 (a) H. Quast, M. Witzel, E.-M. Peters, K. Peters and H. G. von Schnering, *Liebigs Ann. Chem.*, 1995, 725; (b) H. Quast, C. Becker, M. Witzel, E.-M. Peters, K. Peters and H. G. von Schnering, *Liebigs Ann. Chem.*, 1996, 985; (c) L. M. Jackman, E. Fernandes, M. Heubes and H. Quast, *Eur. J. Org. Chem.*, 1998, 2209; (d) A. C. Goren, D. A. Hrovat, M. Seefelder, H. Quast and W. T. Borden, *J. Am. Chem. Soc.*, 2002, **124**, 3469.
- 30 (a) P. R. McGonigal, C. de Leon, Y. Wang, A. Homs, C. R. Solorio-Alvarado and A. M. Echavarren, *Angew. Chem. Int. Ed.*, 2012, **51**, 13093; (b) S. Ferrer and A. M. Echavarren, *Angew. Chem. Int. Ed.*, 2016, **55**, 11178.
- 31 (a) L. Fensterbank and M. Malacria, *Acc. Chem. Res.*, 2014, **47**, 953; (b) J. Carreras, M. Livendahl, P. R. McGonigal and A. M. Echavarren, *Angew. Chem. Int. Ed.*, 2014, **53**, 4896; (c) R. Dorel and A. M. Echavarren, *Chem. Rev.*, 2015, **115**, 9028; (d) R. Dorel, P. R. McGonigal and A. M. Echavarren, *Angew. Chem. Int. Ed.*, 2016, **55**, 11120; (e) D. Pflasterer and A. S. K. Hashmi, *Chem. Soc. Rev.*, 2016, **45**, 1331.
- 32 (a) D. J. M. Lyons, R. D. Crocker, M. Blumel and T. V. Nguyen, *Angew. Chem. Int. Ed.*, 2017, **56**, 1466; (b) M. A. Hussein, V. T. Huynh, R. Hommelsheim, R. M. Koenigs and T. V. Nguyen, *Chem. Commun.*, 2018, **54**, 12970; (c) U. P. N. Tran, G. Oss, D. P. Pace, J. Ho and T. V. Nguyen, *Chem. Sci.*, 2018, **9**, 5145; (d) M. A. Hussein, U. P. N. Tran, V. T. Huynh, J. Ho, M. Bhadbhade, H. Mayr and T. V. Nguyen, *Angew. Chem. Int. Ed.*, 2020, **59**, 1455.
- 33 (a) R. D. Miller and C. S. Yannoni, *J. Am. Chem. Soc.*, 1980, **102**, 7396; (b) P. Luger and K. Roth, *J. Chem. Soc., Perkin Trans.*, 1989, 649; (c) W. W. Win, K. G. Grohmann and L. Todaro, *J. Org. Chem.*, 1994, **59**, 2803; (d) J. Siegwarth, J. Bornhoft, C. N'ather and R. Herges, *Org. Lett.*, 2009, **11**, 3450.
- 34 (a) V. Macho, R. D. Miller and C. S. Yannoni, *J. Am. Chem. Soc.*, 1983, **105**, 3735; (b) I. Sellner, H. Schuster, H. Sichert, J. Sauer and H. N'oth, *Chem. Ber.*, 1983, **116**, 3751; (c) L. M. Jackman, A. Benesi, A. Mayer, H. Quast, E. M. Peters, K. Peters and H. G. von Schnering, *J. Am. Chem. Soc.*, 1989, 111, 1512; (d) S. Schlick, Z. Luz, R. Poupko and H. Zimmermann, *J. Am. Chem. Soc.*, 1992, **114**, 4315; (e) K. Muller, H. Zimmermann, C. Krieger, R. Poupko and Z. Luz, *J. Am. Chem. Soc.*, 1996, **118**, 8006; (f) R. Poupko, K. Muller, C. Krieger, H. Zimmermann and Z. Luz, *J. Am. Chem. Soc.*, 1996, **118**, 8015; (g) Z. Luz, L. Olivier, R. Poupko, K. Muller, C. Krieger and H. Zimmermann, *J. Am. Chem. Soc.*, 1998, **120**, 5526; (h) R. V. Williams, V. R. Gadgil, P. Luger, T. Koritsanszky and M. Weber, *J. Org. Chem.*, 1999, **64**, 1180; (i) A. Benesi, R. Bertermann, H. Forster, M.

- Heubes, L. M. Jackman, T. Koritsanszky, P. Luger, A. Mayer, H. Quast, M. Seefelder and D. Zobel, *J. Am. Chem. Soc.*, 2000, **122**, 4455.
- 35 A. N. Bismillah, J. Sturala, B. M. Chapin, D. S. Yufit, P. Hodgkinson and P. R. McGonigal, *Chem. Sci.*, 2018, **9**, 8631.

# Chapter 4 | Covalent Control of Fluxional Carbon Cages

## 4.0 Synopsis

In this chapter, the control of fluxional carbon cage isomerisation in barbaralane and bullvalene was explored utilizing covalent auxiliaries. For barbaralane, studies were to understand the internal enantiomerization of fluxional carbon cages and the consequences of their adaptive configurations for the transmission of stereochemical information. The  $sp^3$ -carbon stereochemistry of the rigid tricyclic cages is inverted through strain-assisted Cope rearrangements. This dynamic enantiomerization can be stopped, restarted, or slowed by external reagents, while the configuration of the cage is controlled by neighbouring, fixed stereogenic centres. As part of a phosphoramidite–olefin ligand, the fluxional cage acts as a conduit to transmit stereochemical information from the ligand while also transferring its dynamic properties to chiral-at-metal coordination environments, influencing catalysis and ligand exchange energetics. For bullvalene, synthesis towards a phosphoramidite-olefin ligand and the pitfalls of this synthesis are discussed. We also explore the dynamics of rotamers versus constitutional isomerisation of sterically hindered carbamates bullvalene building blocks. Analysis of barbaralanes and bullvalenes presented in this chapter were carried out utilizing a variety of solution-state NMR, detailed solid-state analysis such, as single crystal X-ray diffraction, solid-state NMR, and DFT studies.

## Acknowledgement

Dr. Aisha Bismillah carried out variable-temperature NMR spectroscopy and synthesis for the barbaralane chemistry. Toby G. Johnson developed the synthesis for **4.4**, **4.10** and **4.10** and. Dr. Andrew Turley assisted the trapping and release of **4.6** by cycloaddition. Dr. Juan A. Aguilar. assisted with NMR measurements. Dr. Dmitry S. Yufit solved X-ray crystal structures. Dr. Paul R. McGonigal developed the chemistry towards the ligand **L<sub>BB</sub>** and metal complexes **L<sub>BB</sub>PdCl<sub>2</sub>** & **L<sub>BB</sub>RuCp(NCMe)·PF<sub>6</sub>**. Mary Kate Rylands helped developed the bullvalene chemistry and obtaining the single crystal of **4.23** for XRD.

## 4.1 Introduction

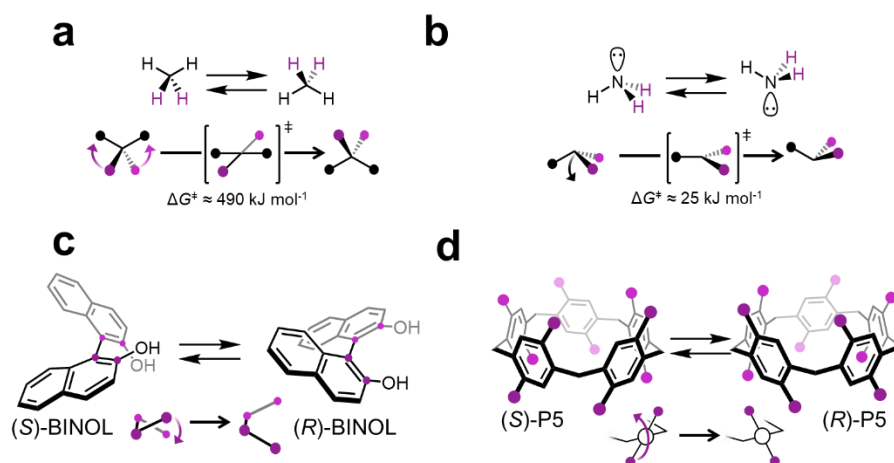


**Figure 4.1.** Dynamic stereochemical interconversion of different types of chirality. a) typical  $sp^3$ -carbon centres cannot undergo intramolecular interconversion of enantiomers due to the energy barrier of the square pyramidal transition state being higher in energy than the C-H bond dissociation. b) The dynamic stereochemical inversion of  $sp^3$ -nitrogen centres. c) The dynamic stereochemical inversion of axial chiral BINOL. d) The dynamic stereochemical inversion of planar chiral pillarenes.

The hugely varied three-dimensional (3D) structures—and therefore the hugely varied properties—of many organic molecules emerge from combining just a few types of atomic building blocks. For example, 19 of the 22 proteinogenic amino acids are formed solely from  $sp^2$ - or  $sp^3$ -hybridized carbon, nitrogen and oxygen atoms, capped by hydrogen substituents. Of this small array of elemental building blocks, it is tetrahedral  $sp^3$ -carbon<sup>1–4</sup> and  $sp^3$ -nitrogen<sup>5,6</sup> atoms that have the potential to form stereogenic centres, creating chiral structures. Chirality also arises in organic molecules by virtue of motifs other than stereogenic atoms. However, although stereochemical inversion of some planar chiral motifs<sup>7,8</sup>, helices<sup>9–11</sup> and stereogenic  $sp^3$ -nitrogen centres<sup>9,12,13</sup> can occur rapidly and reversibly through low-barrier conformational isomerism,  $sp^3$ -carbon centres cannot generally undergo spontaneous stereochemical changes (Figure 4.1). For example, the energy barrier to pyramidal inversion of methane is greater than its C–H bond dissociation energy<sup>14–16</sup>. Accordingly, unlike other stereogenic motifs<sup>7–11</sup>,  $sp^3$ -carbon centres cannot generally adapt to surrounding chiral moieties and cannot be controllably switched by the application of external stimuli. Instead, intermolecular reactions are usually necessary<sup>17,18</sup> to invert individual stereogenic carbon centres, proceeding through mechanisms involving high-energy bond-breaking and bond-making steps<sup>19</sup> with

pentavalent transition states<sup>17</sup> (for example, S<sub>N</sub>2 reactions) or trigonal intermediates<sup>18</sup>, such as carbocations, carbanions or radicals. Of course, it is this stability of sp<sup>3</sup> - carbon's tetrahedral geometry that makes it essential to the chiral skeletal diversity of organic compounds. It allows for predictable synthesis of configurationally stable molecules. Yet, the stability also limits the extent to which the complex 3D connectivity of aliphatic structures can exhibit dynamic, adaptive stereochemistry<sup>20</sup>. There have been impressive, but rare, examples of small covalent systems<sup>20–24</sup> capable of sp<sup>3</sup> - carbon enantiomerization by low-barrier intramolecular processes. However, they do so without external control of their rate or direction to a single stereoisomer. Only multicomponent interlocked molecules, in which a ring shuttles along a prochiral axle<sup>25,26</sup>, have been amenable to external control. There have been no compact and controllable dynamic sp<sup>3</sup> -carbon building blocks. Therefore, it has not been possible to investigate the transmission of stereochemical information through such systems.<sup>5,12,27</sup>

#### 4.1.1 Aim & Objectives

To investigate the transmission of stereochemical information through a dynamic chiral sp<sup>3</sup>-carbon centre, we studied a series of chiral fluxional carbon cages<sup>21,23–25</sup> that exhibit responsive sp<sup>3</sup>-carbon-centred stereochemistry, adapting to and transmitting surrounding stereochemical information. By applying density functional theory (DFT) calculations and solution- and solid-state NMR spectroscopy, in combination with X-ray crystallography, we establish the extent to which their dynamic Cope rearrangements<sup>28,29</sup> are controlled by neighbouring, fixed stereogenic centres. We have found that a substantial energetic bias of more than 10 kJ mol<sup>-1</sup> can be exercised over the stereochemical equilibria by a single fixed stereocentre. The rearrangements proceed rapidly at rates more commonly associated with low-barrier conformational changes of aliphatic systems (for example, a cyclohexane ring-flip energy barrier of ~43 kJ mol<sup>-1</sup>) rather than a configurational change. We show that these rapid constitutional dynamics can be halted by covalent modification of the cage through a [2 + 2 + 2] cycloaddition reaction, then subsequently restarted after a cycloreversion. The rearrangement rate is also attenuated upon coordination of the fluxional cage to Pd(II) or Ru(II) as part of a phosphoramidite–olefin ligand. By its inclusion in the simple ligand design, the fluxional cage transmits stereochemical information to the

metal ion through the covalent ligand backbone. This property is exploited in creating chiral-at-metal stereogenic centres that adopt the configurational dynamics of the cage. Furthermore, utilising the phosphoramidite ligands developed for barbaralane system, work towards mimicking the same binding motif (phosphorous-based olefin bidentate ligands) on the more complex fluxional bullvalene can allow for biasing the isomerisation distribution of the **BVs**.

## 4.2 Dynamic $sp^3$ -Carbon Centre Chirality of Fluxional Carbon Cages

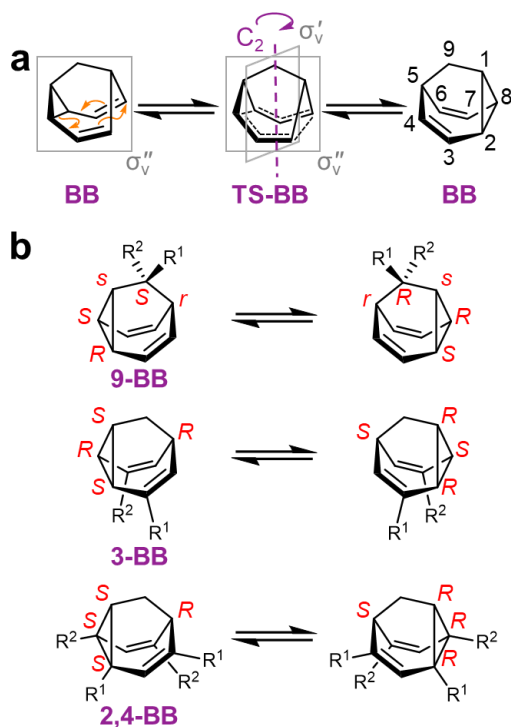
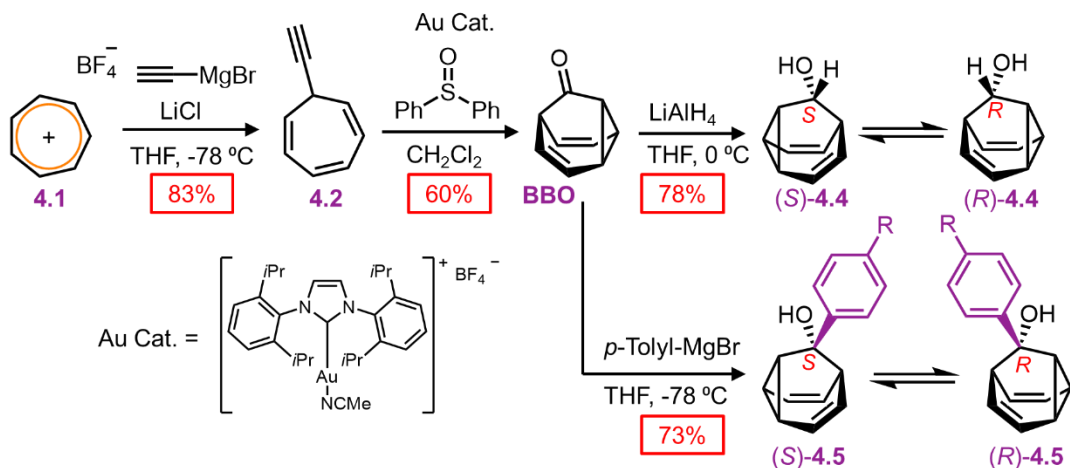


**Figure 4.2.** Multiple dynamic  $sp^3$ -carbon centres. Fluxional  $sp^3$ -carbon stereochemistry arises in barbaralanes when (a) the structures interchanged by their Cope rearrangements are (b) desymmetrized with either of the three substitution patterns shown. Cahn–Ingold–Prelog priorities are chosen to be  $R^1 > C > R^2$  for the assignment of absolute configuration. **3-BB** and **2,4-BB** each have four chirotopic (*R/S*) centres whereas the **9-BB** pattern gives rise to five stereogenic centres of which three are chirotopic and two are achirotopic (*r/s*).

The Cope rearrangement of barbaralane, **BB**, is an example (Fig. 4.2) of a narcissistic isomerisation<sup>22,30</sup>—it gives rise to a degenerate structure through a transition state, **TS-BB**, bearing an internal mirror plane ( $\sigma_v'$ ) that is not present in the ground-state structure. We noted that by desymmetrising **BB** (Fig. 4.2a) using either a **9-BB**, **3-BB**, or **2,4-BB** substitution pattern, the mirror plane present in the ground state ( $\sigma_v''$ ) is lost while the mirror plane formed in the transition state ( $\sigma_v'$ ) is retained. As a result, the Cope rearrangement inverts simultaneously some, or all, of the four or five stereogenic

centres present in the structure. Given that the rearrangement of **BB** is known to proceed with a remarkably low Gibbs free energy of activation,  $\Delta G^\ddagger$ , of 32.3 kJ·mol<sup>-1</sup>,<sup>31–35</sup> chiral **9-BB**, **3-BB**, or **2,4-BB** derivatives should undergo rapid enantiomerization. We targeted 9-barbaralol **4.4** (Scheme 4.2) as a convenient example of the **9-BB** substitution pattern that bears a hydroxyl group for synthetic elaboration.

### 4.3 Synthesis of Fluxional Carbon Cages



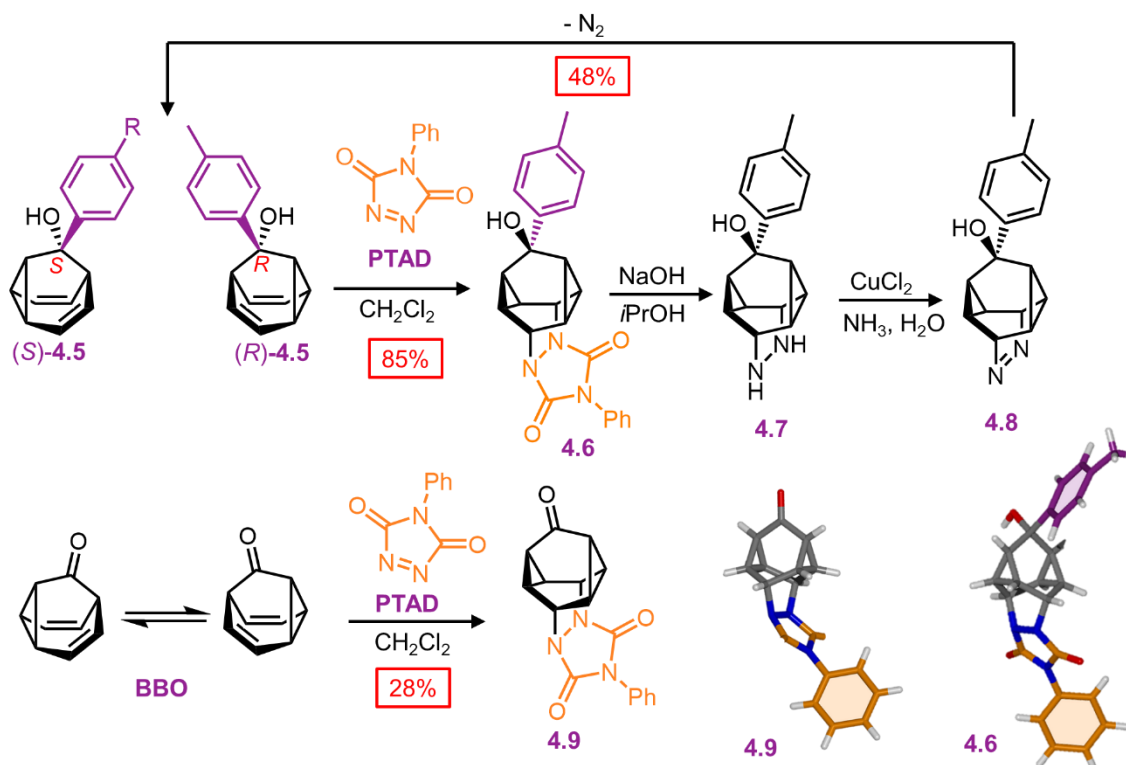
**Scheme 4.1.** Synthesis of barbaralane **BBO**, 9-barbaralol (**4.4**), and 9-(tolyl)-barbaralol (**4.5**).

The synthesis of **9-BBs** was previously developed by past members of the McGonigal group. For our studies, the synthesis of the control **9-BBs** is illustrated in Scheme 4.1. When labelling **4.4** and subsequent compounds, a single stereochemical descriptor is included to indicate the configuration at position 9 of the barbaralane (Figure 4.1a), e.g., (*R*)-**4.4** and (*S*)-**4.4**, omitting the additional stereochemical labels of positions 1, 2, 5, and 8 for simplicity (Fig. 4.1a).

Starting from the commercially available tropylium tetrafluoroborate (**4.1**) and freshly prepared ethynyl turbo Grignard, the addition reaction to the tropylium cation produced the desired ethynyl cycloheptatriene (**4.2**) in good yield. Using the established method from Echavarren et al.<sup>36,37</sup> using gold catalysis to activate enynes towards cycloisomerisation and the presence of oxidant, the barbaralane **BBO** was obtained in moderate yields. **BBO** was reduced with  $\text{LiAlH}_4$  under mild conditions generating the dynamic chiral  $\text{sp}^3$ -carbon centre of interest yielding the parent 9-barbaralol (**4.4**). 9-(Tolyl)-barbaralol was made using the Grignard reagent, *p*-tolylmagnesium bromide, generating the dynamic chiral  $\text{sp}^3$ -carbon centre of the fluxional cage. These

barbaralanes will be parent shapeshifting molecules of these covalently tagged chiral auxiliary studies.

#### 4.4 Reversible Freezing of Fluxional Cages



**Scheme 4.2.** Control of the  $sp^3$ -C stereochemistry is exerted by a cycloaddition reaction, which freezes and symmetrizes the structure, before subsequent cycloreversion re-establishes the dynamic stereochemical equilibrium.

To control over the fluxional enantiomerisation, we sought to exploit the reactivity of the barbaralanes' skipped diene units. The fluxional rearrangements can be stopped entirely by engaging the alkene units in covalent bonding. An enantiomerising mixture of 9-(*p*-tolyl)barbaralol **4.5** or barbaralone **BBO** engages (Scheme 4.2) in a [2+2+2] cycloaddition reaction with 4-phenyl-3*H*-1,2,4-triazole-3,5(4*H*)-dione (PTAD) giving rise to **4.6** and **4.9** respectively. This reaction halts the rearrangement whilst also symmetrizing the structure by forming a second cyclopropyl group. Subsequently, the fluxional cage can be regenerated (Scheme 4.2) in a two-step transformation through diazine **4.8**, which undergoes cycloreversion with the loss of  $N_2$  upon oxidation with  $CuCl_2$ . Single crystal XRD data was obtained for both **4.6** and **4.9**, confirming the freezing of the fluxional nature of the cage and the symmetrisation of structure. The  $^1H$

NMR spectra show (Figure 4.3) that this reaction halts the Cope rearrangement observed in (*R*)/(*S*)-**4.5** whilst also symmetrising the structure overall by forming a second cyclopropyl ring (**4.6**). The fluxional cage is easily regenerated in a two-step transformation through compound **4.7** (evidence in the crude NMR), which undergoes cycloreversion upon oxidation with  $\text{CuCl}_2$ . A  $^1\text{H}$  NMR spectrum of the crude mixture of **4.7** displays characteristic proton resonances of the diazinane C-H (labelled as protons  $\text{H}_1$  and  $\text{H}_2$ ) and N-H environments (labelled as protons  $\text{H}_3$  and  $\text{H}_4$ ).

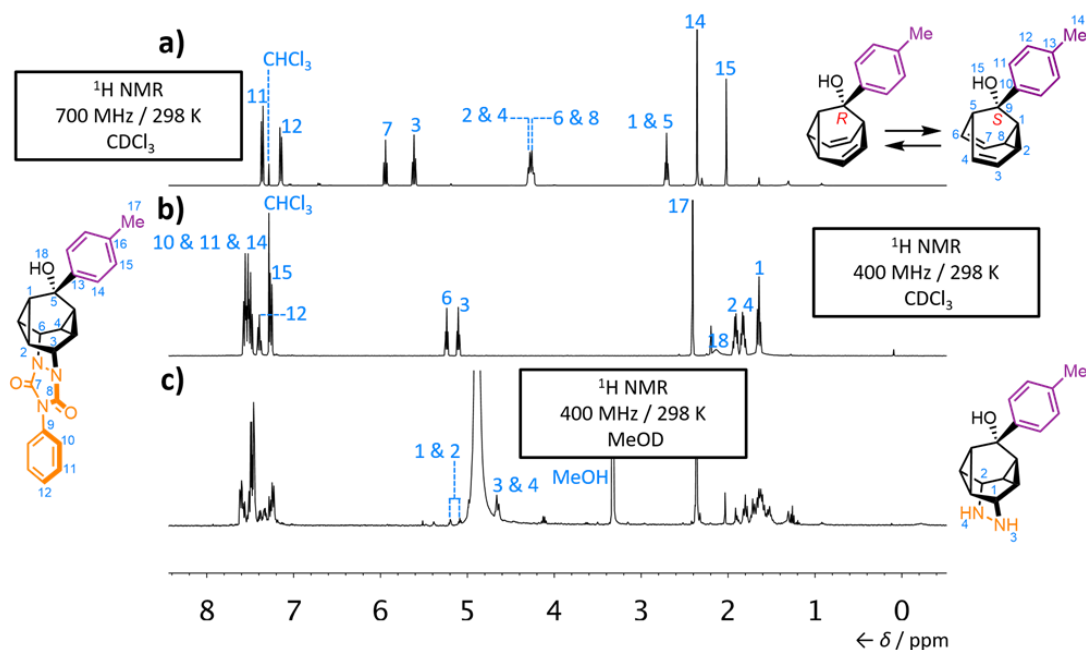
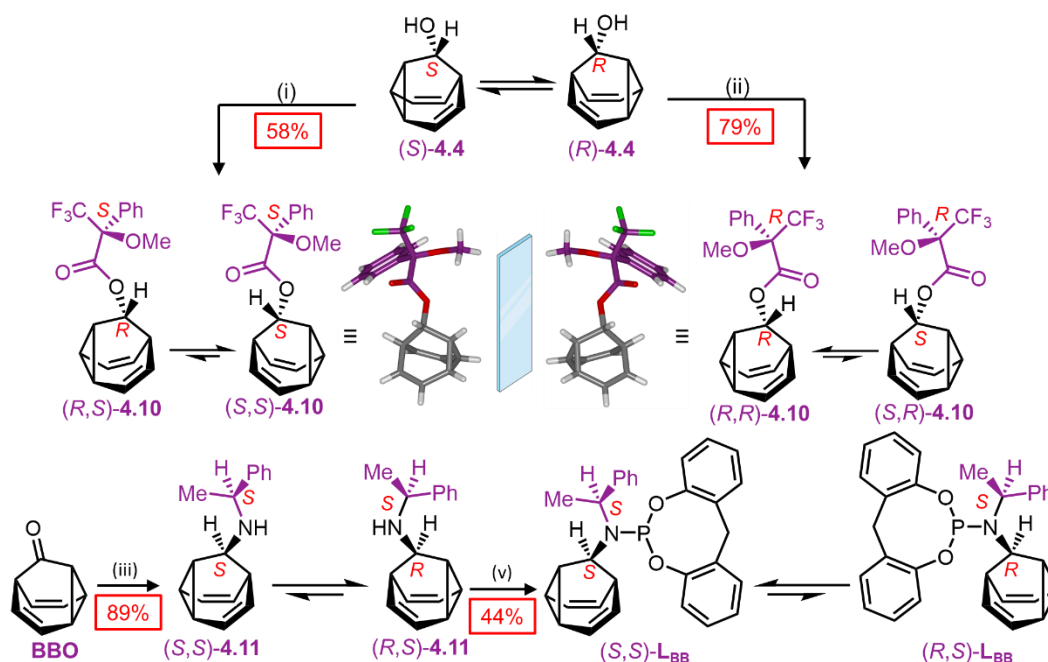


**Figure 4.3.** Partial  $^1\text{H}$  NMR spectra of (a) (*R*)/(*S*)-**4.5**, (b) **4.6** and (c) **4.7**. The spectra show the stopping and restarting of the Cope rearrangement observed in (*R*)/(*S*)-**4.5**.

### 4.5 Diastereomeric adaptation

As mentioned earlier, we targeted 9-barbaralol **4.4** (Scheme 4.2) as it is a convenient motif using the **9-BB** substitution pattern, bearing a hydroxyl group as a synthetic handle. Treatment of **4.4** with Mosher's acid chloride (Scheme 4.2) produces a set of Mosher's esters **4.10** in which the configurationally fixed stereocentre is introduced at a distance of three covalent bonds from the dynamic barbaralane unit. An additional descriptor for the configuration of Mosher's ester group is included in the labels for **4.10**. Derivatization with (*S*)-Mosher's acid ((*S*)-MTPA) gives a dynamic mixture of two diastereomers, (*R,S*)-**4.10** and (*S,S*)-**4.10**, while (*R*)-Mosher's acid ((*R*)-MTPA) gives (Scheme 4.2) the antipodal mixture, (*S,R*)-**4.10** and (*R,R*)-**4.10**.



**Scheme 4.3** | Diastereomeric Adaptation and Manipulation of Chiral Barbaralanes by covalent chiral auxiliaries inducing bias on the stereochemical, Reagents and conditions: (i) 1. (*S*)-MTPA, (COCl)<sub>2</sub>, hexanes, DMF, rt to −20 °C, 16 h, 2. DMAP, Et<sub>3</sub>N, CHCl<sub>3</sub>, rt, 5 d, 58%. (ii) 1. (*R*)-MTPA, (COCl)<sub>2</sub>, hexanes, DMF, rt to −20 °C, 16 h, 2. 1, DMAP, Et<sub>3</sub>N, CHCl<sub>3</sub>, rt, 3 d, 79%. °C, 18 h, 13%. (iii) 1. 3, (*S*)-1-phenylethylamine, AcOH, MeOH, rt, 30 min. 2. NaBH<sub>3</sub>CN, 100 °C, 16 h, 89%. (v) 1. PCl<sub>3</sub>, Et<sub>3</sub>N, CH<sub>2</sub>Cl<sub>2</sub>, 0 °C, 3 h, 2. 2,2'-methylenediphenol, CH<sub>2</sub>Cl<sub>2</sub>, 0 °C to rt, 16 h, 44%.

Further chemical modification to the substituent at position 9 can substantially influence, and even invert, the cage's equilibrium distribution. The phosphoramidite-olefin<sup>38–40</sup> ligand **LBB** was synthesized (Scheme 4.3) by first subjecting **BBO** to reductive amination with (*S*)-1-phenylethylamine to afford a mixture of (*S,S*)-**4.11** and (*R,S*)-**4.11**. Sequential treatment of the amine with PCl<sub>3</sub> then 2,2'-methylenediphenol affords **LBB**. Comparing **LBB** to **4.11** reveals that the differing size and shape of the substituent at position 9 drives the dynamic stereochemical equilibria of the fluxional cage towards opposite configurations. The solution phase equilibrium of the secondary amine is weighted (Table S4.1) towards the (*R,S*)-**4.11** diastereomer by a  $\Delta G_{\text{calc}}$  of 3.8 kJ·mol<sup>−1</sup>, matching the structure observed by X-ray analysis (Scheme 4.2) of a single crystal. By contrast, the (*S,S*)-**LBB** diastereomer of the phosphoramidite is favoured (Table S4.1) with a  $\Delta G_{\text{calc}}$  of 20.2 kJ·mol<sup>−1</sup>. The large magnitude of  $\Delta G$  for **LBB** highlights that the configurational dynamics of the **9-BB** motif (Scheme 4.2) correlate with significant changes in its three-dimensional shape<sup>32</sup> and, therefore, its energy. At the same time, the opposing cage stereochemistry for **4.11** and **LBB** demonstrates that

the malleable  $sp^3$ -carbon configuration adapts to changes in the nearby steric environment.

#### 4.5.1 Characterisation of the Fluxional nature of Chiral Barbaralanes

To understand the dynamics of the fluxional carbon nature through the intramolecular Cope rearrangement, in depth solution and solid-state NMR analysis was conducted (Figure 4.4). Compound **BBO** is an achiral molecule because of an internal mirror plane ( $\sigma_v''$ ) (in the plane of the carbonyl bridge), however, another orthogonal mirror plane ( $\sigma_v'$ ) is effectively present on as a result of the rapid dynamics of the barbaralane core. Due to this apparent mirror plane ( $\sigma_v'$ ), the NMR measurements reveal the exchanging cyclopropane and olefinic environments appear as a broad singlet due the dynamic Cope rearrangement occurring in the fast-exchange regime above the coalescence temperature of this NMR experiment (Figure 4.4a). In contrast, a 9-**BB**-type compound (e.g., (*R*)/(*S*)-**4.4**) lacks the internal mirror plane ( $\sigma_v''$ ) – however, the orthogonal mirror plane ( $\sigma_v'$ ) arising from rapid Cope rearrangement is retained. The removal of the  $\sigma_v''$  mirror plane results in the desymmetrisation of the molecule and subsequently the cyclopropane and olefinic environments split into two sets of two inequivalent peaks remaining in the fast-exchange regime (Figure 4.4b). Covalently linking a chiral tether to the barbaralane core (as observed with (*R,S*)/(*S,S*)-**4.10**) removes the remaining mirror plane ( $\sigma_v'$ ) and entirely desymmetrises the core so that every proton on the barbaralane core has its own unique chemical environment. For example, the broad singlet present in Figure 4.4a labelled as position H<sub>2</sub> changes into four distinctly split peaks in Figure 4.4c. Although desymmetrisation occurs, the chiral tether molecules still exist in solution as a mixture of interconverting nondegenerate diastereoisomers. Since (*R*)/(*S*)-**4.4** in the solution state interconverts between two degenerate isomers, the equilibrium constant, *K*, is 1.0; therefore, the averaged peaks are exactly halfway between the two individual structures in exchange.<sup>36,37</sup> For example, the proton signal corresponding to position 2 and 4 is exactly halfway between the signals for H<sub>2</sub> and H<sub>4</sub> if two structures were fixed in either state. Similarly, the positions of the four peaks (H<sub>2</sub>, H<sub>4</sub>, H<sub>6</sub>, and H<sub>8</sub>) of (*R,S*)/(*S,S*)-**4.10** (Figure 4.3c) represent an average of the interconverting pair of stereoisomers, but weighted by the equilibrium distribution of isomers (where *K* ≠ 1).

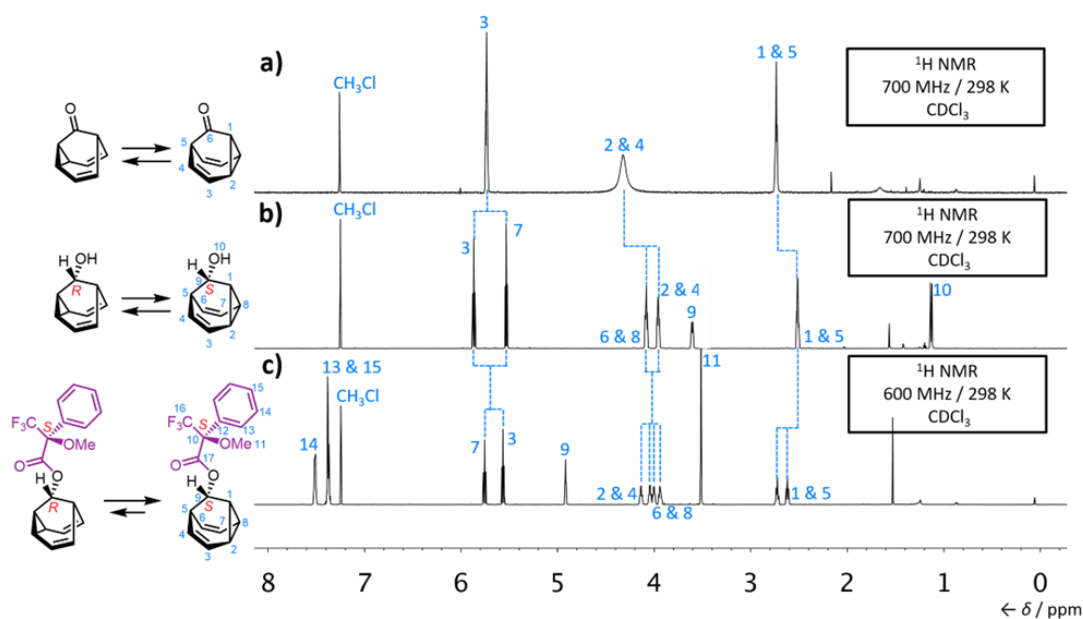


**Figure 4.4.**  $^1\text{H}$  NMR spectra of (a) **BBO**, (b)  $(R)/(S)$ -**4.4** and (c)  $(R,S)/(S,S)$ -**4.10**. The spectra show the sequential desymmetrisation of the barbaralyl core with environments splitting as they become magnetically equivalent.

#### 4.5.2 Variable-Temperature (VT) NMR Spectroscopy of $(R,S)/(S,S)$ -**4.10**

In order to probe the equilibrium further, we recorded solution-phase  $^1\text{H}$  and  $^{13}\text{C}$  NMR spectra of covalently modified barbaralane  $(R,S)/(S,S)$ -**4.10** at low temperatures ranging from 296 K to 149 K (Figures 4.6 and 4.7). At room temperature, the diastereomers appear to exist in a ratio which is almost 1:1 of interconverting configurations, owing to the close proximity of the olefinic and cyclopropane chemical shifts (the proton environments labelled as  $\text{H}_2$ ,  $\text{H}_4$ ,  $\text{H}_6$  and  $\text{H}_8$ ). Cooling below the coalescence temperature separates these environments into the slow-exchange regime, so chemical shifts are closer to those expected for a divinyl cyclopropane and a *cis*-dialkylolefin. Analysis of the chemical shift variation as a function of temperature could have, in principle, allowed quantitative evaluation of the kinetic and thermodynamic parameters determining the dynamic chirality of the carbon stereogenic centre of  $(R,S)/(S,S)$ -**4.10** if both isomers could be observed in slow exchange. But in the slow-exchange regime the equilibrium was deemed to shift almost entirely in preference of the thermodynamically favoured diastereoisomer  $(S,S)$ -**4.10** (Figure 4.4) on account of the shift in the Boltzmann distribution at low temperature and this result was confirmed by DFT calculations.

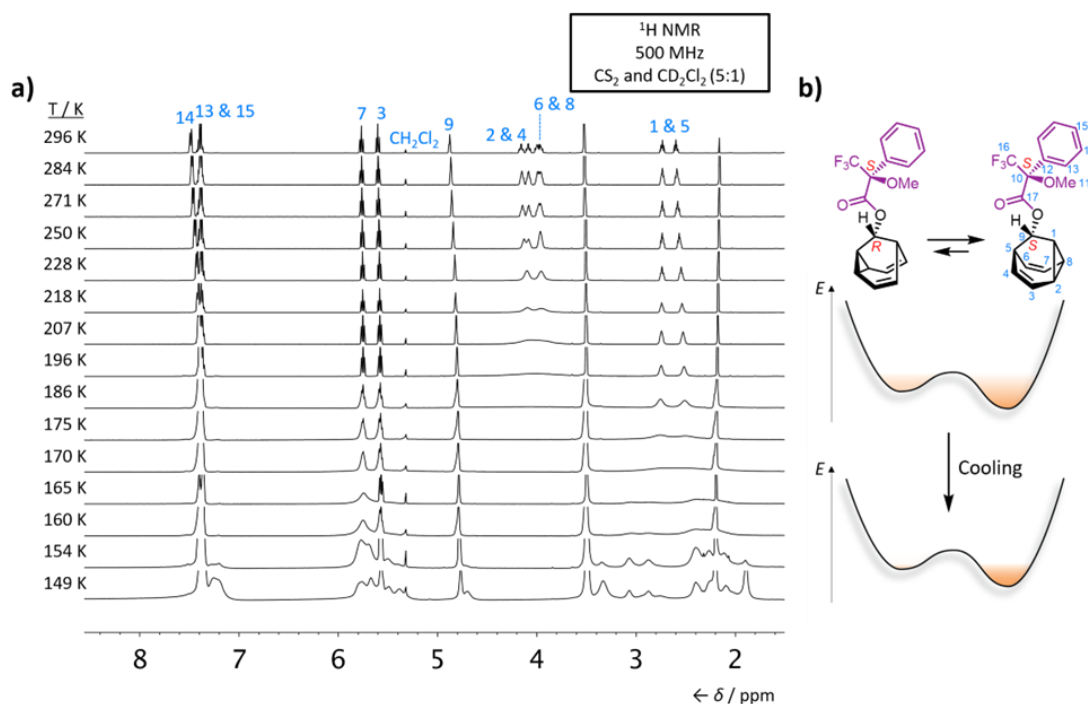


**Figure 4.5.** Partial <sup>1</sup>H VT NMR spectra of (a) (*R,S*)/(*S,S*)-**4.10** (296 K to 149 K) and (b) a schematic illustration of the change in equilibrium population on a simplified potential energy surface as the temperature decreases.

Diastereoisomers (*R,S*)/(*S,S*)-**4.10** are computed to have a ground state energy difference of 6.8 kJ·mol<sup>-1</sup> with the lower energy isomer (*S,S*)-**4.10** being thermodynamically favoured. Overall, the introduction of a covalently bound chiral tether of fixed absolute configuration allows the solution-state equilibrium to shift slightly in favour of the thermodynamically favoured configuration at room temperature. Upon cooling the solution-state equilibrium is shown to be dominated by the thermodynamically preferred diastereoisomer ((*S,S*)-**4.10**).

Furthermore, the dynamics of barbaralanes undergoing a rapid and reversible Cope rearrangement in solution for diastereoisomer (*R,S*)/(*S,S*)-**4.10** is highlight in the VT-<sup>13</sup>C NMR (Figure 4.6). Diastereoisomer (*R,S*)-**4.10** is in fast exchange with isomer (*S,S*)-**4.10**, giving rise to a single set of resonances in the <sup>13</sup>C NMR spectrum recorded at ambient temperature. The chemical shift of each nucleus is indicative of its time-averaged chemical environment. Upon reducing the temperature to 159 K (Figure 4.6), the equilibrium shifts in favour of diastereoisomer (*S,S*)-**4.10**. This is evidenced as the peaks corresponding to the olefinic and cyclopropane environments broaden into the base and re-emerge. For example, two of the olefinic and cyclopropane environments are ~70 ppm at room temperature but at colder temperatures they have shifted to ~25

ppm. Environments labelled as C<sub>1</sub>, C<sub>5</sub>, C<sub>3</sub> and C<sub>7</sub> also broaden into the baseline at higher temperatures and re-emerge at colder temperatures.

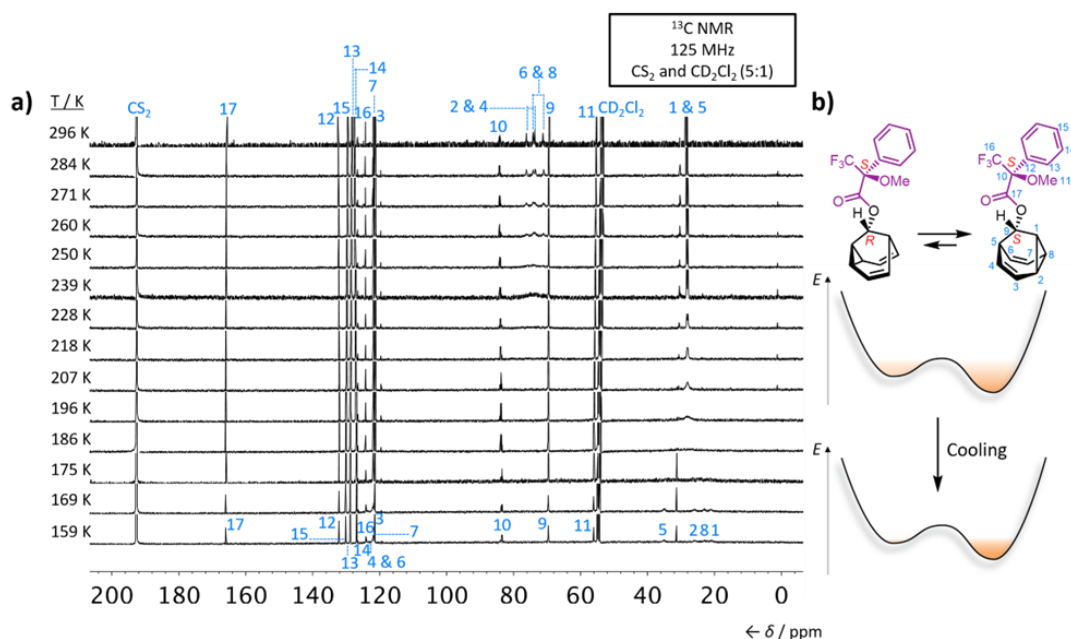


**Figure 4.6.** Partial <sup>13</sup>C VT NMR spectra of (a) (*R,S*)/(*S,S*)-**4.10** (296 K to 159 K) and (b) a schematic illustration of the change in equilibrium population on a simplified potential energy surface as the temperature decreases.

To further probe the dynamics of the barbalane rapid Cope arrangements for diastereoisomers (*R,S*)/(*S,S*)/(*S,R*)/(*R,R*)-**4.10**, analysis of the solid-state structures of (*R,R*)-**4.10** was conducted using <sup>13</sup>C solid-state NMR (ssNMR) spectroscopy (Figure 4.7). ssNMR experiments were performed for (*R,R*)-**4.10** (Figure 4.7b). Comparison to the low-temperature solution-phase <sup>13</sup>C NMR spectrum of (*S,S*)-**4.10** (Figure 4.7c) supports the assignment that the diastereoisomer with the same configuration at position C<sub>9</sub> of the barbalane and at chiral tether (i.e., *R* and *R*) is the thermodynamically favoured diastereoisomer and that the equilibrium is slightly shifted in solution at room temperature but is dominant at low temperatures. Comparison of the simulated <sup>13</sup>C NMR spectrum of (*R,R*)-**4.10**<sup>41,42</sup> against the low-temperature solution-phase <sup>13</sup>C NMR spectrum of (*S,S*)-**4.10** and the ssNMR of (*R,R*)-**4.10** also supports our conclusion (Figure 4.7a). The two derivatives studied, (*S,S*)-**4.10** and (*R,R*)-**4.10**, are enantiomers and thus their NMR spectroscopic signals can be directly compared. The upfield (<100 ppm) resonances of the <sup>13</sup>C ssNMR spectrum are well resolved. They match well with the experimental solution and simulated solid-state spectra (Figures 4.6a, 4.7a), allowing for the reliable assignment of the upfield region of the spectra.

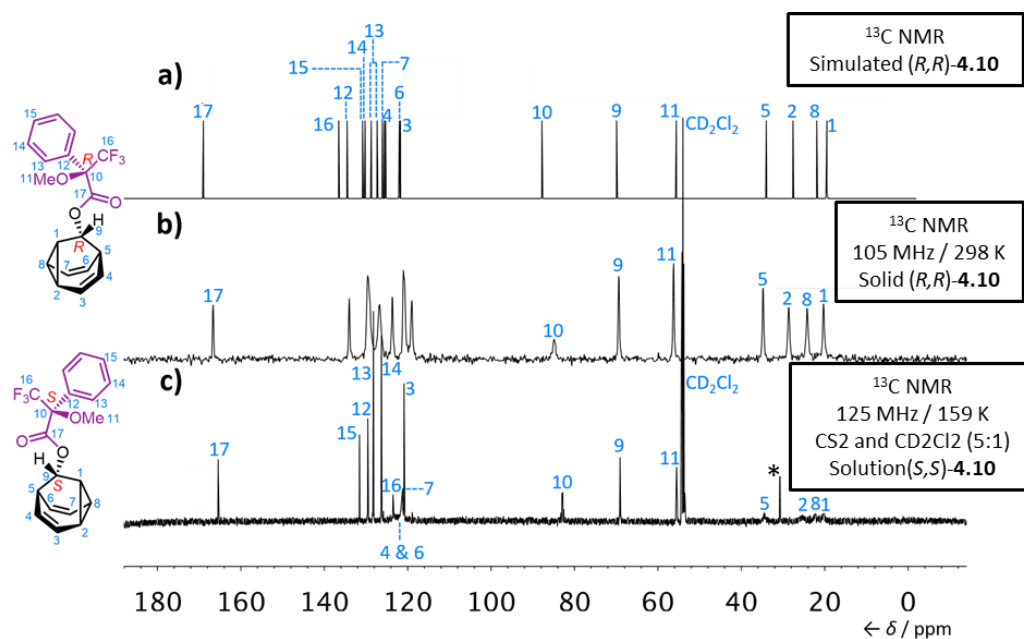


**Figure 4.7.** Comparison of  $^{13}\text{C}$  NMR spectra of  $(R,R)$ -**4.10** and  $(S,S)$ -**4.10** under different conditions: (a) the simulated solid-state spectrum of  $(R,R)$ -**4.10**, (b)  $(R,R)$ -**4.10** in the solid state (as a powder) and (c)  $(S,S)$ -**4.10** in a  $\text{CS}_2$ - $\text{CD}_2\text{Cl}_2$  (5:1) solution at 159 K. The asterisk indicates the resonance of residual acetone.

#### 4.5.3 Modelling Fluxional Behaviour of Chiral Barbaralanes

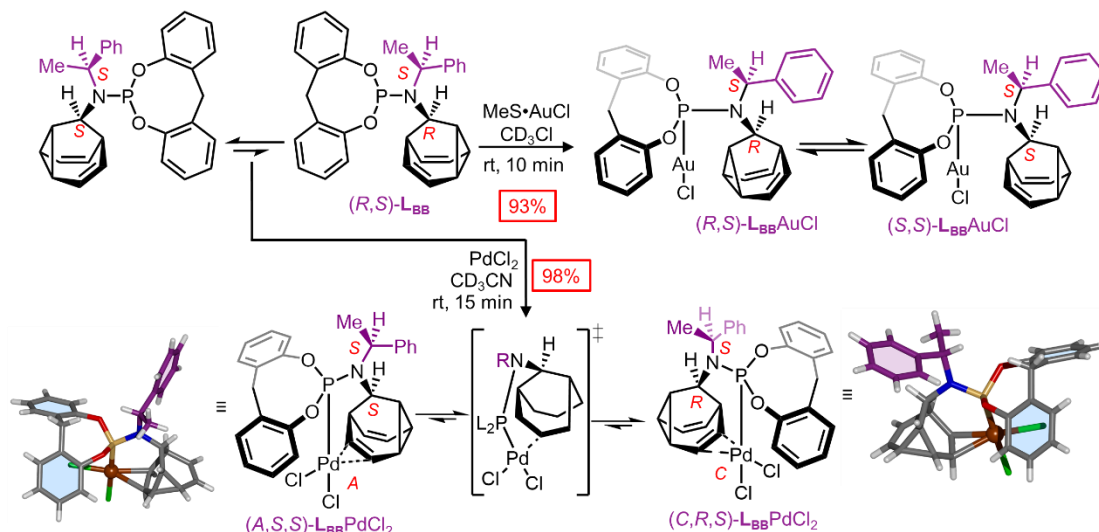
DFT modelling using the  $\omega\text{B97X-D}$  functional<sup>43</sup>, 6-311++G(d,p) basis set<sup>44,45</sup> and a  $\text{CS}_2$  polarizable continuum solvent model was employed to compare (Table S4.1) the stereoisomerisation energetics of **BB**, **4.10** and **4.11**. Using these parameters, the automerization of **BB** is predicted to proceed with an activation energy,  $\Delta G_{\text{calc}}^\ddagger$ , of  $38.5 \text{ kJ}\cdot\text{mol}^{-1}$ , which is  $\sim 6 \text{ kJ}\cdot\text{mol}^{-1}$  higher than the experimentally measured  $\Delta G^\ddagger$  of  $32.3 \text{ kJ}\cdot\text{mol}^{-1}$ , in keeping with previous DFT investigations.<sup>31,33</sup> DFT methods systematically overestimate the energy barrier to Cope rearrangement of barbaralanes, but nevertheless, allow useful comparisons of trends in activation energies and are known to predict accurately the relative ground-state energies of isomers.<sup>31,33</sup> The computationally predicted  $\Delta G^\ddagger$  values for **4.10** ( $35.5 \text{ kJ}\cdot\text{mol}^{-1}$ ) and **4.11** ( $39.5 \text{ kJ}\cdot\text{mol}^{-1}$ ) are very similar to **BB**, indicating that the hydroxyl or ester group substitutions at position 9 do not significantly change the rapid kinetics.

#### 4.6 Metal Coordination of Chiral Fluxional Carbon Cages

To exert control over the fluxional enantiomerization, we sought to further exploit the reactivity of the **BBs**' skipped diene units in terms of coordination of the  $\pi$  electrons to

a transition-metal ion<sup>34</sup> which can modulate the rate of strain Cope rearrangement. Coordination of Pd(II) or Ru(II) to **L<sub>BB</sub>1** causes a reduction in the rate of the Cope rearrangement, as discussed below.

#### 4.6.1 Pd (II) Chiral at Metal Barbaralane complexes



**Scheme 4.4.** Synthesis of Chiral-at-Metal complexes.

**L<sub>BB</sub>** and  $\text{PdCl}_2$  form (Scheme 4.4) a chiral-at-metal<sup>46,47</sup> complex, **L<sub>BB</sub>PdCl<sub>2</sub>**, linking the  $\text{sp}^3$ -carbon configurational inversion to the *A/C* isomerism<sup>48</sup> of the distorted trigonal bipyramidal (TBPY-5-12) coordination environment. *A/C* isomerism is naming convention to the determination of chirality for different geometries other than tetrahedral centre. *A/C* isomerism uses the same principles of assigning priority numbers for determining chirality at other polyhedral where the symbols *R* and *S* are replaced by the symbols *C* and *A* respectively.<sup>48</sup> Both possible stereoisomers, arising from coordination of  $(S,S)\text{-L}_{\text{BB}}$  or  $(R,S)\text{-L}_{\text{BB}}$  through their P centre and an alkene, are observed (Scheme 4.4) in the X-ray crystal structure of the  $\text{PdCl}_2$  complex. The alkene coordination is also evident (Fig. 4.8) in the solution state by  $^1\text{H}$  NMR spectroscopy. For comparison, a monodentate **L<sub>BB</sub>AuCl** complex (Scheme 4.4) was prepared, which shows only small changes in the  $^1\text{H}$  NMR chemical shifts of its alkene signals  $\text{H}_3$  and  $\text{H}_7$  relative to the free ligand (Fig. 4.7b). The room-temperature spectrum of **L<sub>BB</sub>PdCl<sub>2</sub>**, on the other hand, reveals a large change in the chemical shift of  $\text{H}_7$ , consistent with coordination of Pd (II) to the alkene on the same face as the phosphoramidite group.

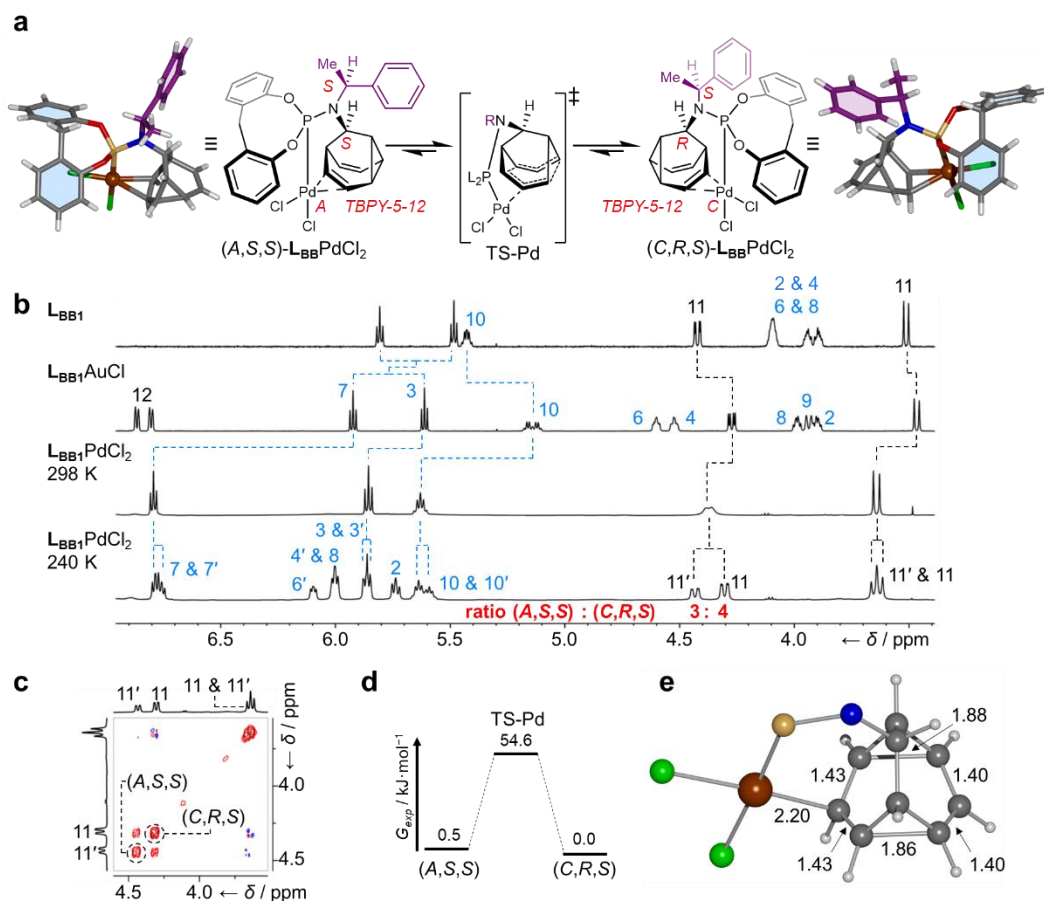


**Figure 4.8.** a) Bidentate coordination of  $L_{BB}$  to  $PdCl_2$  leads to cc-Cope rearrangement in which the Pd ‘walks’ along the side of the BB cage, modulating the rearrangement rate. X-ray crystal structures are shown in stick representation, with a ball for metal ions. Solvent molecules are omitted for clarity. Two structurally similar conformers of each  $L_{BB}PdCl_2$  stereoisomer are present in the unit cell, but only one of each is shown for clarity. b) Partial  $^1H$  NMR (CDCl<sub>3</sub>) spectra: top,  $L_{BB}$  (599 MHz, 298 K); second row,  $L_{BB}AuCl$  (599 MHz, 298 K); third row,  $L_{BB}PdCl_2$  (499 MHz, 298 K); bottom,  $L_{BB}PdCl_2$  (499 MHz, 240 K). Resonances are labelled according to the numbering for  $L_{BB}$  in Fig. 4.4. The spectrum at 240 K shows the two  $L_{BB}PdCl_2$  complexes in slow exchange in a ratio of 3:4. c, A partial  $^1H$ - $^1H$  EXSY NMR spectrum (499 MHz, CDCl<sub>3</sub>, 240 K, mixing time  $\tau_m = 200$  ms) showing exchange peaks (red) between resonances of the minor ( $H_{11'}$ ) and major ( $H_{11}$ ) diastereomers as well as COSY peaks (blue) of geminal proton pairs. d, Free energy diagram for the cc-Cope rearrangement. e, Ball-and-stick representation of the DFT-calculated ( $\omega$ B97X-D/6-311++G(d,p)/SDD/CS<sub>2</sub>)<sup>49</sup> geometry of  $L_{BB}PdCl_2$ , showing the BB cage at the transition state, TS-Pd. A truncated structure omitting phosphorus and nitrogen substituents is shown for clarity with selected bond lengths given in Å.

At room temperature, several of the proton resonances of  $L_{BB}PdCl_2$  are broadened due to exchange. The signals were resolved by recording a series of low temperature  $^1H$  NMR spectra (Figure 4.9). Signals corresponding to the two stereoisomers are present in an equilibrium ratio of 3:4 ( $K = 1.33$ ) at 240 K, corresponding to a small free energy difference,  $\Delta G_{exp}$ , of 0.5 kJ  $mol^{-1}$  between the two isomers. Consistent with this

observation, DFT calculations predict (Table S4.1) a small  $\Delta G_{\text{calc}}$  of  $1.8 \text{ kJ mol}^{-1}$  in favour of (C,R,S)-**L**<sub>BB</sub>PdCl<sub>2</sub>.

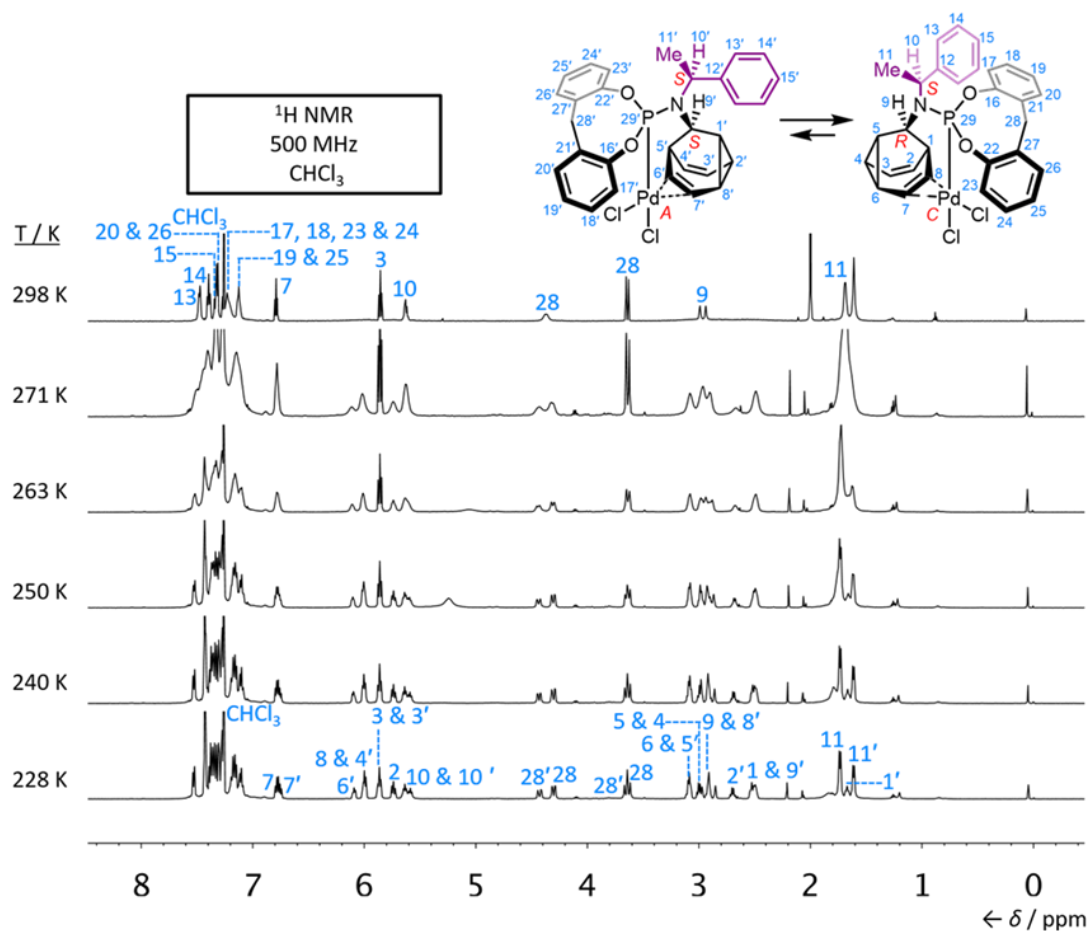


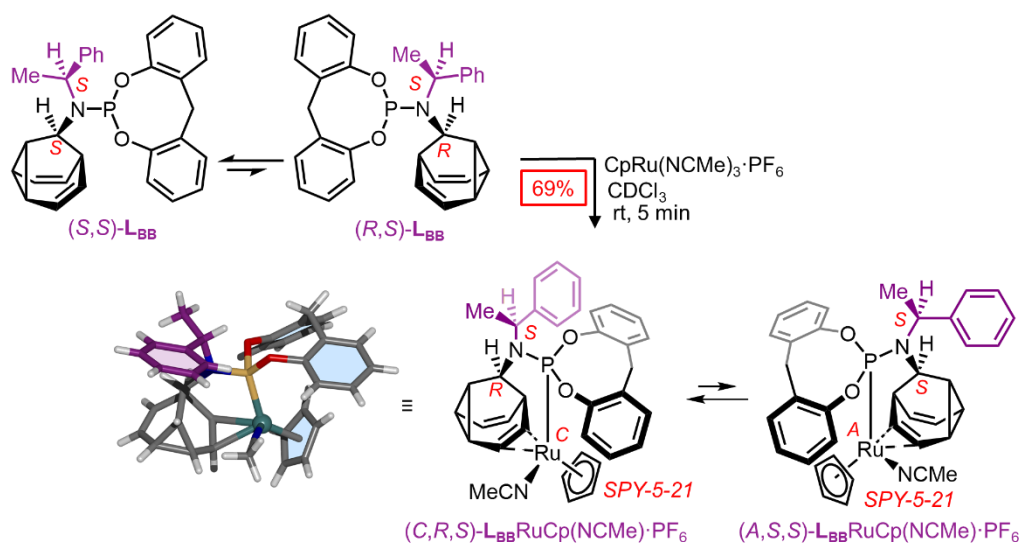
**Figure 4.9.** Partial  $^1\text{H}$  VT NMR spectra of (A,S,S)/(C,R,S)-**L**<sub>BB</sub>PdCl<sub>2</sub> (298 K to 228 K). The spectra at 298 K show that the diastereoisomers are in fast exchange, whereas at 228 K the diastereoisomers enter the slow-exchange regime and are in a ratio of 1.3:1 of (C,R,S)-**L**<sub>BB</sub>PdCl<sub>2</sub> to (A,S,S)-**L**<sub>BB</sub>PdCl<sub>2</sub>.

Further NMR and DFT analyses elucidate the mechanism by which the **L**<sub>BB</sub>PdCl<sub>2</sub> complex isomerizes. Depending on the placement and nature of substituents around the Cope substrate, metal coordination can either stabilize a charged, intermediate species as part of a stepwise associative rearrangement mechanism, or it can increase the rate of a concerted rearrangement pathway by stabilizing the transition state.<sup>50</sup> Consequently, Pd(II) salts and other cationic metal ions are known to accelerate Cope rearrangements<sup>51,52</sup>. Remarkably, coordination of the Pd(II) to one face of the fluxional cage in **L**<sub>BB</sub>PdCl<sub>2</sub> has the opposite effect, slowing down the Cope rearrangement. Unlike **4.10**, for example, whose  $^1\text{H}$  NMR resonances (499 MHz) enter the slow exchange regime below 160 K (Figure 4.5), the slower

rearrangement of  $\mathbf{L_{BB}PdCl_2}$  is resolved by  $^1\text{H}$  NMR spectroscopy at the higher temperature of 240 K. Using 2D  $^1\text{H}$ - $^1\text{H}$  exchange spectroscopy (EXSY) at 240 K (Figure 4.8c), we measured a rate of exchange,  $k$ , of  $6.48\text{ s}^{-1}$ , indicating a  $\Delta G^\ddagger_{\text{exp}}$  of  $54.6\text{ kJ mol}^{-1}$  for  $\mathbf{L_{BB}PdCl_2}$  (Figure 4.8d). The DFT-calculated transition-state structure (Figure 4.8e) shows pairs of equidistant C–C bonds, as would be expected for a coordination-coupled Cope (*cc*-Cope) rearrangement (Figure 4.8a) in which the Pd(II) remains bound to the cage through a concerted rearrangement step. The DFT-predicted  $\Delta G^\ddagger_{\text{calc}}$  of  $60.6\text{ kJ mol}^{-1}$  for this *cc*-Cope mechanism matches well with the  $\Delta G^\ddagger_{\text{exp}}$  of  $54.6\text{ kJ mol}^{-1}$ .

These data indicate that the metal ion ‘walks’ along one side of the **BB** cage as the Cope rearrangement proceeds, moving back and forth in sync with the pericyclic reaction.<sup>50</sup> Consequently, the **BB** not only transmits the stereochemical information from the fixed  $sp^3$ -carbon stereocentre through its dynamic  $sp^3$ -carbon framework, but it also imparts a novel mechanism of intramolecular configurational change at a pentavalent stereocentre, which differs from the established pseudorotation and turnstile mechanism.<sup>51</sup>

#### 4.6.2 Interfacing Ligand Exchange on Chiral at Metal Barbaralane Complexes



**Scheme 4.5** | Transfer of Dynamic  $sp^3$ -Carbon Stereochemistry in Chiral-at-Ru(II) Complexes. giving an observed rate constant  $k_{\text{obs}}$  of  $2.56 \times 10^{-3}\text{ s}^{-1} \pm 10\%$ . Using the Eyring equation, this rate corresponds to a free energy of activation  $\Delta G^\ddagger$  of  $87.8\text{ kJ mol}^{-1}$ .

The dynamic  $sp^3$ -carbon stereochemistry of  $\mathbf{L_{BB}}$  can also be linked to an intermolecular ligand exchange process. Cyclopentadienyl (Cp) half-sandwich Ru(II) complex,<sup>53</sup>

**LBB**RuCp(NCMe)·PF<sub>6</sub> (Scheme 4.5) has a stereogenic, distorted square pyramidal Ru(II) centre coordinated to a labile MeCN ligand. X-ray analysis (Scheme 4.5) of the crystalline sample reveals the identity of the energetically favoured isomer to be (C,R,S)-**LBB**RuCp(NCMe)·PF<sub>6</sub>. DFT also supports this assignment (Table S3), predicting a  $\Delta G_{\text{calc}}$  of 6.7 kJ·mol<sup>-1</sup>. Ru(II) coordination slows the Cope rearrangement sufficiently for a single stereoisomer to be resolved as a metastable species under ambient conditions. Upon dissolving single crystals of **LBB**RuCp(NCMe)·PF<sub>6</sub> obtained by slow evaporation, a series of <sup>1</sup>H NMR spectra were collected in CDCl<sub>3</sub> at 298 K where the equilibrium was established over a period of several minutes. The <sup>1</sup>H NMR spectra shows the presence of a single complex (Fig. 4.10) with resonances distinct from non-coordinated **LBB**. After allowing the sample to fully equilibrate at room temperature for four hours, A 4:1 equilibrium mixture of (C,R,S)-**LBB**RuCp(NCMe)·PF<sub>6</sub> and (A,S,S)-**LBB**RuCp(NCMe)·PF<sub>6</sub> is obtained favouring the thermodynamic product with a  $\Delta G$  of 4.0 kJ·mol<sup>-1</sup>. In order to determine the dynamic stereoisomerisation rate of **LBB**RuCp(NCMe)·PF<sub>6</sub>, Assuming a first-order process with rate-limiting dissociation of MeCN, the rate was estimated (Fig. 4.11) as the gradient of a straight line fitted to a plot of natural logarithm of the peak intensity against time, giving an observed rate constant  $k_{\text{obs}}$  of  $2.56 \times 10^{-3} \text{ s}^{-1} \pm 10\%$ . Using the Eyring equation, this rate corresponds to a free energy of activation  $\Delta G^\ddagger$  of 87.8 kJ·mol<sup>-1</sup>.

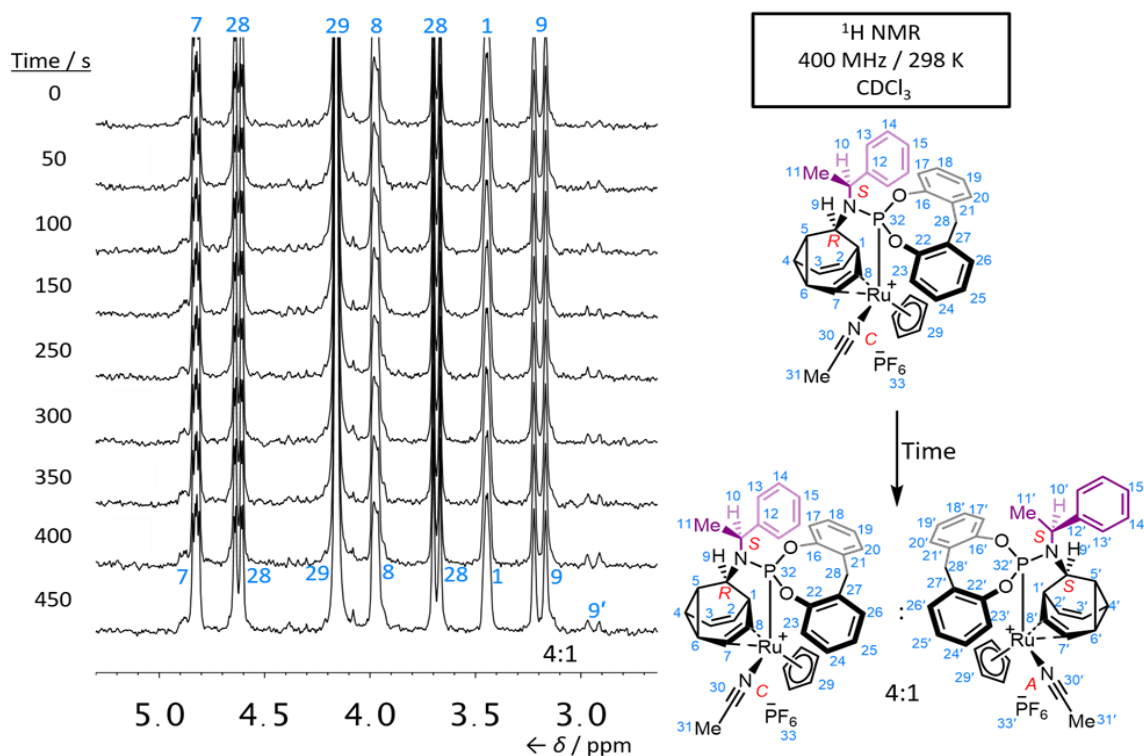


**Figure 4.10.** Partial  $^1\text{H}$  NMR spectra (400 MHz,  $\text{CDCl}_3$ , 298 K) of  $\text{L}_{\text{BB}}\text{RuCp}(\text{NCMe})\cdot\text{PF}_6$  obtained by acquiring spectra sequentially immediately after dissolving a crystalline sample of  $(C,R,S)\text{-L}_{\text{BB}}\text{RuCp}(\text{NCMe})\cdot\text{PF}_6$ . The growth of the signal at 2.9 ppm shows the equilibration to form  $(A,S,S)\text{-L}_{\text{BB}}\text{RuCp}(\text{NCMe})\cdot\text{PF}_6$ .

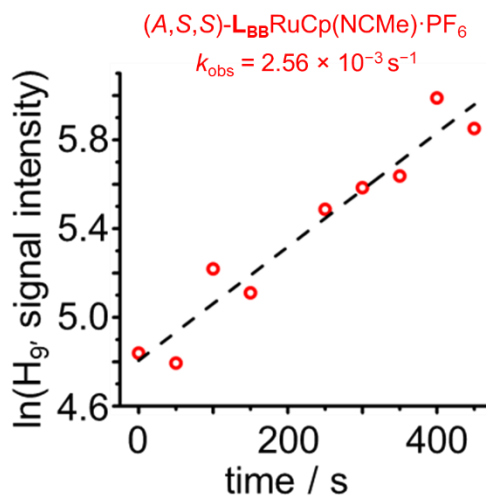


**Figure 4.11.** Integration of the  $^1\text{H}$  NMR ( $\text{CDCl}_3$ , 400 MHz, 298 K) resonance corresponding to  $\text{H}_g$  of  $(A,S,S)\text{-L}_{\text{BB}}\text{RuCp}(\text{NCMe})\cdot\text{PF}_6$  upon dissolving a crystalline sample of  $(C,R,S)\text{-L}_{\text{BB}}\text{RuCp}(\text{NCMe})\cdot\text{PF}_6$  reveals a first-order increase in concentration with  $k_{\text{obs}} = 2.56 \times 10^{-3} \text{ s}^{-1}$ .

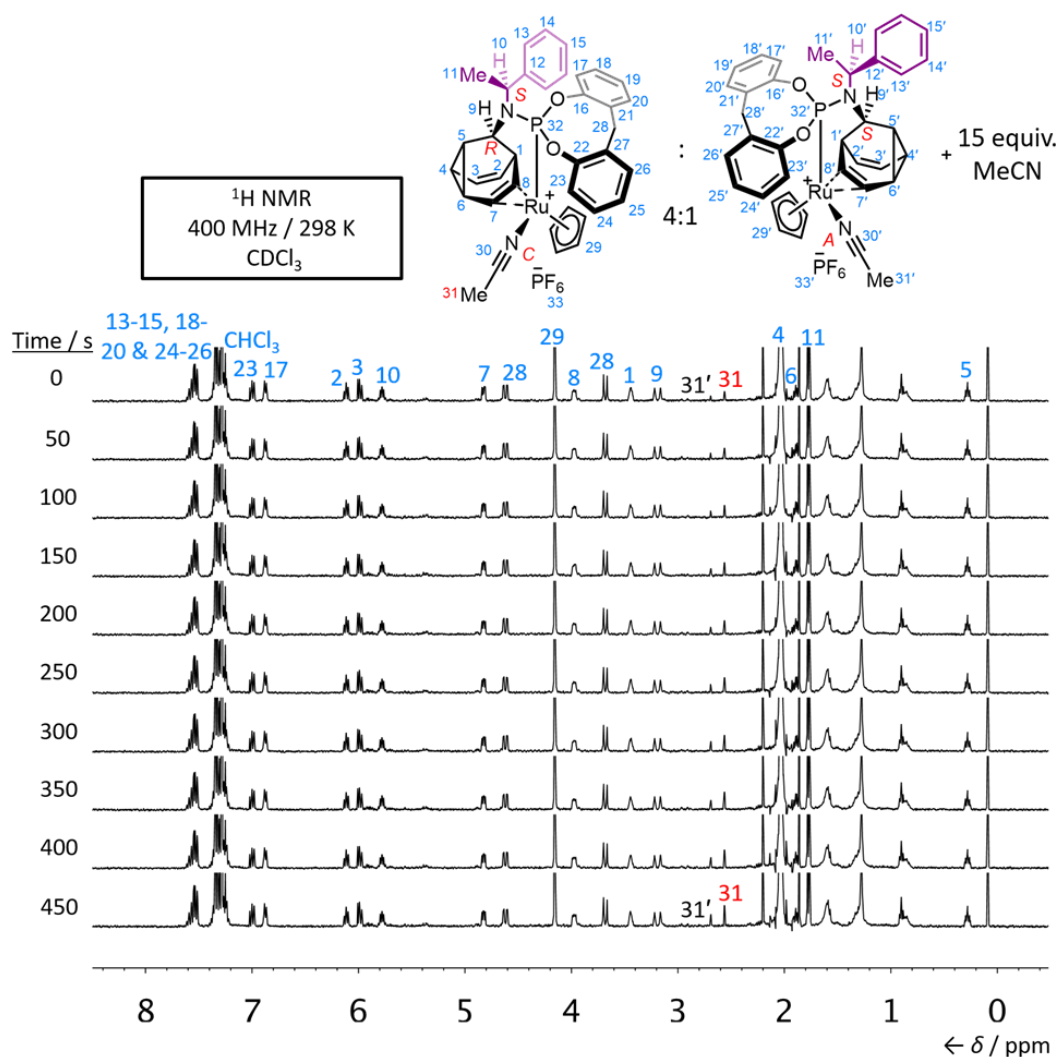


**Figure 4.12.** Partial  $^1\text{H}$  NMR spectra of a 4:1 equilibrium mixture of  $(C,R,S)\text{-L}_{\text{BB}}\text{RuCp}(\text{NCCD}_3)\cdot\text{PF}_6$  and  $(A,S,S)\text{-L}_{\text{BB}}\text{RuCp}(\text{NCCD}_3)\cdot\text{PF}_6$  immediately after the addition of 15 equiv. MeCN showing the increase in the intensity of signals (31 and 31') corresponding to coordinated MeCN. Note: Although the spectra show a 4:1 equilibrium mixture of  $(C,R,S)\text{-L}_{\text{BB}}\text{RuCp}(\text{NCCD}_3)\cdot\text{PF}_6$  and  $(A,S,S)\text{-L}_{\text{BB}}\text{RuCp}(\text{NCCD}_3)\cdot\text{PF}_6$ , only the assignment of the major diastereoisomer ( $(C,R,S)\text{-L}_{\text{BB}}\text{RuCp}(\text{NCCD}_3)\cdot\text{PF}_6$ ) is shown (blue and red labels), with the exception bar the signal corresponding to 31' (black label).

In order to determine the rate of MeCN exchange, the MeCN ligand of  $\text{L}_{\text{BB}}\text{RuCp}(\text{NCMe})\cdot\text{PF}_6$  was exchanged for  $\text{CD}_3\text{CN}$  by dissolving 4.6 mg of the complex in  $\text{CDCl}_3$  containing small amount  $\text{CD}_3\text{CN}$  and standing overnight before evaporating solvent under reduced pressure. The resulting  $\text{L}_{\text{BB}}\text{RuCp}(\text{NCCD}_3)\cdot\text{PF}_6$  complex was then dissolved in  $\text{CDCl}_3$  at 298 K. A solution of MeCN (~15 equiv.) in  $\text{CDCl}_3$  was added and rapidly mixed before a series of sequential  $^1\text{H}$  NMR spectra were recorded (Figure 4.12). The growth in the signals corresponding to non-deuterated MeCN proton environments of  $(C,R,S)\text{-L}_{\text{BB}}\text{RuCp}(\text{NCMe})\cdot\text{PF}_6$  ( $\text{H}_{31}$ ) and  $(A,S,S)\text{-L}_{\text{BB}}\text{RuCp}(\text{NCMe})\cdot\text{PF}_6$  ( $\text{H}_{31'}$ ) is shown in Figure 4.12.

**L<sub>BB</sub>RuCp(NCMe)·PF<sub>6</sub>** (**H<sub>31</sub>'**) was monitored over several minutes. Assuming first-order processes with rate-limiting dissociation of CD<sub>3</sub>CN, rates were estimated (Figure 4.13) as the gradients of straight lines fitted to plots of natural logarithm of the peak intensity against time, giving observed rate constants,  $k_{\text{obs}}$ , of  $1.27 \times 10^{-3} \text{ s}^{-1} \pm 10.7\%$  and  $1.45 \times 10^{-3} \text{ s}^{-1} \pm 13.5\%$  for (*C,R,S*)-**L<sub>BB</sub>RuCp(NCMe)·PF<sub>6</sub>** and (*A,S,S*)-**L<sub>BB</sub>RuCp(NCMe)·PF<sub>6</sub>**, respectively. Note that these two figures are within experimental error of one another and very close to the observed rate of dynamic stereoisomerisation. Using the Eyring equation, these rates corresponds to free energies of activation  $\Delta G^\ddagger$  of 89.5 and 89.2 kJ·mol<sup>-1</sup> for (*C,R,S*)-**L<sub>BB</sub>RuCp(NCMe)·PF<sub>6</sub>** and (*A,S,S*)-**L<sub>BB</sub>RuCp(NCMe)·PF<sub>6</sub>**, respectively.

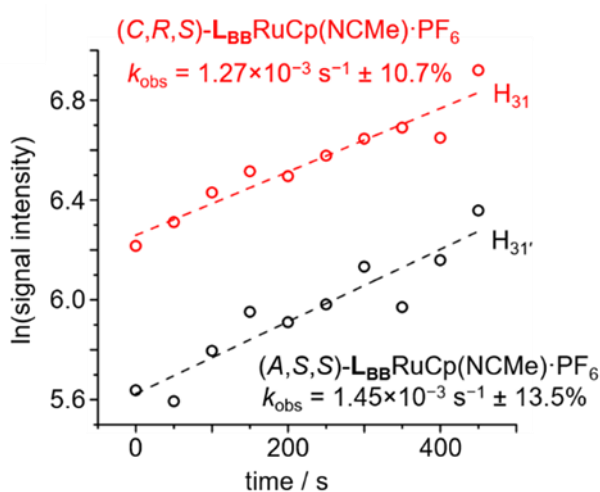


**Figure 4.13.** Plot of the natural logarithm of signal intensity for the two MeCN signals against time, showing the linear trend consistent with a first-order process with rate-limiting ligand dissociation.

Comparison of this value to (1) maxima of the computed potential energy surface (Table S4.1), (2) a CD<sub>3</sub>CN exchange experiment (Figure 4.11) and (3) literature measurements of MeCN dissociation from Cp half-sandwich Ru(II) complexes<sup>55</sup> suggests that the cc-Cope and MeCN exchange processes occur at similar rates. To achieve the (*C,R,S*)-to-(*A,S,S*) isomerization observed by NMR, the complex must undergo both ligand exchange and cc-Cope steps (Figure 4.14). Overall, the energetic bias towards (*C,R,S*)-**L<sub>BB</sub>RuCp(NCMe)·PF<sub>6</sub>** and observation of its stepwise stereomutation to (*A,S,S*)-**L<sub>BB</sub>RuCp(NCMe)·PF<sub>6</sub>** illustrate that the fluxional *sp*<sup>3</sup>-carbon cage mediates the transfer of stereochemical information with high fidelity from the single, fixed benzylamino stereocentre through its rigid, tricyclic structure.

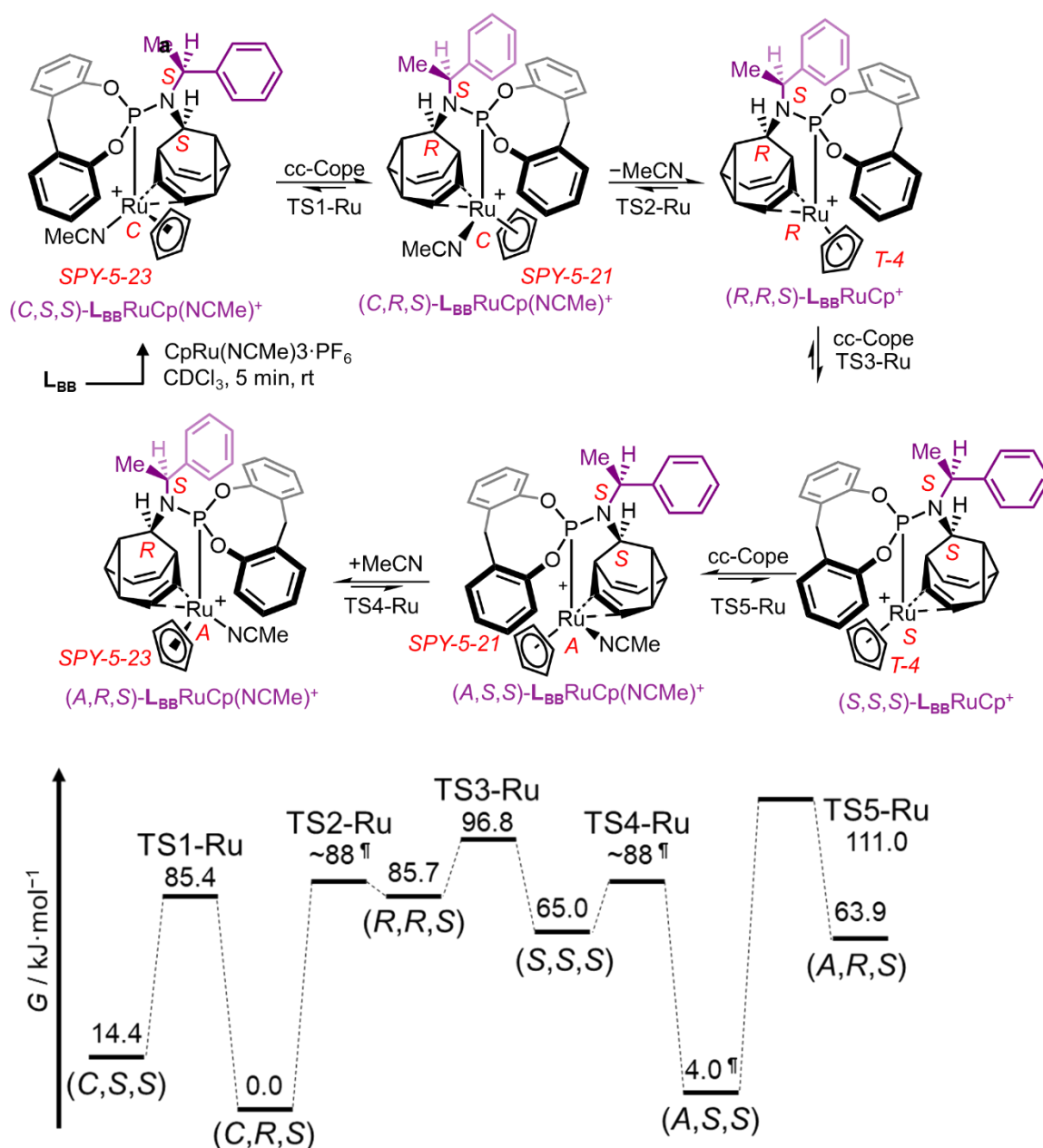


**Figure 4.14.** Four diastereomeric square pyramidal complexes are linked by *cc*-Cope rearrangements and exchange of an MeCN ligand, which proceeds through two intermediate tetrahedral complexes. A non-coordinated PF<sub>6</sub><sup>-</sup> counterion is omitted from the structural formula of each complex for clarity. A potential energy surface for isomerization based on calculated  $\Delta G$  and  $\Delta G^\ddagger$  for the *cc*-Cope processes ( $\omega\text{B97X-D/6-311++G(d,p)/SDD/CS}_2$ ). <sup>¶</sup> Experimentally measured ligand exchange  $\Delta G^\ddagger$  values (kJ·mol<sup>-1</sup>), through TS2-Ru and/or TS4-Ru, are shown for reference.

## 4.7 Controlling Bullvalene Isomerisation using Phosphorus-Olefin Ligands

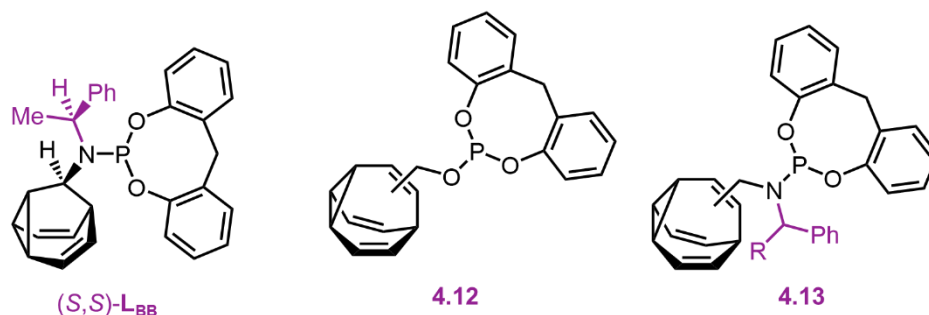
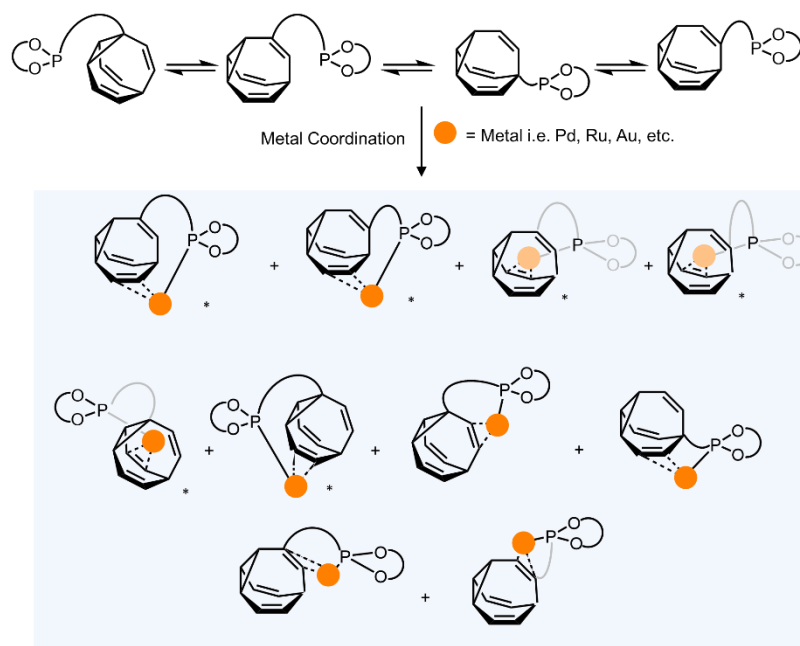


**Figure 4.15.** Synthetic aims of this project: bidentate phosphite (**4.12**) and phosphoramidite (**4.13**) ligands incorporating a **BV** core.

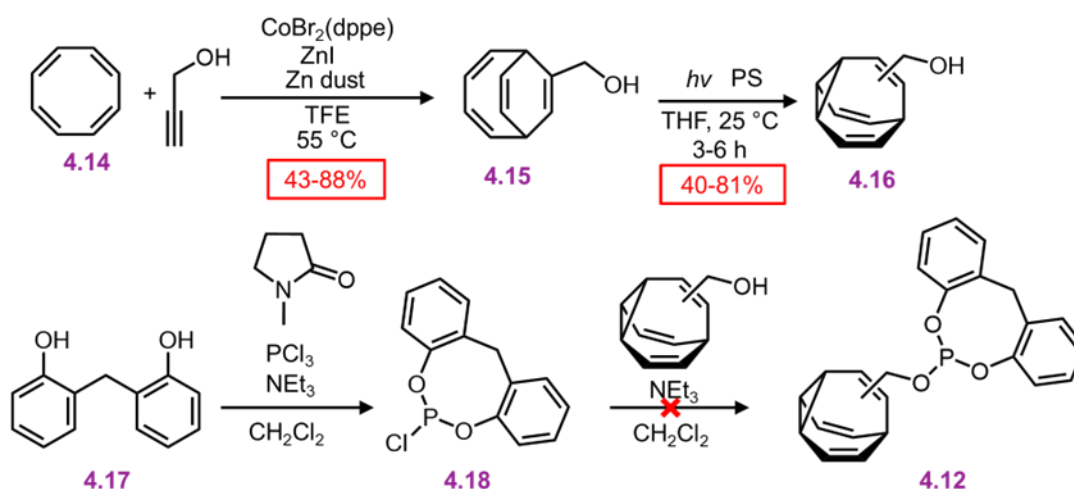
The control of the dynamic  $sp^3$ -C centre of barbaralane utilising the chiral phosphoramidite ligands allowed the induction of chiral information to a metal centre. Mimicking the same binding motif (phosphorous-based olefin bidentate ligands) on the more complex fluxional bullvalene can allow for biasing the isomerisation distribution of the **BVs** (Figure 4.15). Fallon *et al.*<sup>54</sup> on BV-based metal cages (Figure 3.7) demonstrated that anions encapsulated in the cages exert a geometric constraint; the isomer distributions of the BV ligands (**3.7**) in the cage are locked to maintain sufficient space inside the cage for the counter anion.<sup>1</sup> It is expected that metal binding will exert similar control over the isomer distributions of the target ligands of this project. BV's fluxional nature means **4.12** and **4.13** will have variable geometries and bite angles; certain geometries of **4.12** and **4.14** will favour metal binding more than others. Figure 4.16 shows some of the potential ways in which **4.12** and **4.13** might bind to a metal centre.



Possible dynamic mixture of coordination isomers in equilibrium

**Figure 4.16.** Schematics showing different ways in which target ligands **4.12** and **4.13** might bind to a metal centre (orange circle) via their phosphorus atoms and a bullvalene alkene moiety. The BVs with \* are chiral. Both enantiomers of each are shown.

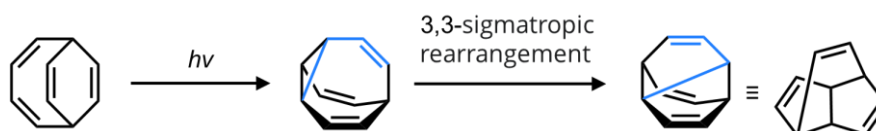
## 4.8 Synthesis towards phosphite BV ligands



**Scheme 4.6.** Synthesis towards phosphite-based buvallane ligand.

Scheme 4.6 shows synthesis towards the phosphite-based ligand, **4.12** using the mono(hydroxymethylene) bullvalene **4.16** as a precursor. Using modified literature procedure from Fallon et al.<sup>56</sup>, cobalt-catalysed cycloadditions of COTT with propargyl alcohol to form the desired bicyclo[4.2.2]deca-2,4,7,9-tetraenes (BDT) **4.15** in moderate yields. Following the cycloaddition, a photorearrangement of **4.15** to **4.16**

was carried out using 365 nm light in the presence of a photosensitiser, 9*H*-thioxanthen-9-one. The photorearrangement of BDT **4.15** to BV **4.16** shown in Scheme 4.6 was challenging to optimize due to undesired photochemical [3,3] sigmatropic rearrangement of the bullvalene product **4.16** to a complex mixture lumibullvalenes we could not fully characterise. Recently, Pauluat et al. synthesis a series of fluorescent bullvalenes using bis(hydroxymethyl)bullvalene as a precursor and was able to isolate and fully characterise the bis(hydroxymethyl)lumibullvalene.<sup>57</sup>



**Scheme 4.7.** By-product of the photorearrangement of bullvalene.<sup>57</sup>

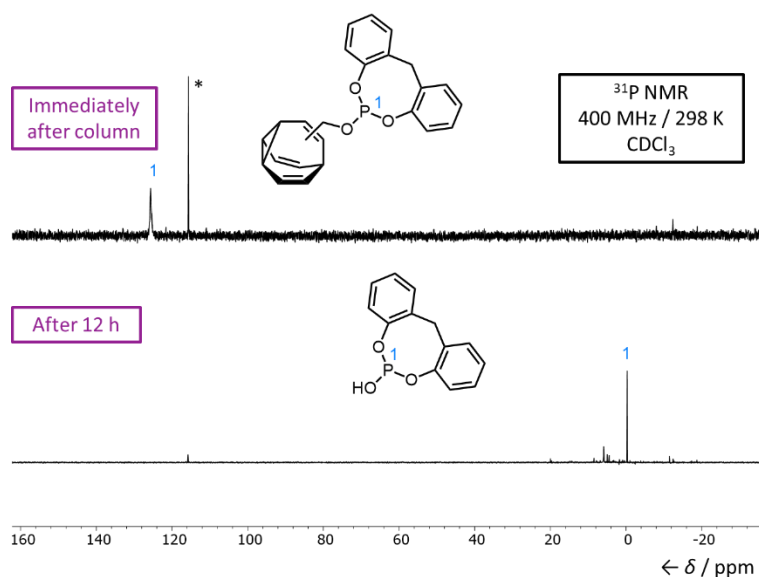
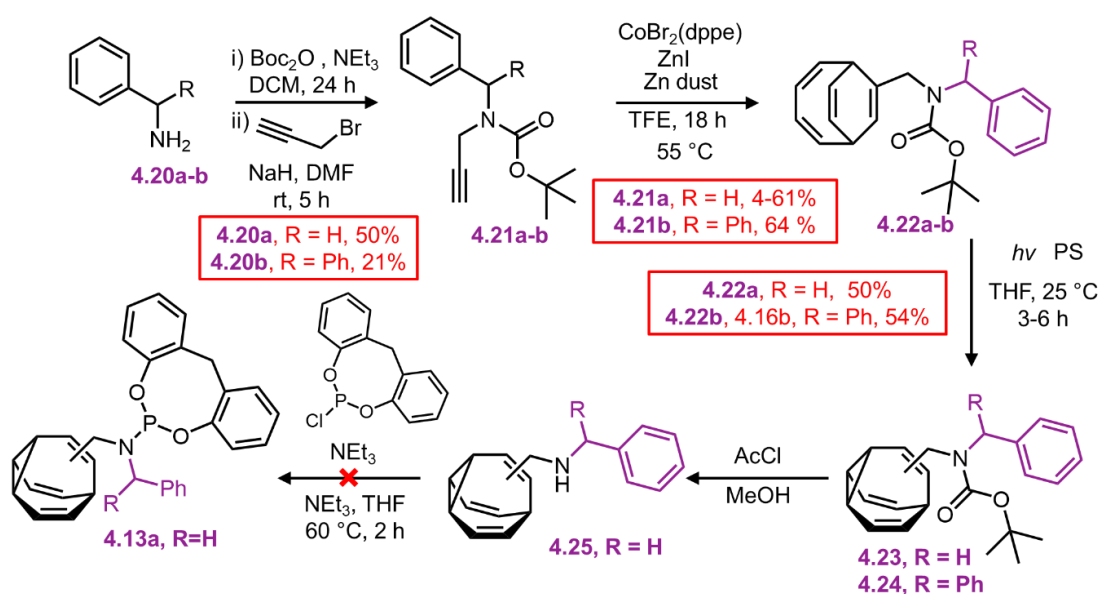


**Figure 4.17.** Partial <sup>31</sup>P NMR spectra of one of the fractions obtained during an attempted synthesis of **4.12** (top) and the same fraction after 12 h storage under N<sub>2</sub> (bottom). The phosphorous peak potentially corresponding to **4.12** is labelled as is the peak corresponding to the hydrolysis product.<sup>58</sup>

Synthesis of phosphite ligand **4.12** was attempted using the one-pot procedure shown in Figure 4.6. The phosphorochloridite intermediate, **4.18**, is formed *in situ* since phosphorochloridites are susceptible to hydrolysis.<sup>58</sup> *In situ* formation of **4.12** was attempted by treatment of crude phosphorochloridite intermediate **4.18** with hydroxymethyl bullvalene, however, there was no successful isolation of product due

to the P-O bonds in phosphites such as **4.12** being susceptible to hydrolysis and oxidation. Purification was attempted by flash column chromatography using neutral alumina to limit acid or base-catalysed hydrolysis of the products on the column. The column fractions were analysed using NMR spectroscopy (Figure 4.17). The crude  $^{31}\text{P}$  NMR spectrum contained peaks in the range of 126 ppm expected for **4.12**<sup>59</sup> from the chromatography purification attempt. 12 h after the isolation of the desired fraction, the  $^{31}\text{P}$  NMR revealed the disappearance of peaks in the range of 125-150 ppm and the presence of multiple peaks between -25-25 ppm, suggesting that phosphonate species were formed via hydrolysis reactions during and after purification of the reaction products.



**Scheme 4.8.** Attempted synthesis of phosphoramidite olefin ligand **4.12**

Moving forward, **4.13** became a synthetic aim since it closely resembles **L<sub>BB</sub>** (Scheme 4.8). Starting from commercially available benzyl aniline **4.20a** and benzhydryl aniline **4.20b**, the amine was protected with Boc-anhydride followed by a nucleophilic substitution reaction with propargyl bromide to make the desired amine substituted alkyne **4.21**. Cobalt-catalysed cycloadditions of COTT using amine alkyne formed the desired amine BDTs **4.22ab**. The photorearrangement of *N*-boc methyl amine BDT **4.22ab** to *N*-boc methyl amine bullvalene **4.23** and **4.24** was carried out using 365 nm light in the presence of, 9*H*-thioxanthen-9-one (Scheme 4.8). Only the benzyl derivative **4.23** was carried forward to make the phosphoramidite olefin ligand **4.13a**. The deprotection of the amine was carried out using acetyl chloride in anhydrous

methanol to make HCl *in situ* to yield the free amine **4.25**. NMR analysis revealed that the free amine **4.25** was not stable in storage, so once the deprotection of **4.23** was conducted, the crude product reacted immediately after purification. Initial attempts toward the synthesis of the phosphoramidite olefin ligand **4.13a** used the one-pot procedure to make the phosphorochloridite intermediate **4.18**. **BV** carbamate **4.25** was deprotonated and reacted with **4.18** to attempt to synthesize the phosphoramidite olefin ligand. The crude  $^{31}\text{P}$  NMR revealed no signals that could be associated with a phosphoramidite type ligand.<sup>60</sup> To solve this issue with the phosphoramidite reaction, phosphorochloridite intermediate **4.18** was synthesised and isolated separately. **4.18** was synthesised using literature procedure by Feringa et al.<sup>61</sup> and it was stored under nitrogen in a glovebox where it was stable in excess of 2 months. Strictly anhydrous conditions were sought for the formation of **4.13a** since it was expected to be potentially susceptible to hydrolysis.<sup>62</sup> The reaction was attempted by stirring **4.25** with 1.1 equiv of **4.18** in the presence of base at 60 °C; a change in composition was observed by NMR spectroscopy. The crude products were purified by flash column chromatography using neutral alumina to limit their immobilisation on the column. A promising fraction with a phosphorous signal at 138 ppm in its  $^{31}\text{P}$  spectrum was isolated; this  $^{31}\text{P}$  spectrum is shown in Figure 4.18. This chemical shift is similar to the analogous **BB** ligand **LBB** (136 ppm); this suggested that **4.13a** was formed.<sup>62</sup> In an attempt to induce metal binding, 0.8 equiv. of the metal complex  $\text{PdCl}_2(\text{MeCN})_2$  was added to the promising fraction immediately after its isolation. Addition of the complex  $\text{PdCl}_2(\text{MeCN})_2$  may have exacerbated the degradation of **4.13a**, since Pd(II) salts sometimes catalyse the oxidation of phosphoramidites. While many biaryl phosphoramidites are chromatographically and air stable<sup>61</sup>, however, some are susceptible to aerobic oxidation<sup>62</sup> and hydrolysis<sup>63</sup>. The experimental evidence presented suggests that **4.13a**, like **4.12**, is not air stable. The same issues of instability of **4.12** is experienced by **4.13a** instability due hydrolysis or oxidation. The most important factor affecting stability of the phosphoramidite ligand is the lack of steric bulk around the phosphorus centre in **4.13a**. The benzhydryl **BV** derivative, **4.22b**, should solve this issue of steric with the additional phenyl adjacent to the nitrogen atom.

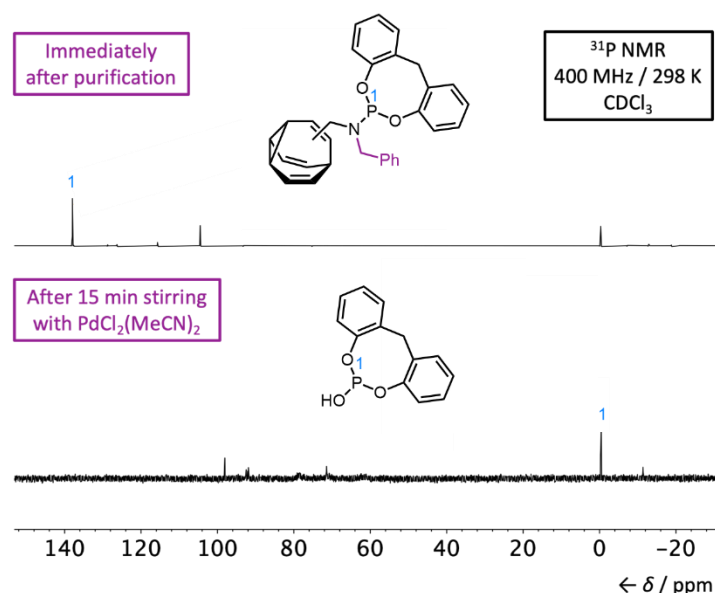


**Figure 4.18.** Partial  $^{31}\text{P}$  NMR spectra of a promising fraction obtained during an attempted synthesis of **4.13a** (top) and the same fraction after 15 min stirring with 0.8 equiv of  $\text{PdCl}_2(\text{MeCN})_2$  (bottom). A phosphorous peak potentially corresponding to **4.13a** is labelled, as is the peak corresponding to the hydrolysis product.<sup>63</sup>

## 4.9 Fluxional Cages influencing Carbamate Rotamers

Rotations about single bonds must overcome a rotational energy barrier to interconvert one conformer to another. Free rotation occurs if the energy barrier is low leading to certain molecules existing as a rapidly equilibrating mixture of multiple conformers. If the energy barrier is high enough then there is restricted rotation, a molecule may exist for a relatively long time period as a stable rotational isomer or rotamer. Rotamers have become a popular molecular motion concept in molecular machines<sup>64</sup> and the use of rotamers have played an important role in axial chirality<sup>65</sup> and asymmetric catalysts<sup>66</sup>. Upon inspection of the BDT carbamates **4.22ab**, solution-state NMR revealed these BDT carbamates have a rotation barrier about the N-CO bond of the carbamate group (Figure 4.19). Figure 4.19 revealed **4.22a** have proton signals derived from the presence of dynamic diastereomers that are in slow exchange at r.t. in  $\text{CDCl}_3$ . Proton  $\text{H}_1$  is split into a pair of diastereomer peaks that integrate to 1 together (1:1 ratio), the ppm difference between the two peaks is too large to be from  $J_{\text{H-H}}$  coupling from the vinyl proton  $\text{H}_{10}$  or  $\text{H}_8$ . Additionally, the *t*-butyl proton  $\text{H}_{19}$  is also split into a pair of diastereomer peaks indicating the presence of observable rotamers in slow exchange. Solution state NMR analysis of **4.22a** revealed unusual splitting patterns in the  $^{13}\text{C}$  NMR spectrum. In the HSQC correlation spectrum of **4.22a**, certain proton

environments were correlated with two carbon peaks when they were expected to be correlated with a single carbon peak; an example of this is shown in Figure 4.20. The features of the spectra can be rationalised by the fact that **4.22a** is present as a pair of diastereomers.

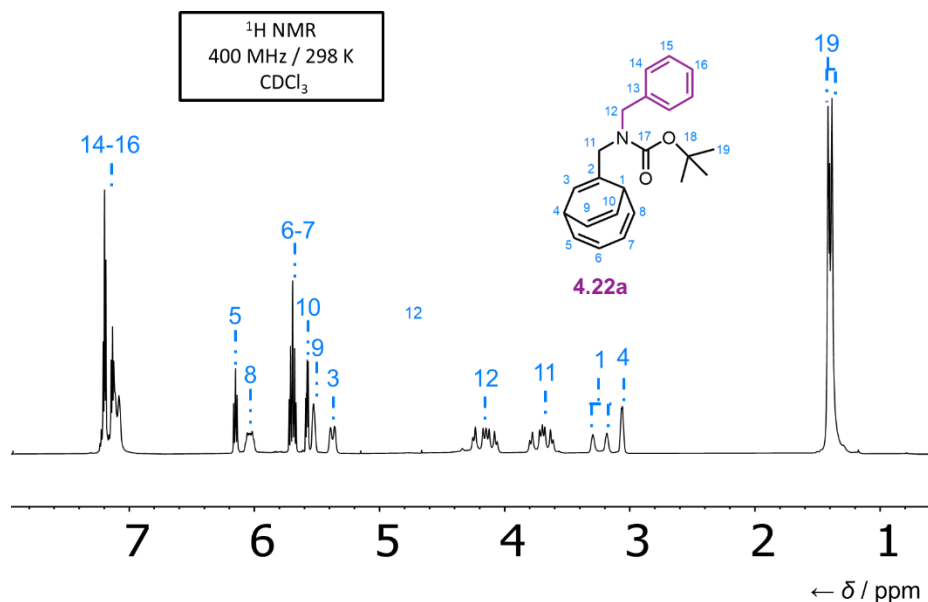


**Figure 4.19.** Partial  $^1\text{H}$  NMR spectrum of mono(*N*-benzyl)methylene amine BDT(**4.22a**) with peaks labelled with corresponding protons.

These observable pair of diastereomer proton and carbon peaks are most likely due to the rotation barrier of N–CO bond. The barrier to rotation around the N–CO bond in amides depends on the bulkiness and electronic properties of surrounding moieties. When the energetic barrier to rotation is sufficiently high, it results in the generation of *E/Z* diastereomers; an example of this is shown by (*E/Z*)-**4.26** in Figure 4.21.<sup>67</sup> **4.22b** has an additional phenyl which increases the steric bulk around the NCO bond. Solution state NMR analysis revealed similar patterns of proton signal peak splitting, however, these diastereomer peaks are broadened into the baseline of the NMR spectrum ( $\text{H}_1$ ,  $\text{H}_{11}$ ,  $\text{H}_{12}$ ) possibly due to sample being above the coalescence temperature to enter slow exchange of the diastereomers. The *E* and *Z* isomers of **4.22ab** were assigned using the Cahn-Ingold-Prelog priority rules highlighted in Figure 4.21b. Unfortunately, COSY, HMBC and HSQC correlations were used to deconvolute and assign the peaks of the two diastereomers; however, the assignments could not be attributed specifically

to the *E* and *Z* isomers. In both **4.22ab**, show both there is no favoured structure (1:1 *E/Z*).

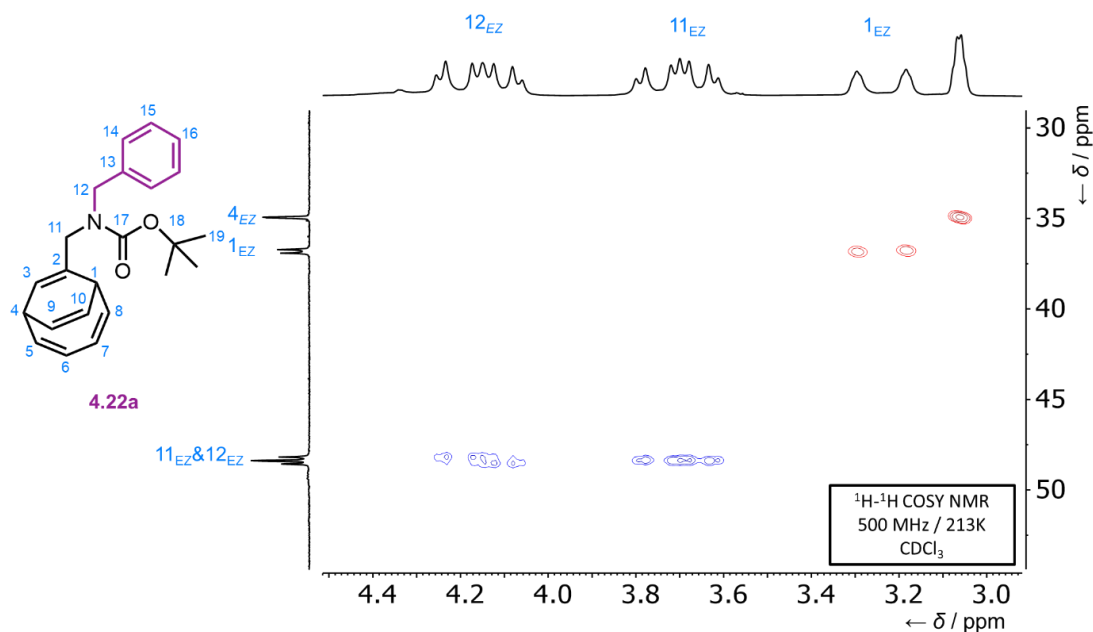


**Figure 4.20.** Partial HSQC spectrum of **4.22a**. The zoomed-in region gives an example of a proton environment ( $H_1$ ,  $H_{11}$ ,  $H_{12}$ ) which is directly correlated to 3 carbon environments; this arises since **4.22a** is present in the solution as two diastereomers.

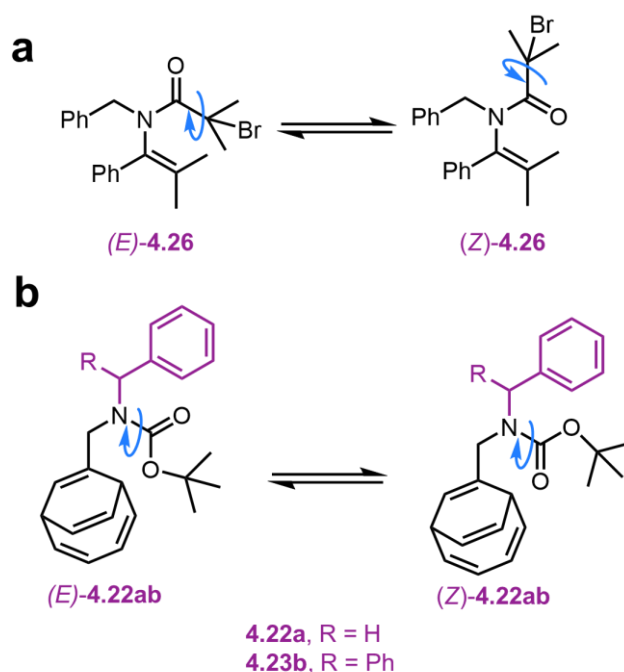


**Figure 4.21.** Example of an amide (**56**) with a sufficiently high barrier to rotation around its N-CO bond that it exists as a pair of diastereomers in solution.<sup>67</sup> Structural formulae of the diastereomers of mono(*N*-benzyl-Boc)methylene amine BDT.

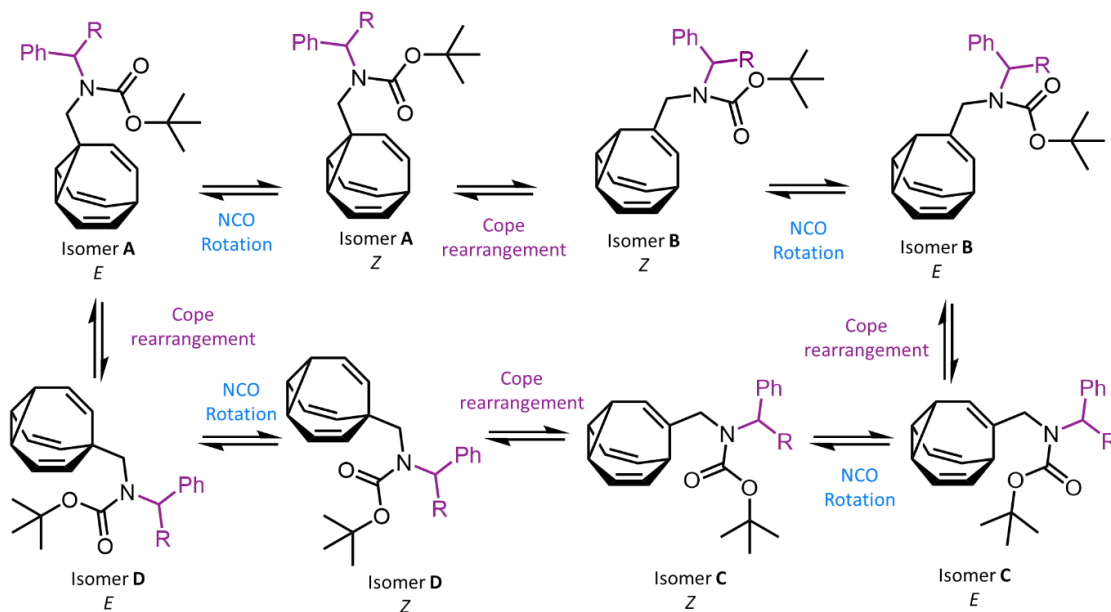


**Figure 4.22.** Schematic of the constitutional isomers along with rotational isomers along NCO bond of bullvalene carbamates (4.23, 4.24).

The irradiation of the **BDT** to **BV** opens a new avenue to explore, where the rotation barrier of NCO should still be present and now the fluxional nature of the cage can additionally influence this barrier and the ratio of rotamers. Compared to bullvalene carbamates 4.23–4.25, the BDT carbamate (4.22ab) can be thought of a ‘static’ isomer of bullvalene. The conformation of the positional isomers of bullvalene should have varying steric effects on the rotation barrier of the NCO between the *E/Z* forms of the carbamates, effecting the rate of rotational isomerisation of the compound (Figure 4.22). Also, the steric bulk of the carbamate should affect the isomer distribution of positional conformers of the **BV**. To test our hypothesis of dynamic interplay between the rotational isomerisation (N–CO bond) vs positional isomers (**BV**), computational modelling using DFT was conducted to predict the isomer distribution of positional isomers and rotamers of each positional isomer. The predicted isomer distribution can be used to help decipher the experimental isomer distribution of these BV carbamates between positional and rotational isomers.

#### 4.10 Modelling the Interplay between Rotational and Constitutional Isomerism of Bullvalene Carbamates

In this computational study, MM2 energy minimisation was used on the positional isomers (4.23a–d, 4.24a–d) of each bullvalene to quickly optimize the geometry of starting structure from a ChemDraw file. Confab conformer search software was used

to find all rotamers within 63 kJ/mol for each positional isomer. All these identified rotamers of each positional isomer were used as the starting geometry for full optimisation.

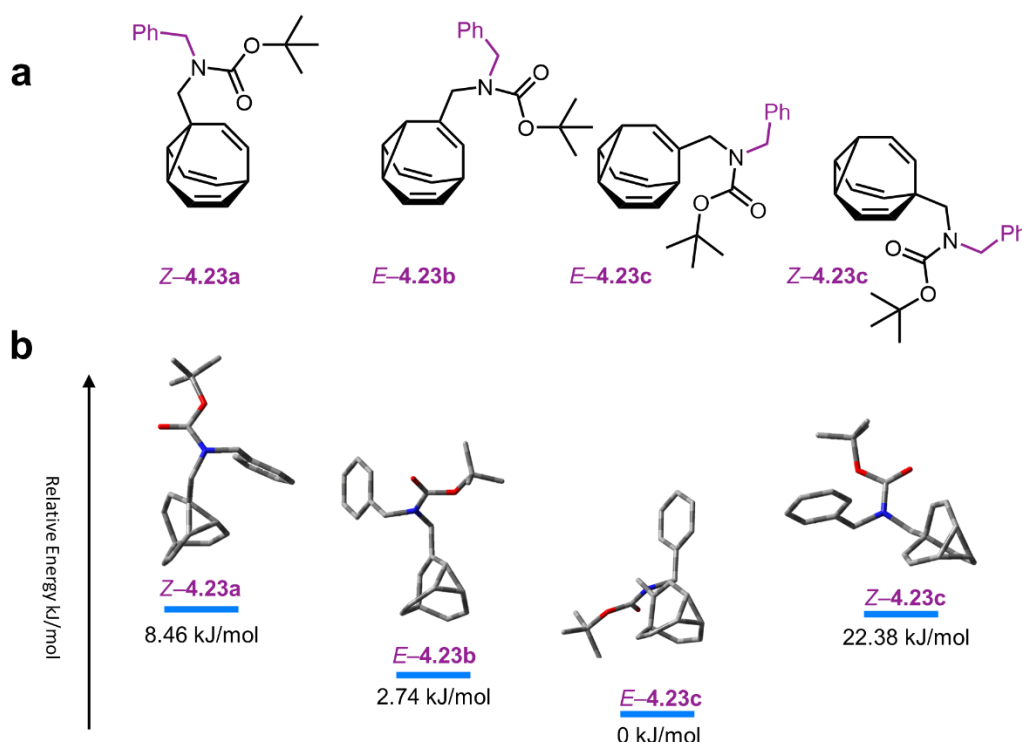


**Figure 4.23.** Plot of the ground state geometries and relative energies of the four constitutional isomers of mono(*N*-benzyl)methylene bullvalene carbamate (**4.23**). a) Structures of four constitutional isomers of mono(*N*-benzyl)methylene bullvalene carbamate. b) Geometries and energies of the four constitutional isomers of mono(*N*-benzyl)methylene bullvalene carbamate that were optimised in Gaussian 16 using the B3LYP functional, D3BJ dispersion correction and Def2SVP basis set with the implicit continuous solvation model CPCM.

All isomer geometries were then fully optimized using the hybrid dispersion corrected B3LYP-D3BJ functional and the Def2-SVP basis set with the use of the implicit continuous solvation model CPCM (CDCl<sub>3</sub>). To ensure that the calculations were optimised to an energy minimum, as opposed to transition state structures, frequency calculations were also performed. No imaginary frequencies were found, this confirms that all calculated structures are minima on the potential energy surface. The energy minima geometries and relative energies of each of the four constitutional isomers of **4.23-4.24** are shown in Figure 4.23 & Figure 4.24. In both molecules, **4.23-24**, the vinyl substituted (sp<sup>2</sup>) isomers were found the two most stable isomers with positional isomer C (Figure 4.22, barcode 000 000 001) found to be the most stable.

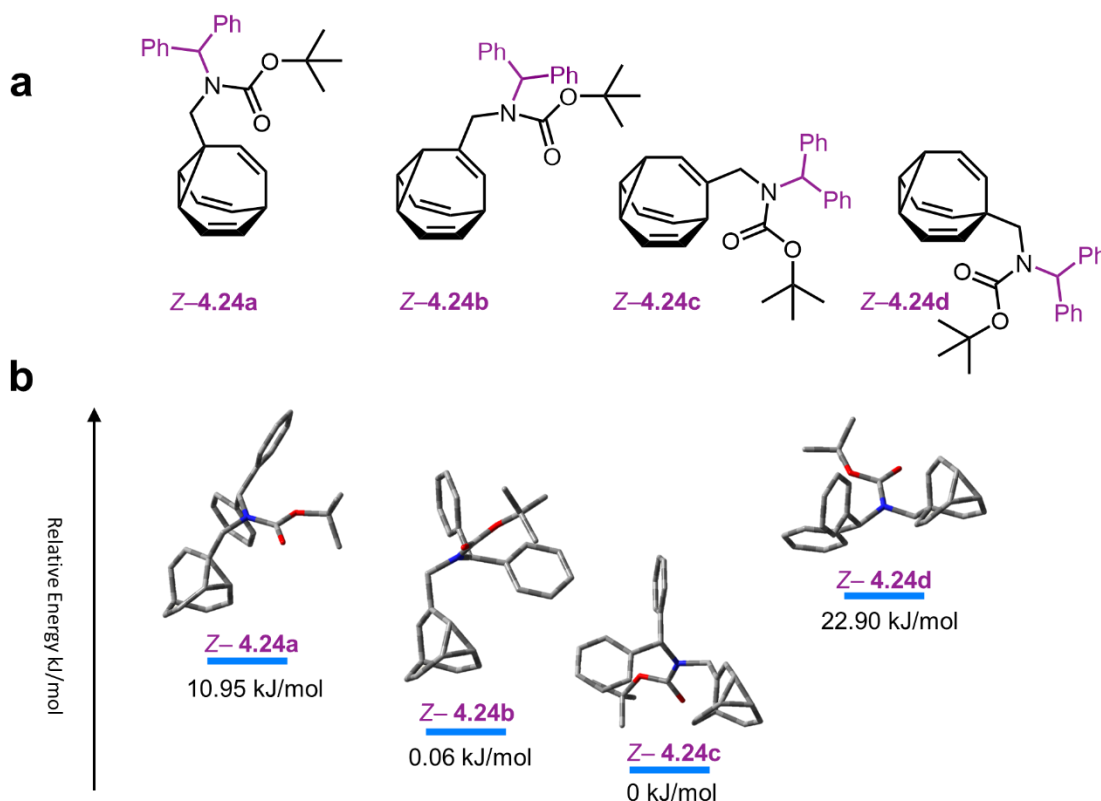


**Figure 4.24.** Plot of the ground state geometries and relative energies of the four constitutional isomers of mono(*N*-benzhydryl)methylene bullvalene carbamate (**4.24**). a) Structures of four constitutional isomers of mono(*N*-benzhydryl)methylene bullvalene carbamate. b) Geometries and energies of the four constitutional isomers of mono(*N*-benzyl)methylene bullvalene carbamate that were optimised in Gaussian 16 using the B3LYP functional, D3BJ dispersion correction and Def2SVP basis set with the implicit continuous solvation model CPCM.

This stability can be rationalised by the conjugative stabilisation they experience between the substituent and the double bond in their **BV** backbones. Fallon et al.<sup>56</sup> have performed similar DFT calculations to determine the relative stabilities of the isomers of mono-substituted **BVs**; these calculations yield the same orders of stability of the isomers of a given **BV** as those determined in this work.<sup>56</sup> To understand the isomer distribution of these **BV** carbamates in terms of positional isomers and rotamers, a predictive model is used by calculating the population distributions at different temperatures based on using the relative energy,  $\Delta G_{\text{calc}}$ , of the isomers and the Boltzmann distribution, EQ 1 (Table 4.1 & Table 4.2). Three different temperatures (213 K, 298 K, 313K) were used to calculate the population distribution of isomers can be verified experimentally using VT NMR. According to the calculated distributions at 213 K, the 4 lowest energy isomers should be present in observable quantities by the low temperature solution state NMR (Table 4.1 & 4.2). The vinyl isomers (B, C) are

predicted to be the two positional isomers present and the rotamers of these vinyl isomers are more stable than positional isomers A & D. This theoretical population distribution can be rationalised as the rotation across the NCO bond to the *E/Z* forms of **BV** carbamates (**4.23-4.24**) are producing more stable isomers then moving away from the conjugative stabilisation of  $sp^2$  bullvalene carbon to the carbamate substituent in the B&C isomers compared to the  $sp^3$  bullvalene carbon (A&D). The computational populations were calculated to aid understanding and assignment of the  $^1\text{H}$  and  $^{13}\text{C}$  NMR spectra of **4.23-4.24**.

$$p_i \propto e^{\frac{-\Delta G_{\text{calc}}}{kT}}$$

**Equation 1.** Theoretical populations,  $p_i$ , of each isomer of **4.23-4.24** at different temperatures (25 °C, -60 °C and +60 °C) were determined using the relative energies,  $\Delta G_{\text{calc}}$ , of the isomers and the Boltzmann distribution ( $k$ ).

**Table 4.1.** Relative energies of the constitutional/rotational isomers of mono(*N*-benzyl)methylene bullvalene carbamate (**4.23**) and their populations at different temperatures.

Isomer	Barcode	$\Delta G_{\text{calc}} / \text{kJ mol}^{-1}$	Population (213 K)	Population (298 K)	Population (333 K)
<b>4.23a – E</b>	000 000 100 0	13.92	0.0%	0.1%	0.3%
<b>4.23a – Z</b>	000 000 100 0	8.46	0.4%	1.4%	1.9%
<b>4.23b – E</b>	000 000 010 0	2.74	10.0%	13.6%	14.6%
<b>4.23b – Z</b>	000 000 010 0	3.69	5.9%	9.3%	10.4%
<b>4.23c – E</b>	000 000 001 0	0	36.4%	34.3%	33.4%
<b>4.23c – Z</b>	000 000 001 0	0.46	47.3%	41.3%	39.4%
<b>4.23d – E</b>	000 000 000 1	25.80	0.0%	0.0%	0.0%
<b>4.23d – Z</b>	000 000 000 1	22.38	0.0%	0.0%	0.0%

**Table 4.2.** Relative energies of the constitutional/rotational isomers of mono(*N*-benzhydryl)methylene bullvalene carbamate (**4.24**) and their populations at different temperatures.

Isomer	Barcode	$\Delta G_{\text{calc}} / \text{kJ mol}^{-1}$	Population (213 K)	Population (298 K)	Population (333 K)
<b>4.24a – E</b>	000 000 100 0	13.92	0.0%	0.1%	0.2%
<b>4.24a – Z</b>	000 000 100 0	10.95	0.1%	0.4%	0.7%
<b>4.24b – E</b>	000 000 010 0	6.41	1.0%	2.8%	3.5%
<b>4.24b – Z</b>	000 000 010 0	0.06	37.8%	35.8%	35.0%
<b>4.24c – E</b>	000 000 001 0	1.03	21.9%	24.2%	24.7%
<b>4.24c – Z</b>	000 000 001 0	0	39.2%	36.7%	35.8%
<b>4.24b – E</b>	000 000 000 1	30.63	0.0%	0.0%	0.0%
<b>4.24b – E</b>	000 000 000 1	22.90	0.0%	0.0%	0.0%

## 4.11 Solution State NMR Analysis of Fluxional Cage Carbamates

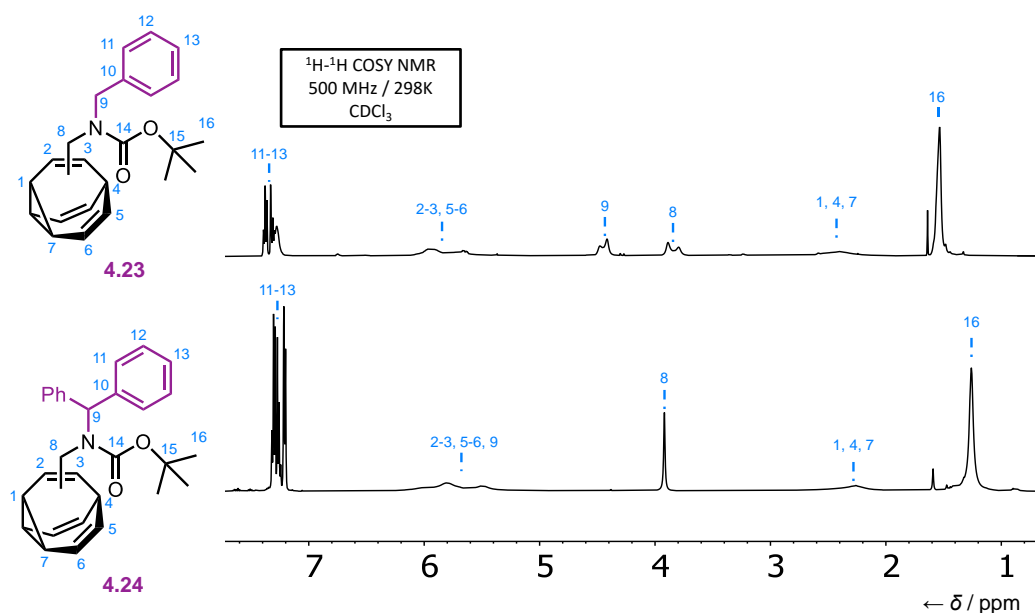
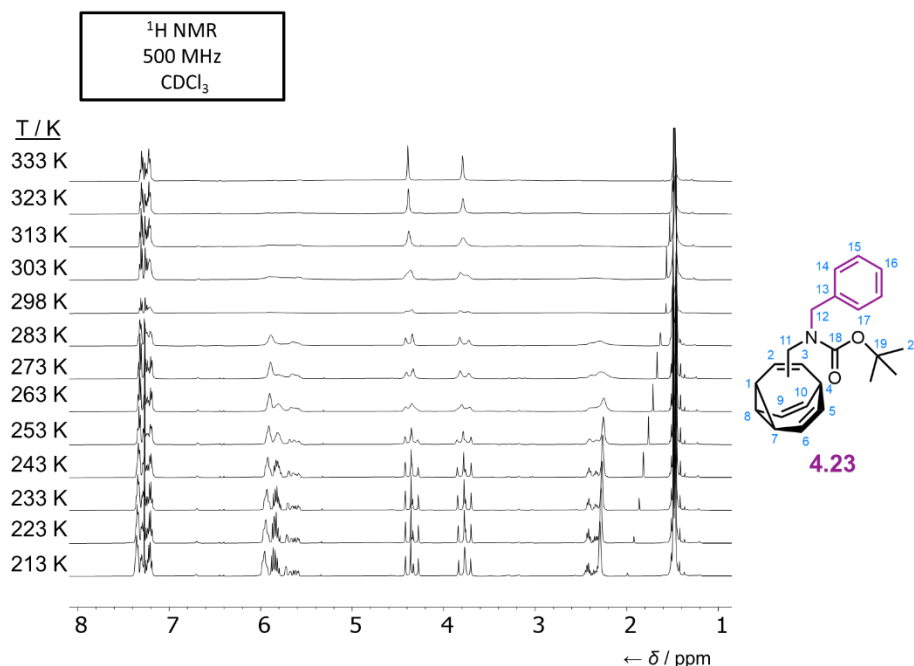


**Figure 4.25.** Partial  $^1\text{H}$  spectra of bullvalene carbamates (**4.23**, **4.24**) recorded at ambient conditions.

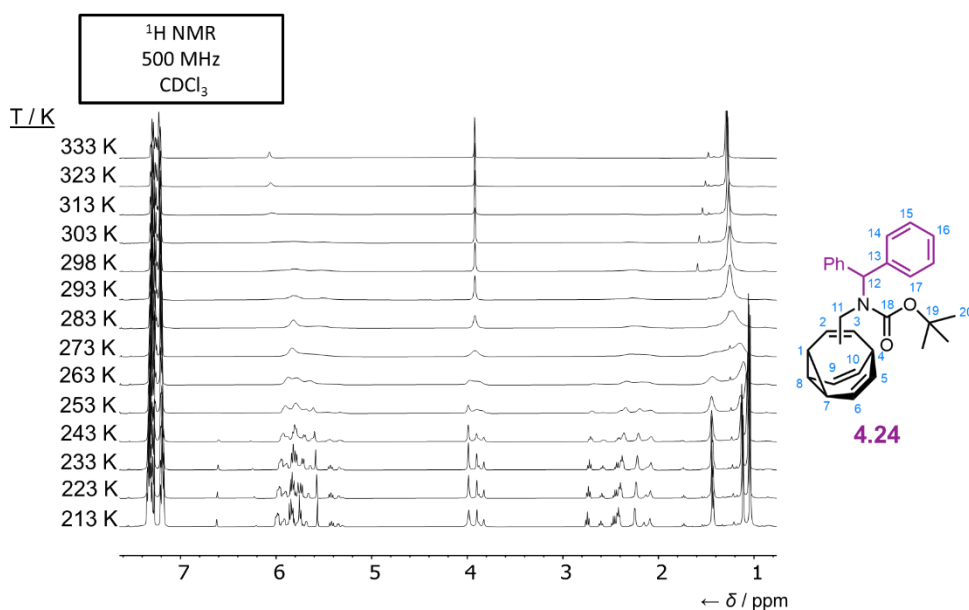
The room temperature solution state  $^1\text{H}$  NMR spectra of **4.23** & **4.24** (Figure 4.25) show the broad peaks characteristic of **BV** protons at room temperature. These broad peaks confirm the fluxional behaviour of **BV**. At room temperature, Cope rearrangements interchange the constitutional isomers of **4.23** & **4.24** (Figure 4.22) at a rate faster than the frequency difference between the discrete chemical environments of those isomers. Hence the **BV** protons of the isomers of **4.24** and **4.23** are represented by just two broad peaks, one representing the vinyl protons and one representing the bridgehead/cyclopropane protons. The chemical shifts of the discrete chemical environments of the isomers are masked within these broad peaks.

VT NMR spectroscopy allows the chemical information masked within the broad peaks in the rt  $^1\text{H}$  NMR spectrum of **BV 4.23 and 4.24** (Figure 4.26 & Figure 4.27) to be revealed. Cooling decreases the thermal energy available to **BVs** and thus slows the rate of its Cope rearrangements. With sufficient cooling, the rate of rearrangement in **4.23** & **4.24** should be slowed such that its constitutional isomers (Figure 4.26 & Figure 4.27) can be visualised by their discrete chemical environments and unique sets of peaks. Integration of the relative areas of these peaks should allow the relative concentration of each isomer in the solution to be determined. Heating **4.24** and **4.23** increases the thermal energy available to it and thus the rate of its Cope rearrangements.

At high enough temperatures, the rate of rearrangement will be rapid fast exchange such that all the BV protons in all the isomers of **BV**s will coalesce into a single peak.



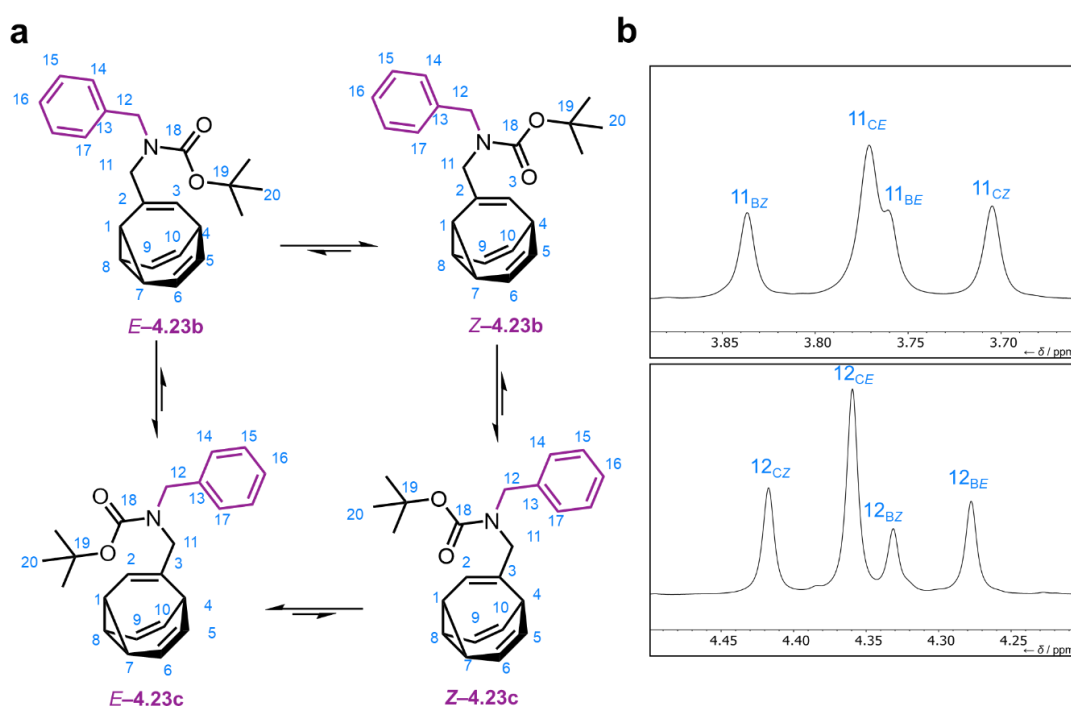
**Figure 4.26.**  $^1\text{H}$  spectra of mono(*N*-benzyl)methylene bullvalene carbamate (**4.23**) recorded from  $-60\text{ }^\circ\text{C}$  to  $+60\text{ }^\circ\text{C}$ .



**Figure 4.27.**  $^1\text{H}$  spectra of mono(*N*-benzhydryl)methylene bullvalene carbamate (**4.24**) recorded from  $-60\text{ }^\circ\text{C}$  to  $+60\text{ }^\circ\text{C}$ .

Variable temperature NMR spectroscopy was used to try and determine the solution state isomer distribution of **BV**s. The  $^1\text{H}$  NMR spectra taken at intervals between  $-60$

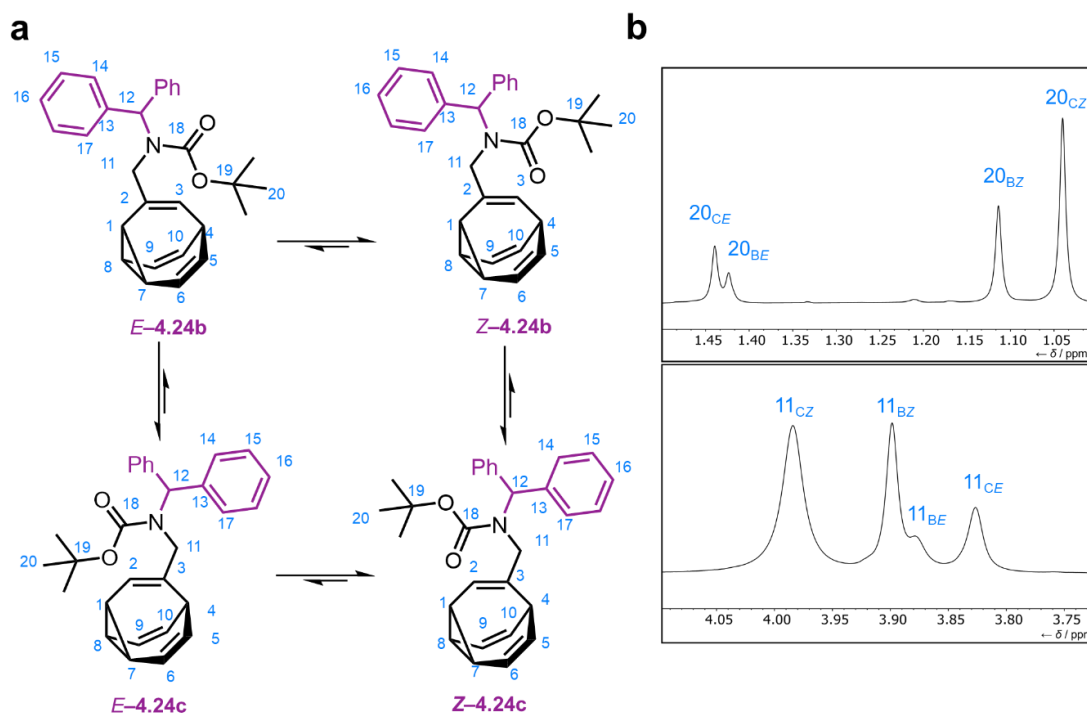
°C and +60 °C are shown in Figure 4.26 and Figure 4.27. Figure 4.26 and Figure 4.27 shows that, as the temperature is increased relative to rt, the BV peaks of **4.23** & **4.24** appear to disappear; they are in fact gradually coalescing and become hidden beneath the baseline. Temperature of 60 °C did not represent a sufficient temperature increase to visualise a single BV peak. Upon cooling, the broad BV peaks are deconvoluted as was expected. Additionally, the methylene peaks ( $H_{11}$  &  $H_{12}$ ) between 3.5 and 4.5 ppm show further splitting upon cooling for **4.23** & **4.24**, caused by ‘freezing out’ out of the *E/Z* diastereomers of **4.23** & **4.24** as well as the positional isomers. At colder temperatures, there is less thermal energy available and so there is no longer free rotation around the N-CO bond in **4.23** & **4.24** within the slow exchange regime.



**Figure 4.28.** Partial  $^1H$  spectra of mono(*N*-benzyl)methylene bullvalene carbamate (**4.23**) were recorded from -60 °C. a) Illustration of Cope arrangement and rotation around the NCO bond to lead to 4 isomers. b) Partial  $^1H$  spectra of methylene protons that show 4 isomers and are assigned according to the positional isomer label and *E/Z* isomerisation.

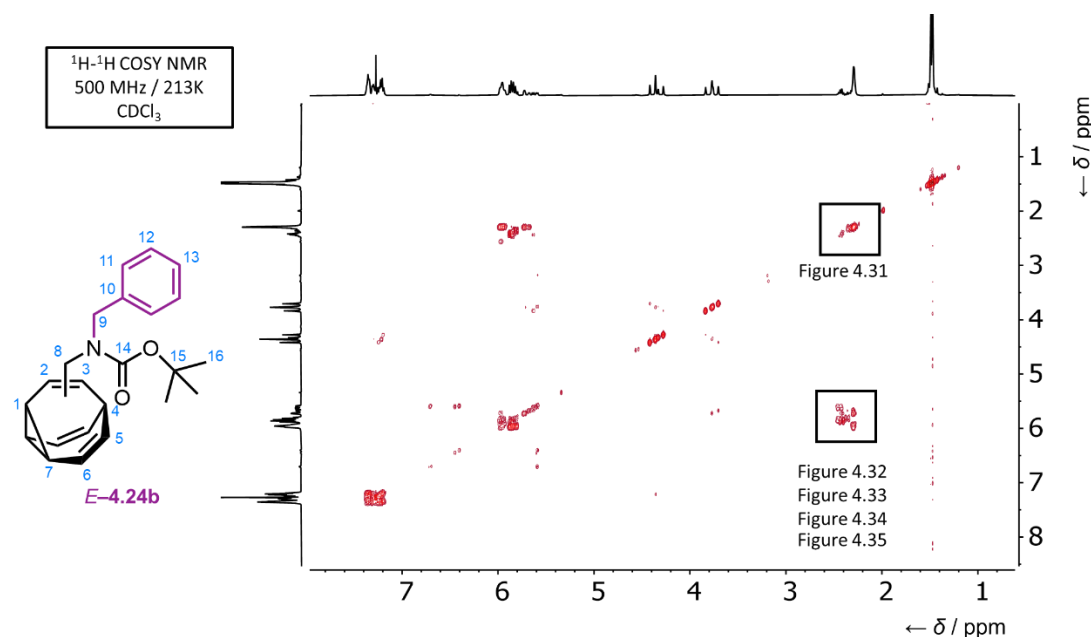
Figure 4.28 and Figure 4.29 shows partial  $^1H$  NMR of the methylene peaks for both BV (**4.23**, **4.24**) and the t-butyl group for **4.24**. Both partial  $^1H$  NMR show singlet peaks (methylene  $H_{11}$  &  $H_{12}$ , t-butyl group  $H_{20}$ ) corresponding to 4 observable isomers present at -60 °C which corresponds well with the computational calculations (Table 4.1 & 4.2). These proton signals should singlets as there is no proton for coupling in proximity. Fallon et al. showed that mono-substituted BV typically only have two

isomers in observable amounts (vinyl isomer C & D) which means the additional peaks in the low temperature NMR can come from the rotamers of these vinyl isomers (Figure 4.22).



**Figure 4.29.** Partial  $^1\text{H}$  spectra of mono(*N*-benzhydryl)methylene bullvalene carbamate (**4.24**) were recorded from  $-60^\circ\text{C}$ . a) Illustration of Cope arrangement and rotation around the NCO bond to lead to 4 isomers. b) Partial  $^1\text{H}$  spectra of methylene protons that show 4 isomers and are assigned according to the positional isomer label and *E/Z* isomerisation.

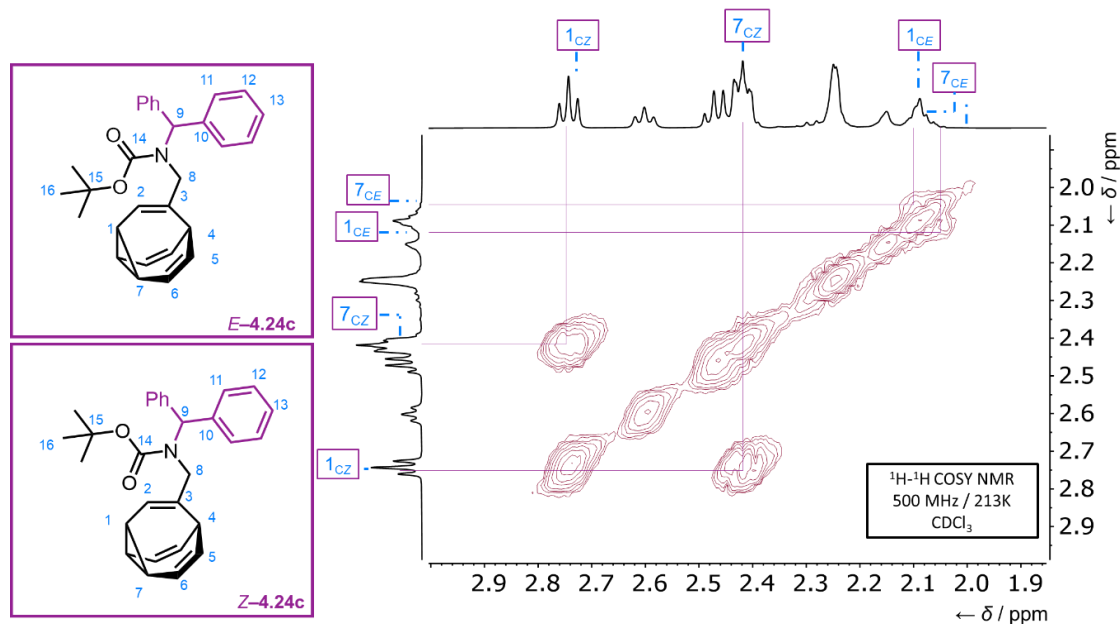
To prove that the 4 observable isomers are the rotamers of vinyl positional isomers,  $\text{H-H COSY}$ ,  $\text{HSQC}$ ,  $\text{HMBC}$ ,  $\text{HSQC-TOCSY}$  at  $-60^\circ\text{C}$  was used to determine if the only positional isomers are truly the vinyl substituent C & D. Bullvalene **4.24** solution state NMR at  $-60^\circ\text{C}$  in  $\text{CD}_3\text{Cl}$  was resolved enough to fully assign the  $^1\text{H}$  and  $^{13}\text{C}$  NMR and will be used as example for discussion of dynamics of the positional and rotational isomers. Firstly, using the aid of the  $^1\text{H}$ - $^{13}\text{C}$   $\text{HSQC-TOCSY}$  (Figure S4.5), the 4 observable isomers can be assigned to a set of proton and carbon signals through the correlations from this NMR experiment. The  $^1\text{H}$ - $^{13}\text{C}$   $\text{HSQC-TOCSY}$  experiment combines  $^1\text{H}$ - $^{13}\text{C}$   $\text{HSQC}$  with a  $^1\text{H}$ - $\text{TOCSY}$  experiments to give through-bond correlations between a  $^{13}\text{C}$ -attached  $^1\text{H}$  to all other coupled  $^1\text{H}$  including long range coupling.



**Figure 4.30.** Full  $^1\text{H}$ - $^1\text{H}$  COSY spectrum of mono(*N*-benzhydryl)methylene amine bullvalene (**4.24**) at  $-60^\circ\text{C}$  with regions used for assignment of the major isomer highlighted.

The preliminary assignment of these sets of proton/carbon signals to a specific isomer was conducted from the predictive computational study based on the population distributions highlighted in Table 4.2. The most dominant isomer is the *Z*-**4.24c** where the bulky *t*-butyl group of the carbamate is away from the bullvalene core, and the carbamate substituent is on the  $\text{sp}^2$  carbon adjacent to the bridgehead carbon of the fluxional cage. This positional isomer is usually the most stable as seen in literature.<sup>56,68</sup> Interestingly, the next most stable isomer is the *Z*-**4.24b** where the bulky *t*-butyl group of the carbamate is away from the bullvalene core, and the carbamate substituent is on the  $\text{sp}^2$  carbon adjacent to the cyclopropyl carbon of the fluxional cage. This observation indicates that the energy minima of the vinyl positional isomers B & C in *Z* form are more stable than *E* rotational isomers. The next most stable isomers are the rotational isomer *E*-**4.24c** followed *E*-**4.24b**. The rotation of the *t*-butyl group does not affect the higher stability of substituent being on the  $\text{sp}^2$  carbon adjacent to the bridgehead carbon rather than adjacent to the cyclopropyl carbon.  $^1\text{H}$ - $^1\text{H}$  COSY was a powerful tool to differentiate the positional isomers from vinyl  $\text{sp}^2$  carbon isomers B&C to the  $\text{sp}^3$  carbon isomers A&D (cyclopropyl & bridgehead carbon). To elucidate the solution state positional isomer populations of BV **4.24**, following the bullvalene NMR analysis developed by the Fallon group<sup>54</sup>, we confirmed the computational prediction of isomers distribution using the  $^1\text{H}$ - $^1\text{H}$  COSY spectrum of **4.24** taken at -

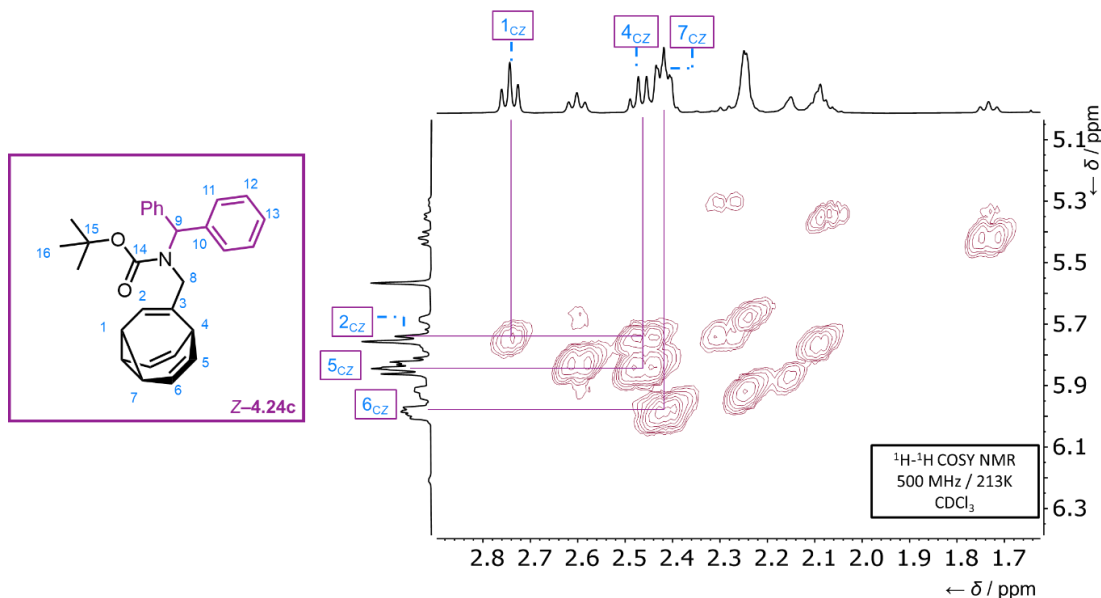
60 °C (Figure 4.30). The process applied for the assignment of the positional and rotational isomers of **4.24** is detailed below and visualised in Figures 4.31 – 4.35.



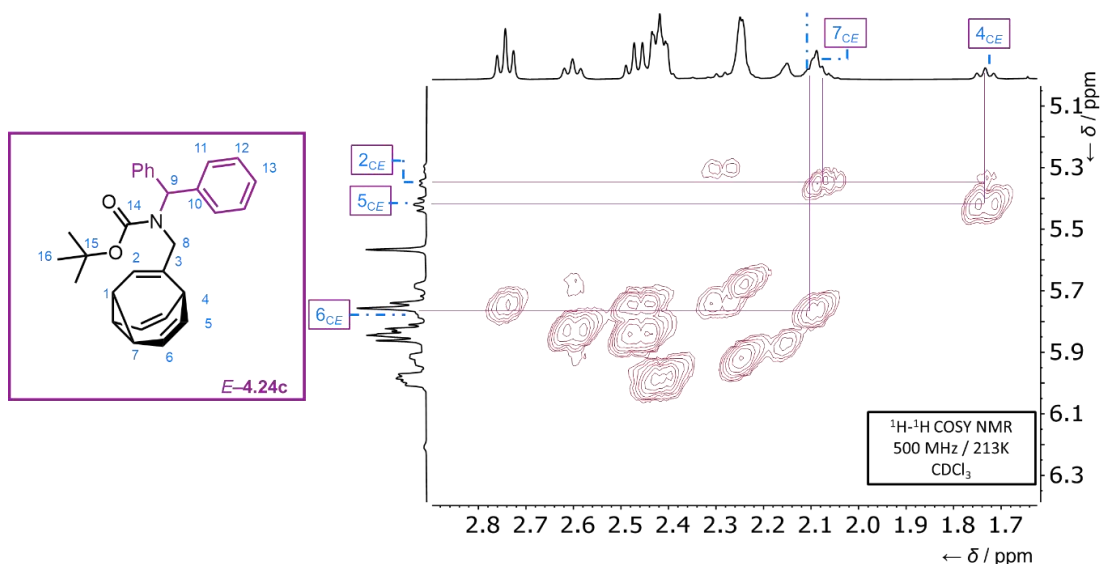
**Figure 4.31.**  $^1\text{H}$ - $^1\text{H}$  COSY spectrum corresponding to the pair of isomer C of mono(N-benzhydryl)methylene bullvalene carbamate (**4.24c**) at -60 °C displaying correlations between  $\text{H}_1/\text{H}_7$ .

Figure 4.30 shows the full  $^1\text{H}$ - $^1\text{H}$  COSY spectrum of **4.24** taken at -60 °C. The visible aliphatic COSY correlation (Figure 4.31) corresponds to the positional *E*-**4.24c** isomer. The signal for the cyclopropyl signals  $\text{H}_{1\text{CE}}$  &  $\text{H}_{1\text{CZ}}$  both displays a single COSY correlation to the aliphatic region to the adjacent cyclopropyl carbons ( $\text{H}_{7\text{CZ}}/\text{H}_{7\text{CE}}$ , Figure 4.31). This correlation can only occur in the positional isomer where carbamate substituent is on the  $\text{sp}^2$  carbon adjacent to bridgehead. The signal  $\text{H}_{1\text{CZ}}$  have 1 COSY correlation to the vinyl region ( $\text{H}_2$ , Figure 4.32) while  $\text{H}_{1\text{CE}}$  cannot be determined due to the signal overlapping with  $\text{H}_{7\text{CE}}$  (Figure 4.33).  $\text{H}_{1\text{CZ}}/\text{H}_{2\text{CZ}}$  is  $\text{J}_3$  COSY correlation representing the adjacent vinyl proton  $\text{H}_2$  meaning that the adjacent vinyl position is unsubstituted. Furthermore, signals  $\text{H}_{7\text{CE}}$  &  $\text{H}_{7\text{CZ}}$  have a COSY correlation to vinyl  $\text{H}_6$ , and in addition,  $\text{H}_{7\text{CZ}}$  has a  $\text{J}^4$  COSY correlation to the vinyl proton  $\text{H}_{2\text{CZ}}$  adjacent to the methylene substituted vinyl position of isomer C (Figure 4.32 & 4.33). The signals  $\text{H}_{4\text{CE}}$  &  $\text{H}_{4\text{CZ}}$  display two COSY correlations to the vinyl region ( $\text{H}_2$  &  $\text{H}_5$ , Figure 4.32 and Figure 4.33), where  $\text{H}_2/\text{H}_4$  couplings are  $\text{J}^4$  COSY correlations. Therefore,  $\text{H}_{4\text{CE}}$  &  $\text{H}_{4\text{CZ}}$  have a substituent adjacent to them and are situated on the bridgehead position. Additionally, the bridgehead carbon signals are found upfield compared to the

cyclopropyl region due to their triply allylic nature which is confirmed by the HSQC (Figure S4.3). These observations confirm that two sets of proton signals discussed above belonging to two **BV** isomers are both from positional isomer C where the  $sp^2$  carbon is adjacent to bridgehead. This result means that these signals belong to the *E/Z* rotamers (rotation about NCO bond) of the vinyl positional isomer **4.24c**.



**Figure 4.32.**  $^1\text{H}$ - $^1\text{H}$  COSY spectrum of conformer of mono(*N*-benzyl)methylene bullvalene carbamate **Z-4.24c** at  $-60\text{ }^\circ\text{C}$  displaying correlations between aliphatic protons ( $\text{H}_1/\text{H}_4/\text{H}_7$ ) and vinyl protons ( $\text{H}_2/\text{H}_5/\text{H}_6$ ).



**Figure 4.33.**  $^1\text{H}$ - $^1\text{H}$  COSY spectrum of conformer of mono(*N*-benzyl)methylene bullvalene carbamate **E-4.24c** at  $-60\text{ }^\circ\text{C}$  displaying correlations between aliphatic protons ( $\text{H}_1/\text{H}_4/\text{H}_7$ ) and vinyl protons ( $\text{H}_2/\text{H}_5/\text{H}_6$ ).

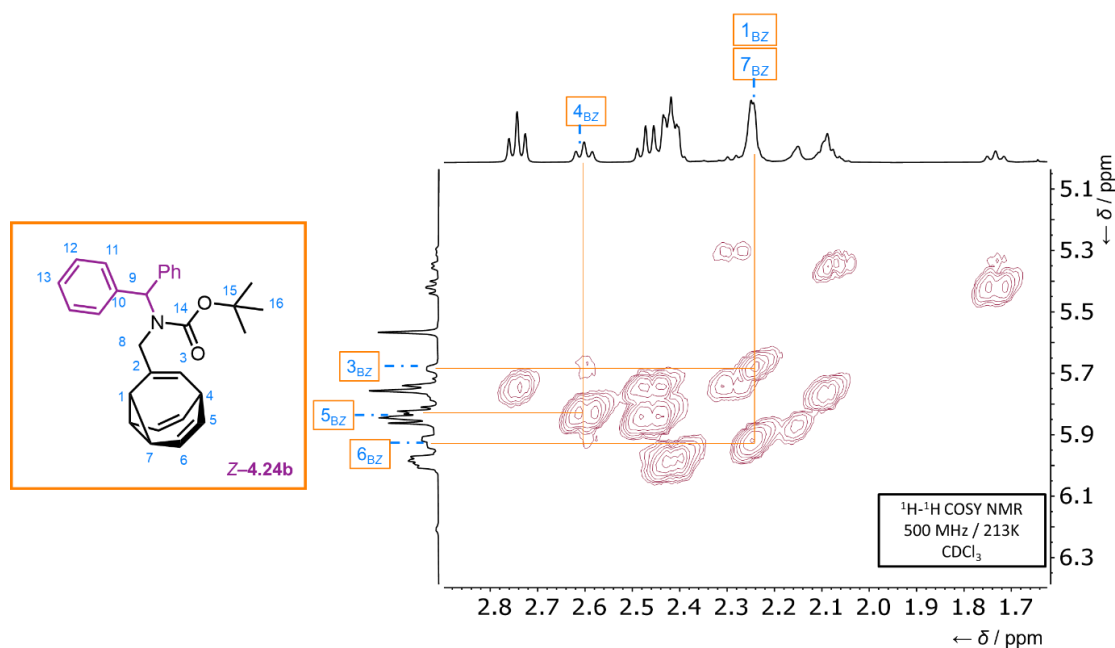


**Figure 4.34.**  $^1\text{H}$ - $^1\text{H}$  COSY spectrum of conformer of mono(*N*-benzyl)methylene amine bullvalene **Z-4.24b** at  $-60\text{ }^\circ\text{C}$  displaying correlations between aliphatic protons ( $\text{H}_1/\text{H}_4/\text{H}_7$ ) and vinyl protons ( $\text{H}_3/\text{H}_5/\text{H}_6$ ).

For Isomer B (*E/Z*-**4.24b**), the aliphatic COSY correlations could not be seen due to overlapping peaks of the adjacent cyclopropyl protons,  $\text{H}_{1\text{B}}$  &  $\text{H}_{7\text{B}}$ , for *E/Z* rotamers (Figure 4.31). The signals for bridgehead protons,  $\text{H}_{4\text{BE}}$  &  $\text{H}_{4\text{BZ}}$ , display multiple COSY correlations to the vinyl region (Figure 4.34 and Figure 4.35). Firstly, the vinyl protons  $\text{H}_{3\text{BE}}$  &  $\text{H}_{3\text{BZ}}$  correlate only to  $\text{H}_{4\text{BE}}$  &  $\text{H}_{4\text{BZ}}$  in  $^1\text{H}$ - $^1\text{H}$  COSY (Figure 4.32 and Figure 4.33) and this proton correlates to  $\text{C}_8$  in HMBC (Figure S4.4). Therefore,  $\text{H}_{3\text{BE}}$  &  $\text{H}_{3\text{BZ}}$  are the protons of  $\text{sp}^2$  carbon adjacent to the substituent  $\text{sp}^2$  carbon  $\text{C}_2$  (Figure 4.32 and Figure 4.33). These correlations support that these two sets of proton signals belong to the positional isomer **4.24b**. The signals for the cyclopropyl  $\text{H}_{1\text{BE}}$  &  $\text{H}_{1\text{BZ}}$  are overlapped with the adjacent cyclopropyl  $\text{H}_{7\text{BE}}$  &  $\text{H}_{7\text{BZ}}$ , however, both overlapped signals  $\text{H}_{7\text{BE}}$  &  $\text{H}_{7\text{BZ}}$  have COSY correlation with the adjacent vinyl proton  $\text{H}_{6\text{B}}$ . Additionally,  $\text{H}_{1\text{BZ}}$  has  $\text{J}^4$  COSY correlation to vinyl proton  $\text{H}_{3\text{BZ}}$  which also correlates to  $\text{H}_{4\text{BZ}}$  on the same arm (Figure 4.32 and Figure 4.33). These observations confirm that both the assignment of the signal for  $\text{H}_1$  &  $\text{H}_7$  as the cyclopropyl position are correct. Additionally, the bridgehead carbon signals  $\text{H}_4$  are found upfield compared to the cyclopropyl region due to their triply allylic nature which is confirmed by the HSQC f(Figure S4.3) further supporting that these set of proton peaks belong to

positional isomer **4.24b**. This result means that these signals belong to the *E/Z* rotamers (rotation about NCO bond) of the vinyl positional isomer **4.24b**.

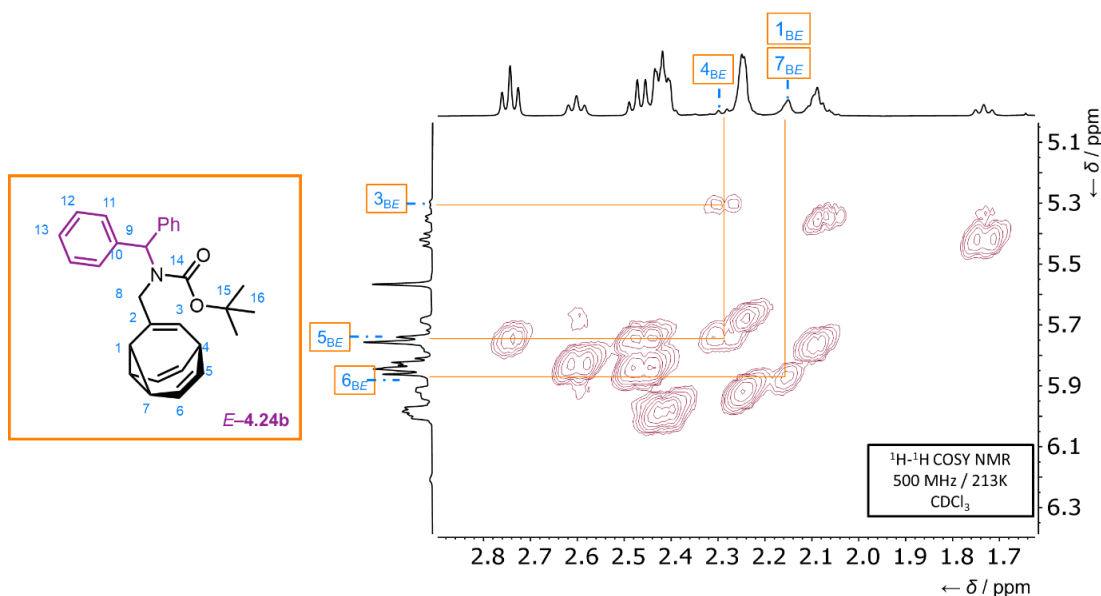


**Figure 4.35.**  $^1\text{H}$ - $^1\text{H}$  COSY spectrum of conformer of mono(*N*-benzyl)methylene amine bullvalene *E*-**4.24b** at  $-60\text{ }^\circ\text{C}$  displaying correlations between aliphatic protons ( $\text{H}_1/\text{H}_4/\text{H}_7$ ) and vinyl protons ( $\text{H}_3/\text{H}_5/\text{H}_6$ ).

## 4.12 Solid State Computational Analysis

Solution phase analysis of **BV** carbamates **4.23** & **4.24** confirmed the fluxional behaviour allowing for interconversion between its different constitutional isomers and rotamers along the NCO bond. To establish the absolute configuration and connectivity between atoms in the solid state, single crystal XRD analysis was performed.

Single crystals of **BV 4.23** were grown by slow cooling of a solution of **4.23** in MeOH, over 48 h, from  $60\text{ }^\circ\text{C}$  to rt. The crystal structure of **4.23**, shown in Figure 4.34, was found to be defined by the  $P2_1/c$  space group with all molecules crystallising as a single diastereomer (*E*) of the constitutional isomer *E*-**4.23b** (Figure 4.36). **BV 4.23** crystallised as the second most stable isomer *E*-**4.23b** determined computationally (Figure 4.21). This solid-state phenomenon is an example of “shape-selective crystallisation”. Shape selective crystallisation is the phenomenon through which fluxional molecules crystallise preferentially as a single isomer in a manner which is controlled by molecular shape and size, irrespective of their solution phase equilibrium distribution.<sup>32</sup>

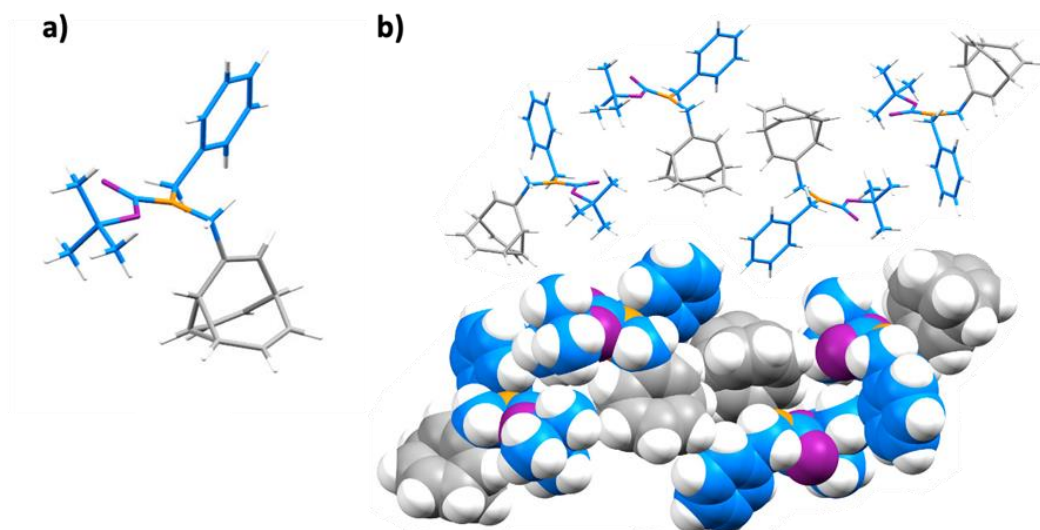


**Figure 4.36.** a) X-ray crystal structure of mono(N-benzyl)methylene amine bullvalene **4.23**. b) crystal packing of **4.23** viewed along the crystallographic b-axis shown in partial stick and space-filling representations.

The Hirshfeld surface (Figure 4.37) for the crystal structure of **4.23** was calculated to give insight into the interactions between the molecules in its crystal lattice. Hirshfeld surfaces show regions of a crystal structure in which interatomic distances are significantly shorter than the sum of the van der Waals radii between the positions. No significantly close interatomic distances were found in the Hirshfeld surface of **4.23**.

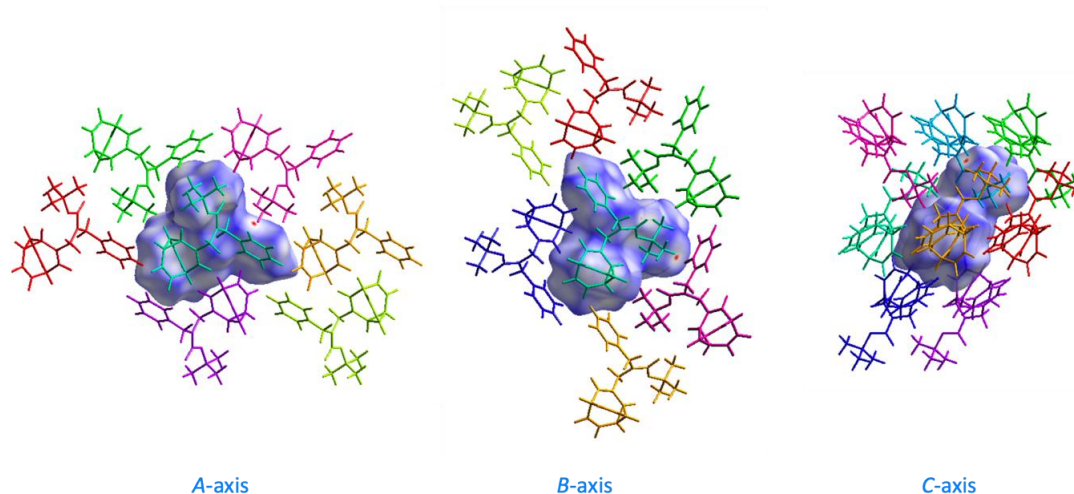


**Figure 4.37.** Solid state superstructure of mono(N-benzyl)methylene amine bullvalene (**4.23**) viewed down the a-, b- and c- crystallographic axes. In each section, the central molecule is overlaid with its calculated Hirshfeld surface and surrounded by its nine nearest neighbours which are coloured to match the corresponding molecules in Table 4.3. The Hirshfeld surfaces show that interatomic distances between molecules of **4.23** are generally greater than (blue) or at (white) the sum of the van der Waals radii. Red regions in the Hirshfeld surfaces indicate close contacts.

This indicated that interactions between molecules of **4.23** are dominated by van der Waals forces. The most significant close contact is a weak C–H $\cdots$ H interaction, shown in Figure 4.38, which is further than the sum of the protons' van der Waals radii.

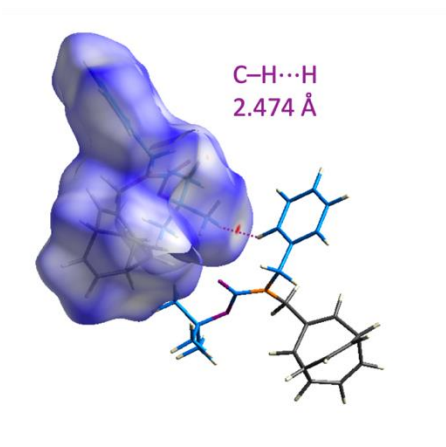











**Figure 4.38.** Hirshfeld surface calculated for the crystal structure of **4.23**. The most significant close contact with a neighbouring molecule is highlighted by the purple dotted line.

To confirm the absence of specific non-covalent bonding interactions, DFT modelling of the solid-state intermolecular interactions in **4.23** was performed. The CE-B3LYP [B3LYP/6-31G(d,p)] theory was used in CrystalExplorer 21.5. The output of this calculation is a breakdown of the total interaction energy between neighbouring molecules in the crystal lattice of **4.23**. The total interaction energy is broken down into contributions by repulsion ( $E_{rep}$ ), dispersion ( $E_{dis}$ ), polarisation ( $E_{pol}$ ) and electrostatic ( $E_{ele}$ ) energies between the molecules of **4.23**. These contributions are summarised for **4.23** in Table 4.3. Table 4.3 shows that the total interaction energies between a given molecule of **4.23**, and its neighbouring molecules, are dominated by dispersion (van der Waals) energies. Consequently, it is concluded that BV **4.23** is an example of a fluxional molecule which undergoes shape-selective crystallisation (Figure 4.36).

Many known fluxional carbon cages adopt fixed structures in the solid state, but some retain a degree of fluxionality. To confirm that **4.23** undergoes shape selective crystallisation at temperatures above 120 K, it should be ensured that **4.23** does not retain its fluxionality in the solid state. Variable-temperature x-ray diffraction measurements could be used confirm this; by examining its C–C bond distances, it would be possible to determine whether **4.23**'s Cope rearrangements occur in the solid state.

**Table 4.3:** Intermolecular interaction energies calculated for the crystal structure of **4.23** at CE-B3LYP- B3LYP- 6- 31G(d,p) theory. The colours refer to the correspondingly coloured neighbouring molecules in Figure 3.28.

Neighbouring Molecule	Interaction Energies / kJ mol <sup>-1</sup>					
	$R / \text{\AA}$	$E_{\text{ele}}$	$E_{\text{pol}}$	$E_{\text{dis}}$	$E_{\text{rep}}$	$E_{\text{tot}}$
	12.01	0.4	-0.3	-11.0	0.0	-9.4
	11.68	-3.8	-0.6	-16.5	9.7	-12.9
	13.33	0.2	-0.2	-10.3	0.0	-8.8
	9.64	-6.1	-1.7	-26.0	16.3	-20.3
	6.04	-12.9	-2.4	-72.5	44.6	-51.0
	8.41	-7.6	-2.4	-35.9	21.7	-27.6
	9.02	-4.0	-0.6	-39.1	17.7	-27.8
	7.30	-8.9	-1.2	-51.3	31.5	-35.5
	11.03	-0.5	-0.1	-7.0	2.2	-5.4

### 4.13 Conclusions and Outlook

Cope rearrangements of shapeshifting molecules such as barbaralanes and bullvalenes has led access to a range of novel inquiries in the field dynamic covalent chemistry as an intramolecular strained fluxional carbon cage platform. For barbaralanes, intramolecular Cope rearrangements simultaneously invert every stereogenic sp<sup>3</sup>-carbon centre of their structures. These configurational rearrangements occur rapidly and reversibly, achieving the uncommon property of dynamic sp<sup>3</sup>-carbon stereochemistry—one that has remained surprisingly rare since Le Bel<sup>4</sup> and van't Hoff<sup>3</sup> first identified tetrahedral carbon as a source of molecular chirality in 1874. Both the rate of sp<sup>3</sup>-carbon inversion and the equilibrium distribution of isomers are sensitive to changes in the **9-BB** structure. On the one hand, the dynamics of the rearrangement processes are controlled through manipulation of covalent bonding or metal coordination of the **9-BB** olefin groups, providing convenient functional handles. On the other hand, the cage adapts its configuration to minimize steric interactions with nearby fixed stereogenic elements and, in so doing, is able to transmit the stereochemical information across its rigid, tricyclic backbone. When interfaced with transition-metal complexes, the dynamic cage conveys a stereochemical preference to

the chiral-at-metal<sup>46,47</sup> centre. Controllable and adaptable  $sp^3$ -carbon stereochemistry of this kind can be exploited in enantioselective synthesis<sup>5,12,27,28,40</sup> and chiral functional materials.<sup>69</sup>

Translating the concept of interfacing shapeshifting molecules with transition-metal complexes, efforts towards synthesising a bidentate bullvalene ligand capable of binding to a metal centre — was not realised. However, an understanding of the factors which influence the stability of diol-derived phosphites and phosphoramidites has been developed. The results of this project agree with assertions in the literature that the stability of phosphites and phosphoramidites depends on the steric bulk around their phosphorous centres. However, quantitative studies which assess the stability of a wide range of phosphite/ phosphoramidite ligands with respect to water and oxygen are needed to better understand the factors influencing their stability. Future research into fluxional ligands should explore the synthesis of phosphites/ phosphoramidites derived from different diols.

Two novel mono-substituted bullvalenes were synthesised: mono(*N*-benzyl-Boc)methylene bullvalene carbamates **4.23** and mono(*N*-benzhydryl-Boc)methylene bullvalene carbamate **4.24**. Solution state analysis (VT NMR, 2D NMR) in combination DFT calculations showed that the steric bulk around the NCO bond allows for rotational isomers to compete with the fluxional nature of bullvalene from the intramolecular Cope rearrangements. It was revealed that the vinyl substituted positions (isomer C & D, Figure 4.20) were the most stable positional isomers and the rotational isomers of these isomers were present in low-temperature NMR which was confirmed with  $^1H$ - $^1H$  COSY, HSQC, HMBC, HSQC-TOCSY.

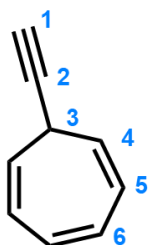
Single crystal XRD analysis of **4.23** was performed and it was found to crystallise as one of its minor solution phase isomers, as determined by DFT calculations. DFT modelling of the solid-state intermolecular interactions in **4.23** confirmed the absence of specific non-covalent bonding interactions. Taken together, these data indicate that **2.23** is a further example of a fluxional molecule which displays dynamic shape selective crystallisation.<sup>32</sup> Future work should investigate the fluxional nature of the bullvalene fluxional cage effect on NCO and CN bond rotation which can lead to interesting dynamic axial chiral applications.

## 4.14 Experimental

### 4.14.1 General Considerations

All reagents were purchased from commercial suppliers (Sigma-Aldrich, Acros Organics, or Alfa Aesar) and used without further purification. Analytical thin-layer chromatography (TLC) was performed on neutral aluminium sheet silica gel plates and visualised under UV irradiation (254 nm). Nuclear magnetic resonance (NMR) spectra were recorded using a Bruker Advance (III)-400 ( $^1\text{H}$  400.130 MHz and  $^{13}\text{C}$  100.613 MHz), Varian Inova-500 ( $^1\text{H}$  500.130 MHz and  $^{13}\text{C}$  125.758 MHz), Varian VNMRs-600 ( $^1\text{H}$  600.130 MHz and  $^{13}\text{C}$  150.903 MHz) or a Varian VNMRs-700 ( $^1\text{H}$  700.130 MHz and  $^{13}\text{C}$  176.048 MHz) spectrometer, at a constant temperature of 298 K unless otherwise stated. For variable-temperature (VT) measurements, operating temperatures were calibrated using an internal calibration solution of MeOH and glycerol. Chemical shifts ( $\delta$ ) are reported in parts per million (ppm) relative to the signals corresponding to residual non-deuterated solvents [ $\text{CDCl}_3$ :  $\delta$  = 7.26 or 77.16.  $\text{CD}_3\text{CN}$ :  $\delta$  = 1.94, 1.32 or 118.26]. Coupling constants ( $J$ ) are reported in Hertz (Hz).  $^{13}\text{C}$  NMR experiments were proton-decoupled,  $^{31}\text{P}$  NMR experiments are decoupled for compounds (*R,S*)/(*S,S*)-**LBB**, (*R,S*)/(*S,S*)-**LBB**AuCl, (*A,R,S*)/(*C,S,S*)-**LBB**PdCl<sub>2</sub>, but coupled for (*C,R,S*)/(*S,S*)-**LBB**RuCp(NCMe)·PF<sub>6</sub>. Assignments of  $^1\text{H}$  and  $^{13}\text{C}$  NMR signals were accomplished by two-dimensional (2D) NMR spectroscopy (COSY, NOESY, HSQC, HMBC). NMR spectra were processed using MestReNova version 10.0. Data are reported as follows: chemical shift; multiplicity; coupling constants; integral and assignment. A Solid-State  $^{13}\text{C}$  NMR spectrum was recorded on Bruker Advance III HD spectrometer at 100.63 MHz with a 3.2 mm (rotor o.d.) magic-angle spinning probe at a spin rate of 10 kHz. The spectrum was recorded using cross-polarisation with total suppression of spinning sidebands with a contact time of 1-ms and a recycle delay of 120-s. The spectrum was recorded at ambient probe temperature (approximately 25 °C) and at a spin rate of 10 kHz. Spectra are reported relative to an external sample of neat tetramethylsilane (referencing was carried out by setting the high-frequency signal from adamantane to 38.5 ppm). Low-resolution Atmospheric Solids Analysis Probe (ASAP)-MS were performed using a Waters Xevo QTOF equipped with an ASAP. High-resolution (HR) electrospray ionisation (HR-ESI) and ASAP (HRASAP) mass spectra were measured using a Waters LCT Premier XE high resolution, accurate mass

UPLC ES MS (also with ASAP ion source). Melting points were recorded using a Gallenkamp (Sanyo) apparatus and are uncorrected. The X-ray single-crystal diffraction data were collected at a temperature of 120.0(2) K using  $\lambda$ MoK $\alpha$  radiation ( $\lambda$ =0.71073 Å). (S,R)-5, (S,R)-4.11 were collected on a Bruker D8Venture (Photon100 CMOS detector, I $\mu$ S-microsource, focusing mirrors) diffractometer. Compounds **4.9**, (A,R,S)/(C,S,S)-**L<sub>BB</sub>PdCl<sub>2</sub>** and (C,R,S)- **L<sub>BB</sub>RuCp(NCMe)·PF<sub>6</sub>** were collected on a Photon III MM (CPAD detector, I $\mu$ S-III-microsource, focusing mirrors) diffractometer. Compounds (R,R)-**4.10**, **4.6**, **4.23** were collected on an Agilent XCalibur (Sapphire-3 CCD detector, fine-focus sealed tube, graphite monochromator) S3 diffractometer. All diffractometers were equipped with Cryostream (Oxford Cryosystems) openflow nitrogen cryostats. All structures were solved by direct method and refined by full-matrix least squares on F<sup>2</sup> for all data using Olex2 and SHELX software. All non-hydrogen atoms were refined anisotropically, hydrogen atoms in structures (S,S)-**4.10**, (R,R)-**4.10**, **4.6**, **4.9**, and **4.23** were freely refined in isotropic approximation, the hydrogen atoms in remaining structures were placed at the calculated positions and refined in riding mode. Crystallographic data for these structures have been deposited within the Cambridge Crystallographic Data Centre as supplementary publication CCDC-2068012– 2068020 and 2173984.



**7-Ethynylcyclohepta-1,3,5-triene:** Anhydrous LiCl (0.52 g, 12.4 mmol) was placed in an oven-dried round-bottomed flask fitted with a septum under an N<sub>2</sub> atmosphere. Anhydrous THF was added (38 mL) and the resulting solution was cooled to –78 °C before adding a solution of ethynyl magnesium bromide (22.5 mL, 12.2 mmol, 0.5 M

in THF) and stirring for 10 min at this temperature. Tropylium tetrafluoroborate (1.00 g, 5.62 mmol) was added to the reaction mixture and the reaction mixture was stirred for 16 h, where the temperature was raised to rt, following removal of the ice bath. The reaction was quenched with a saturated aqueous solution of NH<sub>4</sub>Cl (20 mL), then extracted with Et<sub>2</sub>O (3 × 30 mL). The combined organic extracts were then dried over MgSO<sub>4</sub>, filtered and the solvent removed *in vacuo* (rotary evaporator bath at 16 °C, ≥ 100 mbar). The crude residue was purified by column chromatography (Teledyne Isco CombiFlash Rf+ system, 24 g SiO<sub>2</sub>, n-pentane) to give the title compound as a colourless oil (539 mg, 4.6 mmol, 83%). <sup>1</sup>H NMR (600 MHz, CDCl<sub>3</sub>) δ 6.66 (dd, *J* =

3.7, 2.7 Hz, 2H, H<sub>6</sub>), 6.27 – 6.07 (m, 2H, H<sub>5</sub>), 5.44 – 5.20 (m, 2H, H<sub>4</sub>), 2.64 – 2.42 (m, 1H, H<sub>3</sub>), 2.17 (d,  $J = 2.6$  Hz, 1H, H<sub>1</sub>). Spectroscopic data were consistent with those published previously.<sup>36</sup>

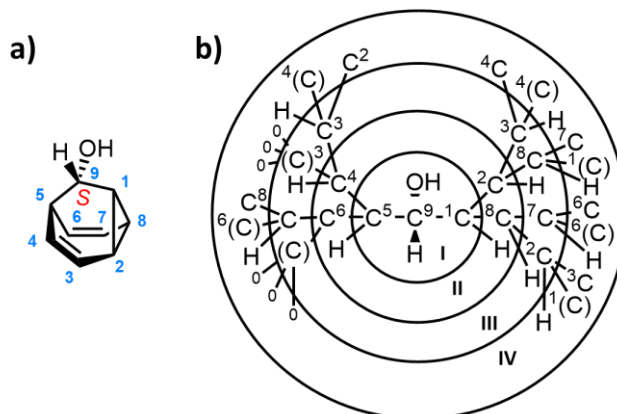
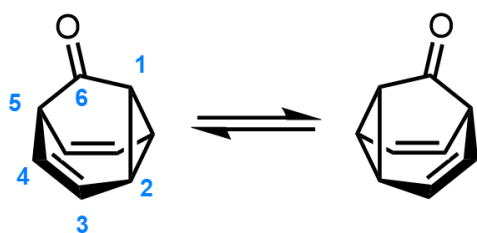


**Figure S4.1.** (a) Structural formula of (S)-1 showing numbering scheme for C atoms. (b) Hierarchical diagram used to assign the precedence of position 1 over position 5 according to the Cahn–Ingold–Prelog priority rules. Assignment of stereochemical descriptors for the barbaralanes follows the Cahn–Ingold–Prelog priority rules. Taking position 9 of (S)-1 as an example (Figure S1a), the priorities are assigned as O > C1 > C5 > H. A hierarchical diagram (Figure S1b) aids in differentiating C1 and C5. The branch of the diagram for C5 has duplicate atoms in sphere III (corresponding to the C–C double bonds), leading to phantom atoms (atomic number 0) in sphere IV. The first duplicate atoms for C1 arise in sphere IV – in this case, the duplicates correspond to (i) the C–C double bonds and (ii) the branches where the diagram arrives back at a position already encountered of the cyclopropyl ring. Consequently, the first phantom atoms for the C1 branch arise in sphere V. Therefore, sphere IV is the first point of difference, in which the C atoms of the C1 branch have precedence over the phantom atoms of the C5 branch.

#### Tricyclo[3.3.1.0<sup>2,8</sup>]nona-3,6-dien-9-one



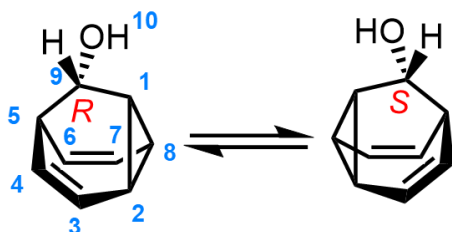
7-Ethynyl- cyclohepta1,3,5-triene (1.0 g, 8.68 mmol) and diphenyl sulphoxide (3.51 g, 17.0 mmol) were charged in a flask and dissolved in anhydrous CH<sub>2</sub>Cl<sub>2</sub> (15 mL) at 25 °C, with no particular precautions taken to exclude air.

(Acetonitrile)[1,3-bis(2,6-diisopropylphenyl)-imidazol-2-ylidene]gold(I)

tetrafluoroborate (309 mg, 0.43 mmol, 5 mol%) was added in one portion at the same temperature and the reaction mixture was stirred for 16 h. The reaction was quenched with 10 drops of Et<sub>3</sub>N and the solvent was removed *in vacuo*. The crude residue was purified by column chromatography (Teledyne Isco CombiFlash Rf+ system, 24 g SiO<sub>2</sub>, hexanes–EtOAc, gradient elution) to give the title compound as a light yellow

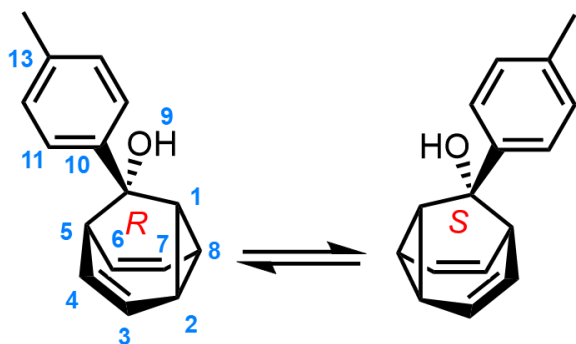
solid (685 mg, 5.18 mmol, 60%).  $^1\text{H NMR}$  (700 MHz,  $\text{CDCl}_3$ )  $\delta$  5.97 – 5.51 (m, 2H,  $\text{H}_1$  and  $\text{H}_5$ ), 4.32 (br s, 4H,  $\text{H}_2$  and  $\text{H}_4$ ), 2.90 – 2.55 (m, 2H,  $\text{H}_3$ ). Spectroscopic data were consistent with those published previously.<sup>36</sup>

**Tricyclo[3.3.1.0<sup>2,8</sup>]nona-3,6-dien-9-ol.**



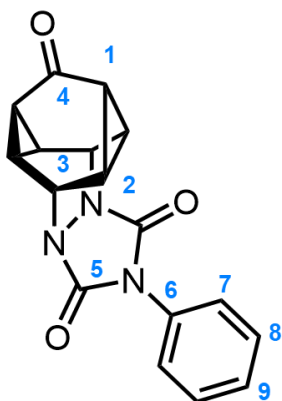
$\text{LiAlH}_4$  (120 mg, 3.16 mmol) was placed in an oven-dried roundbottomed flask fitted with a septum under a  $\text{N}_2$  atmosphere and suspended in anhydrous  $\text{Et}_2\text{O}$  (5 mL). The mixture was cooled to 0 °C and then a solution of

tricyclo[3.3.1.0<sup>2,8</sup>]nona-3,6-dien-9-one (200 mg, 1.51 mmol) in anhydrous  $\text{Et}_2\text{O}$  (5 mL) was added dropwise. The reaction mixture was stirred at this temperature for 3 h. The reaction was quenched with a saturated aqueous solution of potassium sodium tartrate (25 mL) and allowed to warm to rt before being extracted with  $\text{Et}_2\text{O}$  ( $3 \times 30$  mL). The combined organic extracts were dried over  $\text{MgSO}_4$  and the solvent was removed under reduced pressure (rotary evaporator bath at 16 °C,  $\geq 100$  mbar). The crude residue was purified by column chromatography (Teledyne Isco CombiFlash Rf+ system, 24 g  $\text{SiO}_2$ , n-pentane– $\text{Et}_2\text{O}$ , gradient elution) to give the title compound as a white solid (159 mg, 1.18 mmol, 78%). **M. P.** 82 – 84 °C.  $^1\text{H NMR}$  (400 MHz,  $\text{CDCl}_3$ )  $\delta$  5.88 (t,  $J = 7.9$  Hz, 1H,  $\text{H}_3$ ), 5.54 (t,  $J = 7.6$  Hz, 1H,  $\text{H}_7$ ), 4.16 – 4.04 (m, 2H,  $\text{H}_6$  and  $\text{H}_8$ ), 4.02 – 3.92 (m, 2H,  $\text{H}_2$  and  $\text{H}_4$ ), 3.61 (d,  $J = 3.3$  Hz, 1H,  $\text{H}_9$ ), 2.59 – 2.47 (m, 2H,  $\text{H}_1$  and  $\text{H}_5$ ), 1.14 (s, 1H,  $\text{H}_{10}$ ).  $^{13}\text{C NMR}$  (151 MHz,  $\text{CDCl}_3$ )  $\delta$  123.3 ( $\text{C}_3$ ), 120.9 ( $\text{C}_7$ ), 76.4 ( $\text{C}_6$  and  $\text{C}_8$ ), 72.4 ( $\text{C}_2$  and  $\text{C}_4$ ), 62.5 ( $\text{C}_9$ ), 31.8 ( $\text{C}_1$  and  $\text{C}_5$ ). **HRMS-ASAP**  $m/z = 117.0699$  [ $\text{M}-\text{OH}$ ] $^+$ , calculated for  $\text{C}_9\text{H}_9$ : 117.0704.

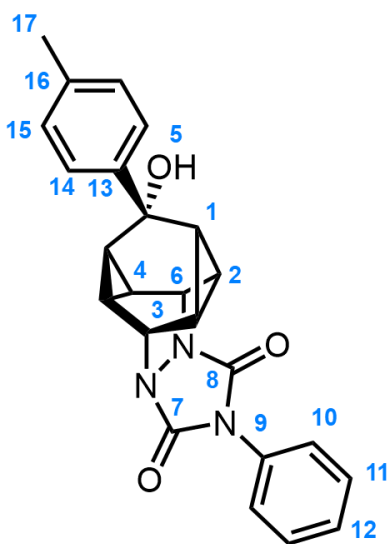
**6-(4-Tolyl)bicyclo[3.2.2]nona-3,8-dien-6-ol.**

Tricyclo[3.3.1.0]nona-3,6-dien-9-one (42.8 mg, 0.32 mmol) was transferred to an oven-dried round-bottomed flask, and the flask was purged with N<sub>2</sub>. Anhydrous THF (10 mL) was added and the solution was cooled to 0 °C. Toly magnesium bromide (2.3

mL, 2.3 mmol, 1 M in THF) was added dropwise to the barbaralone. The reaction mixture was stirred for 16 h, and the temperature was raised from 0 °C to rt, following removal of the ice bath. The reaction was quenched with a saturated aqueous solution of NH<sub>4</sub>Cl (13 mL), then extracted with EtOAc (3 × 20 mL). The combined organic extracts were dried over MgSO<sub>4</sub>, filtered and the solvent was removed under reduced pressure. The crude residue was purified by column chromatography (Teledyne Isco CombiFlash Rf+ system, 12 g SiO<sub>2</sub>, hexanes– Et<sub>2</sub>O, gradient elution) to yield the title compound as a cream-coloured solid (58.5 mg, 0.28 mmol, 73%). **M. P.** 59 – 61 °C. **<sup>1</sup>H NMR** (700 MHz, CDCl<sub>3</sub>) δ 7.33 (d, *J* = 8.2 Hz, 2H, H<sub>11</sub>), 7.12 (d, *J* = 7.9 Hz, 2H, H<sub>12</sub>), 5.91 (t, *J* = 7.7 Hz, 1H, H<sub>7</sub>), 5.58 (t, *J* = 7.6 Hz, 1H, H<sub>3</sub>), 4.28 – 4.24 (m, 2H, H<sub>8</sub> and H<sub>6</sub>), 4.24 – 4.21 (m, 2H, H<sub>4</sub> and H<sub>2</sub>), 2.83 – 2.57 (m, 2H, H<sub>5</sub> and H<sub>1</sub>), 2.33 (d, *J* = 0.7 Hz, 3H, H<sub>14</sub>), 1.98 (s, 1H, H<sub>15</sub>). **<sup>13</sup>C NMR** (176 MHz, CDCl<sub>3</sub>) δ 140.4 (C<sub>10</sub>), 136.8 (C<sub>13</sub>), 128.6 (C<sub>12</sub>), 126.4 (C<sub>11</sub>), 123.2 (C<sub>7</sub>), 120.9 (C<sub>3</sub>), 77.9 (C<sub>4</sub> and C<sub>2</sub>), 75.5 (C<sub>8</sub> and C<sub>6</sub>), 68.6 (C<sub>9</sub>), 38.2 (C<sub>5</sub> and C<sub>1</sub>), 21.2 (C<sub>14</sub>). **HRMS-ASAP** *m/z* = 207.1154 [M-OH]<sup>+</sup>, calculated for C<sub>16</sub>H<sub>15</sub>: 207.1174.

**6-Phenyl-4,6,9-triazahehexacyclo[8.5.0.02,15.03,12.04,9.011,13]pentadecane-5,8,14-trione.**

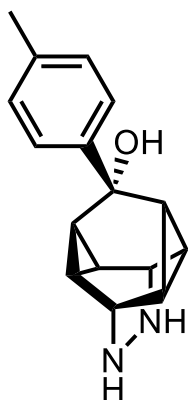
Tricyclo[3.3.1.02,8]nona-3,6-dien-9-one (70 mg, 0.52 mmol) and 4-phenyl-1,2,4-triazoline-3,5-dione (PTAD) (180 mg, 1.03 mmol) were dissolved in anhydrous  $\text{CH}_2\text{Cl}_2$  (2.5 mL). The reaction mixture was heated to 50 °C and stirred for 72 h. The reaction mixture was cooled and diluted with  $\text{CH}_2\text{Cl}_2$  (20 mL), then washed with saturated aqueous  $\text{NaHCO}_3$  ( $3 \times 30$  mL). The organic phase was separated and dried over  $\text{MgSO}_4$ , filtered and the solvent removed under *in vacuo*. The crude residue was purified by column chromatography (Teledyne Isco CombiFlash Rf+ system, 12 g  $\text{SiO}_2$ ,  $\text{CH}_2\text{Cl}_2$ -EtOAc, gradient elution) to yield the desired title as a colourless solid. (45 mg, 0.15 mmol, 28%). **M. P.** 171 – 173 °C (decomp.).  **$^1\text{H}$  NMR** (600 MHz,  $\text{CD}_3\text{CN}$ )  $\delta$  7.56 – 7.48 (m, 4H,  $\text{H}_8$  and  $\text{H}_7$ ), 7.47 – 7.42 (m, 1H,  $\text{H}_9$ ), 5.62 – 4.64 (m, 2H,  $\text{H}_3$ ), 2.33 (ddd,  $J = 7.8, 3.7, 2.7$  Hz, 4H,  $\text{H}_2$ ), 1.67 (t,  $J = 7.7$  Hz, 2H,  $\text{H}_1$ ).  **$^{13}\text{C}$  NMR** (151 MHz,  $\text{CD}_3\text{CN}$ )  $\delta$  202.4 ( $\text{C}_5$ ), 156.8 ( $\text{C}_4$ ), 132.8 ( $\text{C}_6$ ), 123.0 ( $\text{C}_7$ ), 129.4 ( $\text{C}_9$ ), 127.3 ( $\text{C}_8$ ), 48.9 ( $\text{C}_3$ ), 27.4 ( $\text{C}_2$ ), 24.7 ( $\text{C}_1$ ). **HR-ESI MS**  $m/z = 308.1032$  [ $\text{M}+\text{H}$ ] $^+$ , calculated for  $\text{C}_{17}\text{H}_{14}\text{N}_3\text{O}_3$  $^+$ : 308.1035.

**11-Hydroxy-11-(4-tolylphenyl)-5-phenyl-3,5,7-triazatetracyclo[8.2.2.0-2,8.03,7]tetradecane-4,6-dione.**

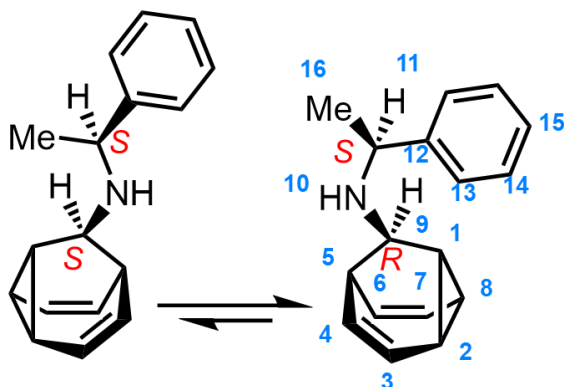
6-(4-Tolyl)bicyclo[3.2.2]nona-3,8-dien-6-ol (15 mg, 0.07 mmol) and 4-phenyl-1,2,4-triazoline-3,5-dione (PTAD) (23 mg, 0.13 mmol) were dissolved in anhydrous  $\text{CH}_2\text{Cl}_2$  (1.0 mL). The reaction mixture was heated to 50 °C and stirred for 24 h. The reaction mixture was cooled and diluted with  $\text{CH}_2\text{Cl}_2$  (20 mL), then washed with saturated aqueous  $\text{NaHCO}_3$  ( $3 \times 30$  mL). The organic phase was separated and dried over  $\text{MgSO}_4$ , filtered and the solvent removed *in vacuo*. The crude residue was purified by column chromatography (Teledyne Isco CombiFlash Rf+ system, 12 g  $\text{SiO}_2$ ,  $\text{CH}_2\text{Cl}_2$ -EtOAc, gradient elution) to yield the title compound as a colourless solid (22 mg, 0.055 mmol,

85%). **M. P.** 186 – 188 °C (decomp.). **<sup>1</sup>H NMR** (400 MHz, CDCl<sub>3</sub>) δ 7.61 – 7.46 (m, 6H, H<sub>10</sub>, H<sub>11</sub> and H<sub>14</sub>), 7.39 (t, *J* = 7.3 Hz, 1H, H<sub>12</sub>), 7.30 – 7.23 (m, 2H, H<sub>15</sub>), 5.24 (t, *J* = 5.4 Hz, 1H, H<sub>6</sub>), 5.11 (t, *J* = 5.4 Hz, 1H, H<sub>3</sub>), 2.41 (s, 3H, H<sub>17</sub>), 2.14 (br s, 1H, H<sub>18</sub>), 2.02 – 1.87 (m, 2H, H<sub>2</sub>), 1.87 – 1.77 (m, 2H, H<sub>4</sub>), 1.64 (t, *J* = 7.7 Hz, 2H, H<sub>1</sub>). **<sup>13</sup>C NMR** (151 MHz, CD<sub>3</sub>CN) δ 156.5 (C<sub>7</sub> or C<sub>8</sub>), 156.4 (C<sub>7</sub> or C<sub>8</sub>), 145.0 (C<sub>13</sub>), 137.7 (C<sub>16</sub>), 133.1 (C<sub>9</sub>), 129.9 (C<sub>15</sub>), 129.8 (C<sub>10</sub> or C<sub>11</sub>), 129.2 (C<sub>12</sub>), 127.2 (C<sub>10</sub> or C<sub>11</sub>), 126.2 (C<sub>14</sub>), 65.4 (C<sub>5</sub>), 50.4 (C<sub>3</sub>), 49.9 (C<sub>6</sub>), 27.4 (C<sub>1</sub>), 21.0 (C<sub>17</sub>), 18.8 (C<sub>2</sub>), 16.0 (C<sub>4</sub>). **HR-ESI MS** *m/z* = 400.1684 [M+H]<sup>+</sup>, calculated for C<sub>24</sub>H<sub>22</sub>N<sub>3</sub>O<sub>3</sub><sup>+</sup>: 400.1661.

#### 6-(4-Tolyl)bicyclo[3.2.2]nona-3,8-dien-6-ol [(R)/(S)-6] from 7



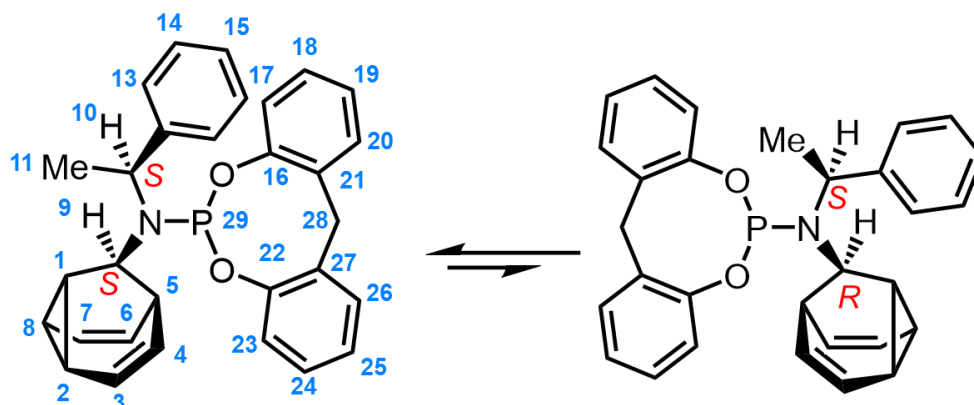
A solution of 11-hydroxy-11-(4-tolylphenyl)-5-phenyl-3,5,7-triazatetracyclo[8.2.2.0<sup>2,8</sup>.0<sup>3,7</sup>]tetradecane-4,6-dione (45 mg, 0.11 mmol) and NaOH (75 mg, 1.88 mmol) in iPrOH (6 mL) were heated to reflux for 24 h under N<sub>2</sub>. Evidence of an intermediate diazinane was observed by acquiring a crude <sup>1</sup>H NMR spectrum of an aliquot (Figure 4.3). The solution was cooled to 0 °C, then HCl(aq) (10%, 1.2 mL) and a solution of CuCl<sub>2</sub> (135 mg, 1.01 mmol) in H<sub>2</sub>O (7.5 mL) was added. After stirring at rt for 4 h, a 35% solution of NH<sub>3</sub> in H<sub>2</sub>O was added dropwise until a blue colour persisted. The reaction mixture was cooled and extracted with EtOAc (3 × 15 mL). The organic phase washed with brine (50 mL) and H<sub>2</sub>O (50 mL). The organic phase was dried over MgSO<sub>4</sub>, filtered and the solvent removed under *in vacuo*. The crude residue was purified by column chromatography (Teledyne Isco CombiFlash Rf+ system, 4 g SiO<sub>2</sub>, hexanes–Et<sub>2</sub>O, gradient elution) to yield 6-(4-tolyl)bicyclo[3.2.2]nona-3,8-dien-6-ol as colourless solid (12 mg).

***N*-(*S*)-1-(Phenylethynyl)-tricyclo[3.3.1.0<sup>2,8</sup>]-nona-3,6-dien-9-amine.**

In an oven-dried round-bottomed flask fitted with a septum under a N<sub>2</sub> atmosphere, tricyclo[3.3.1.0<sup>2,8</sup>]nona-3,6-dien-9-one (80 mg, 0.61 mmol) and (*S*)-(-)-1-phenylethylamine (250  $\mu$ L, 1.96 mmol) were dissolved in anhydrous MeOH (0.80 mL). Glacial acetic acid (25  $\mu$ L) was added

dropwise to the stirred reaction mixture and left for 30 min. Sodium cyanoborohydride (50 mg, 0.80 mmol, 1.2 equiv.) was then added to the reaction mixture, which was left to stir for 16 h at 100 °C. The mixture was quenched with 5 drops of Et<sub>3</sub>N and the solvent was removed under reduced pressure. This material was dissolved in an aqueous solution of NaHCO<sub>3</sub> (50 mL) and extracted with CH<sub>2</sub>Cl<sub>2</sub> (5  $\times$  25 mL). The combined organic extracts were washed with brine (1  $\times$  50 mL), H<sub>2</sub>O (1  $\times$  50 mL), dried over MgSO<sub>4</sub>, filtered and the solvent was removed *in vacuo*. The crude residue was purified by column chromatography (Teledyne Isco CombiFlash Rf+ system, 4 g SiO<sub>2</sub>, hexanes–EtOAc, gradient including 1% Et<sub>3</sub>N in the elution) to give the title compound as a colourless oil (71 mg, 0.30 mmol, 49%). **<sup>1</sup>H NMR** (700 MHz, CDCl<sub>3</sub>)  $\delta$  7.36 – 7.28 (m, 4H, H<sub>13</sub> and H<sub>14</sub>), 7.22 (tt, *J* = 7.2, 1.5 Hz, 1H, H<sub>15</sub>), 5.81 (t, *J* = 7.8 Hz, 1H, H<sub>7</sub>), 5.52 (t, *J* = 7.7 Hz, 1H, H<sub>3</sub>), 4.23 – 4.20 (m, 1H, H<sub>2</sub> or H<sub>4</sub>), 4.14 – 4.11 (m, 1H, H<sub>2</sub> or H<sub>4</sub>), 3.88 (q, *J* = 6.5 Hz, 1H, H<sub>11</sub>), 3.85 – 3.82 (m, 1H, H<sub>8</sub> or H<sub>6</sub>), 3.76 – 3.72 (m, 1H, H<sub>8</sub> or H<sub>6</sub>), 2.35 – 2.33 (m, 1H, H<sub>9</sub>), 2.33 – 2.30 (m, 2H, H<sub>1</sub> and H<sub>5</sub>), 1.28 (d, *J* = 6.5 Hz, 3H, H<sub>16</sub>), 1.03 (br s, 1H, H<sub>10</sub>). **<sup>13</sup>C NMR** (176 MHz, CDCl<sub>3</sub>)  $\delta$  146.1 (C<sub>12</sub>), 128.5 (C<sub>13</sub>), 126.9 (C<sub>15</sub>), 126.9 (C<sub>14</sub>), 123.1 (C<sub>7</sub>), 121.1 (C<sub>3</sub>), 81.4 (C<sub>2</sub> or C<sub>4</sub>), 77.4 (C<sub>8</sub> or C<sub>6</sub>), 71.2 (C<sub>2</sub> or C<sub>4</sub>), 67.4 (C<sub>8</sub> or C<sub>6</sub>), 54.9 (C<sub>11</sub>), 44.6 (C<sub>9</sub>), 29.7 (C<sub>1</sub> or C<sub>5</sub>), 29.1 (C<sub>1</sub> or C<sub>5</sub>), 25.3 (C<sub>16</sub>). **HRMS-ASAP** *m/z* = 238.1592 [M+H]<sup>+</sup>, calculated for C<sub>17</sub>H<sub>20</sub>N: 238.1596.

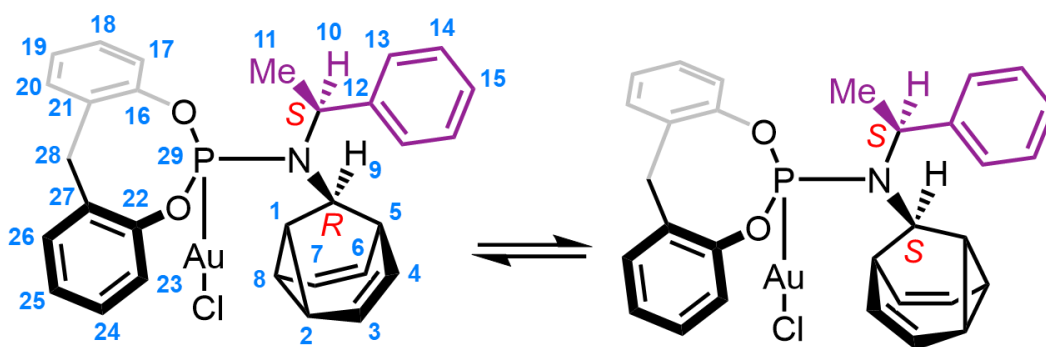
***N*-(1-Phenylethyl)-*N*-{tricyclo[3.3.1.0<sup>2,8</sup>]nona-2,6-dien-9-yl}-9,11-dioxa-10-phosphatricyclo- [10. 4.0.0<sup>3,8</sup>]hexadeca-1(16),3,5,7,12,14-hexaen-10-amine [(*R,S*)/(*S,S*).**



$\text{PCl}_3$  (27.5 mg, 200  $\mu\text{mol}$ ),  $\text{Et}_3\text{N}$  (162 mg, 1.6 mmol) and anhydrous  $\text{CH}_2\text{Cl}_2$  (2.0 mL) were placed in an oven-dried vial under an  $\text{N}_2$  atmosphere and cooled to 0 °C. A solution of *N*-(*S*)-1-(phenylethynyl)-tricyclo[3.3.1.0<sup>2,8</sup>]nona-3,6-dien-9-amine (47.5 mg, 200  $\mu\text{mol}$ ) in anhydrous  $\text{CH}_2\text{Cl}_2$  (2.0 mL) was added dropwise by syringe over 10 min and the resulting mixture stirred at 0 °C for 3 h. A solution of 2,2'-methylenediphenol (40.0 mg, 200  $\mu\text{mol}$ ) in anhydrous  $\text{CH}_2\text{Cl}_2$  (2.0 mL) was added dropwise by syringe over 10 min, then the resulting mixture was allowed to warm to rt and stirred for 16 h. The solution was poured into a mixture of  $\text{H}_2\text{O}$  (30 mL) and brine (5 mL), then extracted with  $\text{CH}_2\text{Cl}_2$  ( $4 \times 10$  mL). The combined organic extracts were dried over  $\text{K}_2\text{CO}_3$  then the solvent was removed *in vacuo*. The crude residue was purified by column chromatography (Teledyne Isco CombiFlash Rf+ system, 12 g neutral  $\text{Al}_2\text{O}_3$ , hexanes– $\text{CH}_2\text{Cl}_2$ , gradient elution), giving the title compound as a colourless solid powder (41.4 mg, 89  $\mu\text{mol}$ , 44%). The ligand was stored in a vial flushed with nitrogen to prevent degradation. **M. P.** 159 – 160 °C.  $^1\text{H NMR}$  (600 MHz,  $\text{CDCl}_3$ )  $\delta$  7.63 – 7.58 (m, 2H,  $\text{H}_{13}$ ), 7.35 (t,  $J = 7.7$  Hz, 2H,  $\text{H}_{14}$ ), 7.31 (dt,  $J = 7.7$ , 2.1 Hz, 2H,  $\text{H}_{17}$  and  $\text{H}_{23}$ ), 7.28 – 7.23 (m, 1H,  $\text{H}_{15}$ ), 7.14 (t,  $J = 7.6$  Hz, 2H,  $\text{H}_{19}$  and  $\text{H}_{25}$ ), 7.03 – 6.97 (m, 4H,  $\text{H}_{18}$ ,  $\text{H}_{20}$ ,  $\text{H}_{26}$  and  $\text{H}_{24}$ ), 5.81 (t,  $J = 7.8$  Hz, 1H,  $\text{H}_3$  or  $\text{H}_7$ ), 5.48 (t,  $J = 7.5$  Hz, 1H,  $\text{H}_3$  or  $\text{H}_7$ ), 5.46 – 5.39 (m, 1H,  $\text{H}_{10}$ ), 4.42 (dd,  $J = 12.8$ , 3.0 Hz, 1H,  $\text{H}_{28}$ ), 4.09 (s, 2H,  $\text{H}_2$  and/or  $\text{H}_4$  and/or  $\text{H}_6$  and/or  $\text{H}_8$ ), 3.97 – 3.86 (m, 2H,  $\text{H}_2$  and/or  $\text{H}_4$  and/or  $\text{H}_6$  and/or  $\text{H}_8$ ), 3.51 (d,  $J = 12.8$  Hz, 1H,  $\text{H}_{28}$ ), 3.12 (d,  $J = 16.4$  Hz, 1H,  $\text{H}_9$ ), 2.65 – 2.59 (m, 1H,  $\text{H}_1$  or  $\text{H}_5$ ), 1.89 – 1.84 (m, 1H,  $\text{H}_1$  or  $\text{H}_5$ ), 1.73 (d,  $J = 7.1$  Hz, 3H,  $\text{H}_{11}$ ).

**$^{13}\text{C}$  NMR** (151 MHz,  $\text{CDCl}_3$ )  $\delta$  152.1 – 152.0 (m, 2C,  $\text{C}_{16}$  and  $\text{C}_{22}$ ), 143.6 ( $\text{C}_{12}$ ), 135.8 – 135.7 (m, 2C,  $\text{C}_{21}$  and  $\text{C}_{27}$ ), 129.9 (d,  $J_{\text{CP}} = 7.4$  Hz, 2C,  $\text{C}_{17}$  and  $\text{C}_{23}$ ), 128.3 ( $\text{C}_{13}$ ), 128.2 ( $\text{C}_{14}$ ), 128.0 (2C,  $\text{C}_{19}$  and  $\text{C}_{25}$ ), 126.8 ( $\text{C}_{15}$ ), 124.8 (d,  $J_{\text{CP}} = 5.1$  Hz,  $\text{C}_3$ ), 124.4 (d,  $J_{\text{CP}} = 6.6$  Hz, 2C,  $\text{C}_{20}$  and  $\text{C}_{28}$ ), 123.2 (d,  $J_{\text{CP}} = 3.0$  Hz, 2C,  $\text{C}_{18}$  and  $\text{C}_{24}$ ), 121.5 ( $\text{C}_7$ ), 74.3 (2C,  $\text{C}_2$  and  $\text{C}_4$ ), 73.2 (2C,  $\text{C}_6$  and  $\text{C}_8$ ), 51.9 ( $\text{C}_{10}$ ), 45.1 (d,  $J_{\text{CP}} = 17.3$  Hz,  $\text{C}_9$ ), 34.3 ( $\text{C}_{28}$ ), 31.7 (d,  $J_{\text{CP}} = 7.2$  Hz,  $\text{C}_1$  or  $\text{C}_5$ ), 30.5 (d,  $J_{\text{CP}} = 5.5$  Hz,  $\text{C}_1$  or  $\text{C}_5$ ), 20.2 (d,  $J_{\text{CP}} = 2.6$  Hz,  $\text{C}_{11}$ ).  **$^{31}\text{P}$  NMR** (243 MHz,  $\text{CDCl}_3$ )  $\delta$  139.3 ( $\text{P}_{29}$ ). **HR-ESI-MS**  $m/z = 466.1923$   $[\text{M}+\text{H}]^+$  calculated for  $\text{C}_{30}\text{H}_{29}\text{NO}_2\text{P}^+$ : 466.1936.

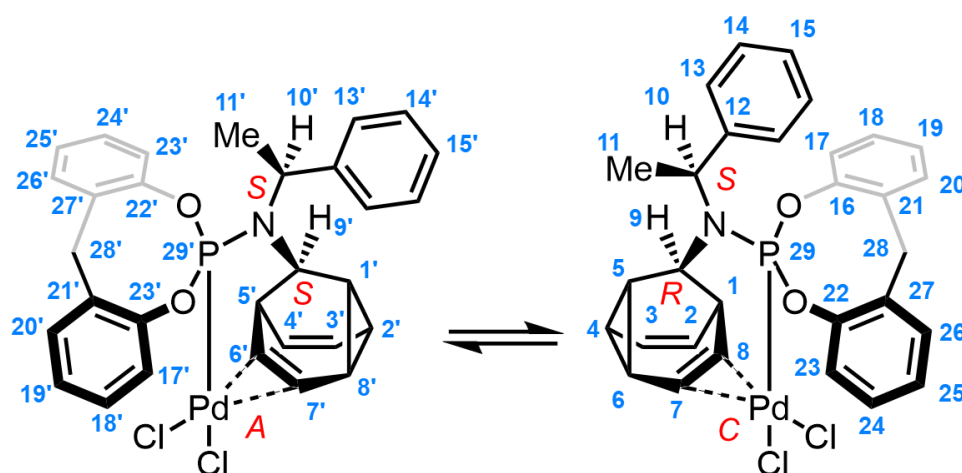
**Chloro({10-[(1-phenylethyl)(tricyclo[3.3.1.0<sup>2,8</sup>]nona-3,6-dien-9-yl)amino]-9-11-dioxo-10-phosphatrimethyl-10.4.0.0<sup>3,8</sup>]hexadeca-1(16),3,5,7,12,14-hexaen-10-yl}gold [(R,S)/(S,S)-L<sub>BBAu</sub>Cl]**



**L<sub>BBAu</sub>** (6.5 mg, 14  $\mu\text{mol}$ ) and  $\text{Me}_2\text{S} \cdot \text{AuCl}$  (4.1 mg, 14  $\mu\text{mol}$ ) were dissolved in  $\text{CDCl}_3$  (0.7 mL) and sonicated for 10 min to dissolve the solids. The mixture was then evaporated under reduced pressure and dried under high vacuum, to give the title compound as a pale yellow solid (9.1 mg, 13  $\mu\text{mol}$ , 93%).  **$^1\text{H}$  NMR** (600 MHz,  $\text{CDCl}_3$ )  $\delta$  7.58 (d,  $J = 7.6$  Hz, 2H,  $\text{H}_{13}$ ), 7.42 (dd,  $J = 7.7, 7.7$  Hz, 2H,  $\text{H}_{14}$ ), 7.34 (t,  $J = 7.4$  Hz, 1H,  $\text{H}_{15}$ ), 7.28 (d,  $J = 7.4$  Hz, 2H,  $\text{H}_{20}$  and  $\text{H}_{26}$ ), 7.17 – 7.11 (m, 2H,  $\text{H}_{18}$  and  $\text{H}_{24}$ ), 7.11 – 7.06 (m, 2H,  $\text{H}_{19}$  and  $\text{H}_{25}$ ), 6.87 (d,  $J = 8.1$  Hz, 1H,  $\text{H}_{17}$  or  $\text{H}_{23}$ ), 6.80 (d,  $J = 8.1$  Hz, 1H,  $\text{H}_{17}$  or  $\text{H}_{23}$ ), 5.92 (dd,  $J = 7.9, 7.9$  Hz, 1H,  $\text{H}_7$ ), 5.61 (dd,  $J = 7.6, 7.6$  Hz, 1H,  $\text{H}_3$ ), 5.14 (dq,  $J = 22.0, 7.0$  Hz, 1H,  $\text{H}_{10}$ ), 4.63 – 4.58 (m, 1H,  $\text{H}_6$ ), 4.55 – 4.49 (m, 1H,  $\text{H}_4$ ), 4.27 (dd,  $J = 13.0, 4.6$  Hz, 1H,  $\text{H}_{28}$ ), 4.02 – 3.96 (m, 1H,  $\text{H}_8$ ), 3.94 (d,  $J = 12.7$  Hz, 1H,  $\text{H}_9$ ), 3.92 – 3.86 (m, 1H,  $\text{H}_2$ ), 3.47 (d,  $J = 13.0$  Hz, 1H,  $\text{H}_{28}$ ), 2.86 – 2.80 (m, 1H,  $\text{H}_5$ ), 2.60 – 2.55 (m, 1H,  $\text{H}_1$ ), 1.96 (d,  $J = 6.9$  Hz, 3H,  $\text{H}_{11}$ ).  **$^{13}\text{C}$  NMR** (151 MHz,  $\text{CDCl}_3$ )  $\delta$  149.0 (d,  $J = 2.9$  Hz,  $\text{C}_{16}$  or  $\text{C}_{22}$ ), 148.6 (d,  $J_{\text{CP}} = 3.1$  Hz,  $\text{C}_{16}$  or  $\text{C}_{22}$ ), 142.9 (d,  $J_{\text{CP}} = 3.6$  Hz,  $\text{C}_{12}$ ), 134.7 (d,  $J_{\text{CP}} = 3.9$  Hz,  $\text{C}_{21}$  or  $\text{C}_{27}$ ), 134.6 (d,  $J_{\text{CP}} = 3.8$  Hz,  $\text{C}_{21}$  or  $\text{C}_{27}$ ), 130.1

(d,  $J_{CP} = 2.2$  Hz, C<sub>20</sub> or C<sub>26</sub>), 130.1 (d,  $J_{CP} = 2.2$  Hz, C<sub>20</sub> or C<sub>26</sub>), 129.1 (C<sub>18</sub> or C<sub>24</sub>), 129.1 (C<sub>18</sub> or C<sub>24</sub>), 128.7 (C<sub>14</sub>), 127.7 (C<sub>13</sub>), 127.6 (C<sub>15</sub>), 126.8 (C<sub>19</sub> or C<sub>25</sub>), 126.8 (C<sub>19</sub> or C<sub>25</sub>), 123.6 (C<sub>7</sub>), 123.2 (C<sub>17</sub> or C<sub>23</sub>), 123.2 (C<sub>17</sub> or C<sub>23</sub>), 121.7 (C<sub>3</sub>), 84.8 (C<sub>4</sub>), 81.0 (C<sub>6</sub>), 53.1 (d,  $J_{CP} = 8.9$  Hz, C<sub>10</sub>), 47.9 (d,  $J_{CP} = 5.9$  Hz, C<sub>9</sub>), 33.5 (C<sub>28</sub>), 31.1 (C<sub>5</sub>), 28.3 (C<sub>1</sub>), 21.7 (d,  $J = 3.4$  Hz, C<sub>11</sub>). **<sup>31</sup>P NMR** (162 MHz, CDCl<sub>3</sub>)  $\delta$  120.9 (P<sub>29</sub>). **HR-ESI-MS**  $m/z = 720.1142$  [M+Na]<sup>+</sup> calculated for C<sub>30</sub>H<sub>28</sub>AuClINaO<sub>2</sub>P<sup>+</sup>: 720.1110.

**Dichloro({10-[(1-phenylethyl)(tricyclo[3.3.1.0<sup>2,8</sup>]nona-3,6-dien-9-yl)amino]-9-11-dioxa-10-phosphatricyclo-[10.4.0.0<sup>3,8</sup>]hexadeca-1(16),3,5,7,12,14-hexaen-10-yl]palladium**



**LBB** (10.0 mg, 21.5  $\mu$ mol) and PdCl<sub>2</sub>·(MeCN)<sub>2</sub> (5.6 mg, 21.5  $\mu$ mol) were suspended in CDCl<sub>3</sub> (0.7 mL) at rt and sonicated for 15 min until a homogeneous solution was formed. The solution was evaporated under reduced pressure to give the title compound as a pale yellow solid (13.5 mg, 0.02 mmol, 98%). Where possible, the <sup>1</sup>H and <sup>13</sup>C NMR resonances of the title compound have been assigned to a site in the structure of a specific diastereoisomer based on two-dimensional spectra acquired in the slow exchange regime (at 240 K). Unambiguous peak assignments are not possible in some cases on account of signal overlap. The number of nuclei represented by each signal is given without adjustment for the uneven population of the two diastereoisomers, which are present in a 1.3:1 ratio of (C,R,S)-**LBB**PdCl<sub>2</sub> to (A,S,S)-**LBB**PdCl<sub>2</sub> at 240 K. **<sup>1</sup>H NMR** (500 MHz, CDCl<sub>3</sub>, 240 K)  $\delta$  7.53 (d,  $J = 7.6$  Hz, 2H), 7.46 – 7.27 (m, 16H), 7.23 – 7.06 (m, 8H), 6.81 – 6.77 (m, 1H, H<sub>7</sub>), 6.77 – 6.73 (m, 1H, H<sub>7</sub>'), 6.10 (dd,  $J = 7.3, 4.6$  Hz, 1H, H<sub>6</sub>'), 6.04 – 5.96 (m, 2H, H<sub>8</sub> and H<sub>4</sub>'), 5.90 – 5.82 (m, 2H, H<sub>3</sub> and H<sub>3</sub>'), 5.74 (t,  $J =$

7.9 Hz, 1H, H<sub>2</sub>), 5.64 (q,  $J = 6.8$  Hz, 1H, H<sub>10</sub>), 5.58 (q,  $J = 6.9$  Hz, 1H, H<sub>10'</sub>), 4.43 (dd,  $J = 13.2, 3.4$  Hz, 1H, H<sub>28'</sub>), 4.30 (dd,  $J = 13.2, 3.3$  Hz, 1H, H<sub>28</sub>), 3.65 (d,  $J = 13.2$  Hz, 1H, H<sub>28'</sub>), 3.61 (d,  $J = 13.2$  Hz, 1H, H<sub>28</sub>), 3.12 – 3.05 (m, 2H, H<sub>6</sub> and H<sub>5'</sub>), 3.02 – 2.95 (m, 2H, H<sub>5</sub> and H<sub>4</sub>), 2.94 – 2.82 (m, 2H, H<sub>9</sub> and H<sub>8'</sub>), 2.73 – 2.64 (m, 1H, H<sub>2'</sub>), 2.57 – 2.40 (m, 2H, H<sub>1</sub> and H<sub>9'</sub>), 1.73 (d,  $J = 7.0$  Hz, 3H, H<sub>11</sub>), 1.69 – 1.64 (m, 1H, H<sub>11'</sub>), 1.61 (d,  $J = 6.8$  Hz, 3H, H<sub>11'</sub>). **<sup>13</sup>C NMR** (151 MHz, CDCl<sub>3</sub>, 240 K)  $\delta$  151.3, 151.2, 151.1, 148.5, 148.4, 139.0 (d,  $J_{CP} = 5.1$  Hz, C<sub>12</sub>), 138.9 (C<sub>12'</sub>), 131.0, 131.0, 130.1, 130.0, 129.4, 129.3, 128.8, 128.7, 128.6, 128.3, 128.2, 127.7, 126.6, 126.1, 125.9, 125.7 (C<sub>2'</sub>), 125.7, 125.1, 123.6, 123.0, 122.6, 108.0 (C<sub>7'</sub>), 107.7 (C<sub>7</sub>), 88.8 (C<sub>6</sub>), 88.5 (C<sub>8'</sub>), 55.6 (d,  $J_{CP} = 5.4$  Hz, C<sub>10'</sub>), 54.5 (d,  $J_{CP} = 5.8$  Hz, C<sub>10</sub>), 45.0, 44.9, 44.7, 44.6, 36.4, 35.2, 33.6 (C<sub>28'</sub>), 33.5 (C<sub>28</sub>), 33.4, 33.3, 29.5, 29.5, 26.8, 25.6, 18.3 (C<sub>11'</sub>), 18.1 (C<sub>11</sub>). The spectral data acquired at 298 K are also given below. At this temperature, the diastereoisomers are in fast exchange and most resonances are resolved, representing an average of the two structures. They are assigned using the labelling system shown for (C,R,S)-LBB<sub>1</sub>PdCl<sub>2</sub>. Some peaks are broadened into the baseline at this temperature, so they are either missing or are reported as broad (br). **<sup>1</sup>H NMR** (499 MHz, CDCl<sub>3</sub>, 298 K)  $\delta$  7.48 (d,  $J = 7.6$  Hz, 2H, H<sub>13</sub>), 7.40 (t,  $J = 7.5$  Hz, 2H, H<sub>14</sub>), 7.36 – 7.33 (m, 1H, H<sub>15</sub>), 7.32 (d,  $J = 7.4$  Hz, 2H, H<sub>20</sub> and H<sub>26</sub>), 7.28 – 7.17 (m, 4H, H<sub>17</sub>, H<sub>18</sub>, H<sub>23</sub> and H<sub>24</sub>), 7.13 (t,  $J = 6.3$  Hz, 2H, H<sub>19</sub> and H<sub>25</sub>), 6.79 (t,  $J = 6.5$  Hz, 1H, H<sub>7</sub>), 6.34 – 5.44 (br, 2H), 5.86 (t,  $J = 7.6$  Hz, 1H, H<sub>3</sub>), 5.67 – 5.58 (m, 1H, H<sub>10</sub>), 4.37 (s, 1H, H<sub>28</sub>), 3.64 (d,  $J = 13.3$  Hz, 1H, H<sub>28</sub>), 3.36 – 2.19 (br, 4H), 2.96 (d,  $J_{HP} = 31.6$  Hz, 1H, H<sub>9</sub>), 1.75 – 1.65 (m, 3H, H<sub>11</sub>). **<sup>13</sup>C NMR** (151 MHz, CDCl<sub>3</sub>, 298 K)  $\delta$  139.4 (d,  $J_{CP} = 3.6$  Hz, C<sub>12</sub>), 130.2 (C<sub>20</sub> and C<sub>26</sub>), 128.9 (C<sub>14</sub>), 128.6 (br), 128.6 (br), 128.3 (C<sub>15</sub>), 128.1 (br, C<sub>13</sub>), 126.3 (br, C<sub>19</sub> and C<sub>25</sub>), 125.4 (br, C<sub>3</sub>), 123.4 (br, C<sub>17</sub>, C<sub>18</sub>, C<sub>23</sub> and C<sub>24</sub>), 107.8 (C<sub>7</sub>), 55.2 (C<sub>10</sub>), 45.1 (d,  $J_{CP} = 15.1$  Hz, C<sub>9</sub>), 33.9 (C<sub>28</sub>), 18.2 (C<sub>11</sub>). **<sup>31</sup>P NMR** (243 MHz, CDCl<sub>3</sub>, 298 K)  $\delta$  72.4 (P<sub>29</sub>). **LRESI-MS**  $m/z = 642.307$  [M+H]<sup>+</sup> calculated for C<sub>30</sub>H<sub>29</sub>Cl<sub>2</sub>NO<sub>2</sub>PPd<sup>+</sup>: 642.0348.

Note on the stereochemical assignment of (A,S,S)/(C,R,S)-LBB<sub>1</sub>PdCl<sub>2</sub>: The complex has been treated as a distorted trigonal bipyramidal complex (see Figure 4.8) for the assignment of stereochemical descriptor to the Pd centre, bearing apical P and Cl ligands, with equatorial Cl and C sites. Although olefin ligands are typically regarded as a monodentate in organometallic nomenclature, it is necessary to treat the

coordinated olefin of **L<sub>BB</sub>** as an  $\eta^2$ -donor to account for its dissymmetry and accurately describe the stereochemical environment of the Pd centre. Consequently, the Pd centre is treated as being formally pentacoordinate. Treating the complex as being square planar and bearing a monodentate ligand would not capture the three-dimensional stereochemistry of the coordination as the olefin ligand is held in an orthogonal orientation to the Cl-Pd-Cl plane. Comparing the theoretical structures Pd1 and Pd2 (Figure S2) illustrates that, even in the absence of a fixed stereocentre as part of the olefin ligand, the Pd coordination environment is chiral. The Cahn–Ingold–Prelog (CIP) priority of the ligands for stereochemical assignment of the Pd is  $\text{Cl} > \text{P} > \text{C}_6 > \text{C}_7$ . Its configuration index is TBPY-5-12. Note also that the stereochemical descriptor for some of the  $\text{sp}^3$ -C stereocentres of the ligand (e.g., the barbaralane 9-position) are changed from the ligand precursor as the Pd coordination alters the CIP priorities assigned to the barbaralane skeleton.

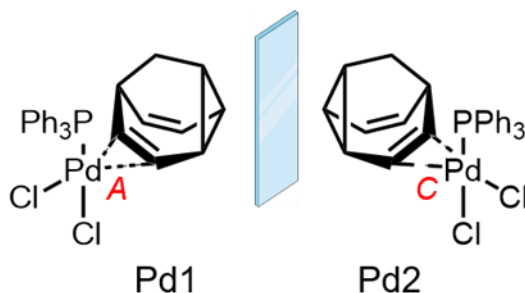
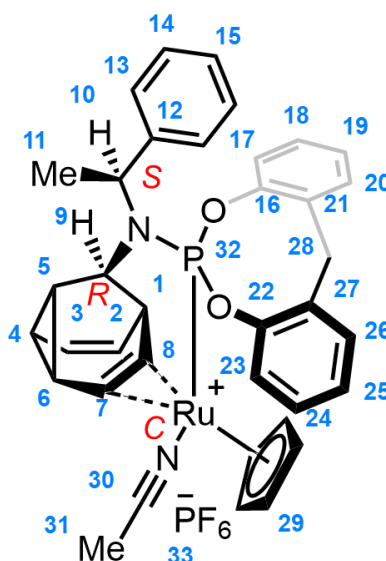


**Figure S4.2.** A theoretical enantiomeric pair of Pd complexes arising from the coordination of a dissymmetric olefin ligand (barbaralane) that is oriented orthogonally to the Cl-Pd-Cl plane.

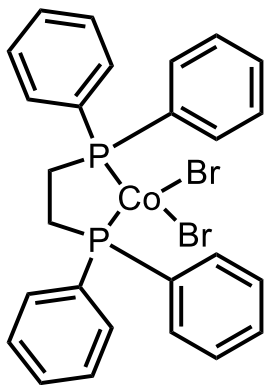
**N-[(1-Phenylethyl)({tricyclo[3.3.1.0<sup>2,8</sup>]nona-2,6-dien-9-yl})ami-no]-19,20-dioxaphospha-2-ruthenpentacyco[9.8.2.0<sup>3,7</sup>,7.0<sup>7,21</sup>,21.0<sup>13,18</sup>]henicosa-7(21),8,10,13,15,17-hexaen-2-yl}acetonitrile hexafluorophosphate [(C,R,S)-L<sub>BB</sub>RuCp(NCMe)·PF<sub>6</sub>]:**



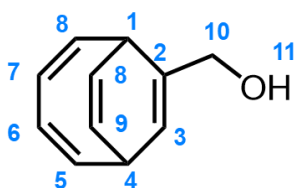
**L<sub>BB</sub>** (6.1 mg, 13.1  $\mu\text{mol}$ ) and **CpRu(NCMe)<sub>3</sub>·PF<sub>6</sub>** (5.7 mg, 13.1  $\mu\text{mol}$ ) were suspended in  $\text{CDCl}_3$  (0.7 mL) at rt and sonicated for 5 min until a homogeneous solution was formed. The resulting complex was isolated by slow diffusion of  $i\text{Pr}_2\text{O}$  vapour into the solution, which led to formation of a yellow precipitate. The mother liquor was decanted and the solid dried under reduced pressure. The resulting crude residue was then redissolved in  $\text{CDCl}_3$  (0.7 mL). The solution was passed through a syringe tip filter then allowed to slowly evaporate to approximately one quarter of the volume, leading to the formation of crystals. The mother liquor was decanted and the solid dried under reduced pressure, affording the title compound as a yellow solid (7.4 mg, 9  $\mu\text{mol}$ , 69%). The title complex is isolated as a single stereoisomer upon crystallisation but equilibrates over a period of several minutes-to-hours at room temperature in  $\text{CDCl}_3$  solution, giving an approximately 4:1 mixture of the (C,R,S)- to the (A,S,S)-complex. NMR spectra for characterisation were obtained using a freshly crystallised sample and measured immediately after dissolution to allow assignment of the (C,R,S)-complex in its near-isomerically-pure form. Where possible, the  $^1\text{H}$  and  $^{13}\text{C}$  NMR resonances of the title compound have been assigned to a site in the structure based on two dimensional spectra. Unambiguous peak assignments are not possible in some cases on account of signal overlap in the aromatic regions. **M. P.** 214 – 216 °C.  **$^1\text{H}$  NMR** (400

MHz, CDCl<sub>3</sub>)  $\delta$  7.62 – 7.49 (m, 3H, H<sub>13-15</sub> and/or H<sub>18-20</sub> and/or H<sub>25-26</sub>), 7.41 – 7.21 (m, 8H, H<sub>13-15</sub> and/or H<sub>18-20</sub> and/or H<sub>25-26</sub>), 6.99 (d,  $J$  = 8.1 Hz, 1H, H<sub>23</sub>), 6.88 (d,  $J$  = 6.9 Hz, 1H, H<sub>17</sub>), 6.12 (t,  $J$  = 7.9 Hz, 1H, H<sub>2</sub>), 5.99 (dd,  $J$  = 9.0, 6.2 Hz, 1H, H<sub>3</sub>), 5.84 – 5.73 (m, 1H, H<sub>10</sub>), 4.82 (dd,  $J$  = 8.0, 4.4 Hz, 1H, H<sub>7</sub>), 4.62 (dd,  $J$  = 12.9, 3.7 Hz, 1H, H<sub>28</sub>), 4.16 (s, 5H, H<sub>29</sub>), 4.01 – 3.94 (m, 1H, H<sub>8</sub>), 3.68 (d,  $J$  = 13.0 Hz, 1H, H<sub>28</sub>), 3.49 – 3.40 (m, 1H, H<sub>1</sub>), 3.19 (d,  $J$  = 22.0 Hz, 1H, H<sub>9</sub>), 2.56 (d,  $J$  = 1.4 Hz, 3H, H<sub>31</sub>), 2.09 – 1.98 (m, 1H, H<sub>4</sub>), 1.93 – 1.84 (m, 1H, H<sub>6</sub>), 1.77 (d,  $J$  = 7.0 Hz, 3H, H<sub>11</sub>), 0.33 – 0.24 (m, 1H, H<sub>5</sub>). **<sup>13</sup>C NMR** (151 MHz, CDCl<sub>3</sub>)  $\delta$  149.3, 141.6 (d,  $J_{CP}$  = 7.3 Hz, C<sub>12</sub>), 135.0, 133.9, 130.8, 129.7 (C<sub>30</sub>), 128.7, S27 128.5, 128.3, 128.1, 128.0, 128.0, 127.0, 126.5, 126.3, 124.7 (C<sub>23</sub>), 123.3 (C<sub>17</sub>), 84.7 (d,  $J_{CP}$  = 2.1 Hz, C<sub>29</sub>), 52.9 (d,  $J_{CP}$  = 6.7 Hz, C<sub>10</sub>), 51.0 (C<sub>7</sub>), 47.4 (d,  $J$  = 15.7 Hz, C<sub>9</sub>), 46.9 (C<sub>8</sub>), 35.5 (d,  $J$  = 19.1 Hz, C<sub>1</sub>), 34.0 (C<sub>28</sub>), 25.0 (C<sub>6</sub>), 24.9 (C<sub>4</sub>), 19.1 (C<sub>5</sub>), 16.2 (C<sub>11</sub>), 4.8 (C<sub>31</sub>). **<sup>19</sup>F NMR** (376 MHz, CDCl<sub>3</sub>)  $\delta$  – 73.0 (d,  $J_{PF}$  = 712.3 Hz, F<sub>33</sub>). **<sup>31</sup>P NMR** (162 MHz, CDCl<sub>3</sub>)  $\delta$  162.8 (d,  $J_{PH}$  = 20.6 Hz, P<sub>32</sub>), –144.3 (hept,  $J_{PF}$  = 712.3 Hz, P<sub>33</sub>). **HR-ESI-MS**  $m/z$  = 667.1605 [M–PF<sub>6</sub>]<sup>+</sup> (calculated for C<sub>37</sub>H<sub>36</sub>N<sub>2</sub>O<sub>2</sub>P<sub>2</sub>F<sub>6</sub>Ru<sup>+</sup> = 667.1590).

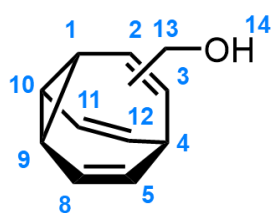
**Note on the stereochemical assignment of (C,R,S)-L<sub>B</sub>B RuCp(NCMe)·PF<sub>6</sub>:** The complex has been treated as a distorted square pyramidal complex for the assignment of stereochemical descriptor to the Ru centre, bearing an apical Cp ligand, with the remaining N, P, and two C coordination sites close to being in a plane.<sup>48</sup> The CIP priority of the ligands for stereochemical assignment of the Ru is Cp > P > N > C<sub>8</sub> > C<sub>7</sub>. Note that Cp ( $\mu_5$ -C<sub>5</sub>H<sub>5</sub><sup>–</sup>) is treated as a pseudo-atom of atomic number 30 and mass number 60 according to convention for arene-type polyhapto ligands.<sup>46</sup> The configuration index of the (C,R,S)- and (A,R,S)-complexes are SPY-5-25, whereas the (C,S,S)- and (A,S,S)-complexes are SPY-5-24. Note also that the stereochemical descriptor for some of the sp<sup>3</sup>-C stereocentres of the ligand (e.g., the barbaralane 9-position) are changed from the ligand precursor as the Ru coordination alters the CIP priorities assigned to the barbaralane skeleton.

**Dibromocobalt;2-diphenylphosphanylethyl(diphenyl)phosphane**

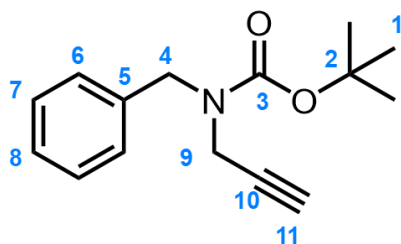
Solid  $\text{CoBr}_2$  (1.01 g, 4.62 mmol) and dppe (1.92 g, 4.82 mmol) were added to THF under Ar and the suspension was stirred for 24 h. The crude product was isolated via vacuum filtration, washed with n-pentane, and dried under vacuum to yield the title compound as a green solid (2.75 g, 4.46 mmol, 97% yield) which was used without further purification or characterisation.<sup>70</sup>

**((2Z,4Z)-bicyclo[4.2.2]deca-2,4,7,9-tetraen-7-yl)methanol.**

$\text{ZnI}_2$  (430 mg, 6.72 mmol) was added to an oven dried microwave vial and heated to 280 °C under vacuum for 5 min.  $\text{CoBr}_2(\text{dppe})$  (402 mg, 0.67 mmol) and activated zinc dust (132 mg, 2.02 mmol) were added to the same vial which was then sealed. The vial was flushed with Ar and evacuated under high vacuum three times. Anhydrous trifluoroethanol (8 mL) was added and three freeze pump thaw cycles undertaken. The reaction mixture was stirred for 15 min at rt and then COTT (700 mg, 6.72 mmol) was added. This was followed by the dropwise addition of propargyl alcohol (0.59 mL, 10.1 mmol) over 1.5 h, after which the reaction mixture was stirred for 22 h at 55 °C. The reaction mixture was filtered through a silica plug and eluted with  $\text{CH}_2\text{Cl}_2$ . The solvent was then removed *in vacuo* and the crude residue purified by column chromatography (Teledyne Isco CombiFlash Rf+ system, 12 g  $\text{SiO}_2$ , hexanes/EtOAc, 0 – 30%) affording the title compound as a yellow oil (955 mg, 5.91 mmol, 88% yield).  $^1\text{H NMR}$  (400 MHz,  $\text{CDCl}_3$ )  $\delta$  6.28 – 6.19 (m, 2H,  $\text{H}_5$  and  $\text{H}_9$ ), 5.81 – 5.74 (m, 2H,  $\text{H}_6$  and  $\text{H}_7$ ), 5.96 – 5.73 (m, 1H,  $\text{H}_8$ ), 5.66 – 5.63 (m, 2H,  $\text{H}_3$  and  $\text{H}_9$ ), 4.33 – 3.90 (m, 2H,  $\text{H}_{10}$ ), 3.54 – 3.42 (m, 1H,  $\text{H}_1$ ), 3.23 – 3.18 (m, 1H,  $\text{H}_4$ ). Spectral data agrees with literature values.<sup>36</sup>

**Tricyclo[3.3.2.0<sup>2,8</sup>]deca-3,6,9-trien-4-yl}methanol.**

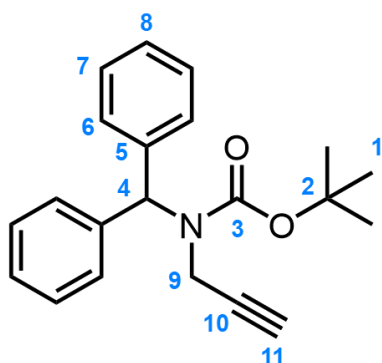
Bicyclo[4.2.2]deca-2,4,7,9-tetraene-7,8 diyl}methanol (145 mg, 0.94 mmol) and thioxanthene-9-one (2 mg, 0.01 mmol) were dissolved in anhydrous THF (2 mL) in an oven-dried microwave vial under Ar. The mixture was stirred for 3 h, while being irradiated with 360 nm UV light (3.4 W array of surface mounted 365 nm LEDs bulbs) at rt. The solvent was then removed *in vacuo* and the crude residue purified by column chromatography (Teledyne Isco CombiFlash Rf+ system, 24 g SiO<sub>2</sub>, hexanes/EtOAc, 0 – 15%) affording the title compound as a clear oil (73 mg, 0.47 mmol, 50% yield). <sup>1</sup>H NMR (400 MHz, (CDCl<sub>3</sub>): δ 5.85 (s, 5H, H<sub>2</sub>, H<sub>5</sub>, H<sub>8</sub>, H<sub>11</sub> and H<sub>12</sub>), 3.96 (s, 2H, H<sub>3</sub> and H<sub>4</sub>), 2.39 (s, 3H, H<sub>4</sub>, H<sub>9</sub> and H<sub>10</sub>), 1.75 (s, H<sub>13</sub>). Spectral data agrees with literature values.<sup>36</sup>

**tert-butyl benzyl(prop-2-yn-1-yl)carbamate**

To a single necked flask loaded with CH<sub>2</sub>Cl<sub>2</sub> (20 mL) and cooled to 0 °C, Et<sub>3</sub>N (2.48 g, 24.5 mmol), benzylamine (2.19 g, 20.4 mmol) and Boc<sub>2</sub>O (4.90 g, 22.4 mmol) were added sequentially. The reaction was stirred at rt for 24 h. The reaction was quenched with H<sub>2</sub>O (50 mL) and the aqueous layer was extracted with CH<sub>2</sub>Cl<sub>2</sub> (3 × 20 mL). The combined organic phases were dried over anhydrous MgSO<sub>4</sub> and the solvent removed *in vacuo* to give the title compound as a colourless oil (3.79 g). Tert-butyl benzylcarbamate (3.79 g, 18.3 mmol) was dissolved in DMF (30 mL) in a two necked flask under an Ar atmosphere. The mixture was cooled to 0 °C and NaH (0.658 g, 27.4 mmol) added. After being stirred at this temperature for 30 min, propargyl bromide (3.2 mL, 36.6 mmol) was added and the mixture was warmed to 20 °C and stirred for 5 h. The reaction was quenched with KOH (2M, 30 mL), extracted with EtOAc (3 × 30 mL) and dried over anhydrous MgSO<sub>4</sub>. The solvent was removed *in vacuo* and the crude residue purified by column chromatography (Teledyne Isco CombiFlash Rf+ system, 24 g SiO<sub>2</sub>, hexanes– EtOAc) affording the title compound as a yellow oil (3.15 g, 12.8 mmol, 70% yield). <sup>1</sup>H NMR (400 MHz, CDCl<sub>3</sub>) δ 7.35 – 7.27 (m, 5H, H<sub>5</sub>, H<sub>6</sub>,

H<sub>7</sub> and H<sub>8</sub>), 4.55 (s, 2H H<sub>4</sub>), 3.90 (s, 2H, H<sub>9</sub>), 2.21 (s, 1H, H<sub>11</sub>), 1.49 (s, 9H, H<sub>1</sub>). **HRMS** **ASAP**:  $m/z = 246.1213$  [M+H]<sup>+</sup>, calculated for C<sub>15</sub>H<sub>20</sub>NO<sub>2</sub><sup>+</sup>: 246.1494.

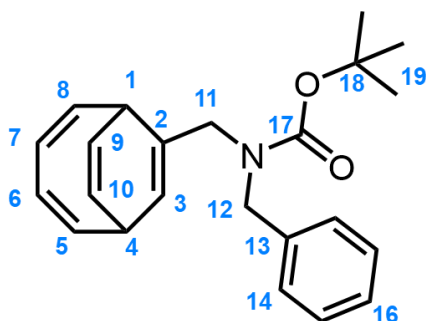
**tert-butyl benzhydryl(prop-2-yn-1-yl)carbamate.**



To a single necked flask loaded with CH<sub>2</sub>Cl<sub>2</sub> (20 mL) and cooled to 0°C, Et<sub>3</sub>N (2.48 g, 24.5 mmol), benzhydrylamine (3.74 g, 20.4 mmol) and Boc<sub>2</sub>O (4.90 g, 22.4 mmol) were added sequentially. The reaction was stirred at rt for 24 h. The reaction was quenched with H<sub>2</sub>O (50 mL) and the aqueous layer was extracted with CH<sub>2</sub>Cl<sub>2</sub> (3 × 20 mL). The

combined organic phases were dried over anhydrous MgSO<sub>4</sub> and the solvent removed *in vacuo* to give the title compound as a colourless oil (6.21 g). Tert-butyl benzylcarbamate (5.18 g, 18.3 mmol) was dissolved in DMF (30 mL) in a two necked flask under an Ar atmosphere. The mixture was cooled to 0 °C and NaH (0.658 g, 27.4 mmol) added. After being stirred at this temperature for 30 min, propargyl bromide (3.2 mL, 36.6 mmol) was added and the mixture was warmed to 20 °C and stirred for 5 h. The reaction was quenched with KOH (2M, 30 mL), extracted with EtOAc (3 × 30 mL) and dried over anhydrous MgSO<sub>4</sub>. The solvent was removed *in vacuo* and the crude residue purified by column chromatography (Teledyne Isco CombiFlash Rf+ system, 24 g SiO<sub>2</sub>, hexanes– EtOAc) affording the title compound as a yellow oil (4.15 g, 13.4 mmol, 64% yield). <sup>1</sup>H NMR (400 MHz, CDCl<sub>3</sub>) δ 7.42 – 7.23 (m, 1H, H<sub>6</sub>, H<sub>7</sub>, H<sub>8</sub>), 5.95 (s, 1H, H<sub>4</sub>), 4.15 (s, 2H, H<sub>9</sub>), 2.43 (s, 1H, H<sub>11</sub>), 1.48 (s, 9H, H<sub>1</sub>). Spectral data agrees with literature values.<sup>71</sup>

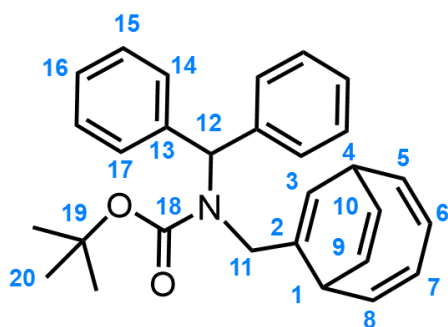
**tert-butyl-N-benzyl-N-(((2Z,4Z)-bicyclo[4.2.2]deca-2,4,7,9-tetraen-7-yl)methyl)glycinate.**



ZnI<sub>2</sub> (61.3 mg, 0.192 mmol) was added to an oven dried microwave vial and heated to 280°C under vacuum for 5 min. CoBr<sub>2</sub>(dppe) (59.3 mg, 0.288 mmol) and activated zinc dust (18.8 mg, 0.096 mmol) were added to the same vial which was then sealed. The vial was flushed with nitrogen and evacuated under high vacuum three times.

Anhydrous trifluoroethanol (1.5 mL) was added, and three freeze pump thaw cycles undertaken. The reaction mixture was stirred for 15 min at rt and then COTT (0.11 mL, 0.960 mmol) was added. This was followed by the dropwise addition of *N*-benzyl-Boc-propargylamine (0.38 mL, 1.44 mmol) over 1.5 h, after which the reaction mixture was stirred for 22 h at 55°C. The reaction mixture was filtered through a silica plug and eluted with EtOAc. The solvent was then removed in vacuo and the crude residue purified by column chromatography (Teledyne Isco CombiFlash Rf+ system, 12 g SiO<sub>2</sub>, hexanes–EtOAc) affording the title compound as a colourless oil (185 mg, 0.53 mmol, 55%). <sup>1</sup>H NMR (700 MHz, CDCl<sub>3</sub>) δ 7.25 – 7.27 (m, 2H, H<sub>14</sub>), 7.17 – 7.21 (m, 2H, H<sub>15</sub>), 7.14–7.15 (m, 1H, H<sub>16</sub>), 6.20–6.23 (m, 1H, H<sub>5</sub>), 6.07 – 6.12 (m, 1H, H<sub>8</sub>), 5.73 – 5.79 (m, 2H, H<sub>6</sub> and H<sub>7</sub>), 5.63 – 5.65 (m, 1H, H<sub>9</sub>), 5.58 – 5.60 (m, 1H, H<sub>10</sub>), 5.42 – 5.46 (m, 1H, H<sub>3</sub>), 4.12 – 4.32 (m, 2H, H<sub>12/12'</sub>), 3.67 – 3/86 (m, 2H, H<sub>11/11'</sub>), 3.35 – 3.37 (0.5H, m, H<sub>1</sub>), 3.24 – 3.26 (0.5H, m, H<sub>1'</sub>), 3.11 – 3.14 (m, 1H, H<sub>4/4'</sub>), 1.44 – 1.48 (m, 9H, H<sub>19</sub>). <sup>13</sup>C NMR (175 MHz, CDCl<sub>3</sub>) δ 155.9 (C<sub>17</sub>), 141.7 (C<sub>8/8'</sub>), 141.6 (C<sub>5/5'</sub>), 141.5 (C<sub>5/5'</sub>), 141.1 (C<sub>8/8'</sub>), 138.4 (C<sub>13/13'</sub>), 138.2 (C<sub>13/13'</sub>), 132.2 (C<sub>2/2'</sub>), 131.6 (C<sub>2/2'</sub>), 128.4 (C<sub>14/14'</sub>), 128.1 (C<sub>16/16'</sub>), 127.6 (C<sub>16/16'</sub>), 127.1 (C<sub>15/15'</sub>), 124.8 (C<sub>6/6'</sub> or C<sub>7/7'</sub>), 124.5 (C<sub>6/6'</sub> or C<sub>7/7'</sub>), 124.4 (C<sub>6/6'</sub> or C<sub>7/7'</sub>), 121.1 (C<sub>3/3'</sub>), 121.0 (C<sub>9/9'</sub> or C<sub>10/10'</sub>), 120.8 (C<sub>9/9'</sub> or C<sub>10/10'</sub>), 120.7 (C<sub>9/9'</sub> or C<sub>10/10'</sub>), 120.1 (C<sub>3/3'</sub>), 79.7 (C<sub>18/18'</sub>), 48.6 (C<sub>12/12'</sub>), 48.4 (C<sub>11/11'</sub>), 48.2 (C<sub>12/12'</sub>), 36.9 (C<sub>1/1'</sub>), 36.7 (C<sub>1/1'</sub>), 35.0 (C<sub>4/4'</sub>), 34.9 (C<sub>4/4'</sub>), 28.5 (C<sub>19/19'</sub>). HRMS ASAP m/z = 350.2120 [M+H]<sup>+</sup>, calculated for C<sub>23</sub>H<sub>28</sub>NO<sub>2</sub><sup>+</sup>: 350.2120. Prime symbols are used in the spectral assignment of 55 to differentiate between its diastereomers.

**tert-butyl-*N*-benzhydryl-*N*-(((2*Z*,4*Z*)-bicyclo[4.2.2]deca-2,4,7,9-tetraen-7-yl)methyl)glycinate.**

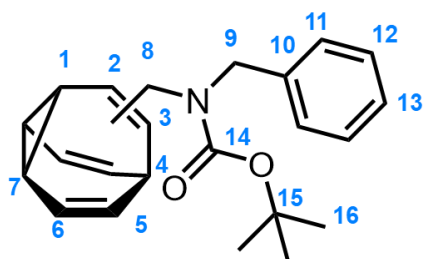


ZnI<sub>2</sub> (61.3 mg, 0.19 mmol) was added to an oven dried microwave vial and heated to 280°C under vacuum for 5 min. CoBr<sub>2</sub>(dppe) (59.3 mg, 0.29 mmol) and activated zinc dust (18.8 mg, 0.10 mmol) were added to the same vial which was then sealed. The vial was flushed with nitrogen and evacuated under high vacuum three times.

Anhydrous trifluoroethanol (1.5 mL) was added, and three freeze pump thaw cycles undertaken. The reaction mixture was stirred for 15 min at rt and then COTT (0.11 mL,

0.96 mmol) was added. This was followed by the dropwise addition of *tert*-butyl benzhydryl(prop-2-yn-1-yl)carbamate (462 mg, 1.44 mmol) over 1.5 h, after which the reaction mixture was stirred for 22 h at 70°C. The reaction mixture was filtered through a silica plug and eluted with EtOAc. The solvent was then removed in vacuo and the crude residue purified by column chromatography (Teledyne Isco CombiFlash Rf+ system, 12 g SiO<sub>2</sub>, hexanes/EtOAc, 0 – 30%) affording the title compound as a colourless oil (194 mg, 0.26 mmol, 50% yield). **<sup>1</sup>H NMR** (700 MHz, CDCl<sub>3</sub>) δ 7.31 – 7.26 (m, 4H, H<sub>15</sub>), 7.26 – 7.22 (m, 2H, H<sub>17</sub> or H<sub>14</sub>), 7.18 (d, *J* = 7.6 Hz, 2H, H<sub>17</sub> or H<sub>14</sub>), 7.13 (d, *J* = 7.5 Hz, 2H, H<sub>16</sub>), 6.24 (s, 1H, H<sub>3</sub>), 6.13 (dd, *J* = 11.3, 8.7 Hz, 1H, H<sub>8</sub>), 5.98 (s, 1H, H<sub>5</sub>), 5.68 (m, 2H, H<sub>6</sub>, H<sub>7</sub>), 5.61 – 5.56 (m, 1H, H<sub>10</sub>), 5.54 (dd, *J* = 8.7, 5.8 Hz, 1H, H<sub>9</sub>), 5.12 – 5.09 (s, 1H, H<sub>12</sub>), 4.25 (s, 1H, H<sub>11/11'</sub>), 3.63 (s, 1H, H<sub>11/11'</sub>), 3.16 (d, *J* = 37.2 Hz, 1H, H<sub>4</sub>), 3.00 (dd, *J* = 7.0, 6.8 Hz, 1H, H<sub>7</sub>), 1.32 (s, 9H, H<sub>20</sub>). **<sup>13</sup>C NMR** (175 MHz, CDCl<sub>3</sub>) δ 156.1 (C<sub>18</sub>), 141.67 (C<sub>6</sub>), 141.2 (C<sub>8</sub>), 140.78 (C<sub>5</sub>), 139.9 (C<sub>13</sub>), 128.9 (C<sub>14</sub>, C<sub>15</sub>, C<sub>16</sub>, C<sub>17</sub>), 128.2 (C<sub>14</sub>, C<sub>15</sub>, C<sub>16</sub>, C<sub>17</sub>), 128.1 (C<sub>14</sub>, C<sub>15</sub>, C<sub>16</sub>, C<sub>17</sub>), 127.1 (C<sub>14</sub>, C<sub>15</sub>, C<sub>17</sub>), 126.9 (C<sub>14</sub>, C<sub>15</sub>, C<sub>17</sub>), 124.6 (C<sub>7</sub>), 124.3 (C<sub>6</sub>), 120.9 (C<sub>10</sub>), 120.8 (C<sub>9</sub>), 119.0 (C<sub>2</sub>), 80.1 (C<sub>19</sub>), 63.8 (C<sub>11/11'</sub>), 48.5 (C<sub>11/11'</sub>), 36.2 (C<sub>4</sub>), 34.8 (C<sub>1</sub>), 28.3 (C<sub>20</sub>). **HRMS** **ASAP** *m/z* = 426.2429 [M+H]<sup>+</sup>, calculated for C<sub>29</sub>H<sub>32</sub>NO<sub>2</sub><sup>+</sup>: 426.2432.

#### *N*-benzyl bullvalene carbamate

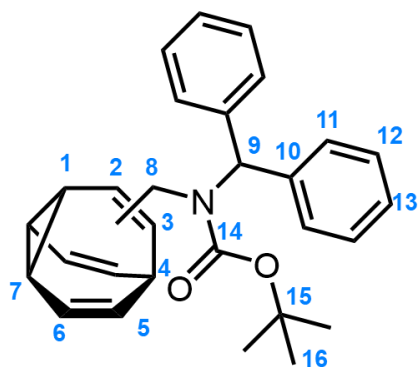


Mono(*N*-benzyl-Boc)methylene amine  
Bullvalene Mono(*N*-benzyl-Boc)methylene amine BDT (180 mg, 0.51 mmol) and thioxanthene-9-one (1 mg, 0.01 mmol) were dissolved in anhydrous THF (1.2 mL) in an oven-

dried microwave vial under Ar. The mixture was stirred for 3 h, while being irradiated with 365 nm UV light (3.4 W array of surface mounted 365 nm LEDs bulbs) at rt. The solvent was then removed in vacuo and the crude residue purified by column chromatography (Teledyne Isco CombiFlash Rf+ system, 8 g SiO<sub>2</sub>, hexanes/EtOAc, 0 – 10%; followed by 12 g gold SiO<sub>2</sub>, hexanes/CH<sub>2</sub>Cl<sub>2</sub> 0 – 100%) to afford the title compound as a white solid (90 mg, 0.26 mmol, 50% yield). M. P. 130-131 °C. **<sup>1</sup>H NMR** (499 MHz, cdcl<sub>3</sub>) δ 7.41 - 7.33 (m, 2H, H<sub>11-13</sub>, Isomer CZ, CE, BZ, BE), 7.32 – 7.28 (m, 1H, H<sub>11-13</sub>, Isomer CZ, CE, BZ, BE), 7.26 – 7.18 (m, 2H, H<sub>11-13</sub>, , Isomer CZ, CE,

BZ, BE)), 6.01 – 5.91 (m, 2H, H<sub>6CE</sub>, H<sub>6CZ</sub>, H<sub>5BZ</sub>, H<sub>5BE</sub>), 5.84 (m, 2H, H<sub>5CZ</sub>, H<sub>5CE</sub>, H<sub>6BZ</sub>, H<sub>6BE</sub>), 5.76 – 5.71 (m, 0.44H, H<sub>2CZ</sub>), 5.68 (s, 0.27H, H<sub>2CE</sub>), 5.63 (d,  $J = 8.8$  Hz, 0.25H, H<sub>3BZ</sub>), 5.59 (d,  $J = 8.4$  Hz, 0.26H, H<sub>3BE</sub>), 4.42 (s, 0.44H, H<sub>8CE</sub>), 4.36 (s, 0.85H, H<sub>8CZ</sub>), 4.33 (s, 0.30H, H<sub>8BZ</sub>), 4.28 (s, 0.42H, H<sub>8BE</sub>), 3.84 (s, 0.39H, H<sub>8BE</sub>), 3.77 (s, 0.80H, H<sub>8CZ</sub>), 3.75 (s, 0.41H, H<sub>8BZ</sub>), 3.70 (s, 0.47H, H<sub>8CE</sub>), 2.47 – 2.39 (m, 0.75H, H<sub>4CZ</sub>, H<sub>1CE</sub>, H<sub>4BZ</sub>, H<sub>4BE</sub>, H<sub>1BZ</sub>, H<sub>1BE</sub>), 2.36 (m, H<sub>4CE</sub>, H<sub>1CZ</sub>), 2.32 – 2.26 (m, 2.75H, H<sub>7CZ</sub>, H<sub>7CE</sub>, H<sub>7BE</sub>, H<sub>7BZ</sub>), 1.49 (s, 3.5H, H<sub>16BZ</sub>, H<sub>16BE</sub>), 1.47 (s, 5.5H, H<sub>16CZ</sub>, H<sub>16CE</sub>). **<sup>13</sup>C NMR** (175 MHz, CDCl<sub>3</sub>) <sup>13</sup>C NMR (126 MHz, cdcl<sub>3</sub>)  $\delta$  156.38, 156.31, 156.22, 156.12, 138.08, 138.03, 137.90, 136.99, 136.57, 134.50, 134.04, 128.79, 128.70, 128.64, 128.09, 127.94, 127.88, 127.80, 127.70, 127.63, 127.55, 127.50, 127.37, 127.30, 127.17, 80.45, 80.42, 80.37, 53.76, 53.30, 52.44, 51.97, 47.42, 47.08, 46.88, 46.81, 31.82, 31.76, 30.01, 29.96, 28.58 (d,  $J = 5.9$  Hz), 21.12, 20.92, 20.68, 20.12, 19.84. **HRMS ASAP**  $m/z = 350.2137$  [M+H]<sup>+</sup>, calculated for C<sub>23</sub>H<sub>28</sub>NO<sub>2</sub><sup>+</sup>: 350.2120.

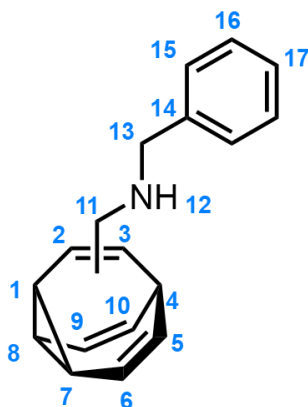
#### N-benzhydryl bullvalene carbamate



Mono(N-benzyl-Boc)methylene amine Bullvalene  
Mono(N-benzyl-Boc)methylene amine BDT (140 mg, 0.28 mmol) and thioxanthene-9-one (1 mg, 0.01 mmol) were dissolved in anhydrous THF (1.2 mL) in an oven-dried microwave vial under Ar. The mixture was stirred for 3 h, while being irradiated with 365 nm UV light (3.4 W array of

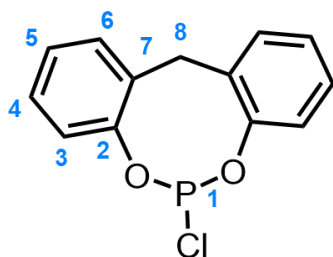
surface mounted 365 nm LEDs bulbs) at rt. The solvent was then removed in vacuo and the crude residue purified by column chromatography (Teledyne Isco CombiFlash Rf+ system, 8 g SiO<sub>2</sub>, hexanes/EtOAc, 0 – 10%; followed by 12 g gold SiO<sub>2</sub>, hexanes/CH<sub>2</sub>Cl<sub>2</sub> 0 – 100%) to afford the title compound as a colourless wax (63 mg, 0.15 mmol, 54% yield). **<sup>1</sup>H NMR** (499 MHz, CDCl<sub>3</sub>)  $\delta$  7.37 – 7.24 (m, 6H, H<sub>11-13</sub>, Isomer CZ, CE, BZ, BE), 7.23 – 7.16 (m, 4H, H<sub>11-13</sub> Isomer CZ, CE, BZ, BE), 6.00 – 5.95 (m, 1.02H, H<sub>6</sub>, Isomer CZ), 5.93 – 5.89 (m, 0.62H, H<sub>6</sub> Isomer BZ), 5.87 – 5.78 (m, 1.62H, H<sub>5</sub>, H<sub>6</sub>, Isomer CZ, BZ, BE), 5.79 – 5.71 (m, 1.31H, H<sub>2</sub>, H<sub>5</sub>, H<sub>6</sub>, H<sub>8</sub> Isomer CZ, CE, BE), 5.66 (d,  $J = 5.7$  Hz, 0.36H, H<sub>3</sub>, H<sub>9</sub>, Isomer BZ), 5.58 (s, 0.61H, H<sub>9</sub>), 5.43 (dd,  $J = 11.0, 8.8$  Hz, 0.47H, H<sub>5</sub>, Isomer CE), 5.34 (d,  $J = 6.9$  Hz, 0.22H, H<sub>2</sub>, Isomer

CE), 5.30 (d,  $J = 8.6$  Hz, 0.19H, H<sub>2</sub>, Isomer BE), 3.99 (s, 0.90H, H<sub>8</sub> Isomer CZ), 3.90 (s, 0.50H, H<sub>8</sub>, Isomer BZ), 3.88 (s, 0.22H, H<sub>8</sub>, Isomer BE) 3.83 (s, 0.36H, H<sub>8</sub>, Isomer CE), 2.73 (t,  $J = 8.7$  Hz, H<sub>1</sub>, 0.59H, Isomer CZ), 2.59 (t,  $J = 8.7$  Hz, 0.39H, H<sub>4</sub> Isomer BZ), 2.46 (t,  $J = 8.6$  Hz, 0.55H, H<sub>4</sub>, Isomer CZ), 2.40 (ddt,  $J = 8.4, 5.3, 2.7$  Hz, 1.01H, H<sub>7</sub>, Isomer CZ), 2.29 (t,  $J = 8.7$  Hz, 0.22H, H<sub>4</sub>, Isomer BE), 2.27 – 2.19 (m, 0.90H, H<sub>1</sub>, H<sub>7</sub>, Isomer BZ), 2.13 (m, 0.32H, H<sub>1</sub>, H<sub>7</sub>, Isomer BE), 2.08 (m, 0.97H, H<sub>1</sub>, H<sub>7</sub>, Isomer CE), 1.74 (t,  $J = 8.8$  Hz, 0.26H, H<sub>4</sub>, Isomer CE), 1.44 (s, 1.32H, H<sub>16</sub>, Isomer CE), 1.43 (s, 0.85H, H<sub>16</sub>, Isomer BE), 1.12 (s, 2.27H, H<sub>16</sub>, Isomer BZ), 1.05 (s, 3.90H, H<sub>16</sub>, Isomer CZ). **<sup>13</sup>C NMR** (126 MHz, CDCl<sub>3</sub>)  $\delta$  156.6 (C<sub>14</sub>CZ or C<sub>14</sub>CE or C<sub>14</sub>BZ or C<sub>14</sub>BE), 156.4 (C<sub>14</sub>CZ or C<sub>14</sub>CE or C<sub>14</sub>BZ or C<sub>14</sub>BE), 140.4 (C<sub>10</sub>CZ or C<sub>10</sub>CE or C<sub>10</sub>BZ or C<sub>10</sub>BE), 140.3 (C<sub>10</sub>CZ or C<sub>10</sub>CE or C<sub>10</sub>BZ or C<sub>10</sub>BE), 140.1 (C<sub>10</sub>CZ or C<sub>10</sub>CE or C<sub>10</sub>BZ or C<sub>10</sub>BE), 140.0 (C<sub>10</sub>CZ or C<sub>10</sub>CE or C<sub>10</sub>BZ or C<sub>10</sub>BE), 137.0 (C<sub>3</sub>CZ or C<sub>3</sub>CE or C<sub>2</sub>BZ or C<sub>2</sub>BE), 136.4 (C<sub>3</sub>CZ or C<sub>3</sub>CE or C<sub>2</sub>BZ or C<sub>2</sub>BE), 135.4 (C<sub>3</sub>CZ or C<sub>3</sub>CE or C<sub>2</sub>BZ or C<sub>2</sub>BE), 134.7 (C<sub>3</sub>CZ or C<sub>3</sub>CE or C<sub>2</sub>BZ or C<sub>2</sub>BE), 129.1 (C<sub>11-13</sub>CZ or C<sub>11-13</sub>CE or C<sub>11-13</sub>BZ or C<sub>11-13</sub>BE), 128.9 (C<sub>11-13</sub>CZ or C<sub>11-13</sub>CE or C<sub>11-13</sub>BZ or C<sub>11-13</sub>BE), 128.6 (C<sub>11-13</sub>CZ or C<sub>11-13</sub>CE or C<sub>11-13</sub>BZ or C<sub>11-13</sub>BE), 128.6 (C<sub>11-13</sub>CZ or C<sub>11-13</sub>CE or C<sub>11-13</sub>BZ or C<sub>11-13</sub>BE), 128.5 (C<sub>11-13</sub>CZ or C<sub>11-13</sub>CE or C<sub>11-13</sub>BZ or C<sub>11-13</sub>BE), 128.3 (C<sub>11-13</sub>CZ or C<sub>11-13</sub>CE or C<sub>11-13</sub>BZ or C<sub>11-13</sub>BE), 128.2 (C<sub>6</sub>CZ or C<sub>6</sub>BZ), 127.8 (C<sub>6</sub>CZ or C<sub>6</sub>BZ), 127.6 (C<sub>5</sub>CE), 127.4 (C<sub>6</sub>CZ or C<sub>6</sub>BZ), 127.2 (C<sub>6</sub>CZ or C<sub>6</sub>BZ), 127.1 (C<sub>6</sub>BE or C<sub>2</sub>CZ or C<sub>5</sub>BE), 127.0 (C<sub>6</sub>BE or C<sub>2</sub>CZ or C<sub>5</sub>BE), 126.6 (C<sub>6</sub>BE or C<sub>2</sub>CZ or C<sub>5</sub>BE), 126.4 (C<sub>6</sub>BE or C<sub>2</sub>CZ or C<sub>5</sub>BE), 126.2 (C<sub>6</sub>BE or C<sub>2</sub>CZ or C<sub>5</sub>BE), 125.1 (C<sub>3</sub>BZ), 122.5 (C<sub>3</sub>BE), 121.5 (C<sub>2</sub>CE), 80.6 (C<sub>15</sub>CZ, C<sub>15</sub>CE, C<sub>15</sub>BZ, C<sub>15</sub>BE), 63.1 (C<sub>15</sub>CZ, C<sub>15</sub>CE, C<sub>15</sub>BZ, C<sub>15</sub>BE), 63.0 (C<sub>15</sub>CZ, C<sub>15</sub>CE, C<sub>15</sub>BZ, C<sub>15</sub>BE), 62.8 (C<sub>15</sub>CZ, C<sub>15</sub>CE, C<sub>15</sub>BZ, C<sub>15</sub>BE, C<sub>8</sub>), 62.4 (C<sub>15</sub>CZ, C<sub>15</sub>CE, C<sub>15</sub>BZ, C<sub>15</sub>BE), 56.9 (C<sub>8</sub>CZ), 54.6 (C<sub>8</sub>BZ, C<sub>8</sub>CE), 51.45 (C<sub>8</sub>CE), 31.9 (C<sub>4</sub>BZ), 30.7 (C<sub>4</sub>CE), 30.1 (C<sub>4</sub>CZ), 29.81 (C<sub>4</sub>BE), 28.5 (C<sub>16</sub>CZ or C<sub>16</sub>CE or C<sub>16</sub>BZ or C<sub>16</sub>BE), 28.4 (C<sub>16</sub>CZ or C<sub>16</sub>CE or C<sub>16</sub>BZ or C<sub>16</sub>BE), 28.1 (C<sub>16</sub>CZ or C<sub>16</sub>CE or C<sub>16</sub>BZ or C<sub>16</sub>BE), 21.8 (C<sub>1</sub>CZ), 20.7 (C<sub>1</sub>BE, C<sub>7</sub>BE), 20.4 (C<sub>7</sub>CZ), 20.2 (C<sub>1</sub>CE, C<sub>7</sub>CE), 20.1 (C<sub>1</sub>BE, C<sub>7</sub>BE), 19.9 (C<sub>1</sub>BZ, C<sub>7</sub>BZ), 19.6 (C<sub>1</sub>CE, C<sub>7</sub>CE). **HRMS ASAP**  $m/z = 426.2433$  [M+H]<sup>+</sup>, calculated for C<sub>29</sub>H<sub>32</sub>NO<sub>2</sub><sup>+</sup>: 426.2432.

**(N-benzyl)methylene amine bullvalene**

Mono(*N*-benzyl-Boc)methylene amine bullvalene (150 mg, 0.429 mmol) was dissolved in anhydrous CH<sub>2</sub>Cl<sub>2</sub> (5.5 mL) under an Ar atmosphere with continuous stirring at rt. CH<sub>3</sub>COCl in MeOH (9 × 0.429 mL, 1 M, 0.429 mmol) was added sequentially to the reaction mixture at 30 min intervals over 4 h. The reaction mixture was poured in to saturated NaHCO<sub>3</sub> (15 mL) and brine (2.5 mL) and the aqueous layer extracted with CH<sub>2</sub>Cl<sub>2</sub> (3 × 10 mL). The

combined organic phases were dried over anhydrous NaSO<sub>4</sub> and the solvent removed *in vacuo*. The crude residue was purified by column chromatography (Teledyne Isco CombiFlash Rf+ system, 8 g neutral Al<sub>2</sub>O<sub>3</sub>, hexanes/EtOAc, 0 – 20%) affording the title compound as a colourless oil (42 mg, 0.17 mmol, 40% yield). **HRMS ASAP**  $m/z$  = 250.1607 [M+H]<sup>+</sup>, calculated for C<sub>18</sub>H<sub>20</sub>N<sup>+</sup>: 250.1596.

**6-Chloro-12H-dibenzo[d,g][1,3,2]dioxaphosphocin**

A three-necked round-bottomed flask, fitted with a stirrer bar and reflux condenser, was oven-dried and purged with Ar. One outlet was connected to a gas scrubber trap containing KOH (30 mL, 6 M). 2,2' methylenediphenol (467 mg, 2.30 mmol) and freshly distilled PCl<sub>3</sub> (1.96 mL,

22.4 mmol) were added to the reaction flask. 1-methyl-2-pyrrolidinone (1.8 μL, 0.018 mmol) was added and the mixture heated to 92 °C and kept at reflux for 1 h. The reaction mixture was allowed to cool and the remaining PCl<sub>3</sub> and HCl removed under reduced pressure using 2 liquid nitrogen traps for 2 h. The flask was vented with Ar and washed with anhydrous diethyl ether (2 mL) which had been dried via percolation through a column packed with neutral alumina under a positive pressure of Ar. The solution was transferred to an oven-dried microwave vial under a pressure of Ar. The solvent was removed under reduced pressure over 1 h to afford the title compound as a pale yellow powder (340 mg, 1.28 mmol, 56% yield) which was stored in a dry nitrogen atmosphere. <sup>31</sup>P {<sup>1</sup>H} NMR (400 MHz, (CDCl<sub>3</sub>): δ<sub>P</sub> 124.80 (s, P), -0.33 (s, 5% hydrolysis). Spectral data agrees with literature values.<sup>38</sup>

## 4.14.2 In Silico Modelling

DFT calculations were carried out in Gaussian 16. The minimum energy (ME) geometries and transition state (TS) geometries of the barbaralane isomers were optimised using the range-separated hybrid (RSH) general gradient approximation GGA functional  $\omega$ B97XD. We selected this functional as it includes dispersion correction and we have previously found that it performs well in estimating the equilibrium distribution of barbaralanes. Calculations were performed using the 6-311++G(d,p) basis set for H, C, N, O, P, Cl atoms and SDD basis set for Ru, Au, and Pd atoms, with a polarizable continuum model (PCM) using the integral equation formalism variant (IEFPCM) to approximate CS<sub>2</sub> as the solvent. CS<sub>2</sub> was chosen as the solvent model to allow for comparison of the calculated data for **4.4** with the experimental results in Figure 4.7, then subsequently to allow a consistent comparison of the calculated data of other compounds with **4.4**. Frequency calculations were carried out to confirm the lack of any negative vibrational frequencies for ME structures and to confirm their presence for TS structures (saddle points). Intrinsic reaction coordinate (IRC) calculations were performed to confirm that TS geometries identified lie on a potential surface linking the two barbaralane ME structures. For compounds with rotatable single bonds that lead to several accessible conformers, (**4.4**, and **L<sub>BB</sub>**) a molecular mechanics conformational search was performed to identify conformers that were then taken on to DFT optimisation. Conformational searches were performed using confab implemented in Open Babel, identifying all conformers predicted to be within 15 kcal·mol<sup>-1</sup> of the lowest energy structure and with a root mean square deviation of 1.0 Å or more. The conformers of **L<sub>BB</sub>AuCl** screened by DFT were prepared manually based on the conformers of **L<sub>BB</sub>** identified by confab. The free energy gaps ( $\Delta G_{\text{calc}}$ ) reported in Table S1 correspond to the difference in energy between the lowest energy conformers of the relevant configurational isomers. The relative energies given for **L<sub>BB</sub>RuCp<sup>+</sup>** and **L<sub>BB</sub>RuCp(NCMe)<sup>+</sup>** take into account the calculated energy of a ‘free’ MeCN molecule at infinite separation in the ligand coordination reaction of **L<sub>BB</sub>RuCp<sup>+</sup>** and MeCN giving **L<sub>BB</sub>RuCp(NCMe)<sup>+</sup>**.

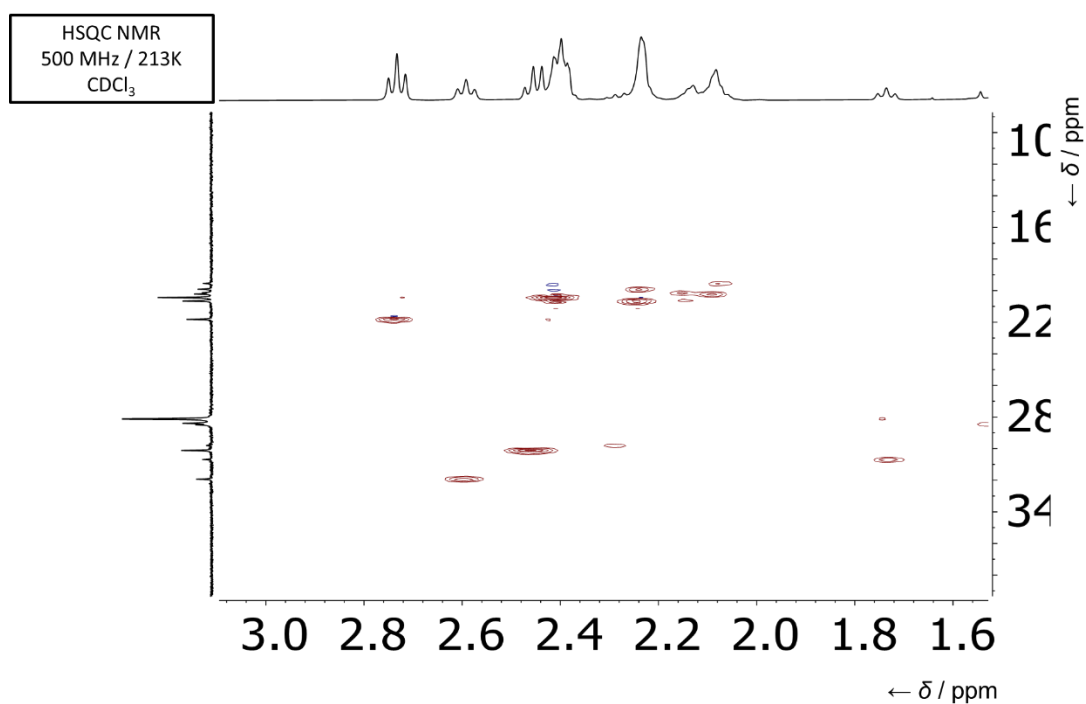
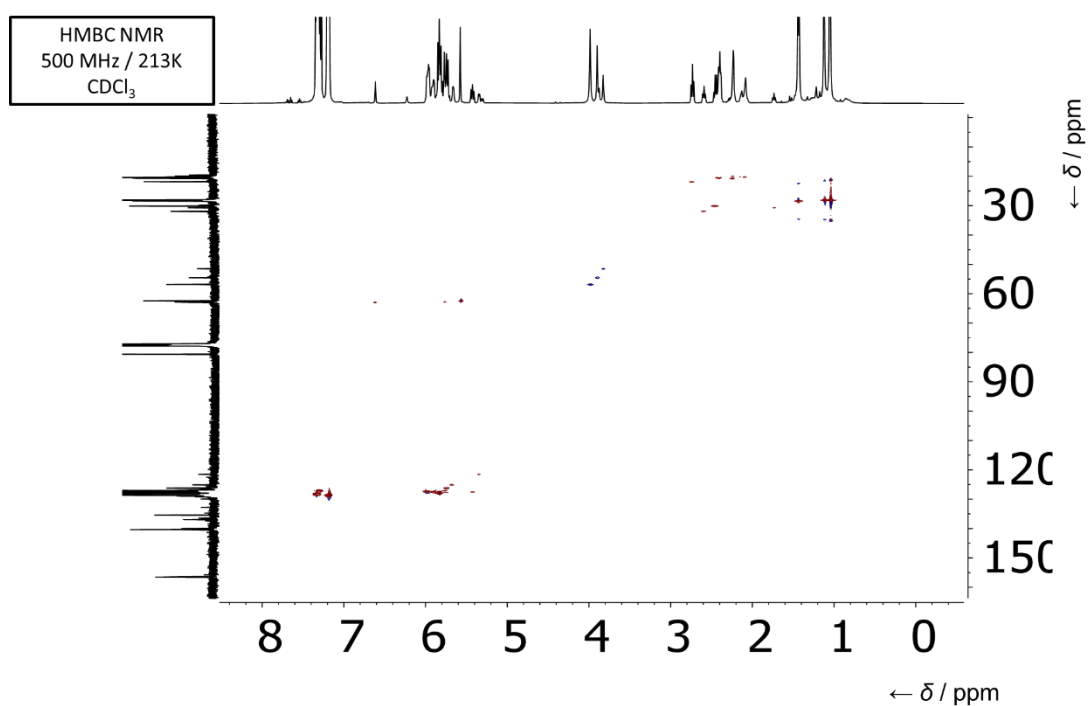
**Table S4.1.** Energetics of the dynamic sp<sup>3</sup>-carbon equilibria.<sup>a</sup>

Compounds	Major Isomer <sup>b</sup>	$\Delta G_{calc}$ ( $\Delta G_{exp}$ ) kJ·mol <sup>-1</sup>	$\Delta G_{calc}^{\ddagger}$ ( $\Delta G_{exp}^{\ddagger}$ ) kJ·mol <sup>-1</sup>
<b>4.4</b>	— <sup>e</sup>	0.0	38.0
( <i>R,S</i> )/( <i>S,S</i> )- <b>4.10</b>	<i>S,S</i>	4.5	35.5
<b>4.5</b>	— <sup>c</sup>	0.0 (0.0 <sup>f</sup> )	47.8 (42.8 <sup>f</sup> )
( <i>R,S</i> )/( <i>S,S</i> )- <b>4.11</b>	<i>R,S</i>	3.8	39.5
<b>L<sub>BB</sub></b>	<i>S,S</i>	20.2	37.7
<b>L<sub>BB</sub>AuCl</b>	<i>R,S</i>	1.1	46.7
<b>L<sub>BB</sub>PdCl<sub>2</sub></b>	<i>C,R,S</i>	1.8 (0.5 <sup>h</sup> )	60.6 (54.6 <sup>h</sup> )
<b>L<sub>BB</sub>I<sub>2</sub>RuCp(NCMe)<sup>+</sup></b>	<i>C,R,S</i>	2.8 (4.0 <sup>i</sup> )	85.4 <sup>j</sup> (87.8 <sup>i</sup> )
<b>L<sub>BB</sub>RuCp<sup>+</sup></b>	<i>S,S,S</i>	25.7	31.8

<sup>a</sup>The DFT calculated free energies  $\Delta G_{calc}$  and  $\Delta G_{calc}^{\ddagger}$  were obtained using the  $\omega$ B97X-D functional, 6-311++G(d,p) basis set for H, C, N, O, P, Cl atoms and SDD basis set for Au, Pd, and Ru atoms, with a polarizable continuum model (PCM) using the integral equation formalism variant (IEFPCM) to approximate CS<sub>2</sub> as the solvent.  $\Delta G_{exp}$  and  $\Delta G_{exp}^{\ddagger}$  values were measured from NMR spectra in the slow exchange regime at suitably low temperatures.

<sup>b</sup>Structure predicted to be lower in energy by DFT. <sup>c</sup>Achiral. <sup>d</sup>Reported in ref 28. <sup>e</sup>The two enantiomers are degenerate. <sup>f</sup>Reported in ref 29. <sup>g</sup>The enantiomeric pair of chiral stereoisomers is predicted to be lower in energy than the *meso* form. <sup>h</sup>Measured at 240 K in CDCl<sub>3</sub>. <sup>i</sup>Measured at 298 K in CDCl<sub>3</sub>. <sup>j</sup>Barrier predicted for coordination-coupled Cope (*cc*-Cope) rearrangement of **L<sub>BB</sub>I<sub>2</sub>RuCp(NCMe)<sup>+</sup>**.

## 4.14.3 Bullvalene Carbamate 4.23 Structure Elucidation

**Figure S4.3.** Partial HSQC NMR spectrum of **4.23**.**Figure S4.4.** Partial HMBC NMR spectrum of **4.23**.

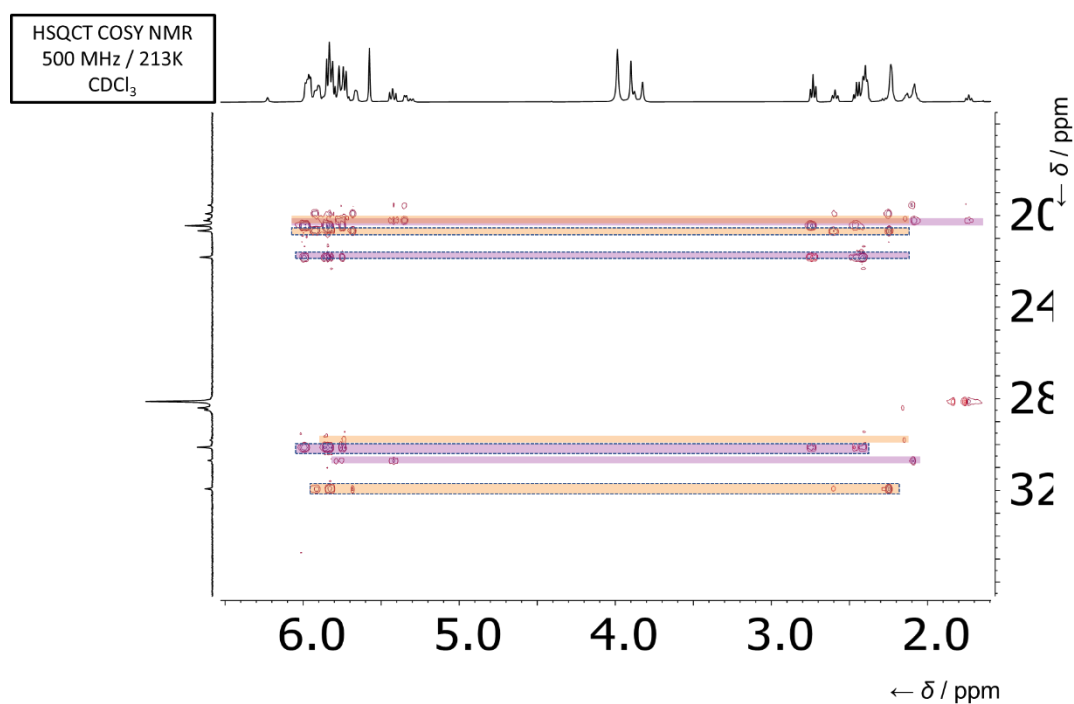


**Figure S4.5.** Partial HSQCTCOSY NMR spectrum of **4.23**. Correlations for *Z*-**4.23b** (orange/dotted line), *E*-**4.23b** (orange), *Z*-**4.23c** (purple/dotted line), and *E*-**4.23c**.

#### 4.14.4 X-Ray Crystallographic Analysis

##### (*S,S*)-**4.10**

Crystals of (*S,S*)-**4.10** suitable for X-ray diffraction were grown by slow evaporation of a saturated Et<sub>2</sub>O solution.

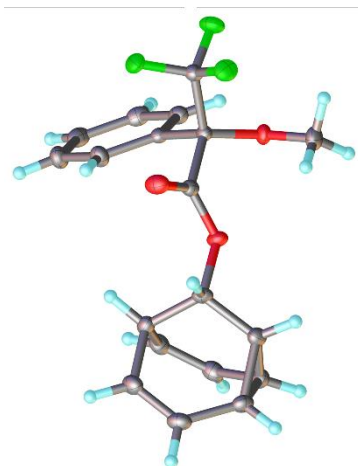


**Figure S4.6.** Solid-state structure of (*S,S*)-**4.10** including probability ellipsoids at 50%.

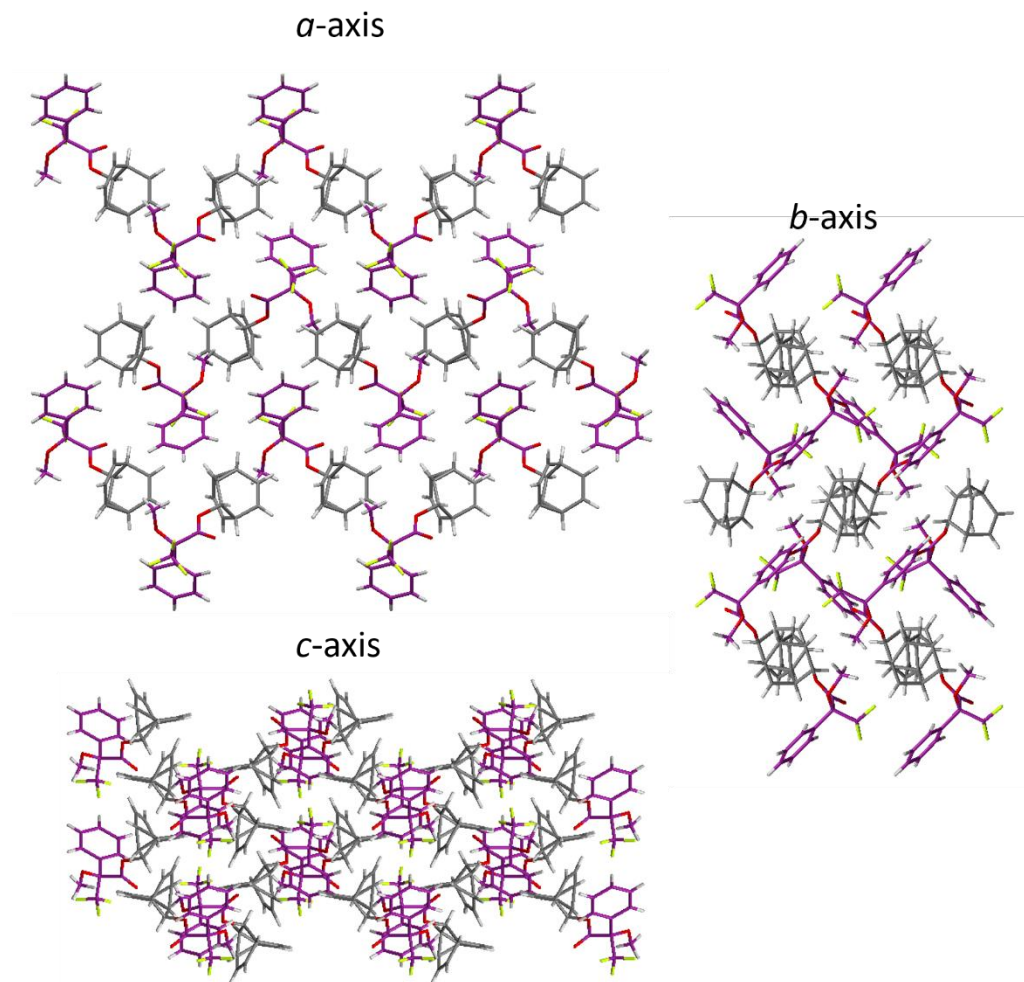


**Figure S4.7.** Solid-state superstructure of (*S,S*)-**4.10** viewed along the three unit cell axes.

**Crystal data for (*S,S*)-**4.10**:**  $C_{19}H_{17}F_3O_3$ ,  $M = 350.32$ , crystal system = orthorhombic, space group =  $P2_12_12_1$ ,  $a = 7.36678(15)$ ,  $b = 12.5886(2)$ ,  $c = 17.2671(3)$  Å,  $\alpha = 90^\circ$ ,  $\beta = 90^\circ$ ,  $\gamma = 90^\circ$ ,  $U = 1601.30(5)$  Å<sup>3</sup>,  $F(000) = 728.0$ ,  $Z = 4$ ,  $D_c = 1.453$  mg m<sup>-3</sup>,  $\mu = 0.120$  mm<sup>-1</sup> (Mo-K $\alpha$ ,  $\lambda = 0.71073$  Å),  $T = 120(1)$  K. 26817 reflections were collected yielding 4452 unique data ( $R_{\text{merge}} = 0.0387$ ). Final  $wR_2(F^2) = 0.0744$  for all data (294 refined parameters), conventional  $R_1(F) = 0.0311$  for 4133 reflections with  $I \geq 2\sigma$ , GOF = 1.014. Flack parameter 0.0(2), Hooft parameter -0.01(19). Crystallographic data for the structure has been deposited within the Cambridge Crystallographic Data Centre as supplementary publication CCDC-2068015.

#### **(*R,R*)-**4.10****

Crystals of (*R,R*)-**4.10** suitable for X-ray diffraction were grown by slow evaporation of a saturated Et<sub>2</sub>O solution.

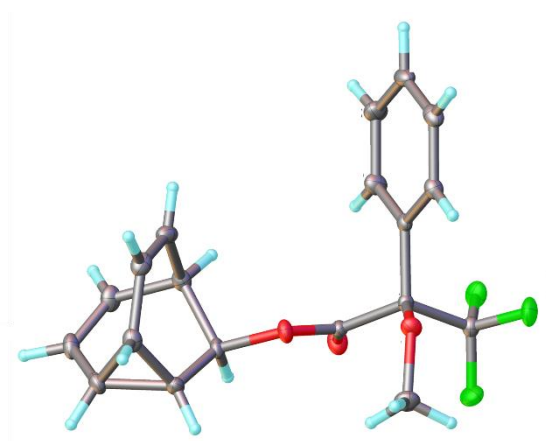


**Figure S4.8.** Solid-state structure of (*R,R*)-**4.10** including probability ellipsoids at 50%.

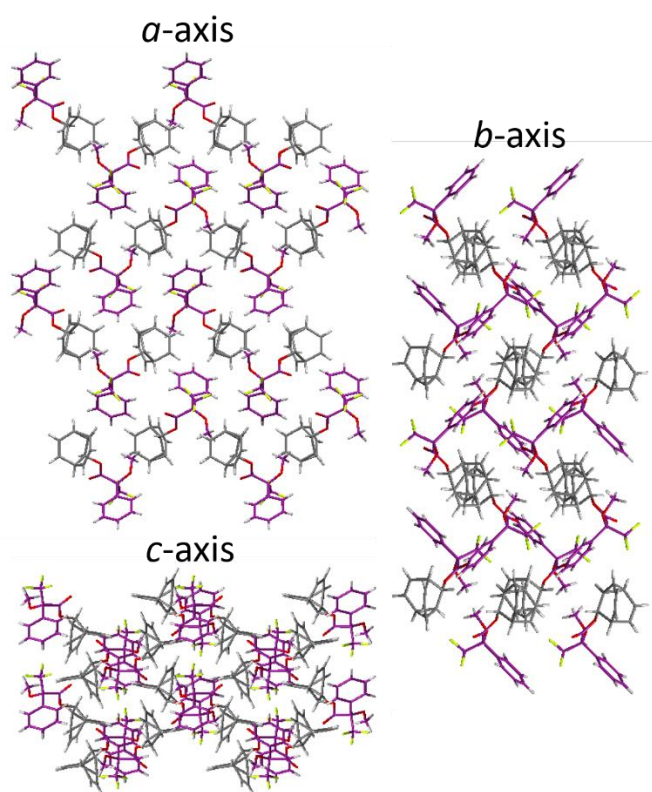


**Figure S4.9.** Solid-state superstructure of (*R,R*)-**4.10** viewed along the three unit cell axes.

**Crystal data for (*R,R*)-**4.10**:**  $\text{C}_{19}\text{H}_{17}\text{F}_3\text{O}_3$ ,  $M = 350.32$ , crystal system = orthorhombic, space group =  $P2_12_12_1$ ,  $a = 7.3559(3)$ ,  $b = 12.5594(5)$ ,  $c = 17.2298(7)$  Å,  $\alpha = 90^\circ$ ,  $\beta = 90^\circ$ ,  $\gamma = 90^\circ$ ,  $U = 1591.79(11)$  Å<sup>3</sup>,  $F(000) = 728.0$ ,  $Z = 4$ ,  $D_c = 1.462$  mg m<sup>-3</sup>,  $\mu = 0.121$  mm<sup>-1</sup> (Mo-K $\alpha$ ,  $\lambda = 0.71073$  Å),  $T = 120(1)$  K. 34205 reflections were collected yielding 4434 unique data ( $R_{\text{merge}} = 0.0342$ ). Final  $wR_2(F^2) = 0.0759$  for all data (294

refined parameters), conventional  $R_1(F) = 0.0309$  for 4069 reflections with  $I \geq 2\sigma$ , GOF = 1.051. Flack parameter -0.1(1), Hooft parameter -0.1(1). Crystallographic data for the structure has been deposited within the Cambridge Crystallographic Data Centre as supplementary publication CCDC-2068016.

#### 4.6

Crystals of **4.6** suitable for X-ray diffraction were grown by slow cooling of a hot and saturated MeCN solution.

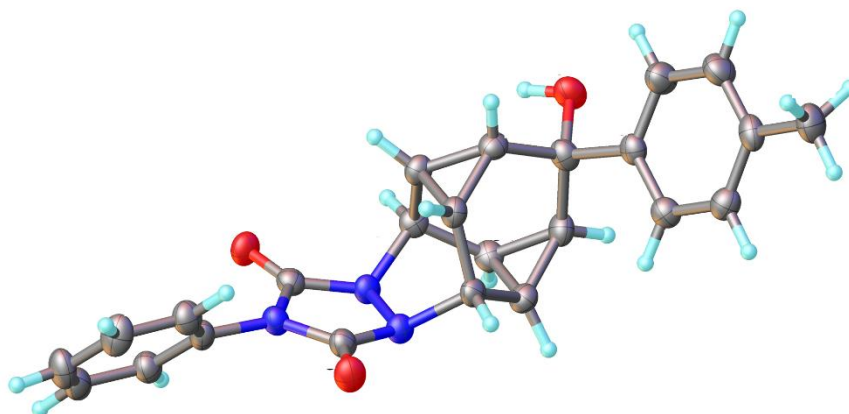


**Figure S4.10.** Solid-state structure of **4.6** including probability ellipsoids at 50%.

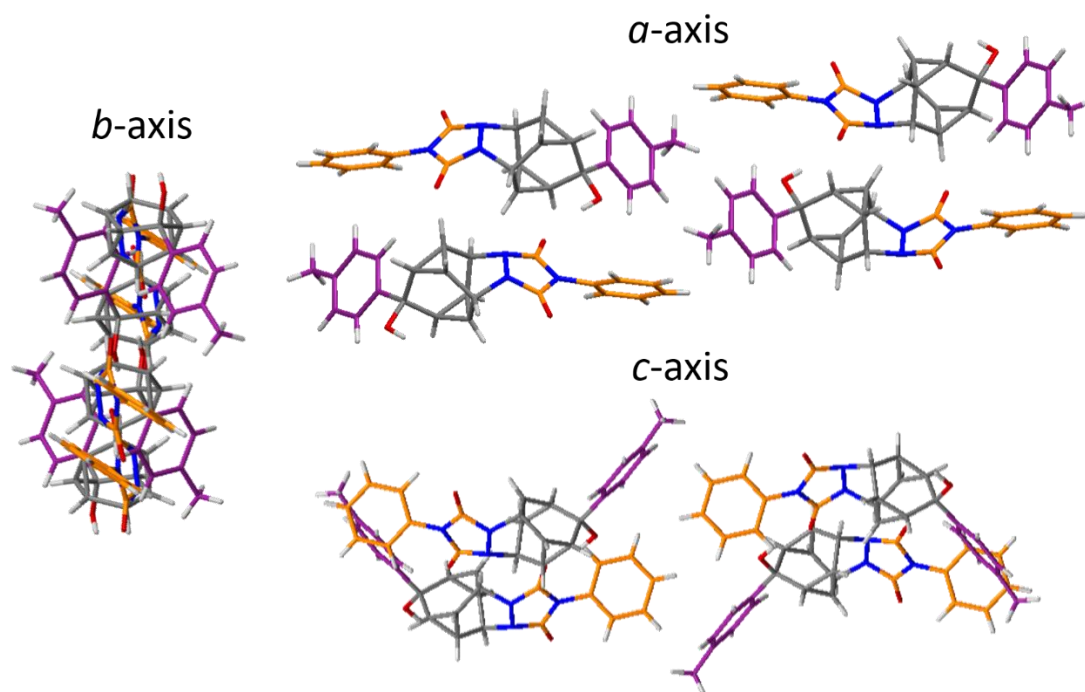


**Figure S4.11.** Solid-state superstructure of **4.6** viewed along the three unit cell axes.

**Crystal data for 4.6:**  $C_{24}H_{21}N_3O_3$ ,  $M = 399.44$ , crystal system = monoclinic, space group =  $P2_1/n$ ,  $a = 6.2961(4)$ ,  $b = 30.3288(13)$ ,  $c = 9.9483(7)$  Å,  $\beta = 98.960(6)^\circ$ ,  $\alpha = 90^\circ$ ,  $\beta = 98.960(6)^\circ$ ,  $\gamma = 90^\circ$ ,  $U = 1876.48(19)$  Å<sup>3</sup>,  $F(000) = 840.0$ ,  $Z = 4$ ,  $D_c = 1.414$  mg m<sup>-3</sup>,  $\mu = 0.095$  mm<sup>-1</sup> (Mo-K $\alpha$ ,  $\lambda = 0.71073$  Å),  $T = 120(1)$  K. 14914 reflections were collected yielding 3695 unique data ( $R_{\text{merge}} = 0.1009$ ). Final  $wR_2(F^2) = 0.1484$  for all data (347 refined parameters), conventional  $R_1(F) = 0.0586$  for 2113 reflections with  $I \geq 2\sigma$ , GOF = 1.039. Crystallographic data for the structure has been deposited within the Cambridge Crystallographic Data Centre as supplementary publication CCDC-2068017.

#### 4.9

Crystals of **4.9** suitable for X-ray diffraction were grown by slow evaporation of a saturated  $CH_2Cl_2$  solution.

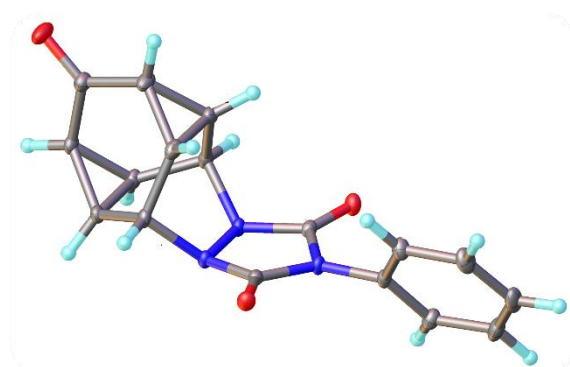


**Figure S4.12.** Solid-state structure of **4.9** including probability ellipsoids at 50%.

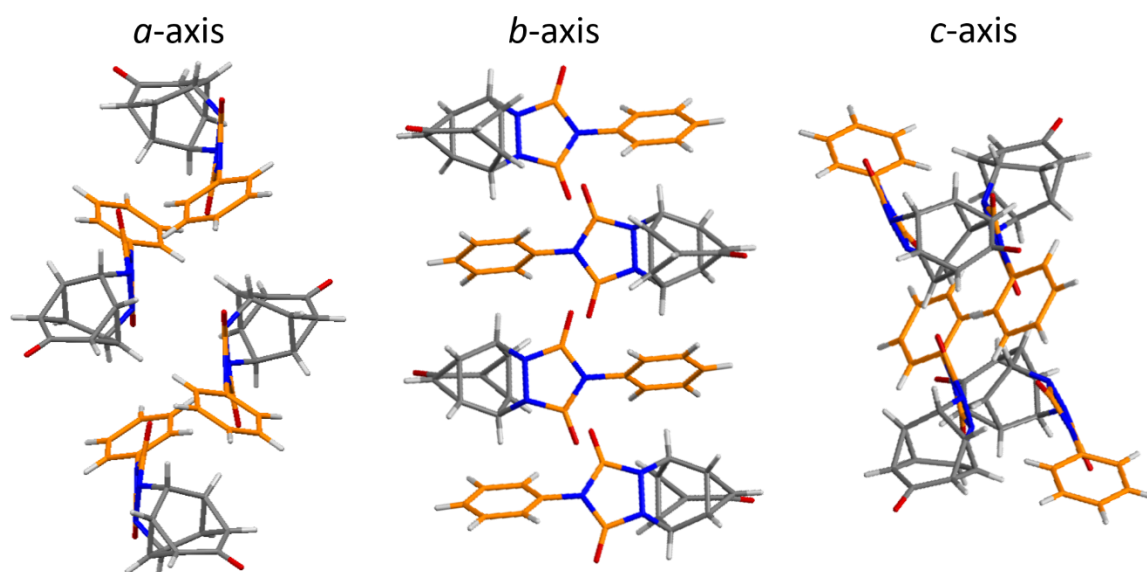


**Figure S4.13.** Solid-state superstructure of **4.9** viewed along the three unit cell axes.

**Crystal data for 4.9:**  $C_{17}H_{13}N_3O_3$ ,  $M = 307.30$ , crystal system = monoclinic, space group =  $P2_1/n$ ,  $a = 14.3555(4)$ ,  $b = 6.2807(2)$ ,  $c = 16.0289(4)$  Å,  $\beta = 110.898(1)^\circ$ ,  $\alpha = 90^\circ$ ,  $\beta = 110.8978(10)^\circ$ ,  $\gamma = 90^\circ$ ,  $U = 1350.14(7)$  Å<sup>3</sup>,  $F(000) = 640.0$ ,  $Z = 4$ ,  $D_c = 1.512$  mg m<sup>-3</sup>,  $\mu = 0.107$  mm<sup>-1</sup> (Mo-K $\alpha$ ,  $\lambda = 0.71073$  Å),  $T = 120(1)$  K. 23181 reflections were collected yielding 3883 unique data ( $R_{\text{merge}} = 0.0441$ ). Final  $wR_2(F^2) = 0.0993$  for all data (260 refined parameters), conventional  $R_1(F) = 0.0381$  for 3549 reflections with  $I \geq 2\sigma$ , GOF = 1.061. Crystallographic data for the structure has been deposited within the Cambridge Crystallographic Data Centre as supplementary publication CCDC-2068019.

**(*R,S*)-4.11**

Crystals of (*R,S*)-4.11 suitable for X-ray diffraction were grown by slow cooling of the sample at a temperature of 5 °C from room temperature and were transferred to the diffractometer by a ‘dry ice’ technique.

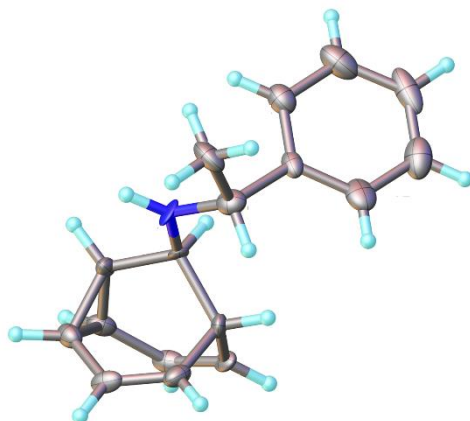


**Figure S4.14.** Solid-state structure of (*S,R*)-4.11 including probability ellipsoids at 50%.

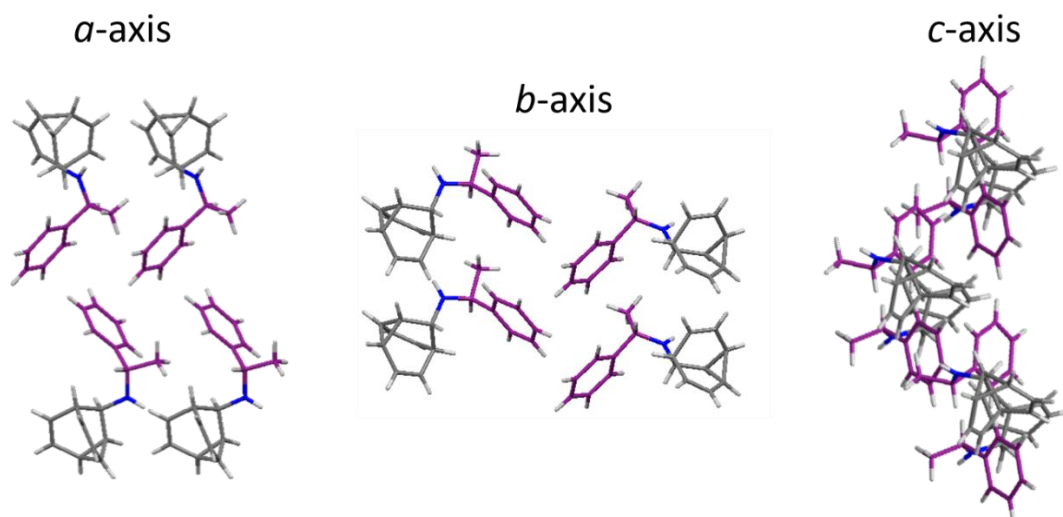


**Figure S4.15.** Solid-state superstructure of (*S,R*)-4.11 viewed along the three unit cell axes.

**Crystal data for (*S,R*)-4.11:** C<sub>17</sub>H<sub>19</sub>N, M = 237.33, crystal system = triclinic, space group = P1, a = 6.1684(9), b = 6.3485(9), c = 28.326(4) Å, α = 84.356(4), β = 104.257(1), γ = 61.967(4)°, U = 974.4(2) Å<sup>3</sup>, F(000) = 384.0, Z = 3, D<sub>c</sub> = 1.213 mg m<sup>-3</sup>, μ = 0.070 mm<sup>-1</sup> (Mo-Kα, λ = 0.71073 Å), T = 120(1) K. 16714 reflections were collected yielding 7522 unique data (R<sub>merg</sub> = 0.1671). Final wR<sub>2</sub>(F<sup>2</sup>) = 0.1735 for all data (490 refined parameters), conventional R<sub>1</sub>(F) = 0.0797 for 2845 reflections with I ≥ 2σ, GOF = 0.912. Flack parameter 5.6(10). Crystallographic data for the structure

has been deposited within the Cambridge Crystallographic Data Centre as supplementary publication CCDC-2068015.

**(*A,S,S*)/(*C,R,S*)-**L<sub>BB</sub>**PdCl<sub>2</sub>**

Crystals of (*A,S,S*)/(*C,R,S*)-**L<sub>BB</sub>**PdCl<sub>2</sub> suitable for X-ray diffraction were grown by slow evaporation of a saturated EtOAc solution. The unit cell contains four independent molecules – two near-identical conformers of (*A,S,S*)-**L<sub>BB</sub>**PdCl<sub>2</sub> and two near-identical conformers of (*C,R,S*)-**L<sub>BB</sub>**PdCl<sub>2</sub>.

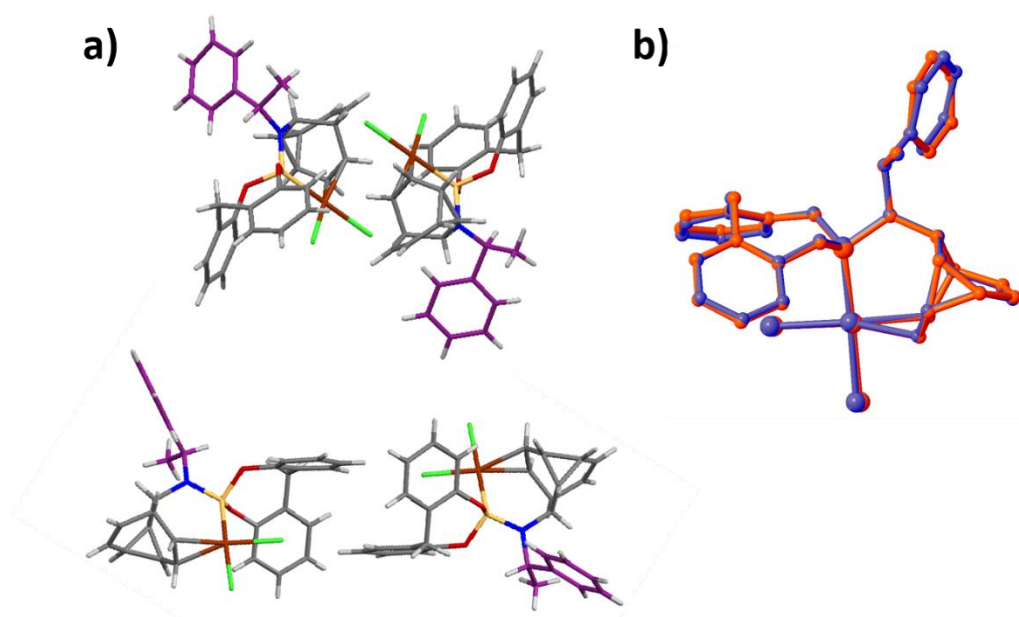


**Figure S4.16.** Solid-state structure of (a) the two near-identical conformers of (*A,S,S*)-**L<sub>BB</sub>**PdCl<sub>2</sub> as well as the two near-identical conformers of (*C,R,S*)-**L<sub>BB</sub>**PdCl<sub>2</sub> and (b) an overlay of two of the near-identical conformers of (*C,R,S*)-**L<sub>BB</sub>**PdCl<sub>2</sub> showing the similarity of their geometries.

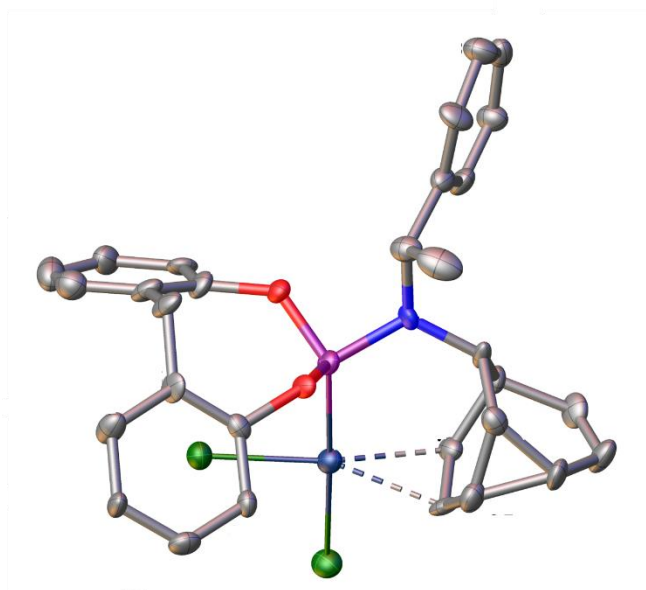


**Figure S4.17.** Solid-state structure of (*A,S,S*)-**L<sub>BB</sub>**PdCl<sub>2</sub> including probability ellipsoids at 50%.

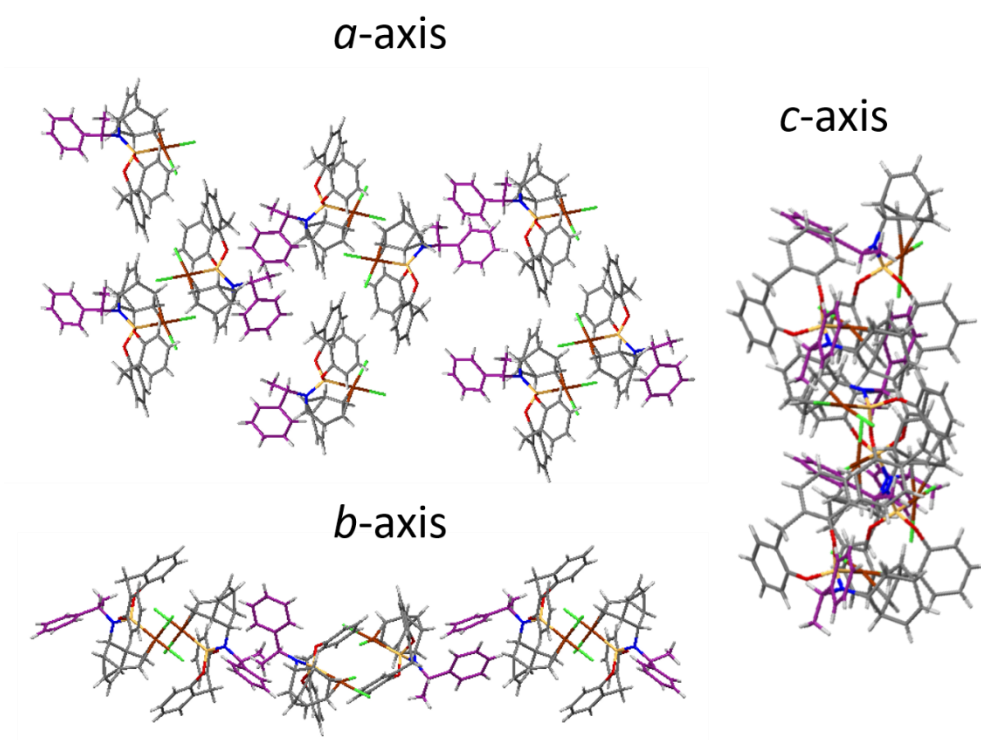


**Figure S4.18.** Solid-state superstructure of (*A,S,S*)/(*C,R,S*)-**L<sub>BB</sub>**PdCl<sub>2</sub> viewed along the three unit cell axes.

**Crystal data for (*A,S,S*)/(*C,R,S*)-**L<sub>BB</sub>**PdCl<sub>2</sub>:** C<sub>30</sub>H<sub>27</sub>Cl<sub>2</sub>NO<sub>2</sub>PPd × 0.625 C<sub>4</sub>H<sub>8</sub>O<sub>2</sub>, M = 697.74, crystal system = triclinic, space group = P1, a = 9.2399(6), b = 12.7855(9), c = 28.2827(19) Å, α = 95.365(2), β = 98.805(2), γ = 110.791(2)°, U = 3047.1(4) Å<sup>3</sup>,

$F(000) = 1424.0$ ,  $Z = 4$ ,  $D_c = 1.521 \text{ mg m}^{-3}$ ,  $\mu = 0.872 \text{ mm}^{-1}$  (Mo-K $\alpha$ ,  $\lambda = 0.71073 \text{ \AA}$ ),  $T = 120(1) \text{ K}$ . 48567 reflections were collected yielding 27453 unique data ( $R_{\text{merge}} = 0.0748$ ). Final  $wR_2(F^2) = 0.1787$  for all data (1500 refined parameters), conventional  $R_1(F) = 0.0711$  for 17333 reflections with  $I \geq 2\sigma$ ,  $\text{GOF} = 1.029$ . Flack parameter -0.01(2), Hooft parameter -0.03(2). Crystallographic data for the structure has been deposited within the Cambridge Crystallographic Data Centre as supplementary publication CCDC-2068019.

**(*C,R,S*)-L<sub>BB</sub>1RuCp(NCMe)·PF<sub>6</sub>**

Crystals of (*C,R,S*)-L<sub>BB</sub>RuCp(NCMe)·PF<sub>6</sub> suitable for X-ray diffraction were grown by slow evaporation of a saturated CDCl<sub>3</sub> solution. A single configurational and conformational isomer, (*C,R,S*)-L<sub>BB</sub>RuCp(NCMe)·PF<sub>6</sub> is present in the unit cell, as a solvate with CDCl<sub>3</sub>.

**Distorted square pyramidal geometry:** Taking the centroid of the  $\mu^5$ -Cp ligand as a coordinated pseudo-atom, the complex can be treated as a distorted square pyramid. The bond angles between the apical Cp and each of the four ligands at the base of the square pyramid are all  $>115^\circ$  (Cp-Ru-P  $131.0^\circ$ , Cp-Ru-N  $121.0^\circ$ , Cp-Ru-C7  $119.8^\circ$ , and Cp-Ru-C8  $120.6^\circ$ ), whereas the bond angles between adjacent coordination sites at the base of the square pyramid are all  $<85^\circ$  (P-Ru-N  $84.4^\circ$ , N-Ru-C7  $83.7^\circ$ , C7-Ru-C8  $36.2^\circ$ , and C8-Ru-P  $80.2^\circ$ ).

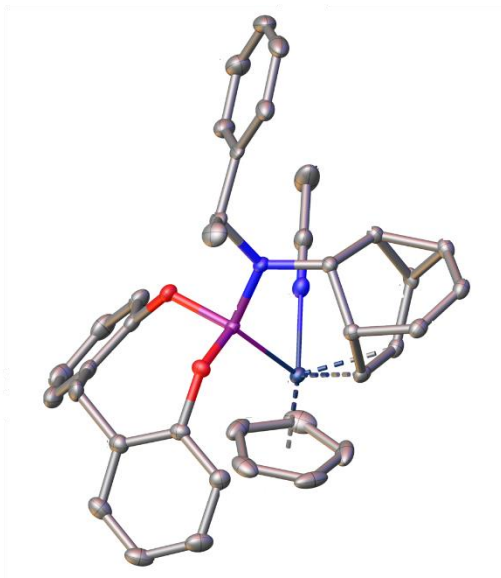


**Figure S4.19.** Solid-state structure of (*C,R,S*)-L<sub>BB</sub>RuCp(NCMe)·PF<sub>6</sub> including probability ellipsoids at 50%. The PF<sub>6</sub><sup>−</sup> counterion is omitted for clarity.

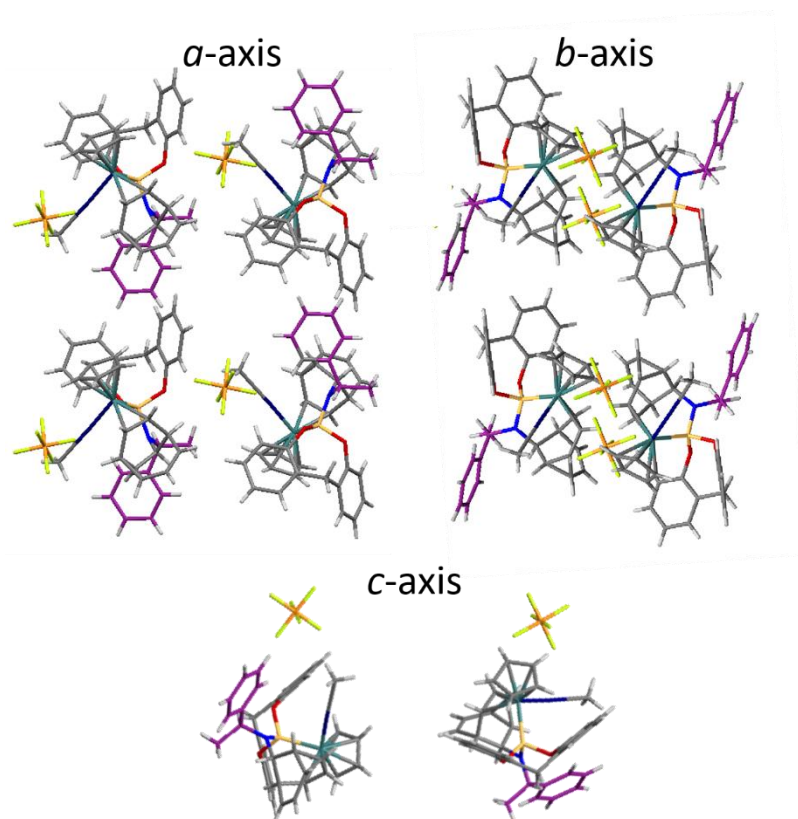


**Figure S4.20.** Solid-state superstructure of  $(C,R,S)\text{-L}_{\text{BB}}\text{RuCp}(\text{NCMe})\cdot\text{PF}_6$  viewed along the three unit cell axes.

**Crystal data for  $(C,R,S)\text{-L}_{\text{BB}}\text{RuCp}(\text{NCMe})\cdot\text{PF}_6$ :**  $\text{C}_{38}\text{H}_{37}\text{Cl}_3\text{F}_6\text{N}_2\text{O}_2\text{P}_2\text{Ru}$ ,  $M = 937.05$ , crystal system = monoclinic, space group =  $P2_1$ ,  $a = 8.7715(3)$ ,  $b = 18.7732(6)$ ,  $c = 11.9803(4)$  Å,  $\alpha = 90^\circ$ ,  $\beta = 100.055(1)^\circ$ ,  $\gamma = 90^\circ$ ,  $U = 1942.48(11)$  Å<sup>3</sup>,  $F(000) = 948.0$ ,  $Z = 2$ ,  $D_c = 1.602$  mg m<sup>-3</sup>,  $\mu = 0.759$  mm<sup>-1</sup> (Mo-K $\alpha$ ,  $\lambda = 0.71073$  Å),  $T = 120(1)$  K. 47392 reflections were collected yielding 11303 unique data ( $R_{\text{merge}} = 0.0405$ ). Final  $wR_2(F^2) = 0.0613$  for all data (489 refined parameters), conventional  $R_1(F) = 0.0300$  for 10892 reflections with  $I \geq 2\sigma$ , GOF = 1.039. Flack parameter -0.019(8), Hooft parameter -0.032(8). Crystallographic data for the structure has been deposited within the Cambridge Crystallographic Data Centre as supplementary publication CCDC-2068020.

## 4.15 References

- 1 K. W. Quasdorf and L. E. Overman, *Nature*, 2014, **516**, 181–191.
- 2 E. L. Eliel and S. H. Wilen, *Stereochemistry of Organic Compounds*, Wiley, 1994.
- 3 J. H. van't Hof, *Arch. Néerl*, 1874, **9**, 445–454.
- 4 J. A. Le Bel, *Bull. Soc. Chim. Fr*, 1874, **22**, 337–347.
- 5 M. P. Sibi, R. Zhang and S. Manyem, *J. Am. Chem. Soc.*, 2003, **125**, 9306–9307.
- 6 J. C. Kizirian, *Chem. Rev.*, 2008, **108**, 140–205.
- 7 S. Fa, K. Egami, K. Adachi, K. Kato and T. Ogoshi, *Angew. Chem. Int. Ed.*, 2020, **59**, 20353–20356.
- 8 H. Liang, B. Hua, F. Xu, L. S. Gan, L. Shao and F. Huang, *J. Am. Chem. Soc.*, 2020, **142**, 19772–19778.
- 9 R. Katoono, K. Sakamoto and T. Suzuki, *Chem. Comm.*, 2019, **55**, 5503–5506.
- 10 X. Chen, T. M. Gerger, C. Räuber, G. Raabe, C. Göb, I. M. Oppel and M. Albrecht, *Angew. Chem. Int. Ed.*, 2018, **57**, 11817–11820.
- 11 S. Akine, S. Sairenji, T. Taniguchi and T. Nabeshima, *J. Am. Chem. Soc.*, 2013, **135**, 12948–12951.
- 12 S. Adachi, N. Takeda and M. P. Sibi, *Org. Lett.*, 2014, **16**, 6440–6443.
- 13 J. H. Rowley, S. C. Yau, B. M. Kariuki, A. R. Kennedy and N. C. O. Tomkinson, *Org. Biomol. Chem.*, 2013, **11**, 2198–2205.
- 14 D. R. Rasmussen and L. Radom, *Angew. Chem., Int. Ed.*, 1999, **38**, 2875–2878.
- 15 M. S. Gordon and M. W. Schmidt *J. Am. Chem. Soc.*, vol. 115, pp. 7486–7492, 1993., 1993, vol. 115.
- 16 C. W. Alexander, W. R. Jackson and R. Spratt, *J. Am. Chem. Soc.*, 1970, **92**, 4992–4993.
- 17 P. Walden, *Berichte der deutschen chemischen Gesellschaft*, 1896, **29**, 133–138.
- 18 P. K. Kancharla, T. Kato and D. Crich, *J. Am. Chem. Soc.*, 2014, **136**, 5472–5480.
- 19 S. Sugiyama, S. Watanabe, T. Inoue, R. Kurihara, T. Itou and K. Ishii, *Tetrahedron*, 2003, **59**, 3417–3425.
- 20 B. Kim, G. Storch, G. Banerjee, B. Q. Mercado, J. Castillo-Lora, G. W. Brudvig, J. M. Mayer and S. J. Miller, *J. Am. Chem. Soc.*, 2017, **139**, 15239–15244.
- 21 M. He and J. W. Bode, *Proc. Natl. Acad. Sci.* 2011, **108**, 14752–14756.
- 22 M. W. Gillick-Healy, E. V. Jennings, H. Müller-Bunz, Y. Ortin, K. Nikitin and D. G. Gilheany, *Chem. Eur. J*, 2017, **23**, 2332–2339.
- 23 A. Sanchez and T. J. Maimone, *J. Am. Chem. Soc.*, 2022, **144**, 7594–7599.
- 24 O. Yahiaoui, H. D. Patel, K. S. Chinner, L. F. Pašteka and T. Fallon, *Org. Lett.*, 2021, **23**, 1157–1162.
- 25 M. Alvarez-Pérez, S. M. Goldup, D. A. Leigh and A. M. Z. Slawin, *J. Am. Chem. Soc.*, 2008, **130**, 1836–1838.
- 26 M. Dommaschk, J. Echavarren, D. A. Leigh, V. Marcos and T. A. Singleton, *Angew. Chem. Int. Ed.*, 2019, **131**, 15097–15100.
- 27 C. Dean, S. Rajkumar, S. Roesner, N. Carson, G. J. Clarkson, M. Wills, M. Jones and M. Shipman, *Chem. Sci.*, 2020, **11**, 1636–1642.
- 28 M. Dommaschk, J. Echavarren, D. A. Leigh, V. Marcos and T. A. Singleton, *Angew. Chem. Int. Ed.*, 2019, **131**, 15097–15100.
- 29 A. C. Cope and E. M. Hardy, *J. Am. Chem. Soc.* 1940, **62**, 441–444.
- 30 P. Brown, F. R. Bruschweiler George R Pettit, T. Reichstein, J. A. Berson and J. M. Balquist, *J. Phys. Chem.* 1946, **50**, 288.

- 31 H. Günther, J. Runsink, H. Schmickler and P. Schmitt, *J. Org. Chem.* 1985, **50**, 289-292.
- 32 A. N. Bismillah, J. Sturala, B. M. Chapin, D. S. Yufit, P. Hodgkinson and P. R. McGonigal, *Chem. Sci.*, 2018, **9**, 8631–8636.
- 33 Y. Y. Ma, M. Yan, H. R. Li, Y. B. Wu, X. X. Tian, H. G. Lu and S. D. Li, *Sci. Rep.*, **9**, 17074
- 34 R. Aumann and M. Runge, *Chem. Ber.*, 1992, **125**, 259–264.
- 35 A. Karton, *Chem. Phys.*, 2021, **540**, 111013
- 36 S. Ferrer and A. M. Echavarren, *Angew. Chem. Int. Ed.*, 2016, **128**, 11344–11348.
- 37 P. R. McGonigal, C. De León, Y. Wang, A. Homs, C. R. Solorio-Alvarado and A. M. Echavarren, *Angew. Chem. Int. Ed.*, 2012, **51**, 13093–13096.
- 38 J. F. Teichert and B. L. Feringa, *Angew. Chem. Int. Ed.*, 2010, **49**, 2486–2528.
- 39 S. L. Rössler, D. A. Petrone and E. M. Carreira, *Acc. Chem. Res.*, 2019, **52**, 2657–2672.
- 40 K. Wakabayashi, K. Aikawa, S. Kawauchi and K. Mikami, *J. Am. Chem. Soc.*, 2008, **130**, 5012–5013.
- 41 J. P. Perdew, K. Burke and M. Ernzerhof, *Phys. Rev. Lett.* 1997, **78**, 1396.
- 42 S. J. Clark, M. D. Segall, C. J. Pickard, P. J. Hasnip, M. I. J. Probert, K. Refson and M. C. Payne, *Z. Kristallogr.* 220, 2005, 567–570.
- 43 J. Da Chai and M. Head-Gordon, *Phys. Chem. Chem. Phys.*, 2008, **10**, 6615–6620.
- 44 T. Clark, J. Chandrasekhar, G. W. Spitznagel and P. V. R. Schleyer, *J. Comput. Chem.*, 1983, **4**, 294–301.
- 45 R. Krishnan, J. S. Binkley, R. Seeger and J. A. Pople, *J. Chem. Phys.*, 1980, **72**, 650–654.
- 46 E. B. Bauer, *Chem. Soc. Rev.*, 2012, **41**, 3153–3167.
- 47 Z. Zhou, S. Chen, Y. Hong, E. Winterling, Y. Tan, M. Hemming, K. Harms, K. N. Houk and E. Meggers, *J. Am. Chem. Soc.*, 2019, **141**, 19048–19057.
- 48 N. G. Connelly, *Nomenclature of Inorganic Chemistry: IUPAC Recommendations*, RSC, 2005.
- 49 D. Andrae, U. H. Iubermann, M. Dolg, H. Stoll and H. Preub, *Theor. Chim. Acta.* 1991, **78**, 247-266.
- 50 M. R. Siebert and D. J. Tantillo, *J. Am. Chem. Soc.*, 2007, **129**, 8686–8687.
- 51 D. J. Tantillo, *Acc. Chem. Res.*, 2016, **49**, 741–749.
- 52 H. Jiao and P. von Ragué Schleyer, *Angew. Chem., Int. Ed.*, 1993, **32**, 1760–1763.
- 53 W. Luginbühl, P. Zbinden, P. A. Pittet, T. Armbruster, H.-B. Bürgi, André Merbach, A. Ludi. *Inorg. Chem.*, 1991, **30**, 2350-2355.
- 54 A. P. Birvé, H. D. Patel, J. R. Price, W. M. Bloch and T. Fallon, , *Angew. Chem. Int. Ed.*, 2022, **61**, e2021154
- 55 A. P. Birvé, H. D. Patel, J. R. Price, W. M. Bloch and T. Fallon, , *Angew. Chem. Int. Ed.*, 2022, **61**, e2021154
- 56 O. Yahiaoui, L. F. Pašteka, B. Judeel and T. Fallon, *Angew. Chem. Int. Ed.*, 2018, **130**, 2600–2604.
- 57 C. Dohmen, H. Ihmels and T. Paululat, *Eur. J Org Chem*, 2022, e202201172.
- 58 R. B. Trillo, J. M. Neudörfl and B. Goldfuss, *Beilstein J. Org. Chem*, 2015, **11**, 313–322.
- 59 I. Bauer, " S Kiirner, " B Pawelke, " S Al-Malaikab and W. D. Habicher, *Polym. Degrad. Stab.* 1998, **62**, 175-186.

- 60 A. N. Bismillah, T. G. Johnson, B. A. Hussein, A. T. Turley, P. K. Saha, H. C. Wong, J. A. Aguilar, D. S. Yufit and P. R. McGonigal, *Nat Chem*, 2023, DOI:10.1038/s41557-023-01156-7.
- 61 L. A. Arnold, R. Imbos, A. Mandoli, A. H. Â M de Vries, R. Naasz and B. L. Feringa, *Tetrahedron*, 2000, **56**, 2865-2878.
- 62 G. Morales Torres, S. Behrens, D. Michalik, D. Selent, A. Spannenberg, S. Lühr, K. M. Dyballa, R. Franke and A. Börner, *ChemistryOpen*, 2017, **6**, 247–253.
- 63 C. Recsei and C. S. P. McErlean, *Tetrahedron*, 2012, **68**, 464–480.
- 64 A. Mondal, R. Toyoda, R. Costil and B. L. Feringa, *Angew. Chem., Int. Ed.*, 2022, **61**, e2022066.
- 65 P. Rodríguez-Salamanca, R. Fernández, V. Hornillos and J. M. Lassaletta, *Chem. Eur. J*, 2022, **28**, e2021044.
- 66 S. Shirakawa, K. Liu and K. Maruoka, *J. Am. Chem. Soc.*, 2012, **134**, 916–919.
- 67 A. J. Clark, D. P. Curran, D. J. Fox, F. Ghelfi, C. S. Guy, B. Hay, N. James, J. M. Phillips, F. Roncaglia, P. B. Sellars, P. Wilson and H. Zhang, *J. Org. Chem*, 2016, **81**, 5547–5565.
- 68 H. D. Patel, T. H. Tran, C. J. Sumby, L. F. Pašteka and T. Fallon, *J. Am. Chem. Soc.*, 2020, **142**, 3680–3685.
- 69 S. M. Morrow, A. J. Bissette and S. P. Fletcher, *Nat. Nanotechnol.*, 2017, **12**, 410–419.
- 70 K. Nogi, T. Fujihara, J. Terao and Y. Tsuji, *Chem. Comm.*, 2014, **50**, 13052–13055.

# Chapter 5 | Non-Covalent Control of Fluxional Carbon Cages

## 5.0 Synopsis

This chapter describes how we studied how non-covalent interactions to influence the internal isomerisation of the barbaralanes. (1) In previous studies by McGonigal et al. 1,9-diaryl-barbaralanes (1,9-**BBs**) have dynamic molecular shape can undergo shape-selective crystallization, the isomerisation of barbaralane is dominated by the shape of the fluxional molecule in solid-state. To further understand this phenomenon, the encapsulation of these 1,9-**BBs** using molecular metal organic cages or metallocages was studied to understand how geometrically confined environment inside the cavity of cage can influence the dynamic regioisomerism in 1,9-**BBs**. Analysis of the host-guest complexes were carried out using solution-state NMR, and single-crystal XRD. (2) To explore new avenues of controlling a dynamic chiral  $sp^3$  carbon centre, we explored how a chiral medium can influence the enantiomerisation of chiral barbaralols thorough non-covalent interactions. Beta-cyclodextrin ( $\beta$ -CD) is a chiral macrocycle capable of chiral discrimination of mixture of enantiomers by encapsulating chiral guests. Encapsulation of chiral **BBs** using  $\beta$ -CD can influence the internal enantiomerization of fluxional carbon cage. Solution state analysis of the  $\beta$ -CD barbaralanes host-guest complexes was conducted using solution-state NMR and ITC to determine binding association constants ( $K_a$ ), host-guest complexation, and thermodynamic parameters ( $\Delta H$ ,  $\Delta S$ ). To determine the presence of a preferred enantiomer of chiral **BBs** in  $\beta$ -CD in solution, enantioselective oxidation of in water was explored using  $\beta$ -CD as chiral reagent. The pitfalls of this synthesis are discussed in this chapter. Evidence of preferred enantiomerisation of chiral **BBs** in  $\beta$ -CD was observed in solid-state using single-crystal XRD and solid-state NMR.

## Acknowledgements

Dr. Aisha Bismillah carried out NMR titration for the binding affinities of **BBs** in  $\beta$ -CD and obtained single crystal of the supramolecular complexes of **BB** in  $\beta$ -CD. Dr. Clare Mahon assisted with ITC measurements of the binding interactions of **BB** in  $\beta$ -CD in solution. Dr. Juan A. Aguilar. assisted with NMR measurements. Dr. Dmitry S. Yufit solved X-ray crystal structures. Prof. Ehmke Pohl and Dr. Stefanie Freitag-Pohl assisted in developing the high throughput crystallisation method and solved X-ray crystal structures.

## 5.1 Non-Covalent Control of Dynamic Regioisomerism of Fluxional Carbon Cage

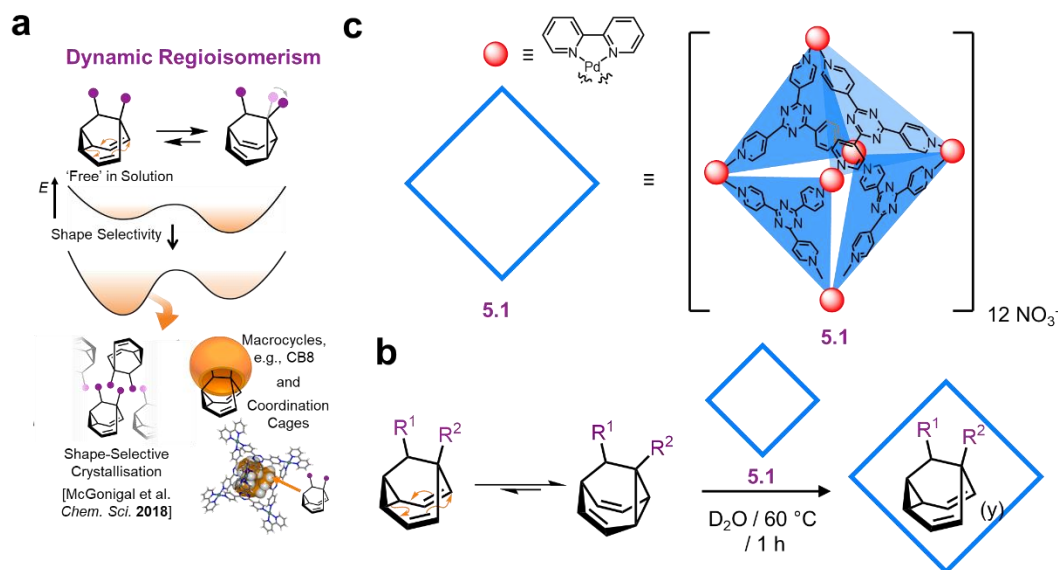


**Figure 5.1.** Dynamic regioisomerism of barbaralanes controlled by coordination cages. a) Schematic illustration of controlled dynamic regioisomerism through metal organic cages. b) the coordination cage used in this study, Pd M<sub>4</sub>L<sub>6</sub> cage aka Fujita cage. c) Conditions of encapsulation of **BBs** using metallocage in D<sub>2</sub>O.

McGonigal et al. previously analysed the adaptation of simple nondegenerate BB mixtures upon changes (Fig. 5.1) in their environment.<sup>1</sup> Each compound in the series possesses a tertiary alcohol and aromatic groups at the C1 and C9-positions of the barbaralane cage. The family of barbaralol compounds incorporated aromatic groups where the *p*-positions of the aromatic rings (R<sup>1</sup> and R<sup>2</sup>) are varied between OMe, F, and H. The Cope rearrangement between pair of non-degenerate valence isomers of these fluxional carbon cages modulate the molecular shape to an extent as the strain present in the tricyclic core of 1,9-**BBs** is slightly different, regulating the relative orientations of the two aromatic rings (dynamic regioisomerism) and this is highlighted in Figure 5.1a. The constitutional preference for pair of valence isomers is heavily influenced by the strain present in the barbaralane carbon cage. In all the barbaralols compounds in the study, the valence isomer where the aromatic ring positioned at C<sub>1</sub> rather than C<sub>5</sub> is thermodynamically favoured. This observation was confirmed by in-depth solution state NMR studies and supported by DFT modelling. The major valence isomers preferred solution-state isomer in every case have relatively small Gibbs free energy differences between isomers  $\Delta G \sim 3\text{--}5 \text{ kJ mol}^{-1}$ . This observation suggests that

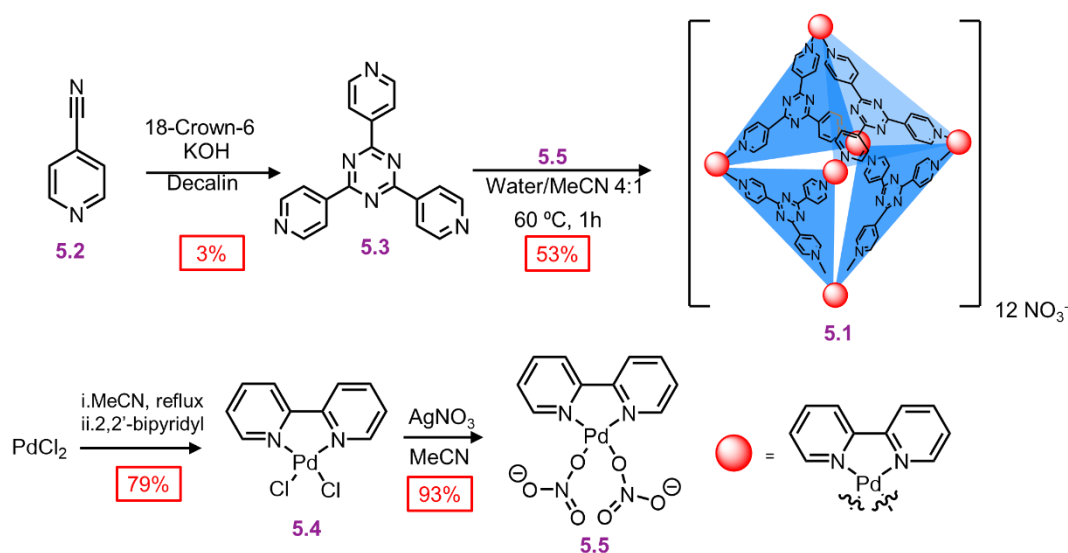
the positions of the **BB** equilibria would be sensitive to changes in the surrounding medium. Upon transitioning from solution to the solid state, the five compounds in this study are no longer a mixture of two constitutional valence isomers. The fluxional mixtures of 1,9-**BBs** undergo dynamic preferential crystallisation<sup>1</sup>, i.e., just one valence isomer from each pair of fluxional carbon cages crystallises from the mixture. For three compounds, the thermodynamically favoured valence isomer was present in the crystal structure, however, for the other two compounds, the minor valence isomer that have higher strained molecular structures were favoured in solid-state crystal structure. Despite the presence of an alcohol group and mildly polarised aromatic rings, the crystal packing is not dictated by any significant and specific noncovalent bonding interactions. Instead, van der Waals interactions constitute the dominant contacts. The most dominant feature of these barbaralane was the V-like molecular shape that dictated the solid-state superstructures. The dihedral angles between the aromatics varied for pair of the valence isomers between relatively wide dihedral angles  $> 67^\circ$  for the major isomers, whereas the dihedral angles are  $< 44^\circ$  for the minor isomers. For major valence isomer solid-state superstructure, the preference for these isomers are to arrange their V-shaped structures head-to-tail, and the minor isomers are arranged head-to-head, allowing their aromatic groups to interdigitate. The size of  $R^1$  and  $R^2$  effects the ability of interdigitation between the V-shaped molecules in crystal packing. Ultimately, these insights of shape-selective crystallisation confirmed the idea that finely balanced shapeshifting equilibria can adapt in response to external interactions with their surrounding medium.

#### 5.1.1 Aim & Objectives

Based on the shape-selective crystallisation of 1,9-**BBs**, herein we studied the dynamic regioisomerism behaviour of 1,9-**BBs** encapsulated in geometrically confined environment in solution and solid state. We hypothesised that this confinement would override the observed dynamic crystallisation of 1,9-**BBs** from previous studies as a host-guest complex. The molecular shape of pair of valence isomers heavily influences which constitutional isomer will be favoured in the cavity of geometrically confined environment. To achieve this goal, a Pd-based metal-organic cage **5.1** shown in Figure 5.1 was chosen as the encapsulating agent for our study. These Pd  $M_4L_6$  metallocages were championed by Fujita et al. to study guests in confined cages for conformation

change<sup>2</sup>, catalysis<sup>3</sup> and new materials application<sup>4</sup>. Encapsulation reactions using **5.1** were carried out in water or D<sub>2</sub>O with no presence of an organic solvent to drive the guest into the hydrophobic cavity of the cage, maximizing the binding affinity of the host and guest. The analysis of encapsulation was conducted using solution state NMR and single crystal XRD to understand the encapsulation in solid-state. Evidence of encapsulation occurring with control of **BBs** such as 9-tolyl-barbaralol **4.5** was observed in solution. Unfortunately, evidence of the desired encapsulation of 1,9-**BBs** using **5.1** could not be determined in solution state and solid state in our hands and discussion on our study and future work is discussed.

## 5.2 Synthesis and Characterisation of Metal-Organic Molecular Cage, Pd M<sub>6</sub>L<sub>4</sub>



**Scheme 5.1.** Synthesis of Fujita cage.

The Pd M<sub>4</sub>L<sub>6</sub> cage or Fujita cage (**5.1**) was synthesized using previously reported synthesis.<sup>2</sup> The formation of the triazine ligand **5.3** through a self-condensation of cyanopyridine **5.2** was achieved at a poor yield, however, this was enough material to move forward in the synthesis. For the Pd vertices, PdCl<sub>2</sub> is cracked using acetonitrile to make a bis-acetonitrile complex and is then reacted with 2,2-bipyridyl to achieve **5.4** in a moderate yield. **5.4** is further reacted with AgNO<sub>3</sub> to replace the Cl<sup>-</sup> ligands with NO<sub>3</sub><sup>-</sup> at high conversion to Pd precursor **5.5**. The metallocage is formed using the triazine ligand **5.3** and Pd vertices **5.5** reacted in water/MeCN solution to obtain the cage **5.1** in moderate yields with NO<sub>3</sub><sup>-</sup> counter anion. To determine if this is a true

molecular cage and not a polymer/oligomer mixture of the ligands & Pd metal, NMR and single-crystal XRD were used to confirm the structure.

### 5.2.1 Structure Determination of Metal-Organic Molecular Cage, Pd M<sub>6</sub>L<sub>4</sub>

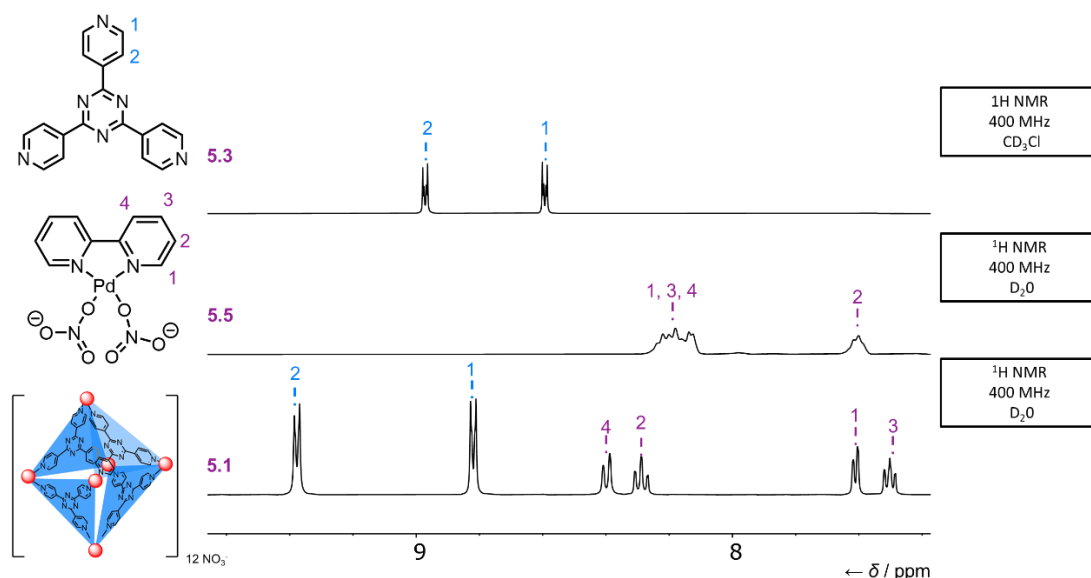


**Figure 5.2.** Partial <sup>1</sup>H NMR of Fujita cage, Triazine **5.3**, and Pd building block **5.5**.

Figure 5.2 shows a partial <sup>1</sup>H NMR stack of the metal-organic cage **5.1** compared to the 2,2-bipyridyl Pd complex (vertices) **5.5** and the triazine ligands **5.3** (faces). Both sets of peaks from **5.5** and **5.3** were present in compound **5.1** with the correct integration ratios. The triazine proton signals for **5.1** significantly shifted downfield indicating coordination to the Pd metal centre. The proton signals of the 2,2 bipyridyl ligand coordinated Pd metal centre along with the NO<sub>3</sub><sup>-</sup> ligands are overlapped, however, compared to the metallogage **5.1**, the 2,2-bipyridyl protons signals are resolved and significantly shifted downfield. This resolving of proton signals is most likely due to the new coordination of the triazine ligand. The <sup>1</sup>H NMR spectrum agrees the literature spectrum of Fujita's cage. To further prove that these sets of peaks corresponding to the triazine ligand and 2,2-bipyridyl belong to one molecule, we used diffusion ordered spectroscopy (DOSY) NMR which reports diffusion coefficients for individual resonances in NMR spectra. DOSY is primarily used to analyse mixtures of small molecules and the oligomeric state of biomolecules. For our study, this technique can determine if we have a mixture of two components (**5.3** and **5.5**) or the metallogage by measuring the diffusion coefficient of the analyte in solution. DOSY NMR of **5.1** was obtained in D<sub>2</sub>O, the proton signals corresponding to triazine and 2,2-bipyridyl

molecule all correlate to the same diffusion coefficient,  $D = 1.56 \times 10^{-10} \text{ m}^2/\text{S}^{-1}$ , meaning the proton signals of both components come from one molecule.

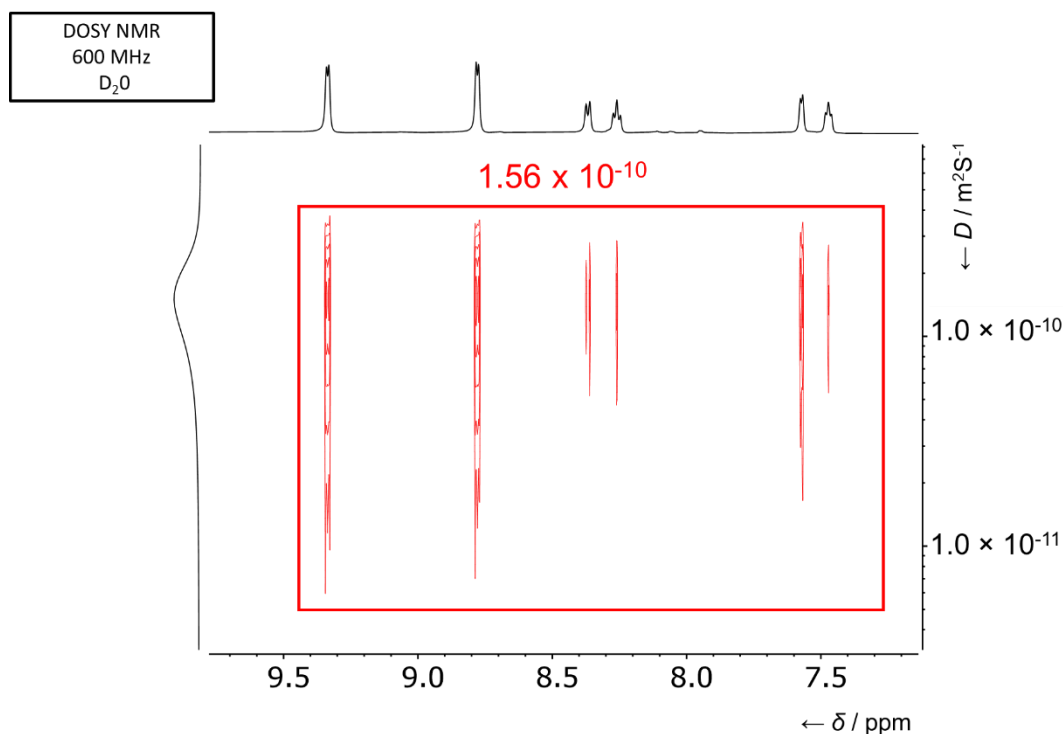


**Figure 5.3.** DOSY NMR of Fujita Cage with a diffusion coefficient  $D = 1.56 \times 10^{-10} \text{ m}^2/\text{S}^{-1}$ .

To further prove that the metallocage **5.1** was synthesised, single crystals of metallocage **5.1** was obtained by slow evaporation in 4:1 MeCN/water solution. The crystal structure was solved; however, disorder was present in cavity of the cage meaning the  $r^2$  value was outside acceptable range for publication. Figure 5.4 shows the crystal structure of the metallocage, confirmed that the metallocage **5.1** was synthesised with desired  $\text{Pd M}_4\text{L}_6$  conformation needed for our encapsulation study.

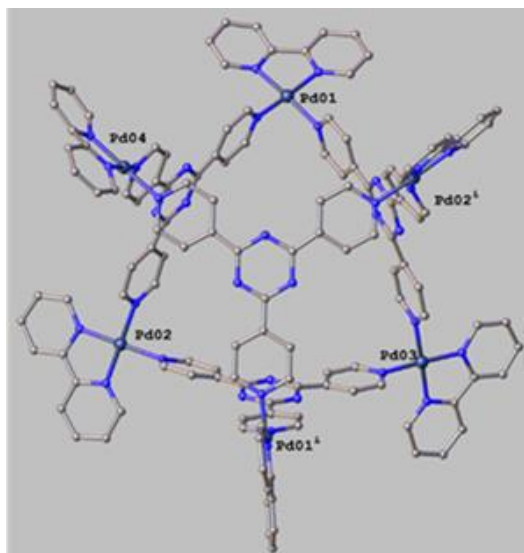


**Figure 5.4.** Crystal structure of metallocage, **5.1**.

### 5.3 Encapsulation of Barbaralanes using a Metal-Organic Molecular Cage, Pd M<sub>6</sub>L<sub>4</sub>

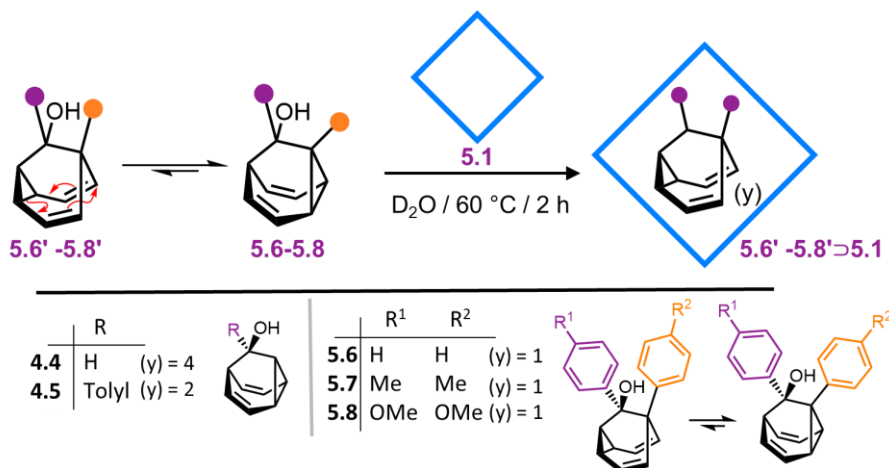


**Figure 5.5.** The different BBs used in the encapsulation.

The confirmation of metallocage **5.1** being synthesised allowed the study of the dynamic regioisomerism of the 1,9-**BBs** fluxional nature in geometric confined space in solution and solid state. Encapsulation of a myriad of barbaralols were conducted in D<sub>2</sub>O to analyse the reaction by *in situ* solution-state NMR. Figure 5.5 illustrates how the encapsulation using **5.1** as host with control **BBs** such as the parent barbaranol **4.4**, and 9-(tolyl)-barbaranol **4.5** has minimal molecular shape change between the pairs of enantiomers from the dynamic regioisomerism. The series of 1,9-**BBs** used in this study is highlighted in Figure 5.5 The selected 1,9-**BBs** range from the smaller 1,9-diphenyl-barbaranol (**5.6**) compared to the bulkier 1,9-ditolyl-barbaranol (**5.7**) and the electron

rich 1,9-dianisoyl-barbaralol (**5.8**). For 1,9-**BBs**, the major isomer in solution is usually the valence isomer  $C_1$  has an aryl group and is a part of the cyclopropane. This claim is supported by in depth solution and solid state NMR, single crystal XRD and DFT modelling by McGonigal et al.<sup>1</sup> For example, the dianisyl derivative **5.8**, both solution-state and solid-state, the major valence isomer **5.8** was favoured. We hypothesised that for 1,9-**BBs** to be encapsulated by the metallocage **5.1**, the minor valence isomer will be favoured even with more strained molecular structure as the molecular shape of this isomer allow for better fit.

### 5.3.1 Solution-State Analysis of the Encapsulation of Control Barbaralanes using Metallocage **5.1**

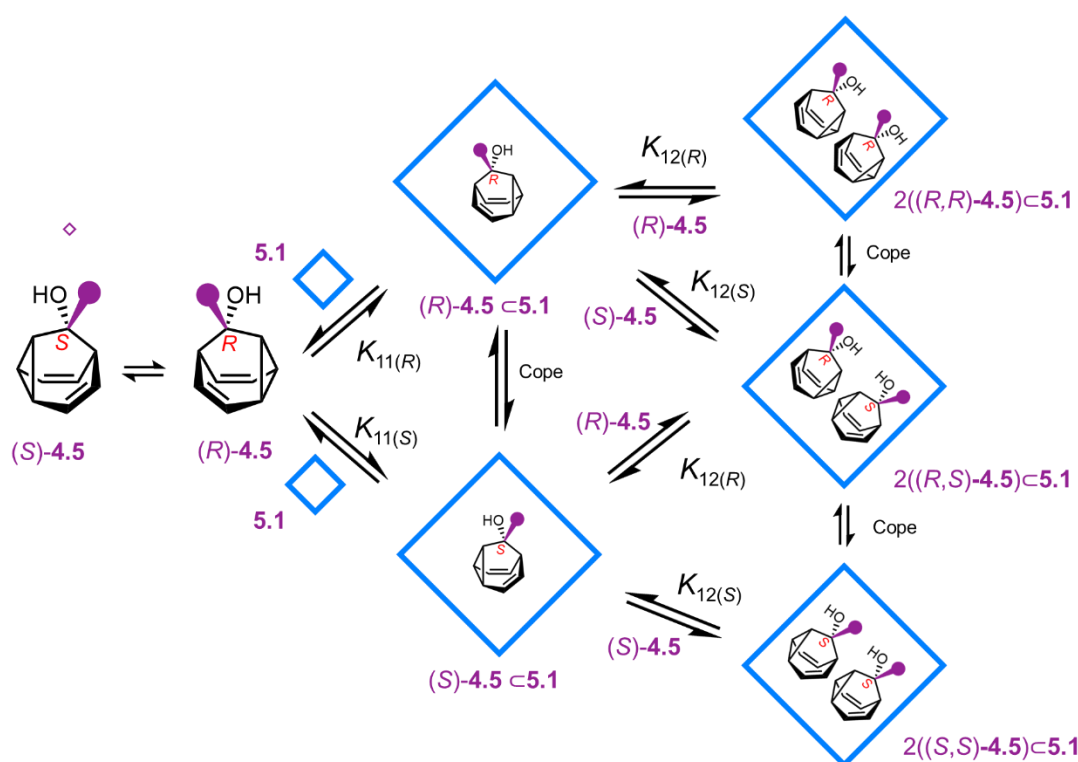


**Figure 5.6.** A schematic representing the formation of the two 1:1 complexes between (*R/S*)-**4.5** and the metallocage **5.1** along with enantiomerisation of chiral barbaralol via cope rearrangement. The formation of the three 1:2 complexes from an additional barbaralol guest inside the metallocage **5.1** along with the enantiomerisation of chiral barbaralol via cope rearrangement.

To understand the binding affinity of a generic barbaralane guest to the metallocage **5.1**, 9-(tolyl)-barbaralol **4.5** was used for initial encapsulation conditions. Fujita et al. was able to encapsulate 1-adamantanol effectively in water and in the solid-state with 4 (1-adamantanol) inside metallocage **5.1** in crystal structure reported. The barbaralane

carbon cage of 9-(tolyl)-barbarolol **4.5** has the similar structure and size as 1-adamantanol except there is an additional tolyl group on C<sub>9</sub>. We hypothesize that up to two 9-(tolyl) barbaralols will fit in the cavity of **5.1**. Figure 5.6 shows how the fluxional dynamics of the encapsulation towards 1:1 complex (HG,  $K_{11}$ ) and 1:2 complex (HG2,  $K_{12}$ ) and the enantiomerisation of barbaralol guest via Cope rearrangements. This enantiomerization can lead to independent  $K_{11}$  and  $K_{12}$  binding constants for the *R* and *S* enantiomers if the rate of enantiomerization is slower than the rate of encapsulation by the metallocage **5.1**. The rate of enantiomerisation can be affected by the encapsulations as the confined cavity cage can lead to higher energy barrier between enantiomeric pair which can lead to independent  $K_{11}$  and  $K_{12}$  binding constants for the enantiomers. There are five possible states of these host-guest complexes excluding isomers from the different orientation of the guests.

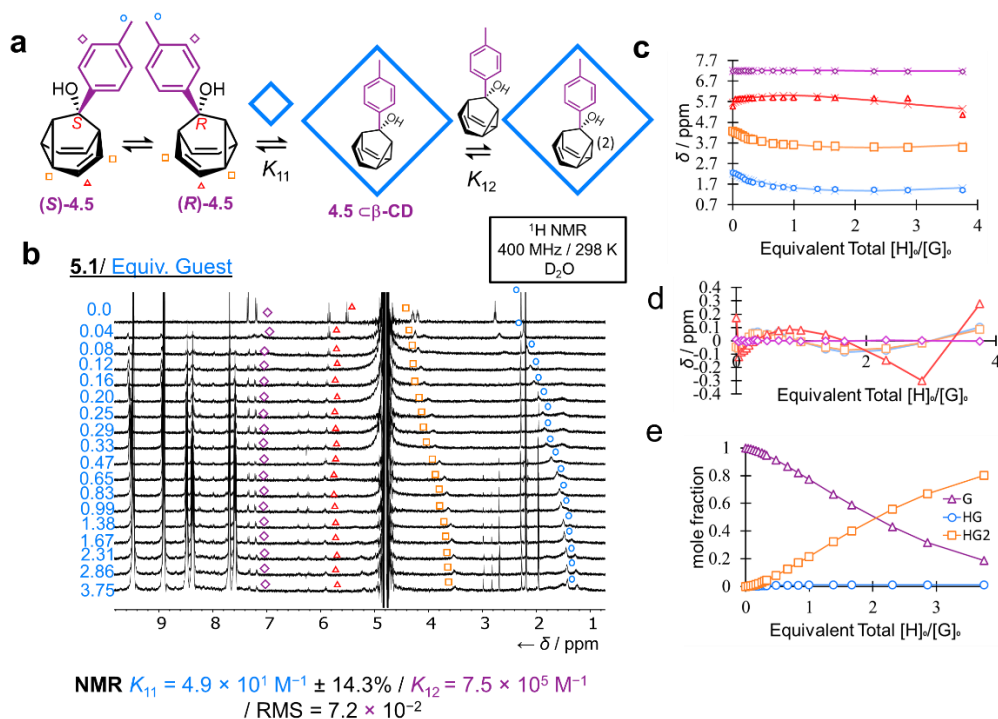


**Figure 5.7.** NMR titration of BBs with Fujita Cage PdM<sub>4</sub>L<sub>6</sub> showing the binding affinity of guest in host. a) Schematic showing the binding between (S/R)-**4.5** and the metallocage **5.1** highlighting the equilibria between 1:1 HG complex ( $K_{11}$ ) and 1:2 HG complex ( $K_{12}$ ). b) Plot of the change of proton signals,  $\Delta\delta$ , of the barbaralol protons against the ratio guest (**4.5**)/host (**5.1**), the fit line was generated by Bindfit non linear regression analysis for 1:2 HG binding using L-BFGS-B method. c) Plot of residuals from line fit present in plot B showing the quality of fit. d) Plot of mole fractions of the guest **4.5**, the 1:1 HG complex, and 1:2 HG complex between **4.5** and metallocage **5.1**.

To conduct a quantitative analysis of the intermolecular interactions of this system in solution, the most common approach is the supramolecular titration method. We decide

to use NMR as it is sensitive to the supramolecular interaction(s) of interest. The resulting information from a physical property change (i.e.  $\Delta\delta$ ) from the supramolecular interactions can be compared and fitted to binding models to obtain information such as the association constant  $K_{11}$  and  $K_{12}$ . Thordarson et al.<sup>5</sup> have highlighted considerations needed for NMR titrations, and the parameters we need to keep in mind. We proceeded with NMR titration in D<sub>2</sub>O to increase the binding affinity of the barbaralol guest to hydrophobic cavity of the Fujita cage. The guest concentration was constant at 0.5 mM and the host solution was 5 mM and had guest solution at 0.5 mM to account for dilution of the guest solution from the titration. Figure 5.7b shows the <sup>1</sup>H NMR titration of guest, 9-(tolyl)- barbaralol **4.5** with the metallocage **5.1** host. The host **5.1** was used as the titrating solution instead of the guest solution as the solubility is limited for 9-(tolyl)-barbaralol guest. From the supramolecular titration experiment, 4 proton signals of the guest shown in Figure 5.7 were tractable through ppm shifting throughout the titration. However, as the equivalence of the host **5.1** increased, the peaks broaden into the baseline, hindering accuracy in tracking the  $\Delta\delta$  ppm of the selected signals. Interestingly, the 4 proton signals that could be tracked were all on the same vinyl bridge of the barbaralane on the same face as the tolyl group, and tolyl group proton signals as well. This observation gives a hint in the orientation of the binding in the cage in these conditions. The tolyl face of one 9-(tolyl)-barbaralol could be facing outside void face of the metallocage to the free solvent or inside the cavity of the metallocage interacting with a second 9-(tolyl)-barbaralol inside the cage. The tolyl proton and cyclopropane vinyl position have largest magnitude change in the NMR titration meaning there could be more close contacts between the cage and barbaralols. The 4 proton signals peaks that were tractable were chosen to develop a binding model to find the binding affinity of the encapsulation reaction, as a global fit would improve the quality of the model. The binding model was determined using the Bindfit program, an online binding fit calculator that uses non-linear regression analysis via a python program to develop a fit for classical supramolecular titration data. After looking at all the different possible binding model, A 1:2 HG2 binding model that indicates a cooperative binding mode. The fitted values of  $K_{11}$  and  $K_{12}$  are  $4.9 \times 10^1 \text{ M} \pm 14.3\%$  and  $7.5 \times 10^5 \text{ M}^{-1} \pm 14.7\%$ , respectively, based on this model. The RMS is  $7.2 \times 10^{-2}$  and covariance  $3.1 \times 10^{-2}$  indicating the quality of fit is acceptable

compared to similar studies.<sup>5</sup> This fit reveals that 1:2 HG<sub>2</sub> is the thermodynamic product in solution as the  $K_{12}$  is larger than  $K_{11}$  1:1 HG. This binding model indicates a cooperative binding mode. This difference in  $K$  constants is highlighted by the mole fraction present in the experiment which is shown in Figure 5.7. Bias to the enantiomerisation of the barbaralol guest by encapsulation could not be determined as the rapid interconversion could not be observed at 298 K and VT NMR could not be used with this system due to the solvent being D<sub>2</sub>O which will freeze before the coalescence temperature could be reached. Accurate binding was difficult to determine due to limited access to the NMR facilities, the walk-up service had to be used, varying temperature of NMR probe could cause issues during the titration experiments.

#### 5.4 Encapsulation of 1, 9 Disubstituted Barbaralanes using Metallocage 5.1

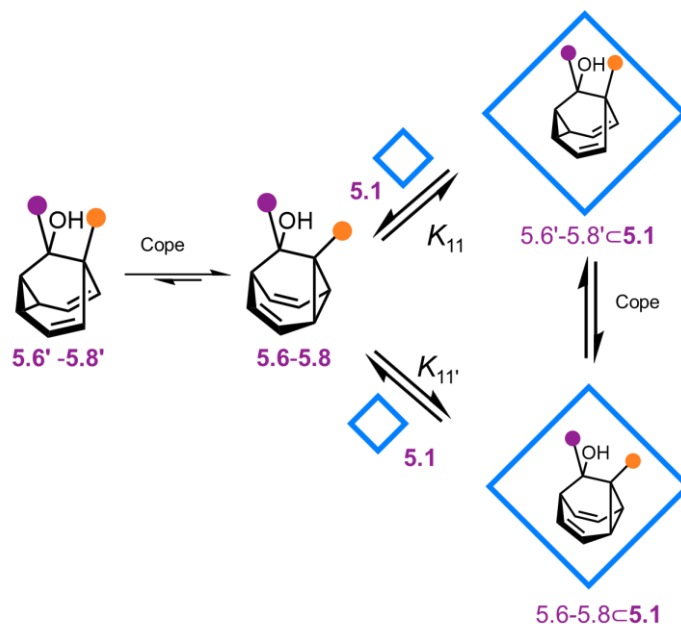


**Figure 5.8.** A schematic representing the formation of the two 1:1 complexes between (*R/S*)-5.6-5.8 and the metallocage 5.1 along with enantiomerisation of chiral barbaralol via cope rearrangement.

The dynamic regioisomerism of 1,9-disubstituted **BBs** highlighted in Figure 5.1 can be tested by studying the effect on shape selective crystallization being affected by geometric confined medium such as metallocage **5.1**. The dynamics of the encapsulation of 1,9-**BBs** competing valence isomerisation of 1,9-**BBs** guests via cope rearrangements is highlighted in Figure 5.8. Unlike the control 9-(tolyl)-barbaralol, we hypothesize only one 1,9-**BBs** can fit in the cavity of the metallocage **5.1** so the binding association constant is  $K_{11}$ . Due to the valence isomerisation, there is  $K_{11}$  and  $K_{11'}$  for the major and minor isomerisation if the rate of encapsulation is faster than rate of valence isomerisation which could be driven by the hydrophobic cavity of the cage if both isomers can fit in the cage. There also possibility for the isomerisation of the 1,9-**BBs** inside the cage *via* cope rearrangement, however it will be heavily influenced by the constrained cavity environment of the metallocage. Figure 5.9 shows  $^1\text{H}$  NMR of the encapsulation reaction of a range 1,9-**BBs** (**5.6-5.8**) (10 equiv.) in  $\text{D}_2\text{O}$  using Fujita cage (1 equiv.) **5.1** at 60 °C for 3 h. The encapsulation reaction is a suspension of the guest (**5.6-5.8**) in  $\text{D}_2\text{O}$  with the dissolved metallocage and after reaction is complete, the unsolubilized guest is filtered off via syringe filter. No proton could be observed of for the barbaralol guest for aromatic/vinyl protons, relatively minimal proton signals for the aliphatic protons compared to the metallocage which could not be assigned. The proton signals of the metallocage are slightly shifted compared to the control metallocage which could be evidence of binding, however this observation would indicate poor encapsulation yield of these 1,9-**BBs** with metallocage **5.1**. Using classic supramolecular NMR experiments could not be done as the solubility of the 1,9-**BBs** in  $\text{D}_2\text{O}$  was limited and attempts to make guest  $\text{D}_2\text{O}$  solutions revealed that the magnitude of the proton signals of the 1,9-**BBs** were too small to track changes over the full titration window. This issue with the 1,9-**BBs** NMR experiments meant that solution-based studies were not viable methods to study the dynamic regioisomerism of **BBs** in geometric confined environment in the metallocage in our hands.

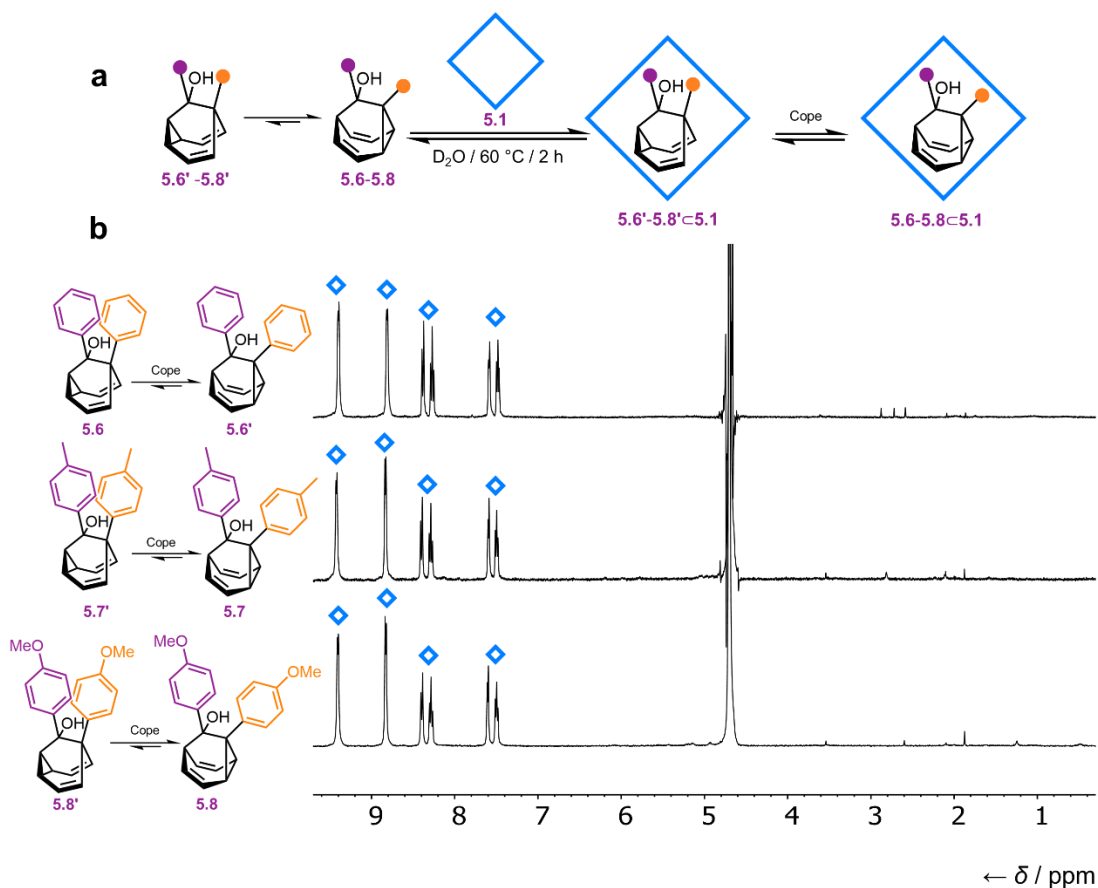


**Figure 5.9.** Partial  $^1\text{H}$ NMR stack with 1,9-BBs encapsulation using Fujita cage **5.1**.

### 5.5 Solid State Analysis of Encapsulation of Barbaralanes using Metallocage **5.1**

To understand if the confined geometric confined space of metallocage **5.1** can affect the dynamic regioisomerism of 1,9-BBs, we decide to grow single crystals of a variety of host-guest complexes different barbaralanes with the metallocage. The solid-state superstructure (crystal packing) can have an influence on the valence isomerisation if encapsulated by the metallocage **5.1** based on previous studies of the shape-selective crystallisation of barbaralanes. In the solid-state, the dynamic isomerisation could be frozen which will allow us to determine if the geometric confined cavity of the metallocage can influence the isomerisation of 1,9-BBs.

**Table 5.1.** Summary of Crystallisation attempts using crystal tubes

Barbaralane (eq.)	Metallocage (eq)	Solvent (mM)	Left to evaporate
<b>4.4 (1.5)</b>	1	1.23	Precipitate
<b>4.4 (5)</b>	1	1.23	Precipitate
<b>4.4 (10)</b>	1	1.23	Precipitate
<b>4.5 (1.5)</b>	1	1.23	Precipitate
<b>4.5 (5)</b>	1	1.23	Precipitate
<b>4.5 (10)</b>	1	1.23	Disorder crystals
<b>5.6 (1.5)</b>	1	1.23	Precipitate
<b>5.6 (5)</b>	1	1.23	Precipitate
<b>5.6 (10)</b>	1	1.23	Precipitate
<b>5.7 (5)</b>	1	1.23	Empty Crystals
<b>5.7 (10)</b>	1	1.23	Empty Crystals


For initial experiments, crystallisation of the host guest complexes was conducted in crystallisation tubes containing the host guest solution to grow single crystals *via* slow evaporation. Attempts to encapsulate the guest **BBs** by solubilising the metallocage **5.1** in water (1.23 mM) and suspending the guest **BBs** in solution and heated until limit of solubility of the guest was reached. The free solid guest suspended in solution was removed *via* a syringe filter. The solution was then left in a crystallisation tube to slowly evaporate till crystal or precipitate formed. The only encapsulation attempts that grew crystals was 9-(tolyl)-barbaralol **4.5** and 1, 9-(ditolyl)-barbaralol **5.7**, however, there was large disorder present in the cage cavity and the crystal structures could not be determined.

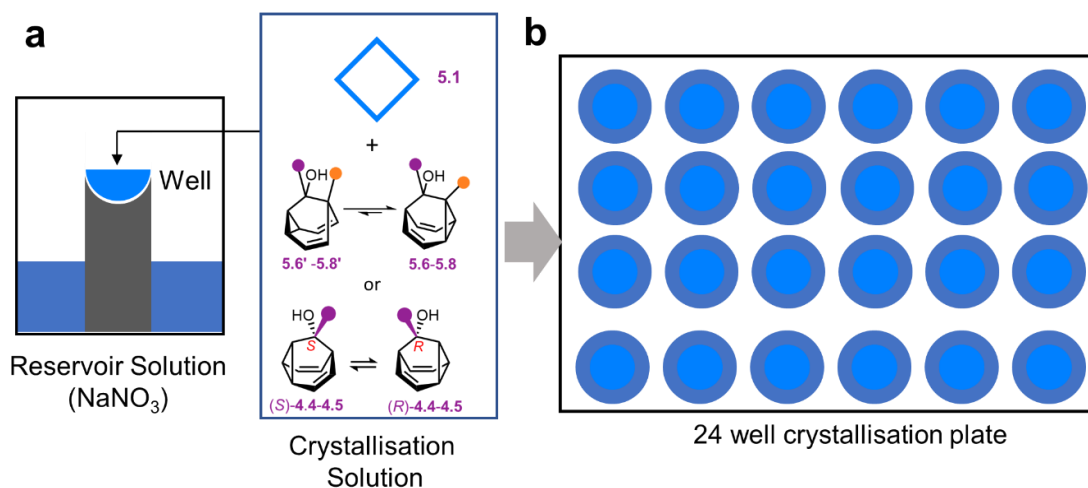


**Figure 5.10.** Schematic of the 24 well plates used for crystallisation of the host-guest complexes with the addition of reservoir solution containing  $\text{NaNO}_3$ .


We sought out a high throughput crystallisation method that required minimal amount of material for the guest and host that can also tolerate the solubility limits of this system, we collaborated with Ehmke Pohl, an expert in protein crystallisation based in Durham University. We utilized 24 well plates with reservoirs (Figure 5.10) that are typically used for protein crystallisation<sup>6</sup> that can be used to rapidly optimize conditions to obtain crystals of the desired host-guest complexes. Figure 5.11-5.13 show schematic examples of the parameters we tried to optimize for the crystallisation of host-guest complexes. We chose the available parent barbaralol **4.4**, 9-(tolyl)-barbaralol **4.5**, and 1,9-(ditolyl)-barbaralol **5.7** to test this high throughput crystallisation method. Overall, higher amounts of crystals were obtained from a variety of conditions. However, the crystals selected from the plates did not have any guests in them as determined from single XRD experiments. The dilute conditions of our guest in these host solutions are hindering the probability of host-guest interaction which is significantly limiting the chance of growing crystals of encapsulate guest in the metallocage. Another issue of this system was the sensitive nature of the molecular cage crystals that easily decompose which indicated a weak crystal lattice. We were able to grow crystals of metallocage **5.1**, and then tried to soak the crystals using the desired guest neat as a melt of barbaralol. However, removing the crystals from the mother liquor led to immediate decomposition of the crystal. This decomposition comes for the limitation of using molecular cage as a crystal host when empty.

HG: 1/1 R: 0 eq	HG: 1/1 R: 0.5 eq	HG: 1/1 R: 1.0 eq	HG: 1/1 R: 1.5 eq	HG: 1/1 R: 2.0 eq	HG: 1/1 R: 2.5 eq
HG: 1/2 R: 0 eq	HG: 1/2 R: 0.5 eq	HG: 1/2 R: 1.0 eq	HG: 1/2 R: 1.5 eq	HG: 1/2 R: 2.0 eq	HG: 1/2 R: 2.5 eq
HG: 1/3 R: 0 eq	HG: 1/3 R: 0.5 eq	HG: 1/3 R: 1.0 eq	HG: 1/3 R: 1.5 eq	HG: 1/3 R: 2.0 eq	HG: 1/3 R: 2.5 eq
HG: 1/4 R: 0 eq	HG: 1/4 R: 0.5 eq	HG: 1/4 R: 1.0 eq	HG: 1/4 R: 1.5 eq	HG: 1/4 R: 2.0 eq	HG: 1/4 R: 2.5 eq

 Crystals present in well

**Figure 5.11.** Crystallisation Plate (4.4): Host (5.1) concentration – 0.5 mM, Guest (4.5) concentration – 0.5 mM, Reservoir solution- 3 M NaNO<sub>3</sub> (aq) – R eq is added as a volume equivalent to the HG solution.

HG: 1/1 R: 0 eq	HG: 1/1 R: 0.5 eq	HG: 1/1 R: 1.0 eq	HG: 1/1 R: 1.5 eq	HG: 1/1 R: 2.0 eq	HG: 1/1 R: 2.5 eq
HG: 1/2 R: 0 eq	HG: 1/2 R: 0.5 eq	HG: 1/2 R: 1.0 eq	HG: 1/2 R: 1.5 eq	HG: 1/2 R: 2.0 eq	HG: 1/2 R: 2.5 eq
HG: 1/3 R: 0 eq	HG: 1/3 R: 0.5 eq	HG: 1/3 R: 1.0 eq	HG: 1/3 R: 1.5 eq	HG: 1/3 R: 2.0 eq	HG: 1/3 R: 2.5 eq
HG: 1/4 R: 0 eq	HG: 1/4 R: 0.5 eq	HG: 1/4 R: 1.0 eq	HG: 1/4 R: 1.5 eq	HG: 1/4 R: 2.0 eq	HG: 1/4 R: 2.5 eq

 Crystals present in well

**Figure 5.12.** Crystallisation Plate (4.5): Host (5.1) concentration – 0.5 mM, Guest (4.5) concentration – 0.5 mM, Reservoir solution- 3 M NaNO<sub>3</sub> (aq) – R eq is added as a volume equivalent to the HG solution.

HG: 1/1 R: 0 eq	HG: 1/1 R: 0.5 eq	HG: 1/1 R: 1.0 eq	HG: 1/1 R: 1.5 eq	HG: 1/1 R: 2.0 eq	HG: 1/1 R: 2.5 eq
HG: 1/2 R: 0 eq	HG: 1/2 R: 0.5 eq	HG: 1/2 R: 1.0 eq	HG: 1/2 R: 1.5 eq	HG: 1/2 R: 2.0 eq	HG: 1/2 R: 2.5 eq
HG: 1/3 R: 0 eq	HG: 1/3 R: 0.5 eq	HG: 1/3 R: 1.0 eq	HG: 1/3 R: 1.5 eq	HG: 1/3 R: 2.0 eq	HG: 1/3 R: 2.5 eq
HG: 1/4 R: 0 eq	HG: 1/4 R: 0.5 eq	HG: 1/4 R: 1.0 eq	HG: 1/4 R: 1.5 eq	HG: 1/4 R: 2.0 eq	HG: 1/4 R: 2.5 eq

Crystals present in well

**Figure 5.13.** Crystallisation Plate (5.7): Host (5.1) concentration – 0.5 mM, Guest (4.5) concentration – 0.5 mM, Reservoir solution- 3 M NaNO<sub>3</sub> (aq) – R eq is added as a volume equivalent to the HG solution.

## 5.6 Non-Covalent Control of Dynamic Point Chirality of Fluxional Cage

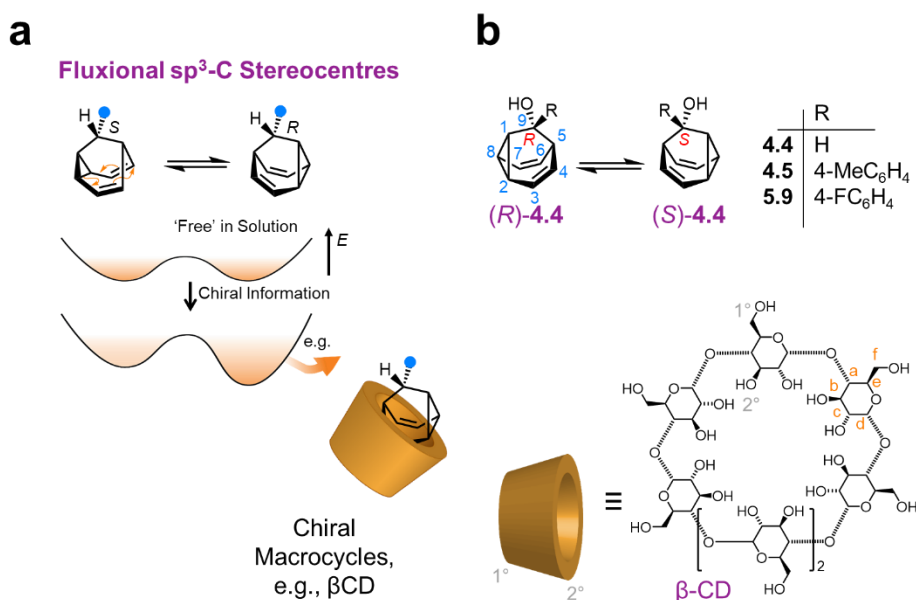


**Figure 5.14.** Non-covalent control of Dynamic  $sp^3$ -C chiral barbaralane using  $\beta$ -CD. a) Schematic of biasing of enantiomerisation using a chiral macrocycle. b) Barbaralane used in this study: barbaralol, 9-p-fluoro-phenyl BBs, and 9-tolyl BBs.

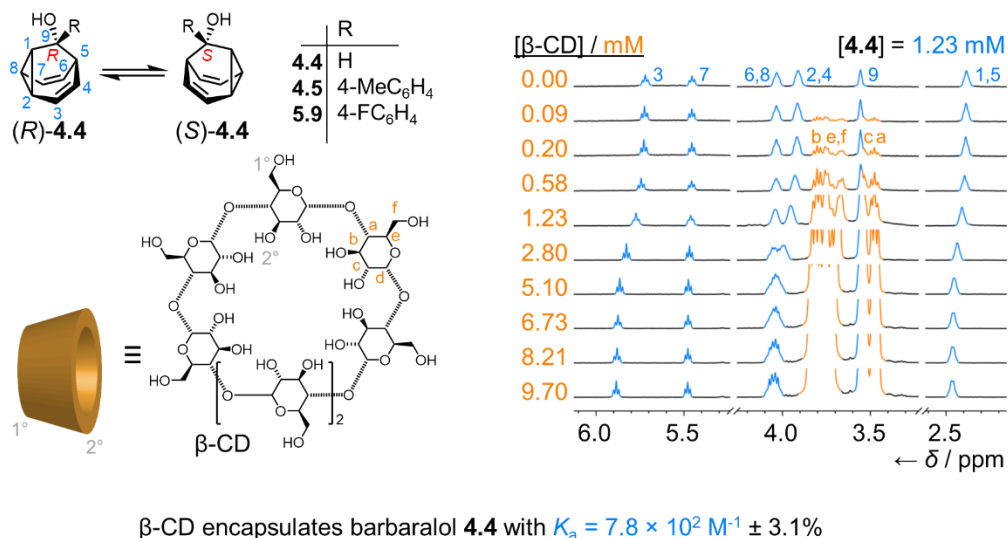
Chapter 3 discussed the control of enantiomerisation of dynamic chiral barbaralanes using covalent chiral auxiliaries. Furthering this effort to control dynamic  $sp^3$ -C chiral **BBs**, we decide to take advantage of using the medium to change the adaption of these chiral **BBs**. Unlike using a metallocage like **5.1** mentioned earlier in the chapter, we used a chiral macrocycle that can influence the chiral centre of **BBs** by favouring of

one of the enantiomers. Figure 5.14 shows how a chiral macrocycle translates chiral information to influence the enantiomerisation of chiral barbaralanes. For this study, we decided to use the parent barbaralol (**4.4**), 9-(tolyl)-barbaralol (**4.5**), 9-(*p*-fluorophenyl)-barbaralol as the molecules to study how the enantiomerization of BBs changes based on non-covalent self-assembly using a chiral macrocycle. We decided to use cyclodextrin-based macrocycle as our chiral host in this study. Cyclodextrins are commonly composed of five or more  $\alpha$ -d-glucopyranoside units in a ring linked by  $\alpha$ -1,4-glycosidic bonds. Frequently used CDs contain six, seven, or eight glucopyranoside monomers, namely,  $\alpha$ -cyclodextrin ( $\alpha$ CD),  $\beta$ -cyclodextrin ( $\beta$ CD), or  $\gamma$ -cyclodextrin ( $\gamma$ CD), respectively.<sup>7</sup> Generally, CDs have a truncated cone structure that has a hydrophilic exterior surface and hydrophobic interior cavity. Owing to the different inclusion ability,  $\alpha$ CD and  $\beta$ CD are commonly used in the design and synthesis of supramolecular materials.<sup>7</sup> Cyclodextrins are chiral and are capable of forming diastereoisomeric complexes with chiral guests. When a cyclodextrin complex of higher stability for one enantiomer of the guest molecule is bound, enantioselective recognition can occur. The difference in stability between the complexes formed with the enantiomers defines the efficiency of this chiral discrimination process.<sup>7</sup> Additionally, cyclodextrins can chirally discriminate between enantiomers even if they are not chemically modified with chiral auxiliaries. While there has been extensive research on using cyclodextrin as chiral sensor for chiral discrimination of mixture of enantiomers, there is no work shown how this same chiral sensor capability of cyclodextrin can bias a dynamic chiral compound with a small energy barrier between chiral enantiomers.<sup>8</sup> The macrocyclic  $\beta$ -CD was chosen based on previous studies from Dr. Aisha Bismillah. The self-assembly of these chiral BBs with  $\beta$ -CD was analysed using the solution and solid-state NMR, calorimetry, single crystals XRD and enantioselective oxidation of chiral BBs using  $\beta$ -CD as chiral reagent.

## 5.7 Encapsulation of 9-Barbaralols using $\beta$ -CD as a host

Encapsulation of the 9 substituted barbaralols (**4.4**, **4.5**, **5.9**) using was conducted in water, to take advantage of the hydrophobic cavity of  $\beta$ -CD as a driving force for binding, based on previous studies using solution state NMR and modelling the binding behaviour using Bindfit, the 9-**BBs** form 1:1 host-guest complexes.

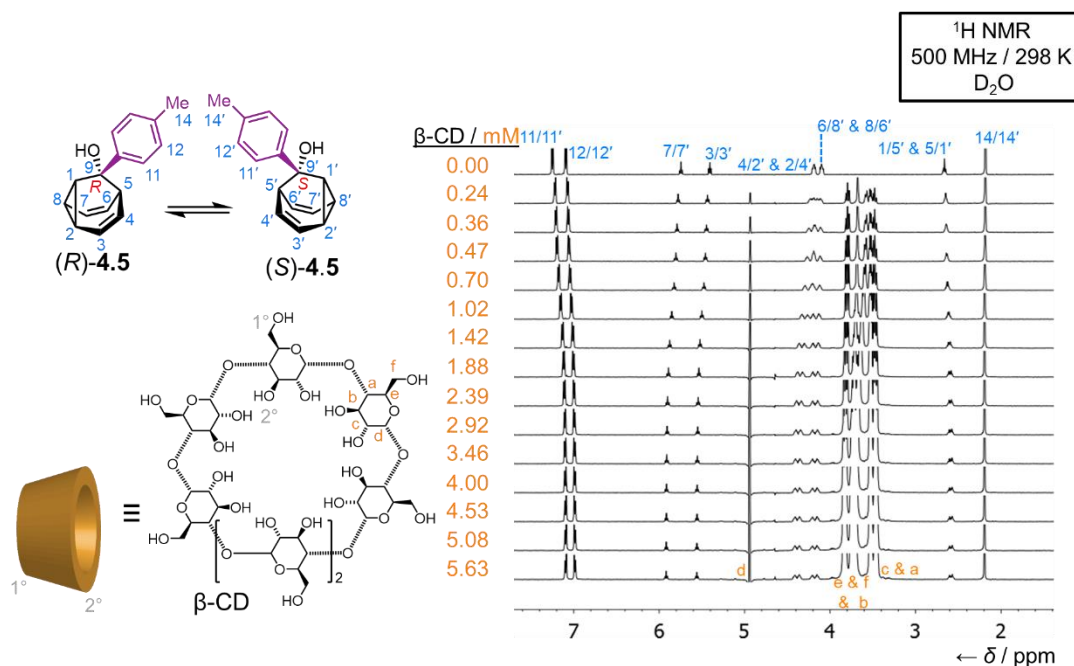
### 5.7.1 Solution State Analysis of Encapsulation



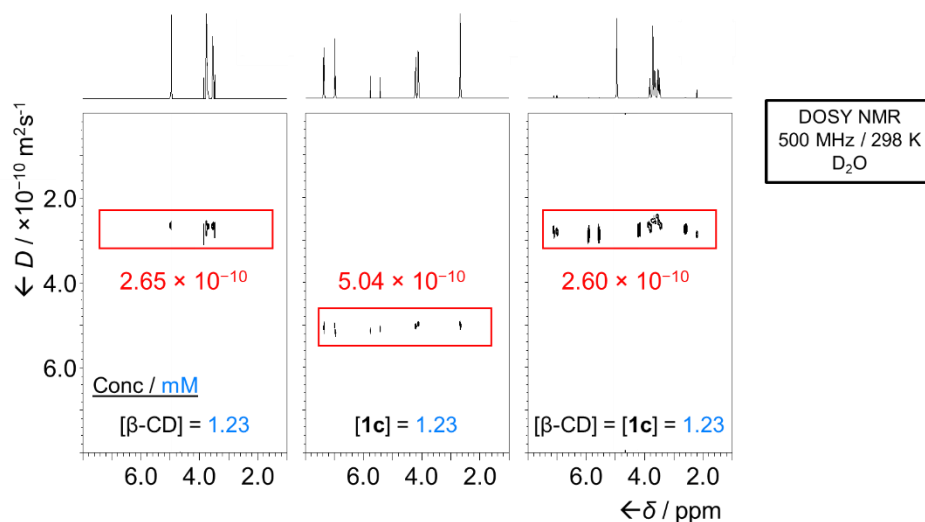
**Figure 5.15.** Partial  $^1\text{H}$  NMR Stack of NMR titration of barbaralol **4.4** using  $\beta$ -CD as a host in  $\text{D}_2\text{O}$  showing a binding mode of 1:1 and  $K_a = 7.8 \times 10^2 \text{ M}^{-1} \pm 3.1\%$

Figure 5.15 shows the titration of the barbaralol **4.4** guest using  $\beta$ -CD and revealing changes in proton signals of the vinyl protons (3,7), the averaged cyclopropyl/vinyl protons (2, 4, 6, 8), and the aliphatic protons (1, 5) as the concentration of host increases showing the binding is occurring. Using the software Bindfit, the binding affinity of **4.4** in  $\beta$ -CD,  $K_a = 7.8 \times 10^2 \text{ M}^{-1}$ , was found. 9-(tolyl)-barbaralol NMR binding study is shown in Figure 5.16 which also has 1:1 binding complex in water. Figure 5.16 shows the titration of the 9-(tolyl)-barbaralol **4.5** guest using  $\beta$ -CD reveals changes in proton signals of the aromatic protons (11, 12), vinyl protons (3,7), the averaged cyclopropyl/vinyl protons (2,4,6,8), and the aliphatic protons (1, 5) as the concentration of host increases showing the binding is occurring. Using the Bindfit software, the binding affinity of **4.5** in  $\beta$ -CD,  $K_a = 5.5 \times 10^3 \text{ M}^{-1} \pm 3.3\%$ . The larger binding affinity of 9-(tolyl)-barbaralol **4.5** compared to the parent barbaralol **4.4** could come from a better fit inside of the cavity of  $\beta$ -CD.

Additionally, binding of the guest 9-(tolyl)-barbaralol and  $\beta$ -CD host was studied using DOSY NMR (Figure 5.17), and it was determined that the peaks for both **BBs** and  $\beta$ -CD where there is 1:1 equivalence in solution correlate to the same diffusion coefficient,  $D = 2.60 \times 10^{-10} \text{ m}^2/\text{s}^{-1}$  which is different coefficient compared to both the **BBs** and  $\beta$ -CD individually. Also, the diffusion coefficient is similar to the diffusion coefficient of  $\beta$ -CD ( $D = 2.65 \times 10^{-10}$ ) which make sense as both the host and the host-guest complex should have similar size.



**Figure 5.16.** Partial  $^1\text{H}$  NMR Stack of NMR titration of 9-(tolyl)-barbaralane **4.5** using  $\beta$ -CD as a host in  $\text{D}_2\text{O}$  showing a binding mode of 1:1 and  $K_a = 5.5 \times 10^3 \text{ M}^{-1} \pm 3.3\%$



**Figure 5.17.** DOSY NMR of  $\beta$ -CD, 9-(tolyl)-barbaralol(**4.5**) and encapsulated 9-(tolyl)-barbaralol in  $\beta$ -CD.

Solution state NMR analysis allows insight into the binding interactions of barbaralane to  $\beta$ -CD by determining binding association constants. However, important thermodynamic parameters such as the enthalpy and entropy of binding cannot be determined using NMR titrations. To understand the thermodynamics of binding in our system, we use isothermal titration calorimetry (ITC) to measure the thermodynamic parameters of the self-assembly interactions of the chiral **BBs** to  $\beta$ -CD.

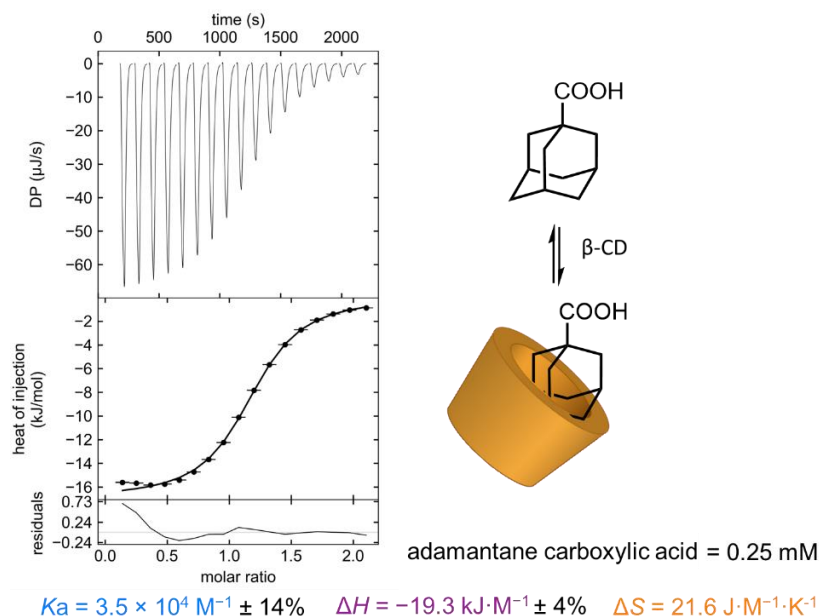


**Figure 5.18.** ITC isotherm of adamantane carboxylic acid binding with  $\beta$ -CD in water with 0.1 M PBS, pH 7.4 buffer solution.

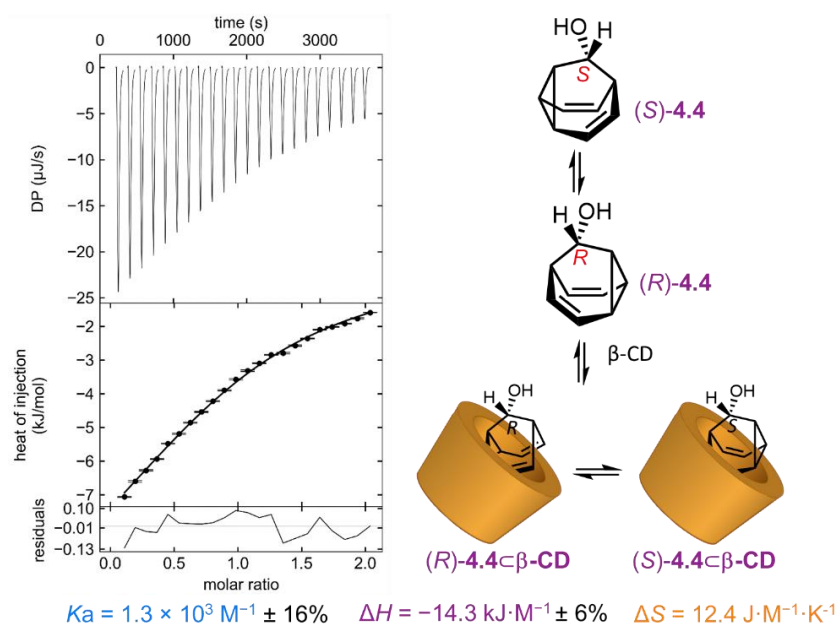


**Figure 5.19.** ITC isotherm of barbaralol (**4.4**) binding with  $\beta$ -CD in water with PBS buffer solution.

To develop a methodology to study the self-assembly of the dynamic chiral barbaralols with  $\beta$ -cyclodextrin by ITC in buffer solution (0.1 M Phosphate-Buffered Saline (PBS), pH 7.4), we used the previously studied adamantane carboxylic acid as a control compound as the molecular shape of this compound is similar to barbaralol.<sup>7</sup> The binding isotherm of  $\beta$ -CD is shown in Figure 5.18. The binding affinity  $K_a$  of adamantane carboxylic acid is  $3.5 \times 10^4 \text{ M}^{-1}$  which is higher than the  $K_a$  of 9-**BBs** determined by the solution state NMR titrations. This ITC experiment was conducted in a buffered solution and has a different ionic strength, however, the difference in binding affinity is most likely due to the molecular shape of adamantane carboxylic acid being a better fit in the cavity of  $\beta$ -CD than the 9-**BBs**. The binding isotherm of this experiment agreed well with the literature binding data adamantane carboxylic acid to  $\beta$ -CD validating our ITC method.<sup>9</sup> For the thermodynamic parameters determined for binding, there is a negative change in enthalpy indicating binding of the host and guest, and a positive change in entropy which is counterintuitive at first as the binding of two molecules to one usually indicates a more ordered system and a loss of entropy. However, the water molecules present in the macrocycle (11 water molecules for  $\beta$ -CD)<sup>7,8</sup> are driven out by the binding event causing an increase in entropy. The parent barbaralol (**4.4**) and 9-(aryl)-barbaralol (**4.5**, **5.9**) were studied using ITC using the same condition as the reference adamantane carboxylic acid. An example of binding isotherm of 9-(tolyl)-barbaralol binding to  $\beta$ -CD using the same conditions as adamantane carboxylic acid shown in Figure 5.19. Focusing on the thermodynamic parameters, there is a negative change in enthalpy indicating binding and the binding event behaviours are similar to the reference compound ( $\Delta H \uparrow$ ,  $\Delta S \downarrow$ ). The binding affinity constants for the 3 compounds study all matched up well with  $K_a$  determined by the NMR titrations data as well. The binding affinity and thermodynamics parameters of **BB** and adamantane carbocyclic acid in  $\beta$ -CD are shown in Table 5.2.

**Table 5.2.** Binding affinities ( $K_a$ ) and Thermodynamic parameters ( $\Delta H$ ,  $\Delta S$ ) of chiral BBs encapsulation using  $\beta$ -CD determined by ITC. Binding affinities of the encapsulation of chiral BBs using  $\beta$ -CD determined by NMR is compared to ITC values. All measurements were conducted in 0.1 M PBS solutions

Substituent (R)	Binding Constant ( $K_a$ )		Thermodynamic Parameters	
	NMR / $10^3 \text{ M}^{-1}$	ITC / $10^3 \text{ M}^{-1}$	$\Delta H$ / $\text{kJ} \cdot \text{M}^{-1}$	$\Delta S$ / $\text{J} \cdot \text{M}^{-1} \cdot \text{K}^{-1}$
<b>H</b>	$0.8 \pm 3\%$	$1.30 \pm 16\%$	$-14.0 \pm 6\%$	12.4
<b>9-Tolyl</b>	$5.5 \pm 3\%$	$5.30 \pm 29\%$	$-11.2 \pm 5\%$	33.8
<b>9-Fluorophenyl</b>	-	$1.74 \pm 6\%$	$-14.4 \pm 2\%$	13.5
<b>Adamantane carboxylate</b>	-	$35 \pm 14\%$	$-19.3 \pm 4\%$	21.6

The solution-based experiments conducted have determined the binding dynamics of barbaralol to  $\beta$ -CD in solution, however, chiral discrimination between the dynamic enantiomers using  $\beta$ -CD could not be determined using these methods. To determine if there is favoured enantiomer of the dynamic chiral barbaralanes in the solution state by the chiral  $\beta$ -CD, we used the chiral macrocycle as an enantioselective reagent to enantioenrich the oxidation of barbaralol using hydrogen peroxide. Figure 5.20 shows that the oxidation of the encapsulated **BBs** using hydrogen peroxide to produce epoxide **5.10**. The figure illustrates the oxidation of the barbaralol enantiomer (*S*)-**4.4** which converts in the epoxide with the opposition chirality((*R*)-**5.10**), the same is true for the barbaralol enantiomer (*R*)-**4.4** to produce (*S*)-**5.10**. The non-denegrate enantiomerisation of **4.4** is occurring in solution, if  $\beta$ -CD does have a preference enantiomer of **4.4** in solution, there should be an enantio-enrichment of one epoxide products ((*R/S*)-**4.4**).

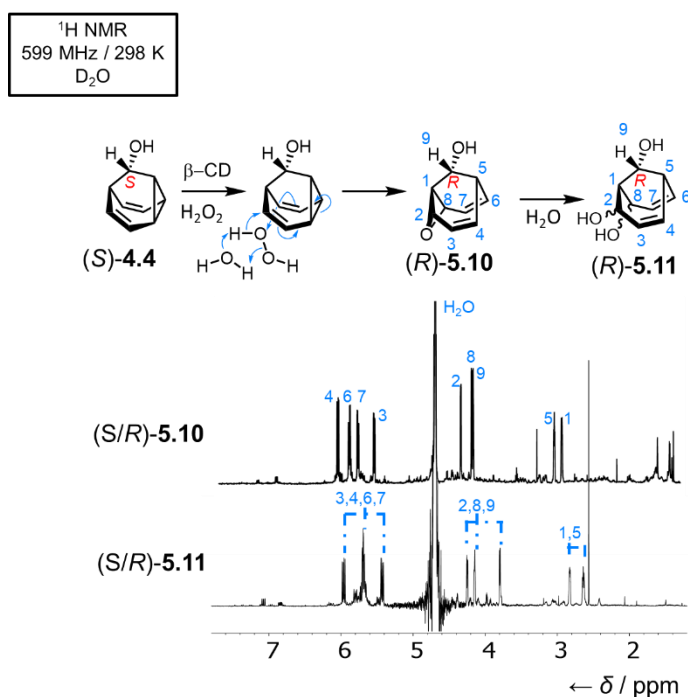


**Figure 5.20.** Enantioselective oxidation of barbaralol **4.4** by using  $\beta$ -CD. The mechanism of the oxidation of **4.4** encapsulated in  $\beta$ -CD using hydrogen peroxide to make an epoxide **5.10** is illustrated.

Screening of enantioselective oxidation conditions to convert chiral **BB 4.4** to epoxide **5.10** using hydrogen peroxide and  $\beta$ -CD as a chiral reagent is highlighted in Table 5.3. The initial oxidation experiments conducted in  $D_2O$  were monitored by NMR, unfortunately the reaction was sluggish with only appreciative amounts of conversion happening after long reaction time ( $> 1$  week). To improve the rate of this oxidation, sodium bicarbonate was used to activate the hydrogen peroxide.<sup>9</sup> This reaction produced many by-products and evidence of the epoxide was present as seen by  $^1H$  NMR (Figure 5.20), however, purification attempts led to decomposition forming the ring open product **5.11** (Figure 5.20). Compound **5.10** could tentatively assign by 2D NMR but unfortunately, we could not confirm by mass spectroscopy. While we could not isolate the original epoxide product pure, the ring product was just as useful as the compound is chiral and the *ee* can be influenced by the control of the enantiomerization of the chiral barbaralol using  $\beta$ -CD. Unfortunately, due to the lack of chromophores present in the ring open product **5.11**, chiral HPLC could not resolve the mixture from the impurities and the enantiomers. The stability issues of this oxidization and the lack of a chromophore has led us to move towards using aryl **9-BBs** to understand the

solution state bias of the enantiomerization of chiral **BBs** using  $\beta$ -CD as a chiral reagent.

**Table 5.3.** Screening of oxidation conditions to convert barbaralol **4.4** to the epoxide **5.10** using  $\beta$ -CD as chiral reagent

Entries	Epoxidation reagent	$\beta$ -CD	Temperature / °C	Reaction time / h	Outcome (%)
1	H <sub>2</sub> O <sub>2</sub> (1.5 eq.)	No	25	16	No reaction
2	H <sub>2</sub> O <sub>2</sub> (1.5 eq.)	No	75	16	No reaction
3	H <sub>2</sub> O <sub>2</sub> (60 eq.)	No	75	24	50 <sup>b</sup>
4	H <sub>2</sub> O <sub>2</sub> (500 eq.)	No	75	24	Decompose
5	H <sub>2</sub> O <sub>2</sub> (500 eq)	No	rt	1.5 weeks	20 <sup>b</sup>
6	H <sub>2</sub> O <sub>2</sub> (1500 eq)	No	rt	1 week	70 <sup>b</sup>
7	H <sub>2</sub> O <sub>2</sub> (1000 eq)	Yes	rt	1 week	5 <sup>b</sup>
8	Oxone (3 eq) <sup>a</sup>	Yes	0→rt	16	40 <sup>b</sup>

(a). Oxidation conditions uses Oxone and acetone to form oxidant.<sup>9</sup> (b) ring open product **5.11** was isolated instead.

## 5.8 Solid-State Analysis of Encapsulation of 9-Barbaralol using $\beta$ -CD

The solution state experiments studying the encapsulation of 9-barbaralol using the chiral macrocycle  $\beta$ -CD did not determine if there is chiral discrimination of the two enantiomers using this system. This is difficult to study due to the small  $\Delta G$  between the two enantiomers, the fluxional nature of barbaralol could not be frozen out using typical VT NMR to enter the slow exchange regime below the coalescence temperature as D<sub>2</sub>O is used the NMR solvent. The freezing of the two enantiomers also could not be determine by DOSY and ITC.

To determine if there are any conditions that allow for favouring of one enantiomer or another using a chiral macrocycle, we grew single crystals of the host-guest complexes to study the solid-state chiral discrimination of the enantiomerisation using  $\beta$ -CD. Crystals of barbaralol, 9-(tolyl)-barbaralol, and 9-(*p*-fluorophenyl)-barbaralol encapsulated by  $\beta$ -CD were obtained by Aisha Bismallah by slow cooling in water which shown in Figures 5.21-5.26. Unmodified cyclodextrin complexes can have a range of binding mode (host-guest: 1:1, 2:1, 1:2, 2:2, etc) with the guest. Our solution state analysis as suggested 1:1 host guest binding in solution. Bohne et al.<sup>10</sup> studied the encapsulation of chiral naphthene with  $\beta$ -CD and determined evidence of 1:1 and 2:2 host-guest complexes with different orientation guests in the macrocycle. This group determined that one of the enantiomers formed host-guest complexes with higher

stability over the other, which demonstrated a chiral recognition process. They did not report a crystal structure of these complexes, the observed chiral recognition was determined by solution studies (NMR, UV, Fluorescence). For our system, we do not have static enantiomers, meaning the dynamics of binding is more complex. For **4.4**, Figure 5.21 shows the 4 isomers of the host guest complex which can come from the enantiomerization of the barbaralol guest and the orientation of the barbaralol in cyclodextrin via 2° and 1° face of the cyclodextrin. Analysis of single crystals of the host:guest complex by single crystal XRD, the crystal structure revealed only one enantiomer is present in the cavity of the molecular in a constant orientation. The (*S*)-**4.4** was present in the crystal and the alcohol group is pointing towards the larger rim 2°. This observation shows that chiral discrimination is process using cyclodextrin is possible in solid-state using a unmodified β-CD. Importantly, this observation validates that original hypothesis of using chiral medium such as chiral macrocycle can influence the enantiomerization of dynamic sp<sup>3</sup>-C chiral barbaralanes, in this case, in the solid state.

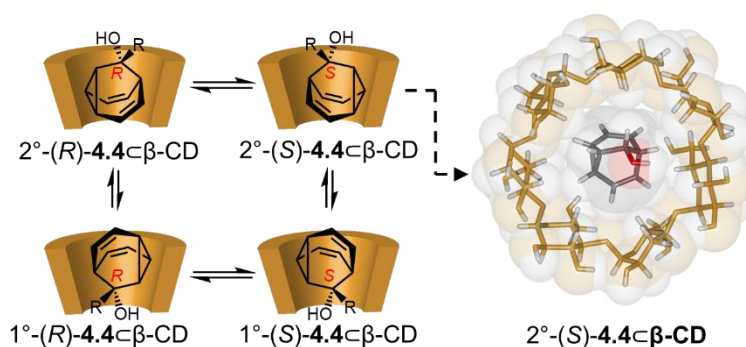


**Figure 5.21.** Crystal Structure of (*R/S*)-**4.4**-[β-CD] showing that there can be 4 states using by orientation and enantiomers.

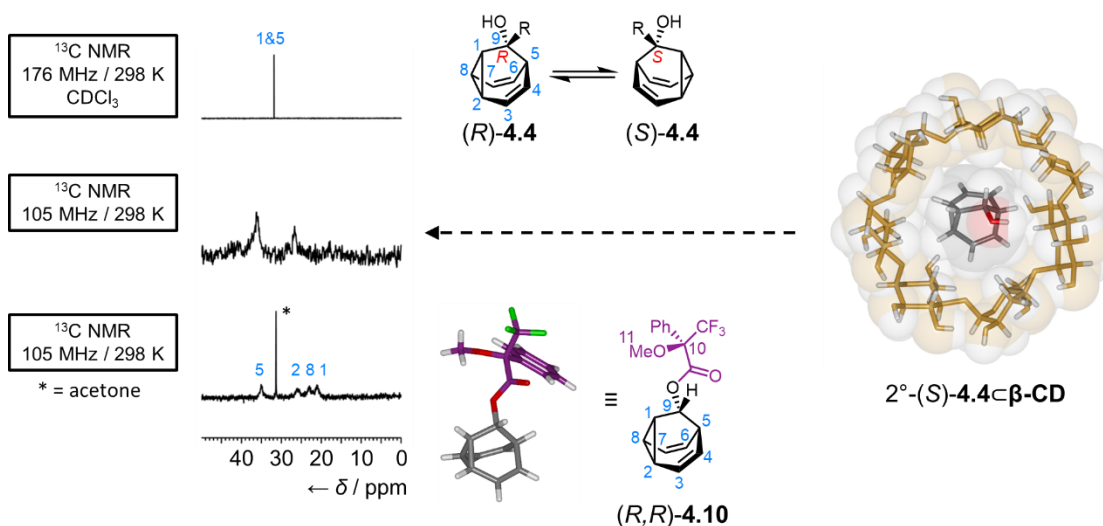


**Figure 5.22.** Comparison of partial  $^{13}\text{C}$  ssNMR of (R/S)-**4.4**,  $2^\circ$ -(S)-**4.4**⊂ $\beta$ -CD, and (R,R)-**4.10**.

It is important to note this crystal structure is determined to 120 K, so in the solid-state, the barbaralol could still be fluxional at ambient temperature. However, there is evidence from the single XRD of **4.4**⊂ $\beta$ -CD that energetic bias to the  $2^\circ$ -(S)-**4.4**⊂ $\beta$ -CD over the 3 other states. To determine if there is fluxional behaviour in solid-state crystal, we used solid-state NMR to obtain  $^{13}\text{C}$  ssNMR of the crystal and compared it to the  $^{13}\text{C}$  NMR of barbaralol **4.4** and Mosher ester **4.10**. For **4.4** in solution, the average carbon signal for  $\text{C}_1$  and  $\text{C}_5$  are overlapped due to dynamic enantiomerisation. For **4.10** in the solid state,  $^{13}\text{C}$  ssNMR, reveal the carbon NMR peaks for aliphatic carbon peaks in the cage is identifiable for  $\text{C}_1$ ,  $\text{C}_2$ ,  $\text{C}_5$ , and  $\text{C}_8$ . This observation means that only one enantiomer, (R,R)-**4.10**, is present in the solid-state crystal that is frozen. For  $2^\circ$ -(S)-**4.4**⊂ $\beta$ -CD, there is an indication of splitting of the aliphatic proton signals of the carbon cage, however, these peaks could not be assigned due to weak carbon signals and broadening.

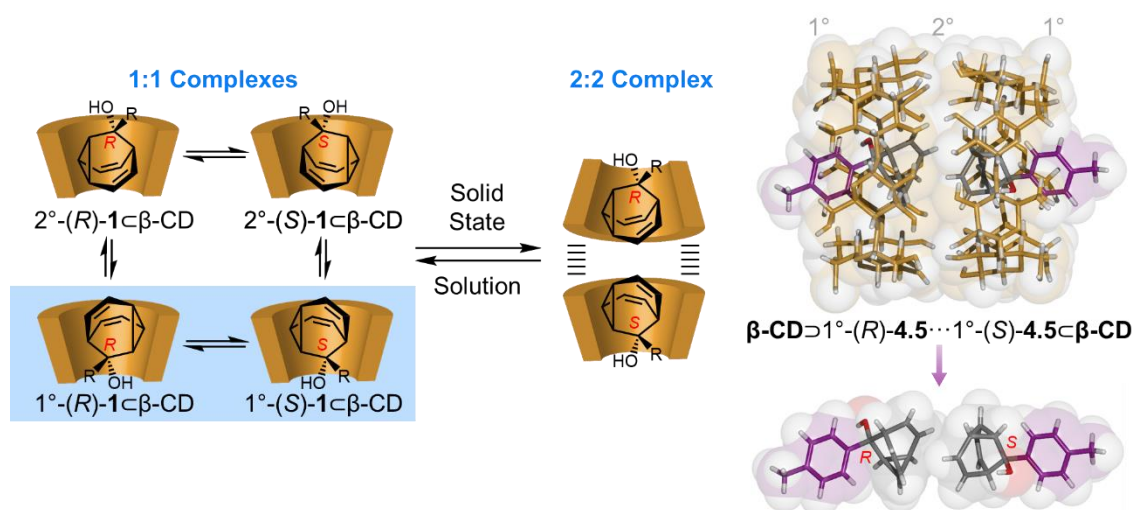


**Figure 5.23.** Crystal Structure of  $1^\circ\text{-(R)-4.5} \subset \beta\text{-CD} \cdots 1^\circ\text{-(S)-4.5} \subset \beta\text{-CD}$  showing that there can be 4 states using by orientation and enantiomers and it crystallizes as a 2:2 complex in a handshake arrangement of R and S inside chiral  $\beta\text{-CD}$  capsule.

When looking at the 9-**BBs** **4.5** and **5.9**, we originally hypothesised that we would see the same 1:1 complexes that have 4 possible host-guest isomers. Figure 5.23-5.24 shows the crystal structure of the 9-(tolyl) and 9-(*p*-fluoro phenyl) **BBs** encapsulated by  $\beta\text{-CD}$ . Both 9-**BBs** form 2:2 complexes in the solid-state crystal packing. In both host guest complexes, it is dimer of **BBs** where it is mismatch of *R* and *S* of the dynamic chiral centre. These dimers repeat throughout the crystal structure moving through unit cell. For 2:2 HG complex of chiral 9-**BBs** and  $\beta\text{-CD}$ , there are 10 possible host guest isomers highlighted in Figure 5.25. For the tolyl **BBs**, the steric bulk of the methyl group on phenyl ring flips the orientation of the **BB** in the macrocycle where the tolyl group and hydroxy group points out of the smaller opening  $1^\circ$ . The vinyl arms of the barbaralanes have van der Waals interactions which could have contributed to resolved single HG isomer in the solid state, illustrating an example of shape-selective crystallization. For the fluoro **BBs**  $\beta\text{-CD}$  (Figure 5.24), the aryl groups and hydroxy group are pointing out of the larger opening  $2^\circ$ , like **4.4**, however, the interactions of the aryl rings could show the bias of this single isomer, illustrating another example of shape-selective crystallisation. This is also an example of chiral discrimination bias that was done with an unmodified  $\beta\text{-CD}$ .

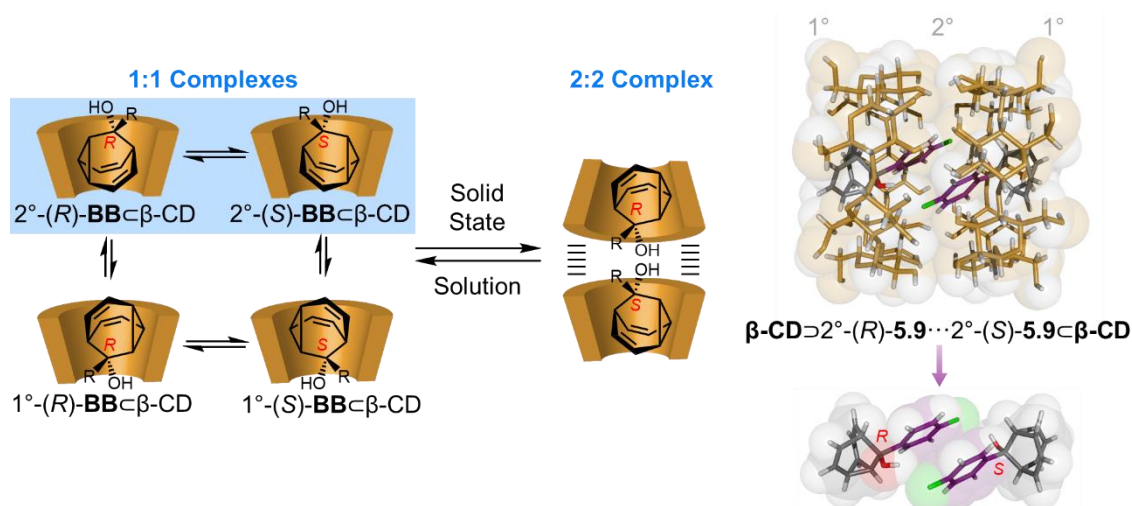


**Figure 5.24.** Crystal Structure of  $2^\circ\text{-(R)-5.9}\beta\text{-CD}\cdots 2^\circ\text{-(S)-5.9}\beta\text{-CD}$  showing that there can be 4 states using by orientation and enantiomers and it crystallizes as a 2:2 complex in a handshake arrangement of R and S inside chiral  $\beta$ -CD capsule.

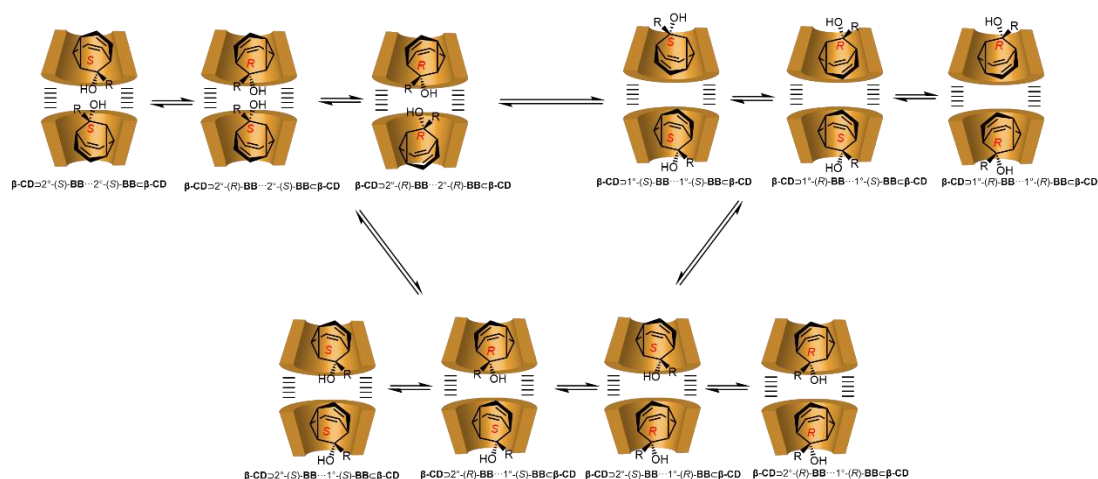


**Figure 5.25.** Schematic illustrating 2:2 complexes of  $\beta$ -CD and chiral 9-BBs showing 10 possible orientations.

## 5.9 Conclusion and Outlook

For dynamic regioisomerism, studies to test a series of 9-BBs (4.4-4.5) and 1,9-BBs (5.6-5.8) to the encapsulation by a metallocage, 5.1. The metallocage 5.1 was synthesised from Pd precursor and triazine ligands and was structurally confirmed by solution state NMR and single crystal XRD. In solution, the control encapsulation experiments using 4.5 was conducted and analysis by classic supramolecular NMR titration revealing up to two 9-BBs (4.5) can fit in the cage (HG, HG2) with cooperative binding model, determined by using the online Bindfit software designed to find binding association constants. 1,9-BBs of interest to understand dynamic regioisomerism in a confined space, in solution was studied by solution state NMR

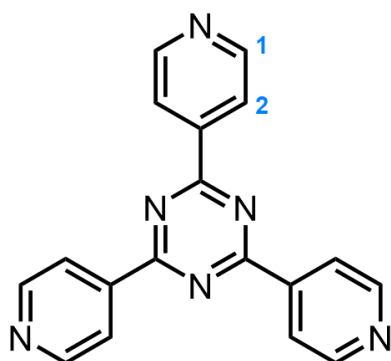
after a series of encapsulation reactions. Unfortunately, the binding affinity was determined to be poor as encapsulation yields showed minimal incorporation of the 1,9-**BBs**. In solid-state, a series of crystallisation conditions were attempted either through crystallisation tubes or high throughput method using 24 well plates for crystallisation, however no successful host-guest complexes crystals were determined. Issues of this system were the sensitive nature of the molecular cage crystals that easily decompose which indicated a weak crystal lattice, and the dilute condition for crystallisation that hindered probability. Fujita et al. developed a methodology of crystallisation of guests inside “crystallisation sponge” or a metal organic framework using the same triazine ligand **5.3** with a cobalt NCS vertices.<sup>11</sup> This MOF has the same cavity structure as the metallocage **5.1**, however the crystal lattice should be more stable allowing for the neat melt method to be viable. Future work will be done to explore this crystallisation sponge option to study dynamic regioisomerism of barbaralanes in the solid state.

For the control of the dynamic  $sp^3$ -C of barbaralanes using chiral macrocycle ( $\beta$ -CD) via self-assembly, we studied a series of chiral barbaralols (**4.4**, **4.5**, **5.9**) for this purpose. Classic supramolecular NMR titration experiments of these chiral barbaralols were conducted by a previous group member, Dr. Aisha Bismillah, and it was determined that the host:guest complexation is 1:1 HG interaction in solution. This binding association constant was determined by using Bindfit software. The binding interactions were further studied using ITC to determine the thermodynamic parameters ( $\Delta H$ ,  $\Delta S$ ) of binding as well as the binding association constant. The 1:1 HG complexation determined by NMR titration was verified using ITC and the binding interactions are determined by non-classical hydrophobic driving force. Solution-state physical characterisation could not determine if the enantiomerisation of chiral barbaralols is influenced by encapsulation using  $\beta$ -CD. Enantioselective oxidation of chiral barbaralols were attempted using hydroperoxide and  $\beta$ -CD as chiral reagent. The reaction was sluggish to lead to the epoxide product **5.10**, however the purified product could not be isolated, it is reasoned that it undergoes a ring opening process to make **5.11** which could be assigned by NMR but could not be isolated as purification is difficult, especially without a chromophore. Solid-state analysis of single crystals for **4.4**, **4.5**, and **5.9** encapsulated by  $\beta$ -CD were determined. For **4.4**, of 4 possible isomers

(orientational, enantiomers) only one is present which showing that the enantiomerisation can be biased by  $\beta$ -CD encapsulation. For **4.5** and **5.9**, 2:2 complexes of the *R/S* mismatch were found in the crystal structure which is one of 10 possible HG isomers. All three crystal structures are examples of shape-selective crystallisation driving the enantiomerisation influence in the macrocycle. Future work towards determining solution state evidence of enantiomerisation preference in the chiral macrocycle involves moving towards using the 9-**BBs** (**4.4** & **4.5**) which has evidence of constitutional bias in solid state and the presence of the chromophore will aid in purification using HPLC.

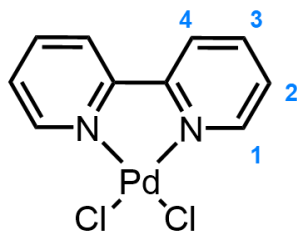
## 5.10 Experimental

### 5.10.1 Synthesis



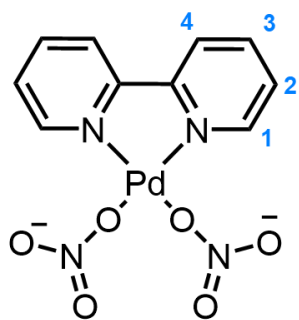
**2,4,6-tri(4-pyridyl)-1,3,5-triazine.** 4-cyanopyridine (10 g, 96.1 mmol), 18-crown-6 (1.0 g, 3.8 mmol), potassium hydroxide (225 mg, 4.0 mmol) and decalin (10 mL) were added in an oven-dried round-bottomed flask fitted with a septum under a N<sub>2</sub> atmosphere stirred at 200 °C under N<sub>2</sub> for 3 h. Once reaction cooled to rt, the oily residue was dissolved in 2 M HCl

solution (250 mL) and passed through a celite filter to remove any insoluble material. The solution obtained was then neutralized with 5 M NaOH producing a pink solid crude. This solid was recrystallized in ethanol (475 mL) to give the title compound as a off white solid (723 mg, 2.32 mmol, 3 %). <sup>1</sup>H NMR (400 MHz, CDCl<sub>3</sub>) δ 8.94 (d, *J* = 5.7 Hz, 6H, H<sub>2</sub>), 8.56 (d, *J* = 5.7 Hz, 6H, H<sub>1</sub>). Spectroscopic data were consistent with those previously reported.<sup>2</sup>

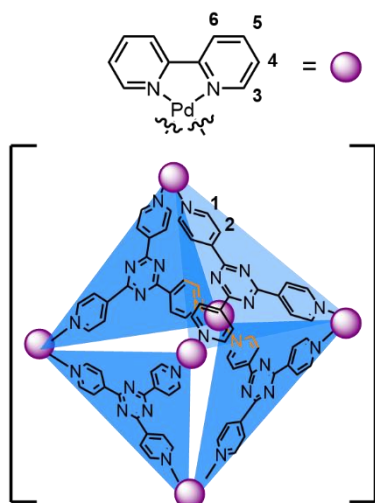


**(2,2'-Bipyridine)dichloropalladium(II).** PdCl<sub>2</sub> (0.90 g, 5.08 mmol) was added to a 250 mL round-bottomed flask and was suspended in MeCN (150 mL). The mixture was heated to reflux for 1h and was filtered hot to remove insoluble material from the solution. 2,2 bipyridyl (0.81 g,

5.19 mmol) was dissolved in MeCN (20 mL) and was added to the reaction mixture and stirred for 1 h at rt. The precipitate was collected and washed with MeCN (50 mL) to give the title compound as an orange solid (1.35 g, 4.07 mmol, 79%). <sup>1</sup>H NMR (400 MHz, DMSO-*d*<sub>6</sub>) δ 9.12 (d, *J* = 5.8 Hz, 2H, H<sub>4</sub>), 8.58 (d, *J* = 8.0 Hz, 2H, H<sub>1</sub>), 8.36 (t, *J* = 7.8 Hz, 2H, H<sub>2</sub>), 7.81 (t, *J* = 6.7 Hz, 2H, H<sub>3</sub>). Spectroscopic data were consistent with those previously reported.<sup>2</sup>

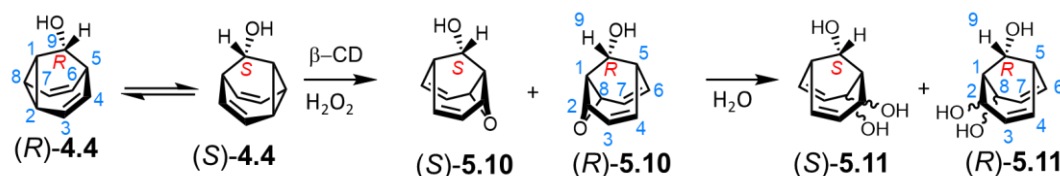


**(2,2'-Bipyridine)dinitropalladium(II).** Pd(bipy)Cl<sub>2</sub> (1.01 g, 3.03 mmol) was added to 500 mL round-bottomed flask and was suspended in MeCN (1.2 L). AgNO<sub>3</sub> (1.03 g, 6.06 mmol) was added to the reaction mixture and left to stir at rt overnight. The precipate (AgCl) was removed *via* celite filter and the solution was dried *in vacuo* to give the title compound a yellow solid (1.11 g, 2.87 mmol, 95%). <sup>1</sup>H NMR (400 MHz, D<sub>2</sub>O) δ 8.33 – 8.21 (m, 4H, H<sub>3</sub> and H<sub>4</sub>), 8.22 (d, *J* = 5.9 Hz, 2H, H<sub>1</sub>), 7.70 (t, *J* = 6.8 Hz, 2H, H<sub>2</sub>). Spectroscopic data were consistent with those previously reported.<sup>2</sup>



**M<sub>6</sub>L<sub>4</sub> Cage.** Pd(bipy)(NO<sub>3</sub>)<sub>2</sub> (12 mg, 0.03 mmol) and 2,4,6-tri(4-pyridyl)-1,3,5-triazine (6.3 mg, 0.02 mmol) was added to 2 – 5 mL microwave vial. Water/MeCN 4:1 solution (4 mL) was added to the reaction vessel and the solution was heated to 60 °C for 1 h. The solution was added to centrifuged and filtered using a syringe filter (0.2 μm). The solvent was removed *in vacuo* to give the title compound pale yellow solid (39 mg, 0.01 mmol, 53%). <sup>1</sup>H NMR (400 MHz, D<sub>2</sub>O) δ 9.46 (d, *J* = 6.0 Hz, 24H, H<sub>2</sub>), 8.90 (d, *J* = 6.0 Hz, 24H, H<sub>2</sub>), 8.49 (d, *J* = 8.3 Hz, 12H, H<sub>6</sub>), 8.38 (t, *J* = 7.9 Hz, 12H, H<sub>4</sub>), 7.70 (d, *J* = 5.8 Hz, 12H, H<sub>3</sub>), 7.59 (t, *J* = 6.8 Hz, 12H, H<sub>5</sub>). Spectroscopic data were consistent with those previously reported.<sup>2</sup>

### 5.10.2 Enantioselective Oxidation Encapsulation of Barbaralols using β-CD



Barbaralol (1 equiv.) was added to β-CD (1.5 equiv.). The solids were dissolved in H<sub>2</sub>O (0.7 mL per 10 mg of barbaralol). The mixture was then heated to 80 °C for 2 h before cooling to rt. NaHCO<sub>3</sub> (10 – 20 equiv.) was then added to the mixture and allowed to

stir for 15 min. 30% w/v  $\text{H}_2\text{O}_{2(\text{aq})}$  (20 equiv.) was then added to the mixture which was allowed to stir for 48 h, after which a 7:3  $\text{CHCl}_3$ : $i$ PrOH mixture was added and the product extracted ( $3 \times 10$  mL). The combined organic extracts were dried over  $\text{MgSO}_4$  and the solvent was removed under reduced pressure. The crude residue was purified by column chromatography (Teledyne Isco CombiFlash Rf+ system, 12 g C18,  $\text{H}_2\text{O}$ – $\text{MeOH}$ , gradient elution). Pure product (*S/R*)-**5.10** could be obtained as decomposition to (*S/R*)-**5.11**.

### 5.10.3 ITC experiments

Isothermal titration calorimetry (ITC) experiments were performed using a Microcal ITC- 200 instrument (Malvern). Barbaralol samples were dialysed into PBS using SpectraPor dialysis tubing (MWCO 2.5– 3 kDa, SpectrumLabs).  $\beta$ -CD samples were dialysed against MilliQ  $\text{H}_2\text{O}$ , lyophilised and dissolved in the same buffer solution. The reference cell was filled with Milli-Q water and the analysis cell filled with Barbaralol solution. Both cells were allowed to reach thermal equilibrium at 293 K before titration. Titrations consisted of a first 0.5  $\mu\text{L}$  injection followed by 23 injections of 2.0  $\mu\text{L}$  aliquots of B. Separate titrations of the binding partner (*i.e.*  $\beta$ -CD) into buffer were used to assess the heat of dilution. The data were baseline-corrected in NITPIC<sup>12,13</sup> and fitted in SEDPHAT using a one-set of sites model.

Single crystal XRD were obtained by Dr. Aisha Bismillah and data for the crystal structures of the  $\text{BB} \subset \beta\text{-CD}$  are published.<sup>14</sup>

## 5.11 References

- 1 A. N. Bismillah, J. Sturala, B. M. Chapin, D. S. Yufit, P. Hodgkinson and P. R. McGonigal, *Chem. Sci.*, 2018, **9**, 8631–8636.
- 2 T. Kusukawa and M. Fujita, *J. Am. Chem. Soc.*, 2002, **124**, 13576–13582.
- 3 M. Yoshizawa, M. Tamura and M. Fujita, *Science*, 2006, **312**, 251–254.
- 4 E. G. Percástegui, T. K. Ronson and J. R. Nitschke, *Chem. Rev.*, 2020, **120**, 13480–13544.
- 5 P. Thordarson, *Chem. Soc. Rev.*, 2011, **40**, 1305–1323.
- 6 N. Chayen, and E. Saridakis, *Nat. Methods*, 2008, **5**, 147–153.
- 7 Q. Da Hu, G. P. Tang and P. K. Chu, *Acc. Chem. Res.*, 2014, **47**, 2017–2025.
- 8 M. Rekharsky and Y. Inoue, *J. Am. Chem. Soc.*, 2000, **122**, 4418–4435.
- 9 H. Yao and D. E. Richardson, *J. Am. Chem. Soc.*, 2000, **122**, 3220–3221.
- 10 H. Tang, A. S. M. Sutherland, L. M. Osusky, Y. Li, J. F. Holzwarth and C. Bohne, *Photochem. Photobiol. Sci.*, 2014, **13**, 358–369.
- 11 Y. Inokuma, T. Arai and M. Fujita, *Nat. Chem.*, 2010, **2**, 780–783.
- 12 T. H. Scheuermann and C. A. Brautigam, *Methods*, 2015, **76**, 87–98.
- 13 S. Keller, C. Vargas, H. Zhao, G. Piszczek, C. A. Brautigam and P. Schuck, *Anal. Chem.*, 2012, **84**, 5066–5073.
- 14 A. Bismillah, *Durham theses*, 2019 Durham University.